Imperial College London

Carbon Electrode for the Oxygen Reduction Reaction

Jingyu Feng

Imperial College London

Department of Chemical Engineering

A thesis submitted for the degree of Doctor of Philosophy

DECLARATION OF ORIGINALITY

I, Jingyu Feng, confirm that the research included within this thesis is my work or that where it has been carried out in collaboration with or supported by others, this is duly acknowledged and my contribution indicated. Parts of this work have been published in peer-reviewed journals, as stated in the List of Publications.

COPYRIGHT DECLARATION

ACKNOWLEDGEMENT

This thesis is submitted in partial fulfilment of the PhD degree requirements from the Imperial College London. The work presented here was performed at the Department of Chemical Engineering, Imperial College London (ICL) and School of Engineering and Materials Science, Queen Mary University of London (QMUL). The project was performed under the supervision of Professor Magda Titirici. The scholarship was awarded from China Scholarship Council (CSC), ICL and QMUL, which enable me to pursue my PhD.

Firstly, I want to thank my supervisor, Professor Maria-Magdalena Titirici, for her guidance and provided me with immeasurable opportunities for collaborations, research facilities, and career developments. I could not have hope for a more inspiring, creative, and supportive work environment. Also, I want to thank Professor Qiang Zhang and the students from his group Dr Tang Cheng, Dr Haofan Wang, Xiaoru Chen, Changxin Zhao, Zhihe Zhang, Jiaxing Li, and Pengyu Chen, it was great to work and chatted with you, which inspired my initial PhD works. I also want to thank Dr Min Yu, Wei Xiong, Man Zhang, Dr Haixue Yan, Dr Haixue Yan, Dr Han Zhang, Dr Jian Yao, Dr Yi Liu, Dr Ana Jorge and her group from QMUL for their collaborations, discussions, and support. Moreover, I want to thank Dr Xiaoqiang Liang for the discussions from the chemistry aspect. I want to thank Dr Bhoopesh, Luke Higgins from the University of Leeds, to support the XAS characterizations. Furthermore, I would like to thank Prof Sarah Haigh and Dr Rongsheng Cai from the University of Manchester to support the STEM characterizations. Meanwhile, I want to thank Emanuele Magliocca, Zahra Rana, Dr Rhod Jervis, Dr Thomas Miller, Prof Dan Brett from University College London for testing alkaline electrolyte membrane fuel cell, performing computer tomography, and many fruitful discussions. I want to thank Dr Andi Di and Zhenyu Guo for the SAXS test and data analysis. Dr Yuanhao Wu from the University of Nottingham for the collaboration and discussion on self-assembly. Dr Barun Chakrabarti from the University of Warick to collaborate on the redox

flow cells project. Dr Arun Periasamy from the University of Surrey for sharing his knowledge and providing guidance. I want to thank Gang Cheng and Prof Cecilia Mattevi from ICL to support XPS measurements. Miralem Salihovic for providing me with hollow carbon spheres. Dr Sivaprakash Sengodan and Tse-Wei Chen for sharing perovskite knowledge. Moreover, I want to thank master and undergraduate students I supervised, Giulio Romario, India Wild, Temiloluwa Majekodunmi, Luye Hou, and many other lovely tutees.

Most importantly, I want to thank my group colleagues, Dr Hui Luo, Dr Kathrin Preuss, Dr Servann Herou, Dr Fei Xie, Dr Philipp Schlee, Dr Alain Li, Dr Heather Au, Dr Saurav Sarma, Dr Maria Crespo, Ruixuan Chen, Zhen Xu, Sabina Nicolae, Pierpaolo Modugno, Mengnan Wang, Angus Pedersen, Simon Kellner, Silvia Favero, Yue Xu, Qian Guo, Richard Lobo, Dr Jesus Barrio, and Yan Yang. My Doctoral journey would not have been the same without the support and companionship of all my friends and colleagues. Lastly, I want to thank my parents and families for their endless support and encouragement.

ABSTRACT

This PhD thesis presents work on developing freestanding carbon electrodes for the oxygen reduction reaction application cost-effectively and sustainably. Within different alternatives to the high-cost Pt catalysts, heteroatoms and transitional metals modified carbon electrocatalysts have shown great promise to reduce the use of Pt. Meanwhile, synthesising freestanding catalysts has drawn interest due to the advantages of being binder-free, fewer manufacturing steps, and high recyclability. The first part of this thesis focuses on synthesising a freestanding carbon electrode with a hierarchical porosity and abundant nitrogen-doped sites. The carbon electrodes were synthesised through hydrothermal carbonization, followed by a pelleting process and further carbonization. Uniformly dispersed nitrogen sites and high specific surface area were obtained for the carbon electrodes. The electrochemical activity showed high stability in the freestanding configuration, and I found only the surface of electrode was reducing oxygen. The second part focuses on improving the carbon electrode's catalytic performance via post functionalization of the as-obtained nitrogen-doped carbon electrodes. Functionalization was carried out by immersing the carbon electrode into Fe solutions and followed by carbonization. The Fe was found to exist mainly as single sites. The electrochemical performance showed doubled current density compared to without Fe, and 100,000 s (27.77 h) stability was observed at 0.5 V. Through ex-situ X-ray absorption spectroscopy and electron paramagnetic resonance studies, Fe sites were found responsible for reducing oxygen. The third part focuses on the scalable synthesis of a low-cost iron, nitrogen co-doped carbon. Powdered iron, nitrogen co-doped carbon catalysts was prepared by hydrothermal carbonization and high-temperature post carbonization. FeN_4 was found to be the main iron existing form in the obtained catalysts. Two different precursors containing Fe^{2+} and Fe^{3+} are compared. Both chemical and structural differences have been observed in

catalysts starting from Fe^{2+} and Fe^{3+} precursors. Furthermore, this catalyst is studied in an anion exchange membrane fuel cell.

LIST OF PUBLICATIONS

Included in the results section

Feng J.; Luo H.; Jervis R.; Di A.; Guo Z.; Cheng G.; Wang H.; Mattevi C.; Zhang Q.; Titirici M., Miniaturised metal-free, N-doped freestanding electrode for the application of oxygen reduction reaction. In preparation. (It includes most of the results from Chapter 3)

Feng J.; Higgins L.; Cai R.; Pedersen A.; Luo H.; Guo Z.; Cheng G.; Wang H.; Mattevi C.; Zhang Q.; Mishra B.; Titirici M., Miniaturised PGM-Free, Fe, N co-doped freestanding electrode for the application of oxygen reduction reaction. In preparation. (It includes most of the results from Chapter 4)

Feng J.; Cai R.; Magliocca E.; Luo H.; Higgins L.; Romario G. L. F.; Liang X.; Pedersen A.; Xu Z.; Guo Z.; Periasamy A.; Brett D.; Miller T.S.; Haigh S.J.; Mishra B.; Titirici M.M., Iron, nitrogen co-doped carbon spheres as low cost, scalable electrocatalysts for the oxygen reduction reaction. Adv. Funct. Mater., accepted manuscript. (It includes most of the results from Chapter 5)

Co-Published

Guo, Z.; Xu, Z.; Xie, F.; **Feng, J.**; Titirici, M., Strategies for High Energy Density Dual-Ion Batteries using Carbon-based Cathodes. Advanced Energy and Sustainability Research 2021, 2100074.

Ramadan, S.; Lobo, R.; Zhang, Y.; Xu, L.; Shaforost, O.; Kwong Hong Tsang, D.; **Feng, J.**; Yin, T.; Qiao, M.; Rajeshirke, A.; Jiao, L. R.; Petrov, P. K.; Dunlop, I. E.; Titirici, M.-M.; Klein, N., Carbon-Dot-Enhanced Graphene Field-Effect Transistors for Ultrasensitive Detection of Exosomes. ACS Appl. Mater. & Inter. 2021, 13 (7), 7854-7864.

Xiong, W.; Porwal, H.; Luo, H.; Araullo-Peters, V.; **Feng, J**.; Titirici, M.-M.; Reece, M. J.; Briscoe, J., Photocatalytic activity of 2D nanosheets of ferroelectric Dion–Jacobson compounds. J. Mater. Chem. A 2020, 8 (14), 6564-6568.

Wu, Y.; Okesola, B. O.; Xu, J.; Korotkin, I.; Berardo, A.; Corridori, I.; di Brocchetti, F. L. P.; Kanczler, J.; **Feng, J.**; Li, W., Shi, Y.; Farafonov, V.; Wang, Y.; Thompson, R.; Titirici, M.-M.; Nerukh, D.; Karabasov, S.; Oreffo, R.; Rodriguez-Cabello J.C.; Vozzi, G.; Azevedo, H.;

Pugno, N.M.; Wang, W.; Mata, A., Disordered protein-graphene oxide co-assembly and supramolecular biofabrication of functional fluidic devices. Nat. Commun. 2020, 11 (1), 1-12.

Luo, H.; Liu, Y.; Dimitrov, S. D.; Steier, L.; Guo, S.; Li, X.; **Feng, J.**; Xie, F.; Fang, Y.; Sapelkin, A., Pt single-atoms supported on nitrogen-doped carbon dots for highly efficient photocatalytic hydrogen generation. J. Mater. Chem. A 2020, 8 (29), 14690-14696.

Jorge, A. B.; Jervis, R.; Periasamy, A. P.; Qiao, M.; **Feng, J.**; Tran, L. N.; Titirici, M.-M., 3D Carbon Materials for Efficient Oxygen and Hydrogen Electrocatalysis. Adv. Energy Mater. 2020, 10 (11), 1902494. (Parts of review are included in Chapter 2)

Chakrabarti, B. K.; **Feng, J.**; Kalamaras, E.; Rubio-Garcia, J.; George, C.; Luo, H.; Xia, Y.; Yufit, V.; Titirici, M.-M.; Low, C. T. J.; Kucernak, A.; Brandon, N. P., Hybrid Redox Flow Cells with Enhanced Electrochemical Performance via Binderless and Electrophoretically Deposited Nitrogen-Doped Graphene on Carbon Paper Electrodes. ACS Appl. Mater. & Inter. 2020, 12 (48), 53869-53878.

Xie, F.; Xu, Z.; Jensen, A. C.; Ding, F.; Au, H.; **Feng, J.**; Luo, H.; Qiao, M.; Guo, Z.; Lu, Y., Unveiling the role of hydrothermal carbon dots as anodes in sodium-ion batteries with ultrahigh initial coulombic efficiency. J. Mater. Chem. A 2019, 7 (48), 27567-27575.

Luo, H.; Papaioannou, N.; Salvadori, E.; Roessler, M. M.; Ploenes, G.; van Eck, E. R.; Tanase, L. C.; **Feng, J.**; Sun, Y.; Yang, Y., Manipulating the optical properties of carbon dots by fine-tuning their structural features. ChemSusChem 2019 12 (19) 4432-4441.

Chakrabarti, B.; Yufit, V.; Kavei, A.; Xia, Y.; Stevenson, G.; Kalamaras, E.; Luo, H.; **Feng, J.**; Tariq, F.; Taiwo, O., Charge/discharge and cycling performance of flexible carbon paper electrodes in a regenerative hydrogen/vanadium fuel cell. Int. J. Hydrog. 2019, 44 (57), 30093-30107.

Yu, M.; Picot, O. T.; Saunders, T. G.; Dlouhý, I.; **Feng, J.**; Titirici, M.-M.; Mahajan, A.; Reece, M. J., Graphene-reinforced silicon oxycarbide composites prepared by phase transfer. Carbon 2018, 139, 813-823.

Wang, H.-F.; Chen, R.; **Feng, J.**; Qiao, M.; Doszczeczko, S.; Zhang, Q.; Jorge, A. B.; Titirici, M.-M., Freestanding Non-Precious Metal Electrocatalysts for Oxygen Evolution and Reduction Reactions. ChemElectroChem 2018, 5 (14), 1786-1804. (Parts of this review are included in section 2.3)

CONTENTS

ACRONYMS

BET	Brunauer, Emmett and Teller
CA	Chronoampertary
CF	Carbon fibre
CNF	Carbon nanofibre
CS	Carbon sphere
CT	Computed tomography
CV	Cyclic voltammogram
DFT	Density functional theory
DOE	U.S. Department of energy
EDS	Energy-dispersive X-ray
EIS	Electrochemical impedence spectroscopy
EPR	Electro paramagnetic resounce
EXAFS	Extend X-ray adsorption fine spectroscopy
FTIR	Fourier transform infrared
HAADF-STEM	High-angle annular dark-field – scanning transmission electron microscopy
ICP-MS	Inductively coupled plasma mass spectrometry
LSV	Linear sweep voltammogram
MS	Mass spectrometry/ mass spectrometric
ORR	Oxygen reduction reaction
PSD	Pore size distribution
RT	Room temperature
SAXS	Small angle X-ray scattering
SEM	Scanning electron microscopy
SSA	Specific surface area
STEM	Scanning transmission electron microscopy
TEM	Transmission electron microscopy
T_g	Glass transition temperature
TGA	Thermogravimetry/ thermogravimetric analysis
WAXS	Wide angle X-ray scattering
XANES	X-raw adsorption near edge spectroscopy
XAS	X-ray adsorption spectroscopy

XPS	X-ray photoelectron spectroscopy
XRD	X-ray diffraction

LIST OF FIGURES

LIST OF TABLES

Chapter 1

INTRODUCTION

1.1 THE NEED FOR RENEWABLE ENERGY

Fossil fuels have dominated recent energy generation and the petrochemical industry to satisfy our daily demands since the first industrial revolution. Most of the technologies developed from then heavily depend on the energy exploitation of fossil fuel, resulting in an increasing demand for fossil fuel and excessive emissions of CO_2. International Energy Agency (IEA) recorded that the global annual energy consumption and CO_2 emission have increased approximately 59 % and 62 % over the last 30 years[1]. With this increasing amount of CO_2 released into the atmosphere, heat caused by infrared radiation has been trapped by the CO_2, and excessive CO_2 starts dissolving into the ocean, abetting global warming[2] and ocean acidification[3]. If the carbon dioxide emission stays on the current status without change, the global annual energy consumption and CO_2 emissions will reach around 14.5 TWy and 35.1 Gt in 2030[1] (**Figure 1.1a**). As projected by International Panel on Climate Change (IPCC), global warming is likely to reach a 1.5 °C increase between 2030 and 2052 compared to the pre-industrial level[4]. Besides, the average pH of the ocean surface will decline to 7.949 in 2050, which means a 69.8 % increase of H^+ concentration relative to the pre-industrial pH level[5] (**Figure 1.1b**). These will significantly impact rainfall patterns, coastal erosion, endanger the ocean creatures, and alter the ranges of some infectious diseases, some of which are already happening worldwide.[6-8] Facing all these evidences, decarbonising the global economy via the implementation of sustainable and environmentally benign technologies across all sectors has become a must-do now for the benefit of future generations who should be inspired to carry on.

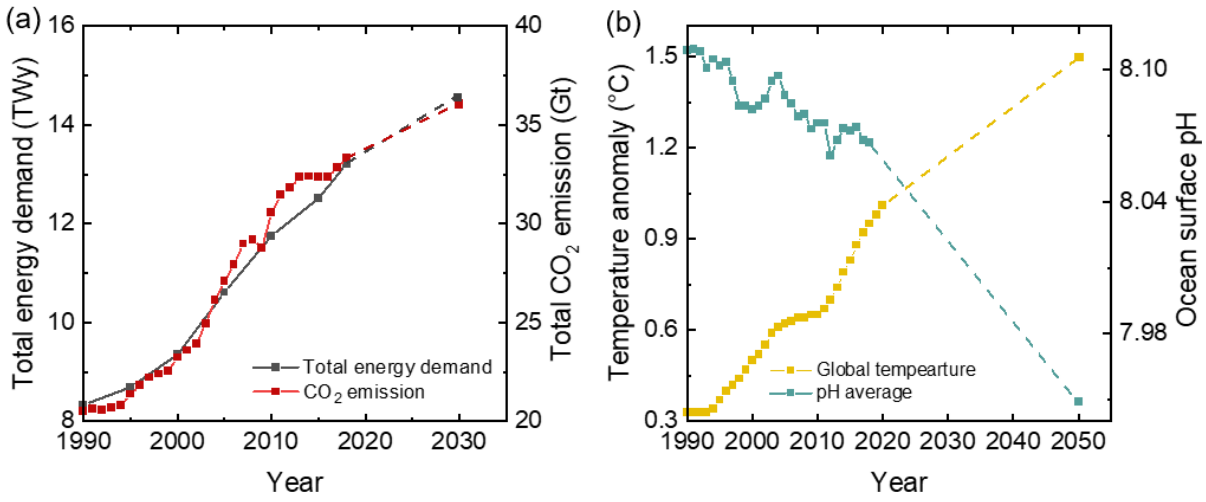

Figure 1.1 (a) Worldwide total energy consumption and CO_2 emissions from 1990 to 2020 and projected total energy consumption/CO_2 emission in 2030; (b) global temperature change relative to the pre-industrial level and ocean surface pH value since over the last 30 years. Data source: IEA[1], NASA, IPCC[4], Dore et al.[9], and Orr et al.[5]

To prevent catastrophic scenarios caused by the increasing CO_2 level, most countries have made pledges, and some of the significant economies have taken actions to limit the rise of CO_2 emissions (**Figure 1.2a**).[10] Significantly, Paris Agreement has united 196 countries set a global warming goal to keep the global average temperature below 1.5 °C (preferable) or 2 °C compared to the pre-industrial level.[11] However, it is frustrating to see the average CO_2 emissions still reached 414.24 ppm with an increasing growth rate of 2 - 3 ppm per year (**Figure 1.2b**). In addition, the CO_2 emission from most sectors also showed a steadily increasing rate over the last decades, in which electricity and heat producers account for the major CO_2 emission sources (**Figure 1.2c**). To reach the net-zero goal, CO_2 emissions from all sectors need to be reduced dramatically from current status to lower than 2 Tton carbon emission by 2050 (**Figure 1.3a**). The CO_2 emission from electricity and heat sectors accounts for the most significant CO_2 emission, need to be reduced ~ 60% by 2030 compared with 2019, and followed by full decarbonisation by 2040.[1]

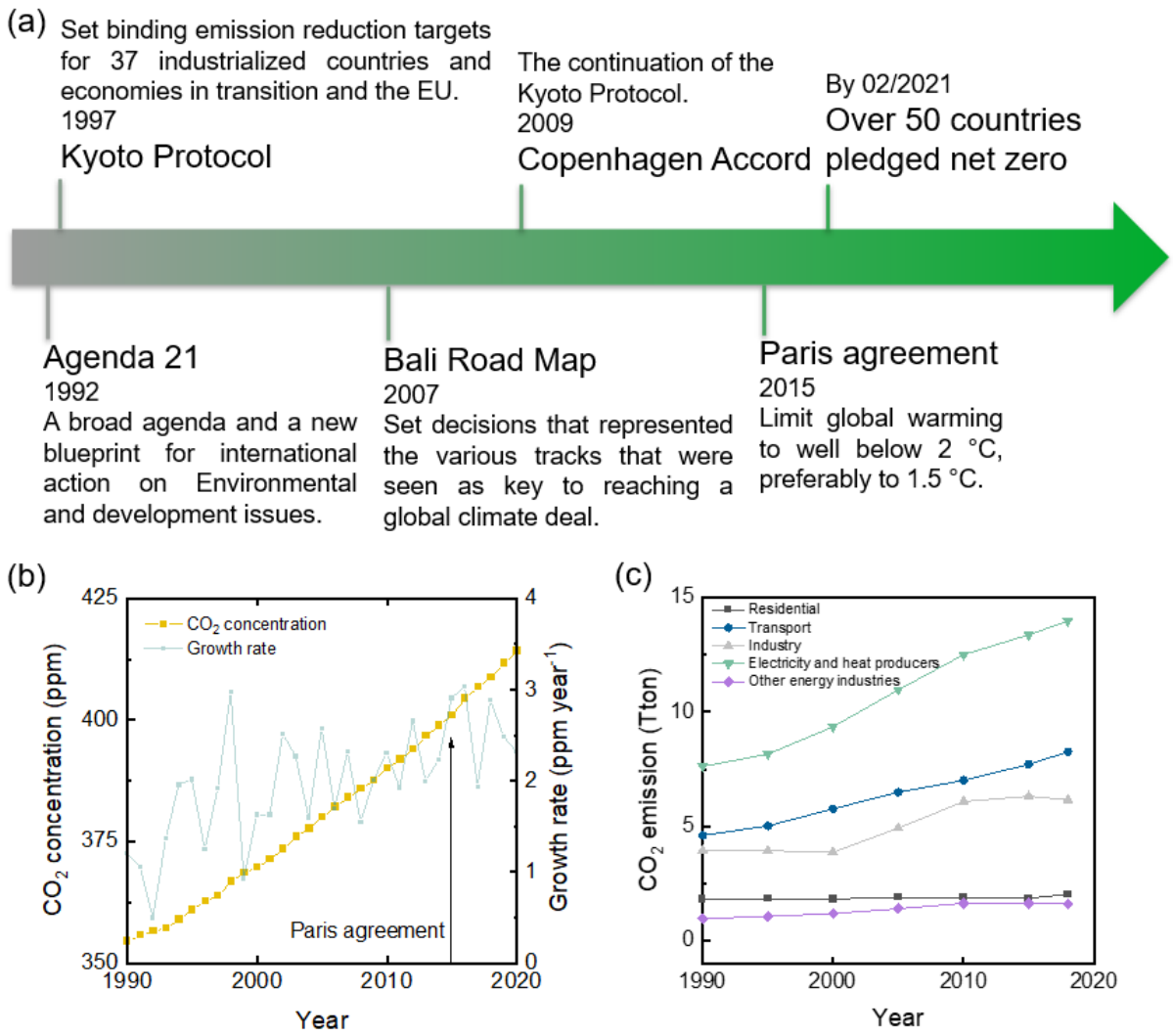

Figure 1.2 (a) The timeline of international actions for carbon neutrality. (b) Average CO_2 concentration and its growth rate record from 1990 to 2020, measured at Mauna Loa Observatory, Hawaii. Data were taken from ref[12] (gml.noaa.gov/ccgg/trends/mlo.html). (c) Worldwide CO_2 emission from the different sectors in 1990 to 2019, data taken from IEA[1].

To fulfil the decarbonization goals, the energy supply sources need to be shifted to renewable energy (**Figure 1.3b**), such as solar, wind, modern solid bioenergy, nuclear energy.[13] Solar and wind energy account for the top two renewable energy sources due to their abundant availability, where a total of 122,000 TWy energy hit on the earth from the sun[14] and 71.5 TWy energy from the wind[15]. However, like tide and wave, they are known as variable renewable energy. The supply patterns are not aligned with variations in demand regarding location and time of supply, which could cause both time and geographical mismatches to the energy demands.[16] Converting and storing energy via energy conversion/storage devices such as

hydrogen-based fuel and batteries has provided a fascinating solution to tackle this problem.[17, 18]

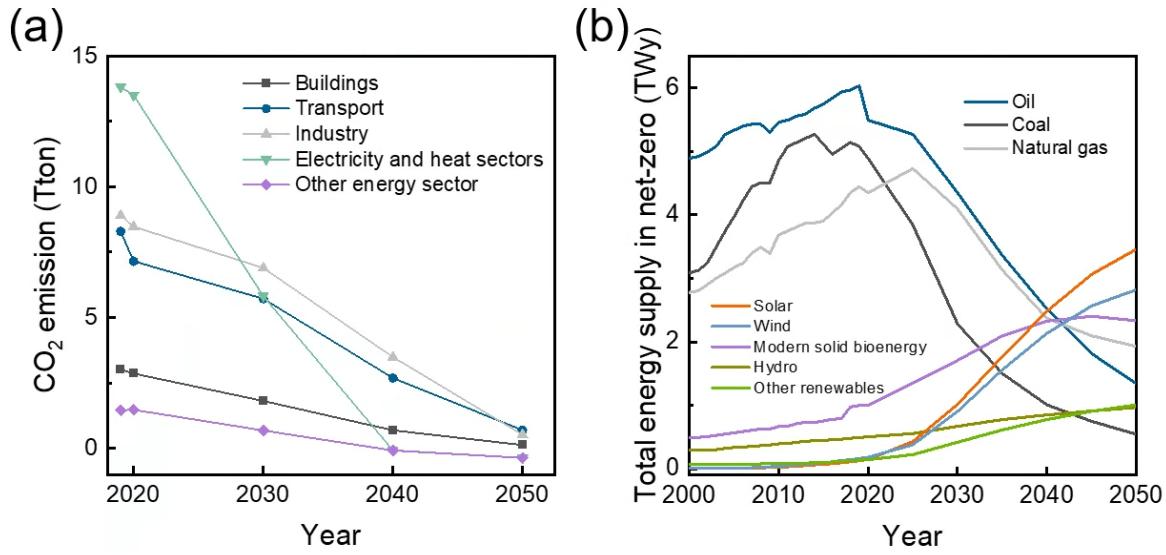

Figure 1.3 (a) Worldwide CO_2 emission in the net-zero scenario from the different sectors in the duration of 2019 to 2050. (b) Total energy supply in the net-zero scenario from 2000 - 2050. Data were taken from IEA[1].

Both batteries and hydrogen-based fuel could store excessive electricity as chemical energy and further use when and where needed, which unlocked the restrictions of the variable renewable energy.[19] Batteries store the electrical energy into chemical energy and discharge through a reverse process to release the chemical energy into electricity. However, it suffers from a trade-off between energy capacity and weight. Besides, the long charging time of batteries also hinders its application. Hydrogen has become one of the most promising zero-emission fuels and chemical precursors for the net-zero future due to its high specific energy[19] and its wide range of implantations. IEA proposed a future low carbon society based on hydrogen in 2015 (**Figure 1.4c**), where hydrogen serves as interlayers to link energy resources and our daily life together.[16] Notably, finding a greener way to produce and utilize hydrogen is challenging hydrogen production currently accompanied by high carbon emissions. [20] With an efficient converting system of hydrogen and electricity/chemicals, hydrogen could play an important role in our daily life.[16]

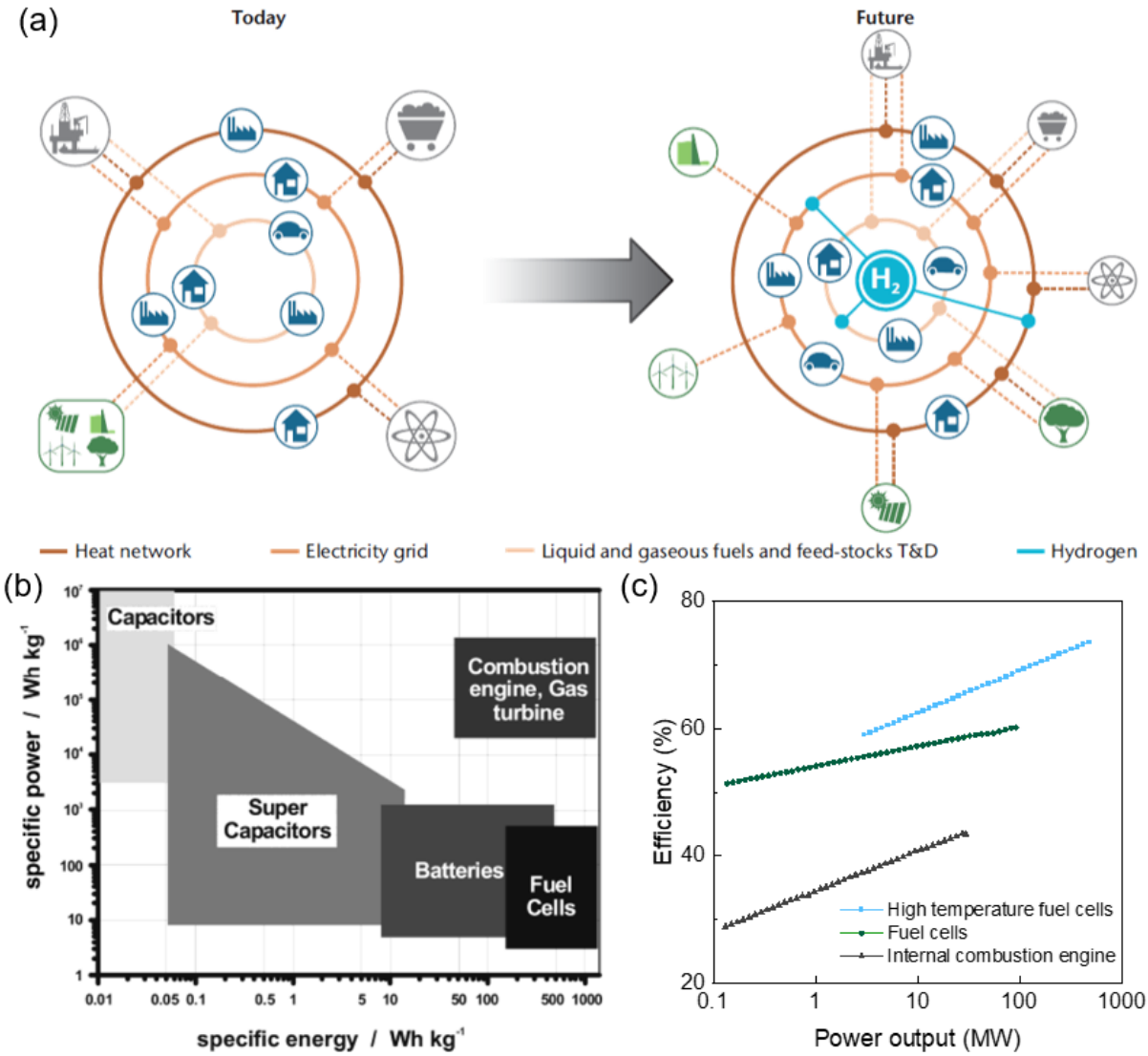

Figure 1.4 (a) IEA proposed a future economy where hydrogen is linked to energy, industries, transportation, and building sectors. Figure adapted from Ref[16]. (b) Ragone plot of energy storage domains for fuel cells, batteries, supercapacitors, combustion engines, and gas turbines. Figure adapted from Ref[21]. (c) Comparison of efficiency and power output of fuel cells, the internal combustion engine and high-temperature fuel cells. Data were taken from IEA[16].

1.2 Electrochemical Energy Conversion - Fuel Cells Technology

Hydrogen fuel cells could continuously produce electricity via electrochemical reactions with continuous fuel input (hydrogen), which plays an essential role in utilising hydrogen.[16, 19] Fuel cells concept was first demonstrated in 1838 where it was described as 'gas voltaic battery' to recompose water by combining electrodes in a series circuit.[22, 23] Since then, there have been efforts to understand the mechanism, reduce cost, and improve the performance of the fuel cells. After over a century, in 1932, the first commercial hydrogen fuel cell was invented, and

in the 1960s, the alkaline fuel cells (AFC) were applied on space shuttle (Gemini earth-orbiting mission, 1962-1965) for its high electrical efficiency and less weight[24]. Besides, fuel cells show higher efficiency than conventional combustion engines with fewer energy converting steps, which are not limited by the 'Carnot cycle'.

Different fuel cells have been developed to fit different working conditions and requirements, where alkaline electrolyte membrane fuel cells (AEMFC) and proton-exchange membrane fuel cells (PEMFC) are the most developed ones. The solid electrolyte membrane was applied in AFC to reduce the influence from the CO_2 ($CO_2 + 2KOH \rightarrow K_2CO_3 + H_2O$), where K^+ is limited when transfer in solid membrane.[25, 26] Compared with PEMFC, AEMFC shows less corrosive in alkaline conditions than in acidic conditions.[27, 28] Since the PEMFC has been developed and invested decades ahead than AEMFC, the challenges for AEMFC remains to compete with PEMFC, such as cost and durability.[28]

In recent decades, fuel cells have been applied in cars, buses[29], residential energy supply[30], light-duty fleet[31], portable devices[32], wastewater treatment [33], and stationary power supply[34]. Fuel cells have been projected to play an essential role in decarbonization in the transportation sector with high specific energy density[35], fast charging speed (3 - 5 mins to refill the hydrogen), reliable safety, and power grid compatibility[19]. The basic working principles for fuel cells are simple: oxygen reduction reaction (ORR) at cathode and hydrogen oxidation reaction (HOR) at anodes. At the anode, hydrogen loses one electron and turns into H^+, while at the cathode, oxygen is reduced and gains two electrons to become O^{2-}. The extra electron loss in oxygen could lead to side reactions such formation of H_2O_2 and, therefore, flawed the whole process (a more detailed mechanism could be found in Chapter 2). Typical polarization curves of PEMFC (**Figure 1.5**) revealed that the applied overpotential for HOR catalysts are much smaller than ORR catalysts, where the HOR reaction is controlled primarily by the mass transport of H_2. Therefore, more catalyst is needed on the cathode to catalyze the ORR reaction

than HOR. [36]

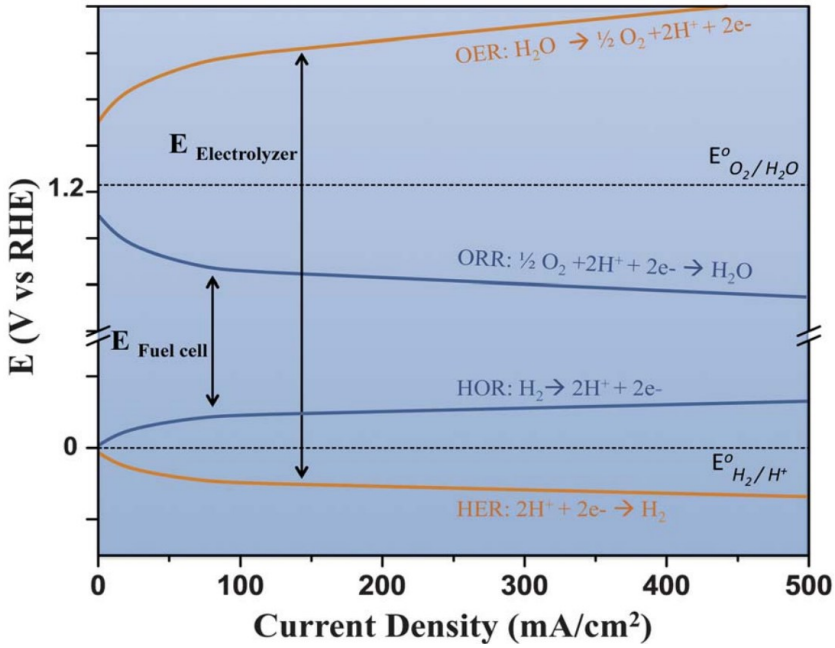

Figure 1.5 Theoretical polarization curves of typical PEMFC and Electrolyzer. Figure adapted from Ref[36].

So far, Pt-based catalysts perform best in fuel cells and are the materials that have been widely applied commercially. However, they suffer from scarcity and high cost, while further stability improvements are also required.[37] Predicted scenarios show that over 8 million fuel cell electric vehicles will be deployed globally by 2030 to fulfil the net-zero goal, which will require 420 (or 75 tonnes of the optimised Pt loading) tonnes of Pt-based catalysts in the vehicles section only and thus resulting in the shortage of Pt (global Pt production in 2019 is 180 tonnes).[1, 38] Pt nanoparticles supported on carbon (Pt/C) are the only commercially available catalyst for fuel cell catalysts. The high loading of Pt group catalysts is identified as the most significant barrier to reducing cost.[39] Pt also suffers from CO poisoning, methanol crossover, and long-term instability due to particle growth and dissolution.[40] Therefore, to achieve widespread and sustainable commercialization of fuel cells, durability and low cost are two essential factors when designing electrocatalysts for fuel cells. U.S. Department of Energy has set the key goal for electrocatalysts which include increasing durability and decreasing cost (US DOE 2025 targets: 5000 hours lifetime and \$ 40/kW_{net} at 500,000 systems/year).[41, 42]

1.3 THESIS OBJECTIVES AND OUTLINE

This research aims to synthesise freestanding electrodes that could be applied in fuel cells in a sustainable and low-cost way. The following objectives achieved this aim:

i) Design and synthesis of biomass-derived carbon electrodes and catalysts for the oxygen reduction reaction.

ii) Characterized the obtained electrode and catalysts with multiple advanced techniques to reveal the performance. These include electrochemical as well as physical-chemical characterization methods.

iii) Specifically, biomass-derived mono sugars such as glucose and xylose were used as precursors to prepare electrocatalysts for the oxygen reduction reaction. HTC process was first applied to convert glucose and xylose into oxygenated nanocarbon spheres, contributing to further functionalization.

iv) Furthermore, the freestanding nitrogen-doped carbon electrodes were made by mixing and pelleting the HTC carbon with nitrogen dopants. This approach gives rise to a new class of electrodes with a unique, highly porous micro-morphology and scalability.

v) Engineering FeN_x sites on the electrodes performed further functionalization of nitrogen-doped carbon electrodes. To date, freestanding electrodes are not used in commercially available energy conversion devices, where this work paves a road for the application of miniaturized fuel cells.

Chapter 1 briefly introduces the motivation for a net-zero goal and a brief introduction to the fuel cells.

Chapter 2 introduces various electrochemical aspects regarding the oxygen reduction reaction and a brief introduction to the use of biomass and hydrothermal carbonization.

Chapter 3 explores the synthesis of freestanding nitrogen-doped carbon electrodes, followed by materials characterizations and electrochemical characterizations. Moreover, optimization of the synthesis of the freestanding electrode was carried on, which studied the thickness, carbonization temperature influence on the carbon electrode. Rhod Jervis performed CT experiments and analysis at UCL, XPS was performed with the help of Gang Cheng, SAXS experiment and data fitting were done by Andi Di and Zhenyu Guo. I performed the rest materials measurements and all electrochemical measurements and analyzed the results.

Chapter 4 introduced iron into the framework and engineered FeNx sites on the carbon electrode, followed by materials and electrochemical characterizations. Rongsheng Cai performed STEM at Manchester, EPR was performed by Angus Pederson, XPS was performed with the help of Gang Cheng, Zhenyu Guo fitted SAXS data. I performed the rest materials characterizations, XAS experiments and structure fitting, and all electrochemical measurements and analyzed the results.

Chapter 5 reports the synthesis of the Fe-N-C catalysts from HTC biomass on a gram scale and explores the iron precursors influence on the final electrocatalysts. This work was trigged by a master project I co-supervised, in which Giulio and India Wild explored materials synthesis. Rongsheng Cai and Hui Luo performed STEM and TEM, EPR was performed by Angus Pederson, Zhenyu Guo fitted SAXS data. I performed the rest of the materials characterizations, XAS experiments and structure fitting (collaborate with Bhoopesh at the University of Leeds), and all electrochemical measurements and analyzed the results.

Chapter 6 gives a brief introduction and working principle of the characterization techniques.

Chapter 7 summarizes this PhD work's main conclusions and concludes this thesis with an outlook for possible future work.

Chapter 2

ELECTROCATALYSIS – LITERATURE REVIEW FOR OXYGEN REDUCTION REACTION

This chapter will briefly introduce the oxygen reduction reaction, the current catalysts for ORR focusing on carbon-based catalysts, and strategies to improve the catalysts' performance. We will also discuss the limitation of existing approaches and the strategies for designing desired catalysts. Moreover, we will focus on non-precious group metal (PGM) catalysts tested in alkaline conditions to serve the contents in the following chapters.

2.1 ELECTROCATALYSTS FOR ORR

Electroreduction of oxygen is the critical reaction that happens at the cathode of the fuel cell. During the oxygen reduction, catalyst sites could bond with oxygen and reduce it into intermediates, resulting in an overall lower energy barrier than without using catalysts. It involves a multi-step electron transfer process which can be divided into two main mechanisms, where 'four-electron' mechanism generates OH^- in alkaline solutions and 'two-electron' mechanism generates H_2O_2.[43] An efficient ORR electrocatalyst should drive the reaction towards four-electron pathways to provide high current efficiency and operating potential since the H_2O_2 reduces the overall efficiency and degrade the membrane in between.[44] Besides, compared to acidic media, ORR in alkaline media lower the electrode potential, which reduces the adsorption energy of ORR intermediates, which means more materials will have a high enough O_2 adsorption free energy to bind the surface and allow the ORR to occur.[45]

The ORR reaction in alkaline conditions can be written as follows:

$$O_2 + * \rightarrow O_2^*$$

$$O_2^* + 2H_2O + 4e^- \rightarrow OOH^* + OH^- + H_2O + 3e^-$$

$$OOH^* + OH^- + H_2O + 3e^- \rightarrow O^* + 2OH^- + H_2O + 2e^-$$

$$O^* + 2OH^- + H_2O + 2e^- \rightarrow OH^* + 3OH^- + e^-$$

$$OH^* + 3OH^- + e^- \rightarrow 4OH^- + *$$

Where * represent adsorbed surface sites, O_2*, OOH*, O*, and OH* represent intermediates adsorbed on the active sites during the oxygen reduction, where each step requires specific free energy to cross the energy barrier.[46] Moreover, the reaction starts when all the free energy shows a downhill trend from oxygen adsorbed to OH^- desorbed on the active sites. Besides, the free energy for each step is directly related to the intermediate adsorbing behaviour. Therefore, modulating the electronic structure of the active sites to redistribute charge density around the active sites could lead to improved kinetics activity of ORR. Strategies such as heteroatom doping, introducing transitional metals or defects have been widely reported.[47-49]

Using DFT to study the intermediates pathway and their free energies have become popular to screen the catalysts.[50] Various active sites and their intermediate pathways have been calculated.[48-50] At U = 1.23 V, the energy barrier for Pt(111) is uphill (yellow line in **Figure 2.1a**). [51] When U = 0.75 V (blue line in **Figure 2.1a**), it reaches a downhill trend where the oxygen reduction starts.[51] For transitional metal-based catalysts(**Figure 2.1b**), the starting potential has been reported at U = 1.09 V for CoN_3-C catalysts[47], U = 0.44 V for Co nanoparticles[47], and U = 0.84 V for FeN_4-OH-C catalysts[49]. As for carbon and heteroatom doped carbon (**Figure 2.1c**), higher energy is required to reduce oxygen. Besides, each intermediate (OOH^*, O^*, OH^*) binds to the active sites via an oxygen atom, leading to a linear relation to each of the adsorption free energies (**Figure 2.2**). The slope of ΔG_O is 2, while ΔG_{OH} and ΔG_{OOH} are 1. This could be considered two chemical bonds formed between O^* and active sites, while only one bond formed between OH*/OOH* and active sites.[52]

Furthermore, based on the scaling relationships, the Volcano plot was used to describe the relation of catalytic activity and free energies. As shown in **Figure 2.1a-c**, the ΔG is related to the equilibrium potential, thus relating to the catalytic activity. For example, the free energies change from O* to OH* is $\Delta G_{O\text{-}OH} = \Delta G_O - \Delta G_{OH}$, and based on scaling relationship, ΔG_O could be written in the function of ΔG_{OH}. Hence, $\Delta G_{O\text{-}OH}$ could be written into the function of ΔG_{OH}. By plotting $\Delta G_{O\text{-}OH}$ (represent one unique catalyst) against the activity (the catalytic performance), the Volcano plot is obtained. Based on these Volcano plots (**Figure 2.1 d-f)**, we could see the catalytic performance from all PGM based, non-PGM based, and metal-free catalysts could be tuned by introducing new structures, ligands, and heteroatoms.[46, 48, 49]

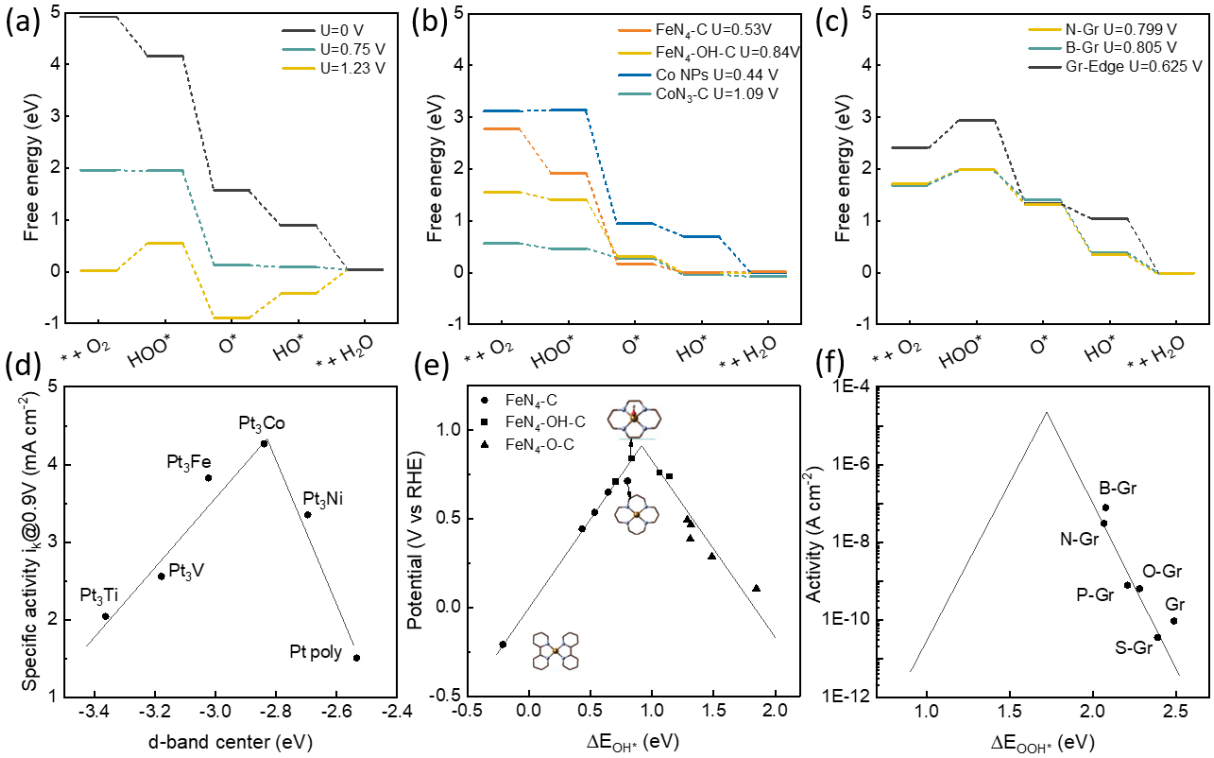

Figure 2.1 (a) Free energy diagrams for dissociative oxygen reduction on Pt (111), the three panel shows the free energy diagram for U = 0 V, U = 0.75 V and U = 1.23 V[51]. (b)free energy diagrams for associative oxygen reduction on FeN_4-C (U = 0.53V), FeN_4-OH-C[49], CoN_3-C (U = 1.09 V), Co NPs (U = 0.44 V)[47]. (c) free energy diagrams for graphitic N doped graphene (N-Gr, U = 0.799 V), graphitic boron-doped graphene (B-Gr, U = 0.805 V), and carbon on graphene edge (Gr-Edge, U = 0.625 V)[48]. (d) Volcano-like relationships between the catalytic properties and electronic structure of d) Pt_3M (M

= Fe, Co, Ni, V) alloys[46], (e) between ΔG_{OH*} and ORR potential for Fe-N_4C structures[49], (f) between ΔG_{OOH*} and activity for heteroatom doped graphene[48].

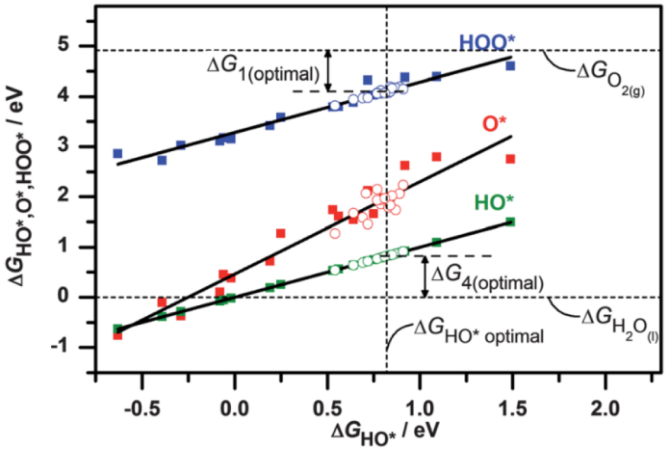

Figure 2.2 Theoretical plot of ORR free energies for adsorbed intermediates and their scaling relationship (Pt-based catalysts). The figure is taken from Ref[53].

Furthermore, oxygen reduction happens at the three-phase boundary of the catalysts, electrolytes, and gas, which means the mass transfer to active sites also plays an essential role in catalytic performance.[54] Besides, good electronic conductivity is also needed for electron transport from active sites to substrate. In terms of mass transfer, porous structure, suitable wettability, and exposed active sites could facilitate catalytic performance. In terms of the electron transfer, the substrate itself should be conductive to minimize the resistance (**Figure 2.3**).

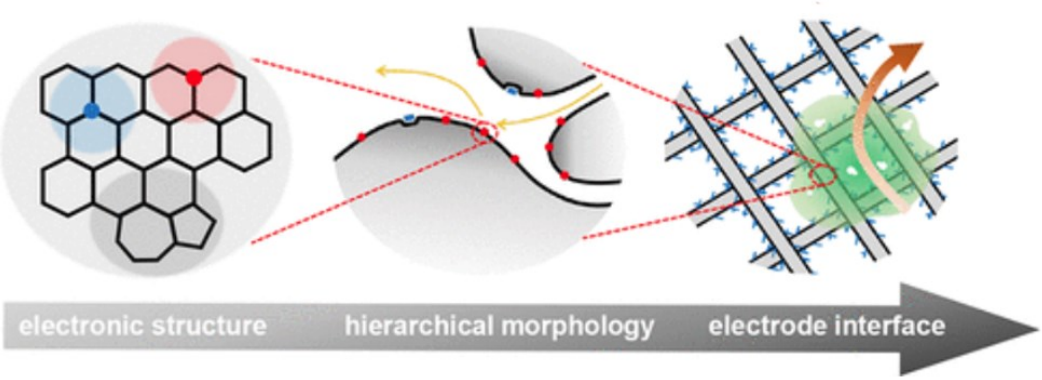

Figure 2.3 Illustration of structure, morphology, and electrode interface with active sites. Figure adapted from Ref[54].

2.2 CARBON-BASED ELECTROCATALYSTS FOR ORR

State of the art Pt-based catalysts such as Pt nanowires[55], Pt_3Ni nanoframe[56], Pt single atoms[57], and Pt-Co catalysts[58] have already reached extraordinary high mass activity selectivity. However, their scarcity and high cost limit the broader applications. Competing with these catalysts in both cost and catalytic activity will require more effort to optimise synthesis routes and engineering catalytic sites. So far, carbon-based catalysts and transitional metal-based catalysts have been two widely studied catalysts. This section presents a brief overview of the carbon and non-PGM based catalysts for ORR.

2.2.1 Metal-free catalysts

2.2.1.1 Dopant free carbon-based catalysts

Without introducing heteroatoms, the electronic structure of carbon atoms could be tuned by introducing defects. The edge of graphite has been demonstrated to be more electroactive for ORR than the basal plane due to the charge polarization of edge carbon atoms; dopant-free and edge-rich carbon materials have been found to show electrocatalytic activity[59-66]. Moreover, the point defects and line defects are also positive for the electrocatalytic performance[67, 68]. The ORR activity introduced by defects was attributed to the redistribution of charge on the surface of catalysts[65].

By carefully engineering the nanostructure of carbon materials, exposed edges and defects could be obtained. Jiang et al. reported defective carbon nanocages (**Figure 2.4**)[69]. Samples with different concentrations of defects have been synthesised, denoted as CNC700, CNC800 and CNC900 (CNC700 showed the highest defect concentration). As shown in **Figure 2.4c**, the onset potential for CNC700 is 0.11 V_{NHE}, and the half-wave potential is 0.05V_{NHE}, which indicated higher ORR activities. The DFT method has been used to investigate the influence of different defective configurations on the ORR process (different defect models can be seen in **Figure 2.4b**). Besides, pentagon and zigzag defects are considered as active sites which

contribute to oxygen reduction. Specifically, the zigzag edge contains a portion of active unpaired π electrons located at the edge carbon atom, whereas unpaired π electrons are paired up to form a stable covalent bond for armchair defects. Subsequently, the free π electron in the zigzag edge facilitates electron transfer to O_2, forming OOH* with less energy required, whereas more energy is required in the armchair sites.

Moreover, modelled catalysts such as highly oriented pyrolytic graphite (HOPG) were applied to further study the defect's influence. Shuangyin et al. presented a model to correlate the promotion of surface charge with the electrocatalytic reaction by using plasma-treated HOPG (**Figure 2.4d**)[68]. The HOPG was treated by plasma at different times to obtain different concentrations of defects. As shown in **Figure 2.4d**, HOPG treated with plasma showed improved ORR activity, in which HOPG exhibited 0.745V_{RHE} onset potential with 1 min plasma treatment while 0.171 V_{RHE} onset potential without plasma treatment. This suggests that defects play a critical role in ORR. To further investigate the role of defects, the HOPG with 5 min plasma treatment (P-HOPG-800) was repaired by annealing at 800°C in Ar atmosphere. As shown in **Figure 2.4f**, the obtained sample (P-HOPG-800) showed a decreased ORR activity.

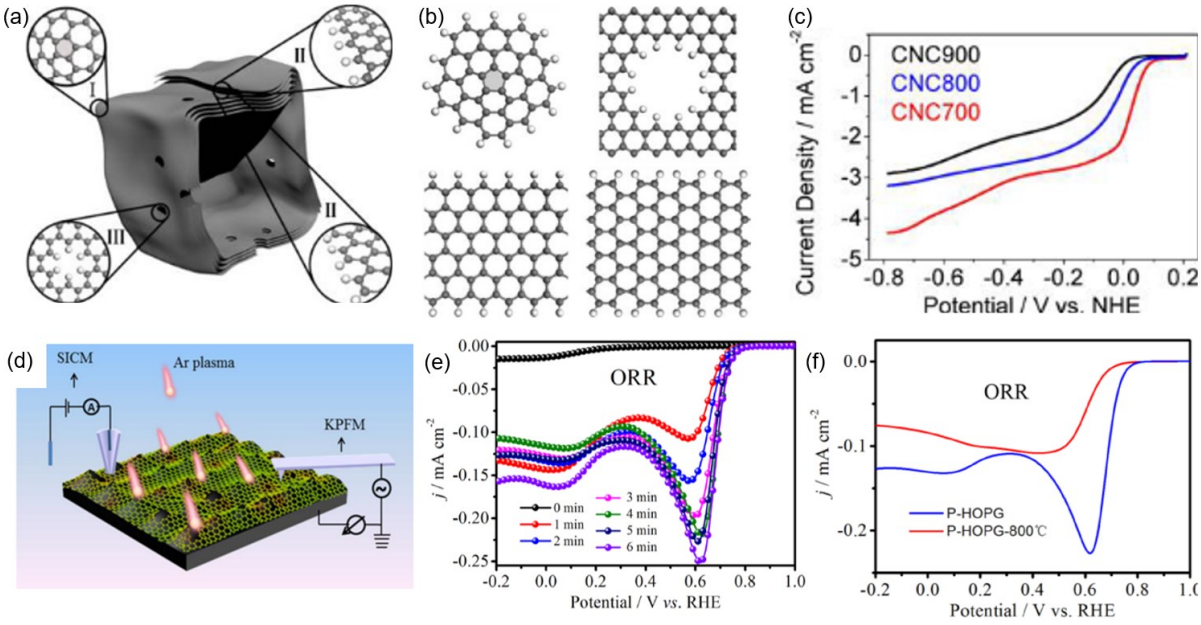

Figure 2.4 (a) schematic structural of carbon nanocages with the locations of different types of defects; (b) different defects model for the pentagon, hole, Zigzag edge, Armchair edge, where grey atoms are carbon while white atoms are hydrogen; (c) LSV curves of carbon nanocages at 10 mV s^{-1} scan rate in 0.1 M KOH under O_2 saturated condition. Figure a-c was taken from Ref[69] (d) schematic of plasma-treated HOPG; (e) LSV curves of HOPG with different plasma treat times in 0.1 M KOH; (f) LSV curves of plasma-treated HOPG before/after annealing at 800 °C in Ar atmosphere. Figure d-f was taken from Ref[68].

2.2.1.2 Heteroatom doped carbon materials

Nitrogen-doped carbon has been the most reported heteroatom doped carbon, and many studies and theoretical studies have shown the increased oxygen reduction activity with nitrogen doping compared without nitrogen doping. Introducing nitrogen modulates the electronic structure of neighbouring carbon atoms, changes the adsorption of ORR intermediates on carbon, and thus lead to better catalytic performance.[70]

In 2009, Dai et al. reported nitrogen-doped vertically aligned carbon nanotubes (VA-CNTs) with excellent ORR performance in alkaline condition[70]. As shown in **Figures 2.5a-b**, they found that the induced nitrogen shows a high positive charge density on adjacent carbon atoms, which facilitates the chemisorption of O_2 and electron transfer for the ORR[70]. Subsequently, their group synthesised the nitrogen-doped graphene, which also showed considerable ORR

performance[71]. The improvement of ORR performance by N-doping cause the charge redistribution, which converts the chemisorption model of O_2 from the end-on adsorption at the nitrogen-free CNT surface to side-on adsorption at the N-doped CNT surface. The parallel diatomic adsorption could effectively weaken the O-O bonding and hence facilitating the reduction of O_2[70].

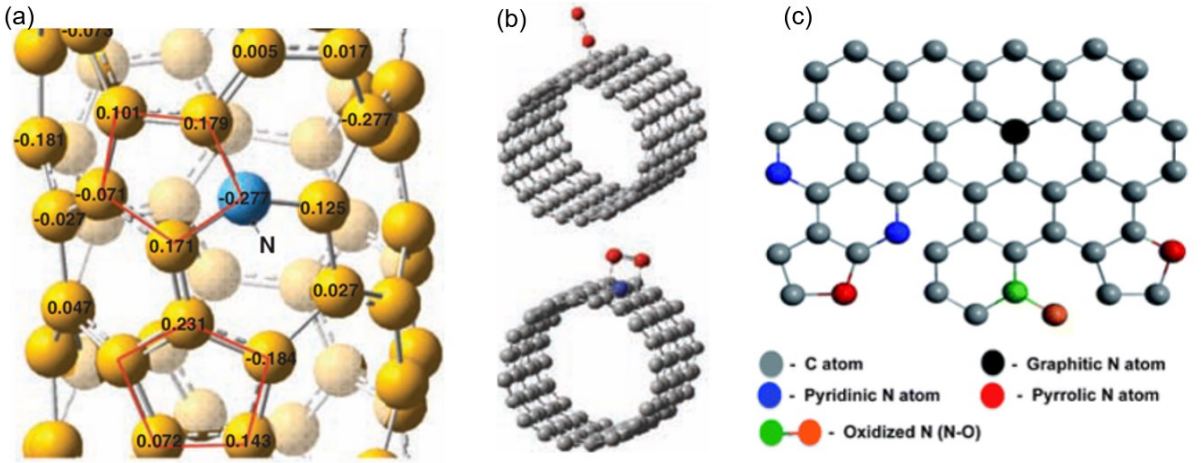

Figure 2.5 (a) calculation of charge-density distribution for N-doped carbon nanotube; (b) schematic of adsorption modes of N-free carbon nanotubes (top) and N-doped carbon nanotubes (bottom). Figure a-b was taken from Ref[70] (c) Different types of doped nitrogen in carbon materials. Figure c was taken from Ref[72].

Different types of N exist inside the N-doped carbon materials, including graphitic, pyrrolic, oxidized and pyridinic N (**Figure 2.5c**). Furthermore, different nitrogen heteroatoms could give rise to different catalytic activities. Lai et al. investigated active sites for N-doped carbon and reported that the graphitic N determined the limiting current density while the pyridinic N will improve the onset potential[73]. Using HOPG as a carbon substrate, Guo et al. exhibited the atoms next to pyridinic N is the active sites for ORR[74]. As shown in **Figure 2.6c**, HOPG with pyridinic N showed higher electrocatalytic activity than with graphitic N. The obtained result suggested the significant role of pyridinic N is responsible for the high catalytic activity site for ORR. [74] The mechanism of ORR for the N-doped carbon materials was also proposed in their work (**Figure 2.6a**). O_2 is first absorbed onto carbon atoms near the pyridinic N, followed by proton-electron pair transfers to the oxygen. Then, it involves two possible pathways. First is the four-

electron pathway, where 2-proton coupled 2-electron transfer to the site and break the OOH bond to form a water molecule. Subsequently, another pair of proton and electron transfers to the site breaks the bond between OH and carbon to form a water molecule. Another pathway is a two-electron pathway, where one proton-electron pair transfers to the OOH* sites to form H_2O_2, and reabsorption or reduction of H_2O_2 is followed. Fewer electrons were transferred in the two-electron pathways, making it less efficient than the four-electron pathway. Therefore, controlling and investigating nitrogen types and nitrogen amount in the nitrogen-doped carbon is essential for this catalyst.

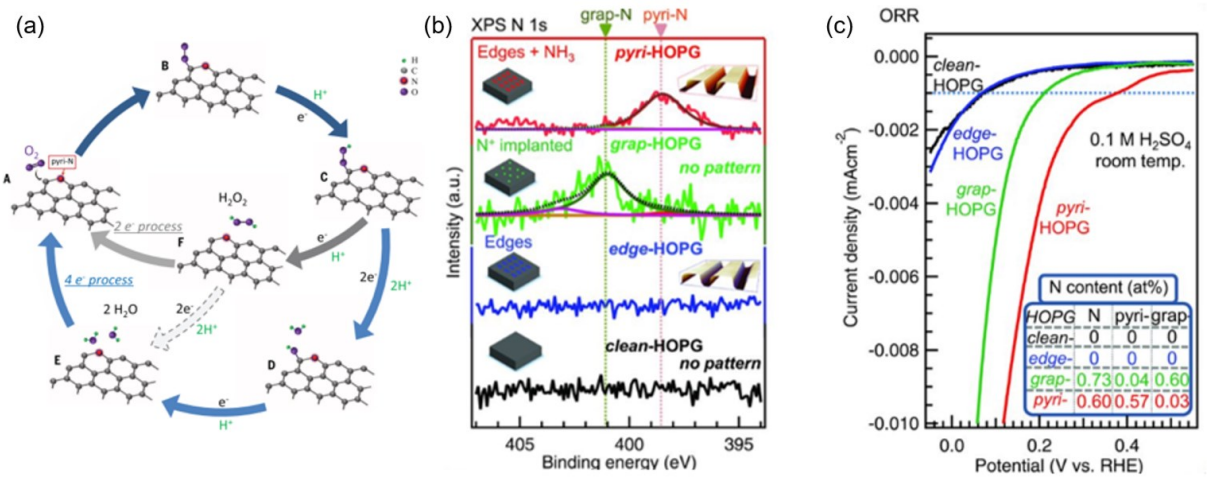

Figure 2.6 (a) Schematic pathway for oxygen reduction reaction on nitrogen-doped carbon materials; (b) XPS spectra of modified HOPG catalysts; (c) LSV curves for modified HOPG catalysts in 0.1M H_2SO_4 at O_2 saturated conditions. Figures are taken from Ref[74].

Furthermore, investigations on non-N heteroatoms doped carbon have been carried out. Such as B-doped CNTs, S-doped graphene, P-doped graphite, I-doped graphene and edge-halogenated graphene nanoplatelets[75-79]. Co-doped carbon-based materials have also been reported and seem to be the more effective strategies to improve the performance of carbon-based materials due to the synergistic effects of synergistic electronic interactions between the different doping heteroatoms and surrounding carbon atoms[80-82].

Besides, biomass has been reported as precursors for electrocatalyst due to its natural 3D hierarchical structure after heat treatment, which facilitates mass and electron transport. By conducting certain post-treatments, structural defects and heteroatom doping could be easily introduced[83, 84]. Chunyi et al. reported a N, S co-doped wood-derived carbon materials for ORR application due to its multichannel mesoporous framework[83]. The wood slices were first delignified to create and open the inner pores. After that, it was treated with dopants and then carbonized, followed by NH_3 activation (the obtained samples were denoted as TARC-N). TARC-N showed superior ORR activity with halfwave potential $E_{1/2}$ = 0.86 $V_{RHE,}$ while halfwave potential for Pt/C is 0.85 V_{RHE}. The excellent ORR activity was attributed to the rich N, S co-doped active sites, synergistic ORR activity, and the hierarchical structure.[83]

2.2.2 PGM-free catalysts

Transitional metals have been considered as convenient alternatives to replace Pt. So far, the most widespread and studied PGM-free catalysts are metal, nitrogen co-doped carbon (M-N-C, M = Fe, Co, Ni, Mn) catalysts.[85, 86] The main influential active sites in M-N-C catalysts are the metal centre in M-N_4 sites.[86, 87] Catalytic properties of M-N sites in carbon matrix are dominated by the centre metal, first shell atoms, and second shell atoms.[88] Furthermore, the matrix structure (includes the degree of graphitization, matrix surface area, defects and nitrogen atoms) also influence the catalytic performance of the catalysts.[89-91]

In 1964, the first M-N_4 (Co-N_4) macrocyclic compound was first presented as an ORR catalyst.[92] After that, researchers found that M-N_4 suffered from poor thermal and chemical stability and electronic conductivity. Pyrolysis of M-N_4 at over 800°C to form M-Nx/C hybrids with strong covalent metal-nitrogen bonds can significantly enhance their stability and activity[93, 94]. Non-precious metals and nitrogen co-doped carbon have been studied, showing improved durability and high ORR activity. Fe, Co-N doped carbon is the most reported ORR catalysts with effective catalytic activity.[95, 96] Different Fe, Co species and their kinetic

activities have been investigated for oxygen reduction (**Figure 2.1b**). Ramaswamy et al. reported that the pyrolysis step relocates the Fe-N_4 active site from a πelectron-rich macrocyclic ligand environment to a relatively πelectron-deficient graphitic carbon environment due to the incorporation of vacant defects and edge-plane sites (**Figure 2.7a**).[97]

Not only the metal centre could influence the catalytic properties of M-N-C, but also the first coordination shell and the second coordination shell could also influence the catalytic activity (**Figure 2.7b**).[88, 98, 99] Theoretical calculations for the overpotential of the ORR were carried out on 11 different Fe-N_x structures with different locations, different coordination numbers and different ligands (**Figure 2.8a**).[99] Where edge FeN_4-C with an OH ligand bonded on the iron centre showed the lowest ORR overpotential within these structures (**Figure 2.8b**). Furthermore, the catalytic pathways could also be altered if the first shell coordinated atoms change. Tang et al. reported that FeC_2N_2 showed a two-electron pathway while FeN_4 showed a four-electron pathway (**Figure 2.8c-e**), which dramatically influenced electrocatalytic performance.[88] Therefore, considering the local environments M-N sites is necessary for understanding the catalysts' catalytic mechanism.

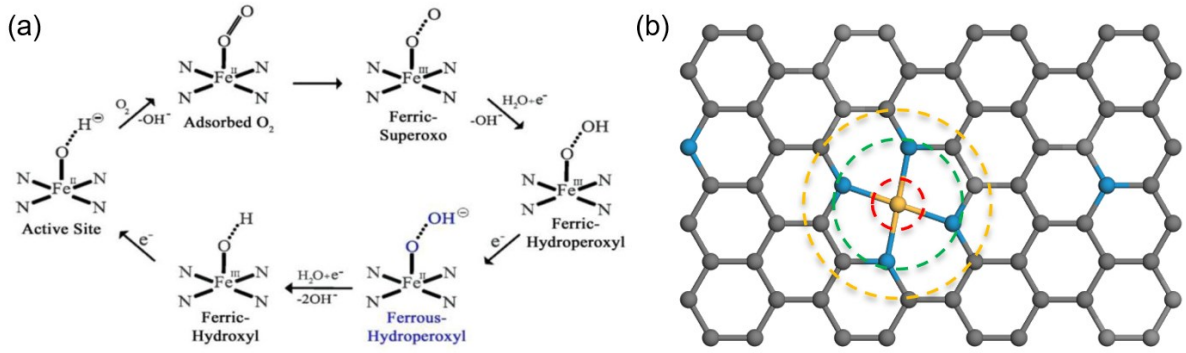

Figure 2.7 (a) Proposed ORR mechanism in an alkaline medium for FeN_4-C structure[97]. Figure a is taken from Ref[97]. (b) Schematic drawing for M-N-C structures (metal atom: yellow; nitrogen atom:

blue, carbon atom: grey. Central metal atom: red dash circle; first coordination shell: red; second coordination shell: green dash circle).

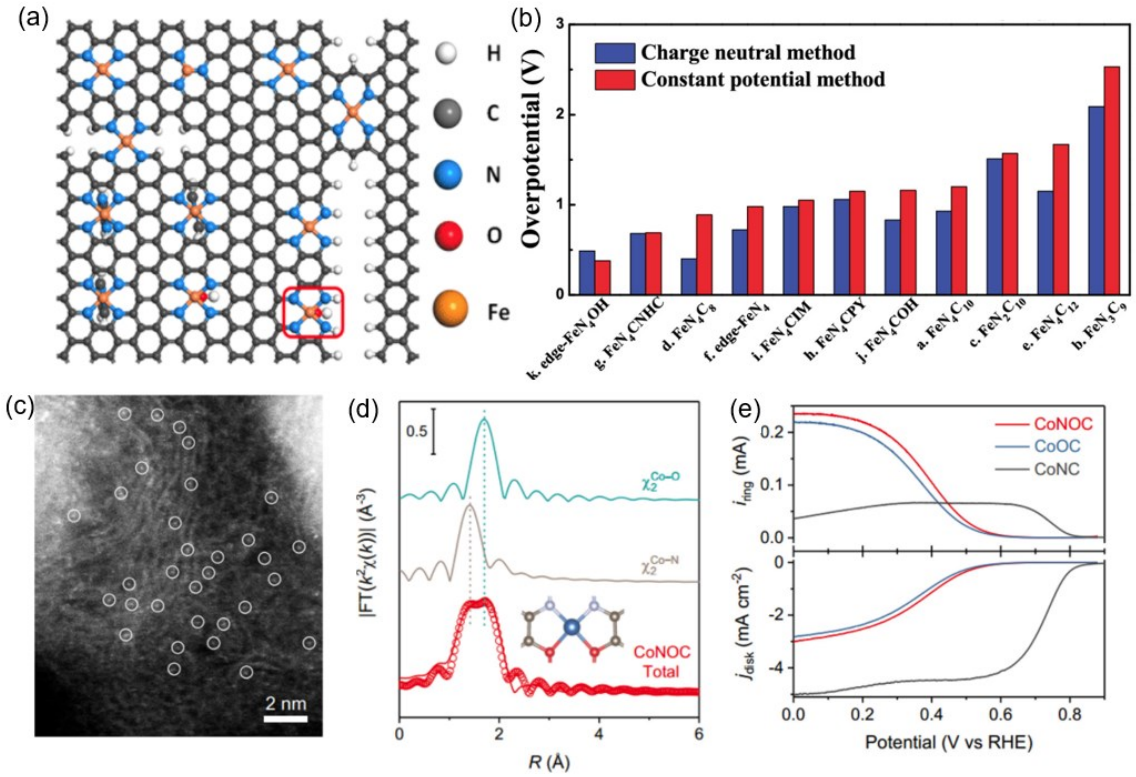

Figure 2.8 (a) schematic structure of different Fe-N sites, edge-FeN_4OH in a red circle has the lowest overpotential from theoretical calculation, (b) comparison of ORR overpotential for different types of Fe-N sites. Figure a-b was taken from Ref[99]. (c) HAADF-STEM image for the CoNOC sample, (d) Co

K-edge EXAFS fittings for CoNOC in R space, (e) LSV curves of ORR obtained in O_2-saturated 0.10 M $HClO_4$ for CoNC, CoOC, and CoNOC samples. Figure e was taken from Ref[88].

Furthermore, anchoring the M-N_4 structure into a carbon matrix usually involves thermal treatment to hybridize them together, forming inactive metal species such as metal particles. Therefore, studying the evolutionary pathways of M-N_4 structures is essential to link the metal precursors to final M-N_4 sites and minimize the formation of unwanted species. Jingkun et al. studied the iron precursors to Fe-N_4 sites via operando XAS study.[100] They revealed that iron could evolve to single free Fe atoms at around 600 °C. From then, nanoparticles will form if there is no presence of nitrogen-doped carbon, resulting from the competition of Fe-O_4 with Fe-N_4 (**Figure 2.9**).[89]

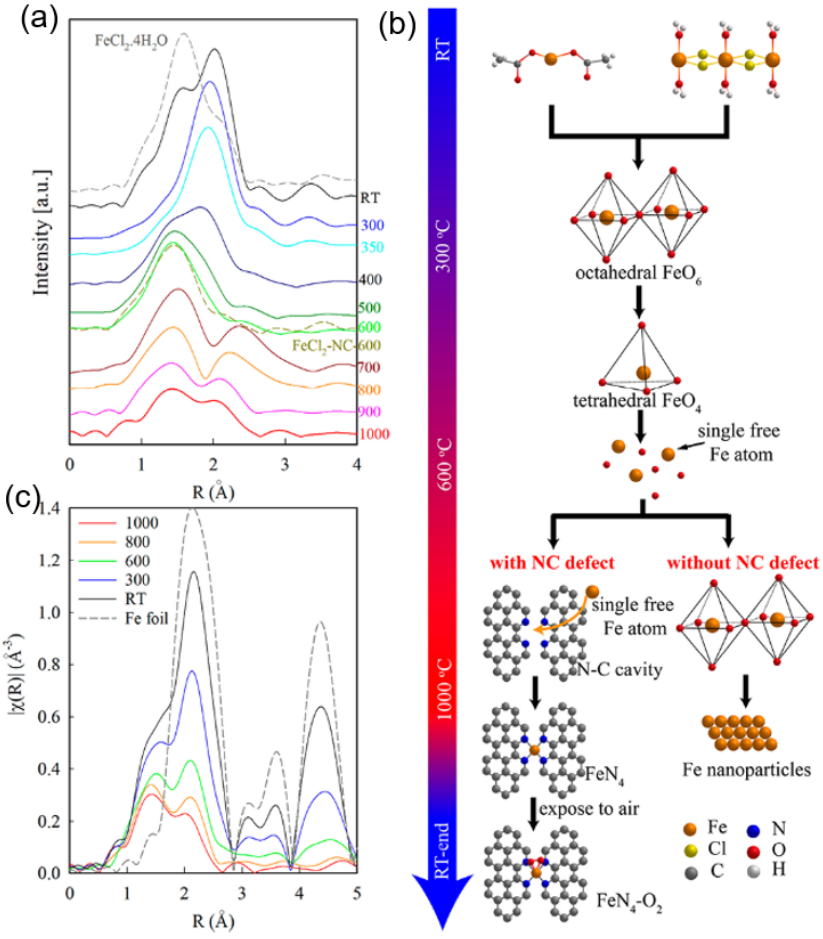

Figure 2.9 (a) Fe-K edge EXAFS fittings of $FeCl_2$ and SiO_2 mixture from room temperature to 1000 °C, and (b) the cooling down process from 1000 °C to room temperature, (c) proposed evolution pathway of iron precursors to final FeN_4 sites carbon. Figure a-c was taken from Ref[100].

Moreover, the structure of the carbon matrix could also influence the performance.[89, 101-111] Li et al. developed N-doped carbon hollow spheres with isolated single Co atomic sites (ISAS-Co/HNCS) (**Figure 2.10a**) by using the template-assisted pyrolysis (TAP) method[108]. As can be found in **Figure 2.10b**, ISAS-Co/HNCS showed excellent ORR performance in acidic medium (0.5 M H_2SO_4), even comparable with commercial Pt/C catalysts where halfwave potential of ISAS-Co/HNCS is $E_{1/2} = 0.773$ V_{RHE} while halfwave potential of Pt/C is $E_{1/2} = 0.79$ V_{RHE} under acidic conditions. By conducting experimental work and DFT calculations, its excellent ORR performance was attributed to its well-dispersed Co atomic sites and hollow spherical structure. Instead of using a spherical structure, a cubic carbon framework with high packing density, a large interior surface and a rigid carbon wall network has also been reported. With the self-assembly nature of cubic Fe_3O_4 particles, a high packing density of nanoparticles could be achieved, leading to an optimized interior surface area[112]. Angang et al. reported cubic carbon frameworks with Fe single atoms anchored on cubic N-doped carbon framework (**Figure 2.10c**) by hard template method which etching the Fe_3O_4 nanocube superlattices away followed by ammonia activation[113]. As shown in **Figure 2.10d**, the obtained well atomic iron dispersed, N doped cubic carbon framework shows remarkable ORR performance in alkaline media with a halfwave potential of 0.883 V_{RHE}. Randomly packed Fe_3O_4 nanocubes were also prepared (Fe-N-DCFs). It showed a lower surface than ordered Fe_3O_4 nanocubes (756 m^2 g^{-1} vs 1180 m^2 g^{-1}) and inferior ORR performance than ordered Fe_3O_4 nanocubes. MOF derived porous carbon has also been a popular catalytic catalyst due to its uniform and easily tuneable morphology[106, 107, 114]. Jianglan et al. reported a concave-shaped MOF derived porous carbon structure with efficient mass transport performance and dense Fe-N-C active sites through SiO_2 coating and preheating treatments for ZIF-8 (**Figure 2.10e**)[115]. The obtained structure gave many mesopores and exhibited a three-fold higher external surface area than the non-concave control sample (650 m^2 g^{-1} vs 215 m^2 g^{-1}). It shows superior ORR performance under acid

conditions. The half-wave potential for concave structure is 12mV higher than the non-concave structure in 0.5 M H_2SO_4 (0.823 V_{RHE} vs 0.811 V_{RHE}), boosted in the fuel cell application because its ten times higher catalysts loading. The role of the active site has also been studied. Meanwhile, the large external surface area and mesoporosity play crucial roles in maximizing active sites density through exposing the initially inaccessible Fe-N_4 moieties and thus enhancing the mass transport in the tri-phase point. Therefore, local coordination structures, synthesis steps, and carbon matrix structure are all crucial for a catalysts with high performance. It's essential to consider all these factors when designing a powerful M-N-C catalysts.

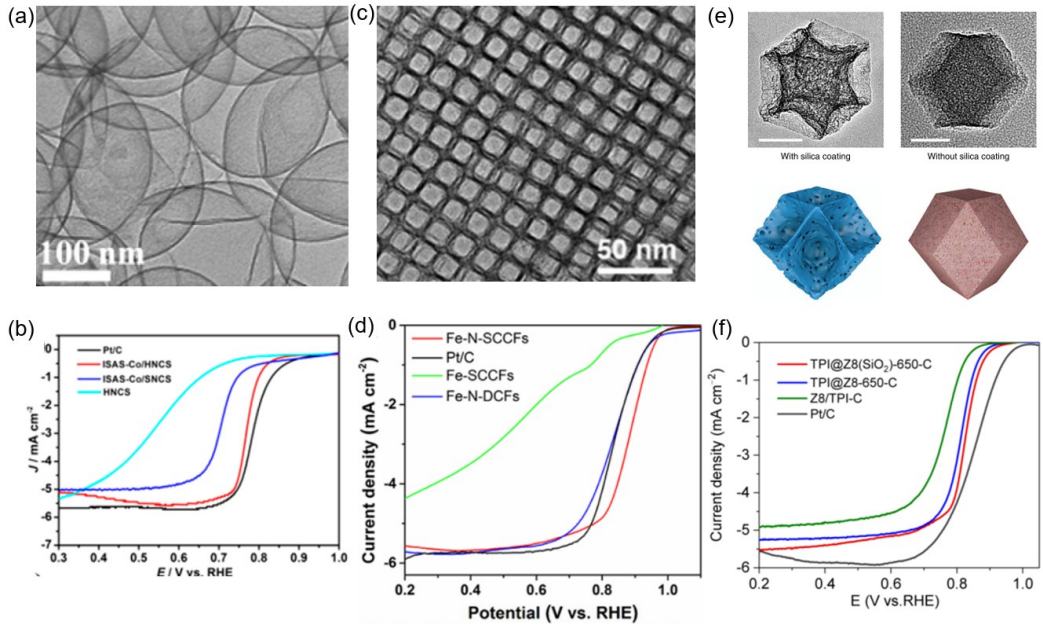

Figure 2.10 (a) TEM images of isolated single Co atomic sites (ISAS-Co/HNCS). (b) Linear sweep voltammetry (LSV) using rotating disk electrode (RDE) technique in O2-saturated 0.5 M H_2SO_4 at 1600 rpm rotation rate. Figure taken from Ref[108]. (c) TEM of the Fe-N-SCCFs. (d) RRDE polarization curves of Fe-N-SCCFs and Pt/C at a scan rate of 10 mV s^{-1} and a rotation speed of 1600 rpm under O_2 saturated 0.1 M KOH electrolyte. Figure taken from Ref[113]. (e) TEM images and cartoons of single-particle concave (left) and nonconcave (right) structures. (f) LSV curves of TPI@Z8(SiO_2)-650-C, TPI@Z8-650-C, Z8/TPI-C and Pt/C at a scan rate of 10 mV s^{-1} and a rotation speed of 1600 rpm in O_2 saturated 0.5 M H_2SO_4 (0.1 M $HClO_4$ for Pt/C). Figure taken from Ref[115].

Besides, biomass itself has a low content of heteroatoms to chelate the metal ion to form smaller metal nanoparticles in the catalysts, suggesting the introduction of dopants. CNT tube structures[116] were also likely to be formed with iron's presence, resulting in an improved

electronic structure favouring four-electron pathways. However, it's challenging to synthesise the M-N_4 into the carbon matrix as the metal tends to aggregate to the particles, reducing the total activity.[117] Low-cost sustainable carbohydrates, such as glucose, gelatin, and chitosan, do not require complex synthesis processes and pre-treatment, which would be ideal materials to obtain single atom M–N–C catalysts on a large scale. Plant biomass[118] and animal biomass[119] have also been shown to obtain M-N_4 sites with a proper pre-treatment to generate pores. The strategies to synthesise single atomic Fe-N_4 sites could be summarised as the 1) Chelating effect to protection metal ion at low temperature (lower than 600 °C).[87] 2) protection of metal ion over 600 °C, introducing the nitrogen source will help transfer Fe into Fe-N_4 instead of iron particles or iron oxides.[98] 3) carbon substrate with high oxygen content and a high surface could also contribute to the high loading of metal sites.[117]

2.3 BIOMASS-DERIVED ELECTROCATALYSTS

Biomass represents the most abundant resource on the planet, a promising source for the future production of fuels, chemicals and materials and could help shift our society from a fossil-based economy to a bio-based economy with immediate significant reductions in CO_2 emissions. With suitable post-treatment methods, various biomass types, which are not in competition with the food supply chain, have been applied to synthesise ORR electrocatalysts (**Figure 2.11**).[120, 121] Biomass is made of mainly cellulose, hemicellulose and lignin. Sometimes there are other carbohydrates which include the monosaccharides (glucose, fructose, galactose), disaccharides (maltose, sucrose, lactose), and polysaccharides (starch, chitin, chitosan, cellulose).

Among many of the example electrocatalysts, biomass is widely applied as carbon support for active sites, which provides surface area, conductivity, and durability in alkaline conditions. Graphene, carbon nanotubes have been popular in carbon materials that could provide high surface area and conductivity and contribute to catalytic activity. Introducing the graphene and

carbon nanotube like structures into the catalysts could boost the catalytic performance and increase the active site's density. Biomass-derived carbohydrates provide building blocks for catalysts. By choosing proper synthesis routes, surface area could reach as high as 2588 $m^2 g^{-1}$ for glucose[122], 1716 $m^2 g^{-1}$ for chitosan[123], and 1209 $m^2 g^{-1}$ for lignin[124], 2091 $m^2 g^{-1}$ for pomelo peels[125], and 1814 $m^2 g^{-1}$ for human hair[126]. In addition, selecting a proper synthesis route to meet the high catalytic catalysts with high reproducibility and scalability is essential for the next step. Also, the carbon surface functional groups can increase active sites loading by anchoring the precursors. An oxygen-rich surface could help separate and protect the active sites during the carbonisation.[127]

However, challenges for biomass-derived carbon remain: biomass alone does not have the right heteroatoms and templating agents to generate enough active sites, resulting in low current density, and it requires pre-treatment to open up the carbon structure's hidden pores. For example, the metal types and amounts may vary with time and places, significantly reducing the catalysts' reproducibility from biomass.[121] Converting the biomass into carbohydrates and designing the catalysts from these building blocks will significantly improve reproducibility.[127]

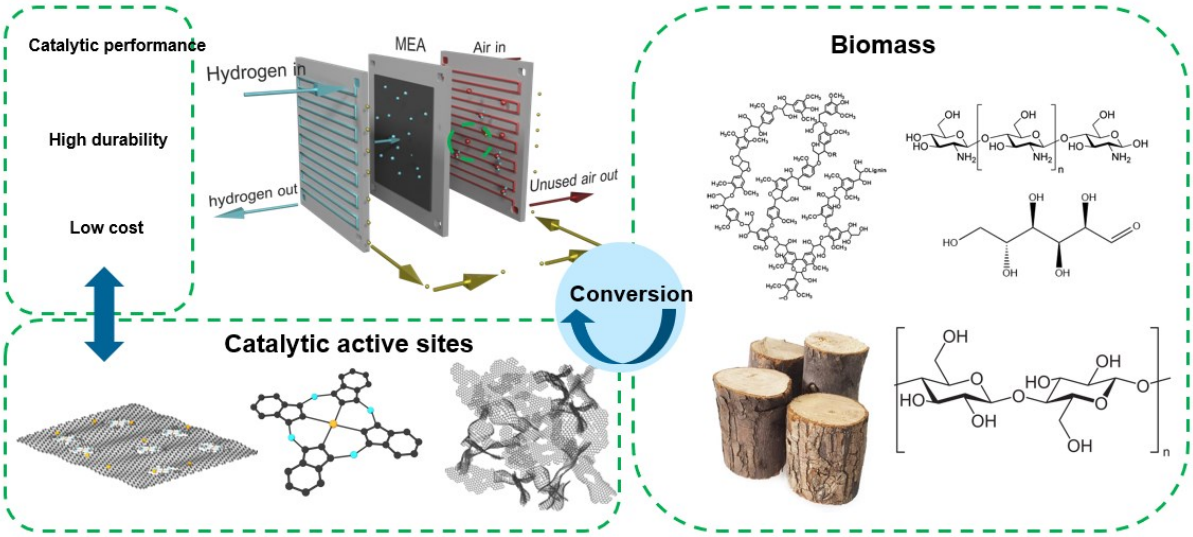

Figure 2.11 Schematic of biomass types and the active sites in the fuel cell cathode side.

2.4 HYDROTHERMAL CARBONIZATION

The hydrothermal carbonization (HTC) process mimics the coal formation process from nature, where it applies temperature and self-generated pressure to convert biomass into coal-like materials. Meanwhile, the duration of the HTC process is only a few hours instead of millions of years as nature does.[128] Hydrothermal carbonization was firstly described by Friedrich Bergius in 1913.[129, 128] Since then, numerous discoveries have been conducted with various biomass resources, temperatures applied, and pH influences on the final produces.[130, 131] During the last decade, hydrothermal carbonization has been used to convert biomass into functional carbonaceous and carbon materials (the carbonaceous material refers to a material with over 60 wt% carbon content and carbon material refers to a material with over 90 wt% carbon content). In this thesis, we will denote the solid carbon materials obtained from HTC as HTC carbon.

Series of work on HTC process and HTC carbon have been reported.[130, 132-135] HTC process includes a series of dehydration, polymerisation and aromatisation reactions which result in a structure of condensed furanic system bridged by aliphatic regions and terminal hydroxyl and carbonyl functional groups (**Figure 2.12a**). Specifically, the HTC product is formed after the dehydration of hexoses to hydroxymethylfurfural (HMF). A complex chemical cascade occurs after forming these intermediates, which involves a simultaneous combination of ring-opening reactions to produce diketones followed by aldol-type condensations with furanic, whilst Diels-Alder reactions may lead to more aromatised structures, with concurrent polycondensation reactions. At the initial stage of polymerization of HMF or furfural, nucleation occurs, and particles grow due to the incorporation of HMF derived monomers and thus resulting in spherical carbonaceous particles.[130] Besides, the structure of the carbonaceous product[136] and its chemical structure evolution pathway during pyrolysis[137] were also studied (**Figure 2.12 b-d**). A core-shell structure was observed for HTC carbon obtained from glucose solution where the core showed condensed aryl-linked furan subunits and shell showed an enriched range of

carboxyl and aldehyde functionalities.

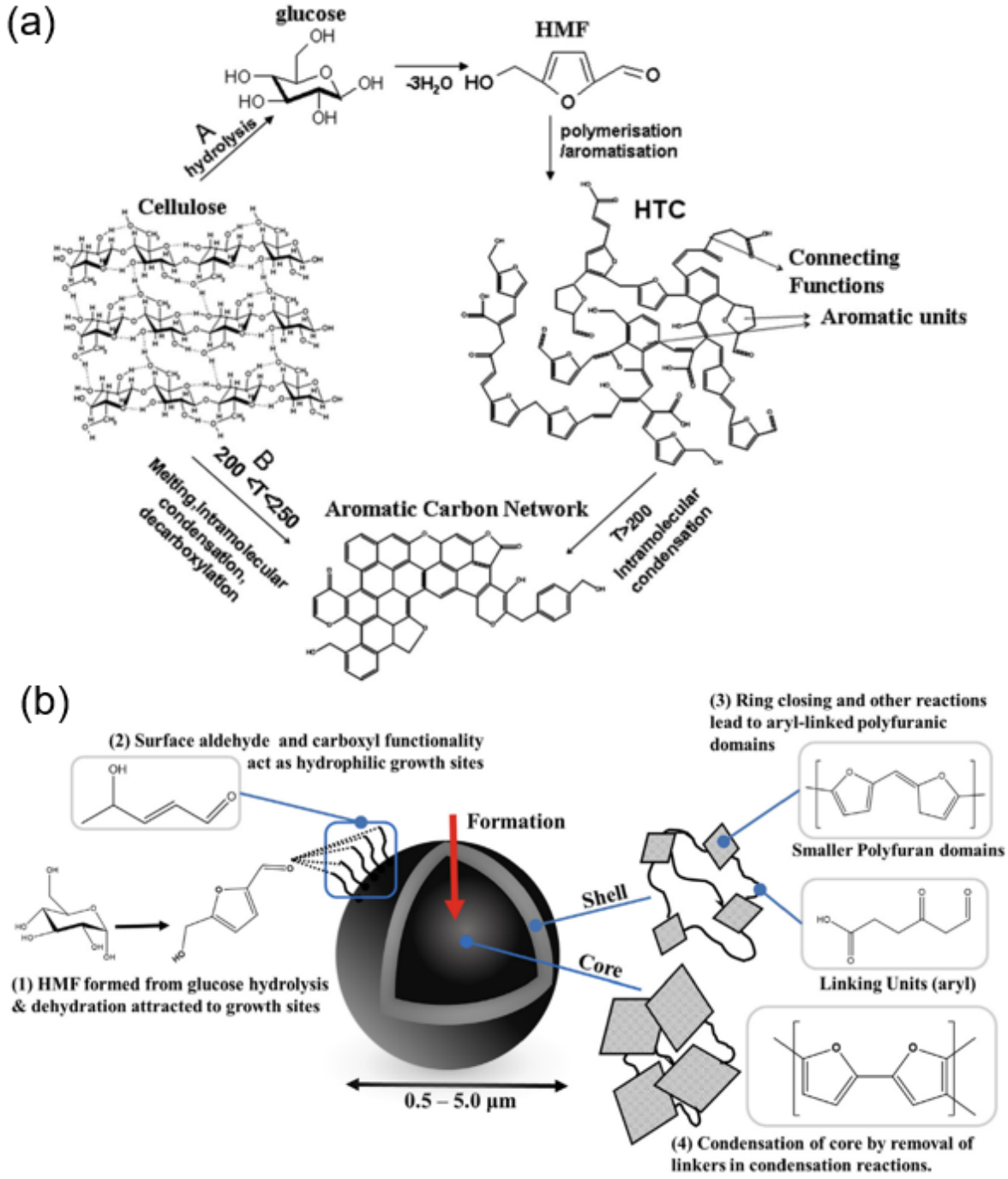

Figure 2.12 (a) Converts cellulose into Hydrothermal Carbon: rout A: via HMF resulting in a furan-rich aromatic network and route B: direct aromatization. Figure adapted from Ref[130]. (b) Schematic of the chemical structure of HTC glucose. Figure adapted from ref[136].

The morphology of the HTC carbons could be controlled to get spherical particles, nanosheets, nanofibers (**Figure 1.9**).[130] The surface chemistry of the resulting materials can be controlled while maintaining the morphology and porosity. Other inorganic components/functional

agents/templates can be quickly introduced during the HTC process to obtain desired chemical and physical structures. Moreover, oxygenated groups located at the surface of resulting particles confer polarity to the resulting materials while simultaneously being removed via post-treatments. Besides, in terms of the green chemistry aspect, the HTC process shows an efficient way of taking CO_2 out of the carbon cycle to reduce the CO_2 present in the atmosphere by converting biomass to solids and thus capturing CO_2, which helps to close the 'carbon cycle'.[138] By incorporating different templates and surfactants in the HTC process, different morphology of HTC products could be obtained,[135] such as hollow nanofibers[139], hollow carbon spheres[140], mesoporous carbon spheres[141], nanosheets[142]. The HTC method of converting biomass and biomass-derived precursors into electrocatalysts was also widely studied in recent years.[120, 143] Followed by post carbonization or activation, high yield, high surface area, higher graphitization, and high performance could be achieved. Some of them are comparable with the commercial Pt/C catalysts for ORR application.[120 121, 143]. However, a large scale HTC synthesised will also need to consider the solution properties as the temperature gradient between the HTC reactor wall and inner solutions could cause convection and lead to an inhomogeneous product.[144]

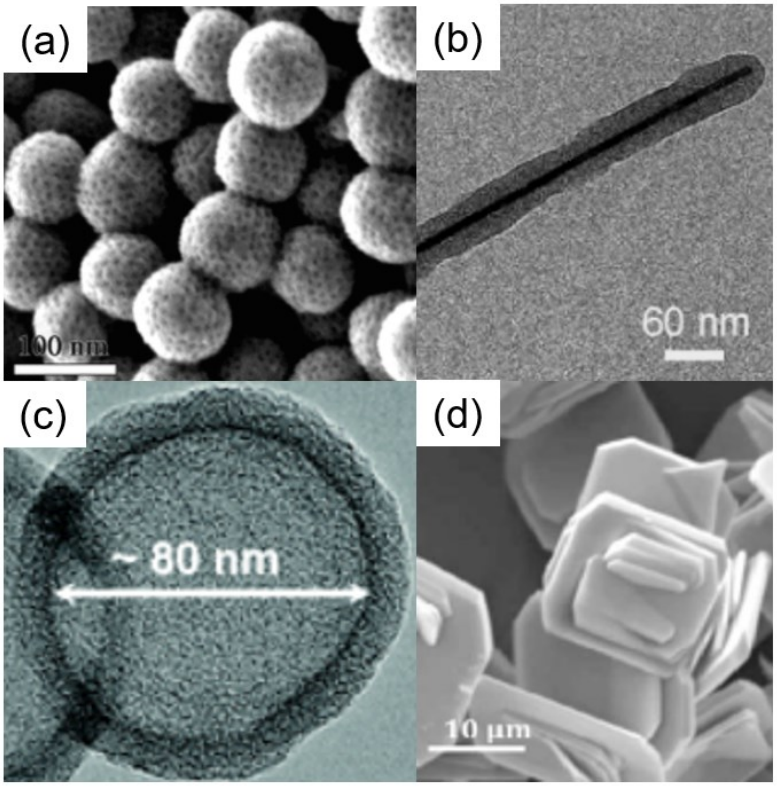

Figure 2.13 (a) SEM images of mesoporous carbon via templating tri-block copolymer Pluronic F127, the size of nanospheres can be varied from 20-120nm by changing the concentration of reagents. Figure adapted from Ref[141]. (b) TEM image of HTC carbon-coated nanofibers, followed by removing Te metal inner to obtain hollow nanofibers. By adjusting the HTC conditions, the growth of carbonaceous nanofibers can be optimized. Figure adapted from Ref[139]. (c) TEM images of hollow spheres from templating HTC carbon on Latex spheres. Figure adapted from Ref[140]. (d) SEM image of vanadium oxides nanosheets obtained via the self-assembling. Figure adapted from Ref[142].

2.5 FREESTANDING ELECTRODE

Tremendous progress has been made to develop powder formed catalysts with excellent ORR performance.[45, 145, 146] Conventional catalyst layers were prepared by mixing powder catalysts with binder and drop cast on the electrode, facilitating mass transfer due to its single-layer configuration.[147] However, transferring lab-made catalysts to large scale applications without losing their activity and stability are still challenging (**Figure 2.14a**).[148] Moreover, the lack of intermediate testing technologies[149, 150], design catalysts with mass transport features[146], and design effective catalysts layers[151-153] have also been major obstacles for effective catalysts electrode in practical devices. Floating cells[154] and gas diffusion electrode[155] have been

reported as intermediate testing methods by providing closer real fuel cell testing conditions. Furthermore, modifying carbon-based supports to increase hydrophilicity and interaction with active sites[156], tuning pore structures of catalysts for better mass transport[157], and modifying surface for faster mass transfer[158] have been proposed as strategies to improve the oxygen diffusion of catalysts. Particularly, developing binder-free, freestanding electrodes is interested in practical energy devices.[159, 160]

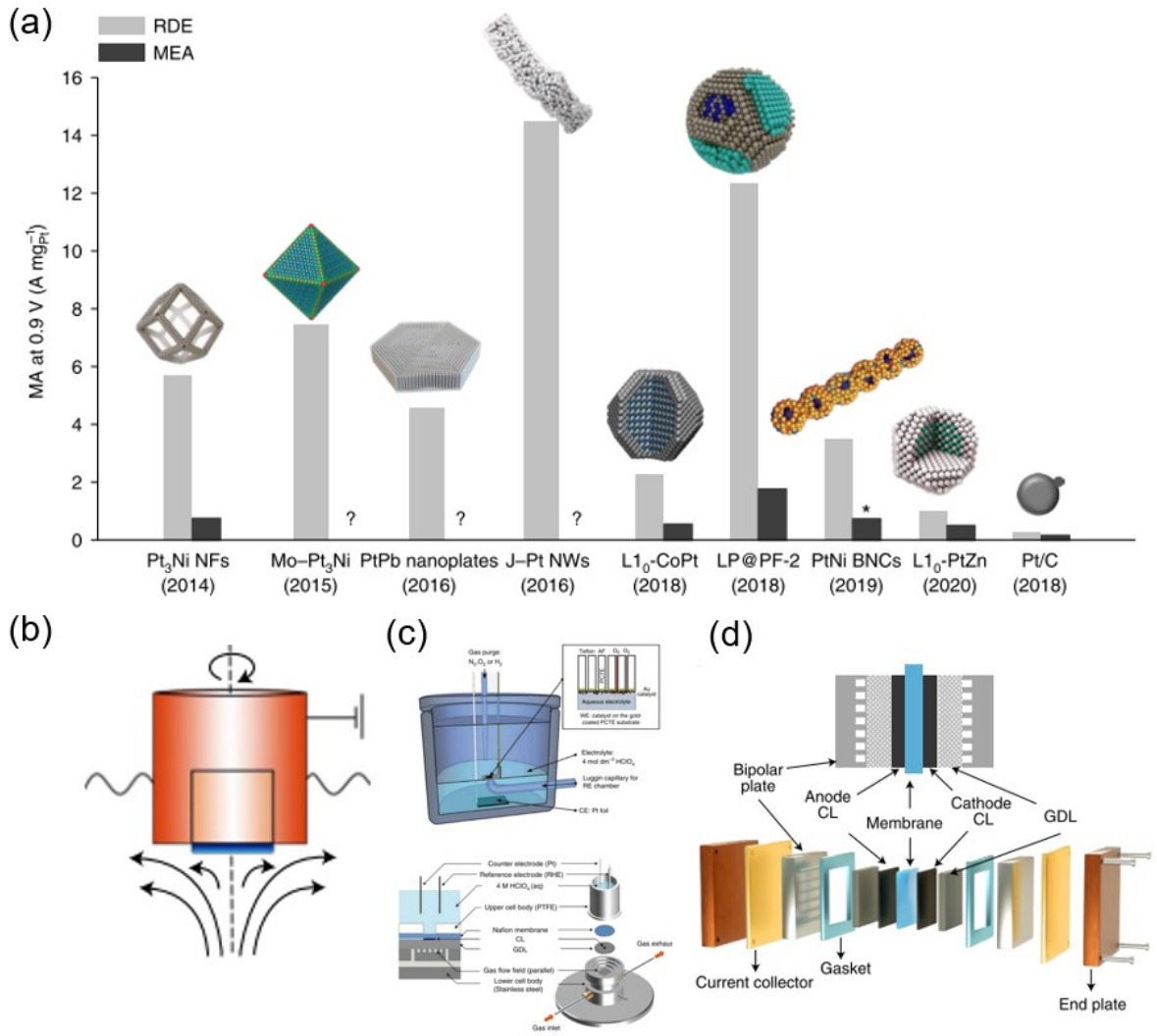

Figure 2.14 (a) Comparison the activity of Pt-based catalysts in RDE and MEA configuration. (b) rotating disk electrode (RDE) configuration. (c) Top: floating electrode configuration[154], bottom: half

cell GDE (gas diffusion electrode) configuration[155]. (d) fuel cell configuration. Figure a-b and d was taken from Ref[148].

So far, carbon fibre mats, metal meshes, freestanding hydrogels, and freestanding metal alloys networks have been reported as binder-free freestanding electrodes, where fibrous are the most popular structures due to their flexibility and simplicity of functionalization.[161-163] To be noted, there have also been alternative names in the literature such as monolith (graphene oxide, hydrogel), self-support electrode (modified carbon fibre paper), and paper electrode (carbon fibre-based electrode). Besides, different fabrication strategies for transition metal-doped carbon have been exhibited, including growing catalysts on carbon fibers[164], catalysts self-assembly and using sacrificial templates such as metal mesh[165]. Liu et al. have reported a free-standing nitrogen-doped carbon nanofiber (N-CNF) based on polyacrylonitrile (PAN), by glueing the fibre mat on RDE to perform ORR.[166] The fibre mat was synthesized via electrospinning using PAN as a precursor and following a 900 °C thermal treatment at N_2 atmosphere with two combustion boats to dope nitrogen by self-generated NH_3 (**Figure 2.15a**). This work sticking N-CNF onto RDE to perform greatly benefits the gas transport during ORR testing (**Figure 2.15a**). Specifically, N-CNF was cut into a 5 mm piece in diameter and then stuck onto RDE with 5 µl 0.5 wt% Nafion solution, which can apply to rotate during the ORR test and thus accelerates the oxygen transport into a freestanding structure. The ORR onset potential and half-wave potentials are -0.034 $V_{Ag/AgCl}$ and -0.182 $V_{Ag/AgCl}$, where the onset potential was about 45 mV more negative than commercial Pt/C catalysts (**Figure 2.15b**). N-CNF exhibits 6.6 % drop in current density after 10,000 s (2.77 h) continuous operation while Pt/C exhibits 16.3 % (**Figure 2.15c**). The comparable onset potential of N-CNF originated from the N-induced charge redistribution and the hydrophilicity of N-CNF, while the stability of N-CNF could be attributed to its free-standing structure.

To improve the catalytic performance, transitional metals are usually efficient dopants for either post-treatment of the freestanding electrode or in-situ doping on the electrode.[160] Cai *et al.* reported N-doped vertically aligned carbon nanotubes on graphene foam (N-VA-CNTs/GF).[165] The electrocatalytic activity was tested by adhering to a piece of N-VA-CNTs/GF film on RDE.[167] Chemical vapour deposition (CVD) was first applied to form graphene foam (GF) on Ni mesh, followed by impregnation with catalysts and growth of vertically aligned carbon nanotubes (VA-CNTs) (**Figure 2.12d**). The Ni mesh was removed by an etching process followed by coating with PANI to produce N-VA-CNTs/GF. To further test the ORR performance of obtained catalysts, electrochemical testing was conducted by cutting N-VA-CNTs/GF films into 1mm diameter pieces and sticking them on the glassy carbon surface with a 1 μL 0.5 wt% of Nafion solution. VA-CNTs/GF annealing at 800 °C has comparable limiting current density to commercial 40 % Pt/C catalysts. Notably, the thickness of VA-CNTs/GF film is much higher than Pt/C catalysts. The durability is illustrated in **Figure 2.12f**, where VA-CNTs/GF shows an 11 % drop after 10,000 s (2.77 h) operation while Pt/C shows a 50 % drop after 20,000 s (5.55 h) operation. As the thickness of GF film is higher than power catalysts, ORR testing may not provide a sufficient evaluation for analysing GF films' activity, but it is still a convenient way to compare different catalysts under the same testing environment.

Moreover, carbon fibres modified by transitional metals have been reported.[164] A hierarchically porous structure of metal atom anchored N-doped carbon flakes supported carbon nanofibers core fabricated through impregnation, carbonization, and acidification. Polyacrylonitrile (PAN) nanofibers were electrospun first and then immersed into a solution containing 2-methylimidazole and cobalt nitrate to form the leaf-like flake on nanofibers. After that, the pyrolysis process was conducted to generate a Co-N site and the acid leaching process to remove the metal clusters. The obtained catalysts (Co SA@NCF/CNF) exhibit fascinating

ORR performance in a 0.1M KOH electrolyte with a halfwave potential $E_{1/2}$ = 0.88 V_{RHE} ($E_{1/2}$ = 0.84 V_{RHE} Pt/C). By conducting experiments and DFT calculations, its superior ORR electrocatalytic performance was attributed to its well dispersed active sites, hierarchical porous structure, conductive nanofiber backbone, and binder-free design.

Notably, a popular method of enlarging the three-phase boundary in fuel cell cathodes is applying a thin and highly hydrophobic micro-porous layer on the substrate material, reducing the liquid saturation in the catalyst layer.[168] The method was first used on noble metal electrocatalysts by applying poly(tetrafluoroethylene) (PTFE) hydrophobic agents onto Teflon treated carbon fibre papers loaded Pt/C catalyst, boosting oxygen diffusion through the cathode. Lu *et al*. illustrated a 'superaerophilic' free-standing structure by growing porous cobalt-incorporated nitrogen-doped carbon nanotube (CoNCNTs) arrays on carbon fibre paper (CFP) with PTFE post-treatment (**Figure 2.15i**)[169]. Compared to commercial Pt/C loaded carbon fibre paper, CoNCNTs possessed abundant three-phase contact point obtained through this 'superaerophilic' construction (**Figure 2.15h**) and significantly increased the utilization of electrocatalysts and catalytic efficiency. The electrochemical performance of this free-standing electrode was measured in a three-electrode glass cell with O_2 bubbled through the electrolyte. CoNCNTs showed a lower onset potential than Pt/C catalyst on PTFE coated Teflon treated carbon fibre paper due to the intrinsic catalytic properties and higher current density as its 'superaerophilic' architecture (**Figure 2.15i**). Notable ORR performance was obtained in a wide pH window (both in acid and base media). Subsequently, PTFE treated CoNCNT carbon fibre paper showed superior stability at high current density, attributed to the high surface area afforded by the morphology and excellent connectivity between the CoNCNT and carbon fibre substrate.

Therefore, a freestanding electrode with high stability and catalytic performance could be obtained by carefully selecting precursors and designing the synthesis method. The micro

structure and macro structure of the freestanding electrode can influence the mass transfer and therefore need to consider when designing a freestanding electrode as catalysts for ORR.

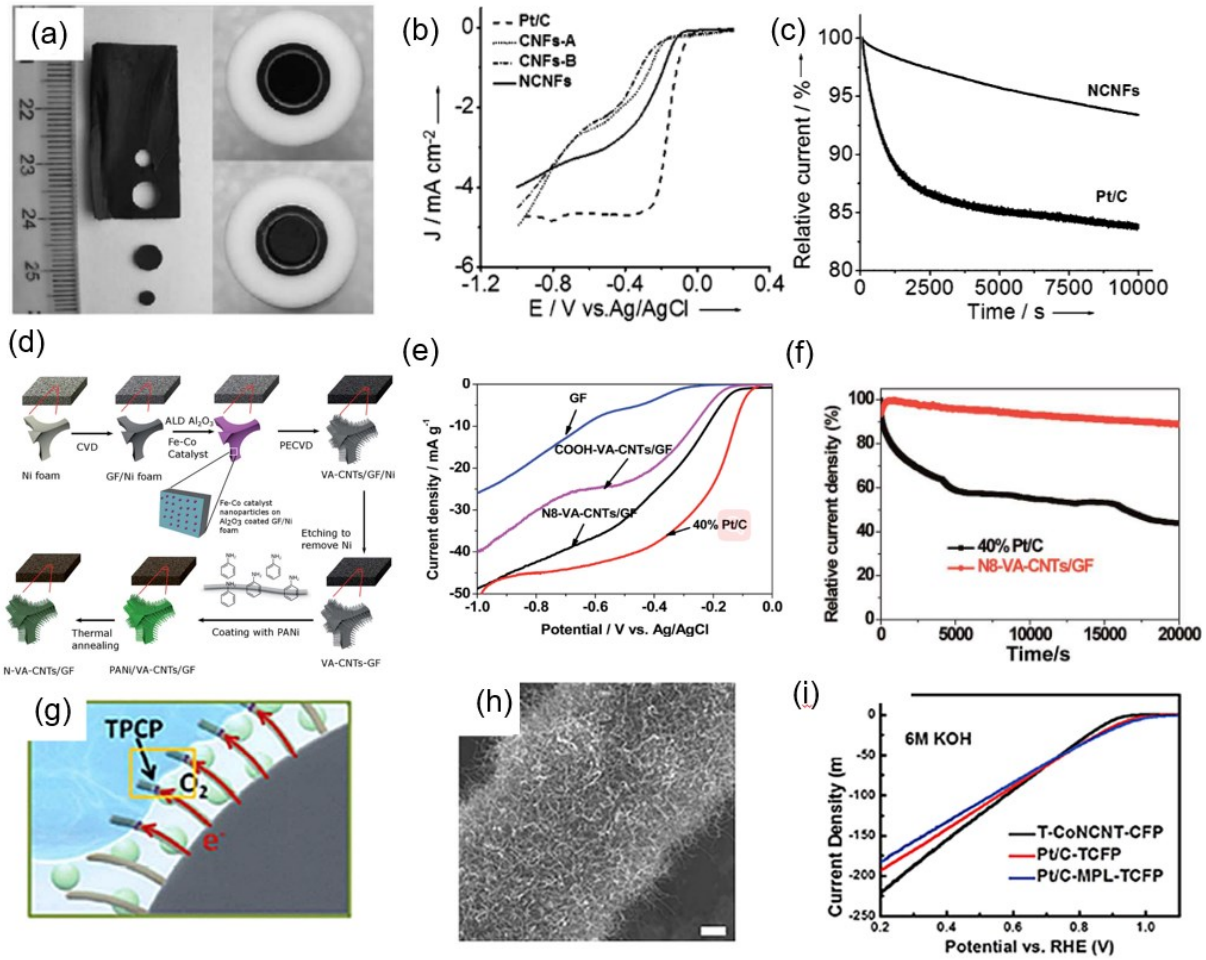

Figure 2.15 (a) Photograph of free-standing films and disk-shaped N-CNF for the electrode modification. (b) LSV of ORR N-CNF and Pt/C in O_2-saturated 0.1M KOH solution at 10 mVs^{-1} scan rate at 1600 rpm. (c) Chronoamperometric response of N-CNF and Pt/C at -0.26 V in O_2-saturated 0.1M KOH at 1600rpm rotation rate. Figure a-c was taken from Ref[166]. (d) synthesis route of N-VA-CNTs/GF, (e) LSV curves of different VA-CNTs/GF in 0.1 M KOH, (f) Durability evaluation of the N8-VA-CNTs/GF and 40% Pt/C for 20,000 s (5.55 h). Figure d-f was taken from Ref[170]. (h) Schematic illustration of the superaerophilic structured electrode by direct growing CoNCNTs on CFP, both electron transport and oxygen-diffusion processes are accelerated, (g) SEM images of the CoNCNTs arrays on carbon fibre paper, the scale bar is 2 μm, (i) LSV curves of the T-CoNCNT-CFP. Figure h-i was taken from Ref[169].

Chapter 3

FREESTANDING CARBON ELECTRODES FOR THE OXYGEN REDUCTION REACTION

3.1 INTRODUCTION

Freestanding electrodes provide advantages such as fewer components in a system, better integration, minimising the manufacturing steps and facilitating recyclability. In addition, freestanding electrodes can be prepared with mechanical strength and made portable & smaller in size. The advantages of binder-free, metallic current collector-free and inactive conductive additive-free made freestanding electrodes highly desirable in electrochemical devices.[171] However, challenges such as high mass transfer barrier, upscale synthesis, and testing configuration remain.

A cost-effective and scalable way to synthesise effective catalysts and supports is necessary to support the commercial uptake of the fuel cell technology. Hydrothermal carbonisation is a green process whereby a biopolymer (cellulose, glucose) is decomposed under hot, compressed water and autogenerated pressure to repolymerise into a more condensed version furan-like carbonaceous material with oxygenated surface groups (**Figure 2.21**). The advantage of this method is the possibility of modulating the morphology and pore structure and hybridising either heteroatoms or inorganics within the structure of the hydrothermal carbons.

This chapter synthesised a nitrogen-doped three-dimensional hierarchical and interconnected carbon network via an easy, cost-effective, and scalable hydrothermal carbonisation method. This carbon electrode will be used as a freestanding, binder-free electrode for the oxygen reduction reaction. We have developed a new way of supporting the freestanding electrode-electrocatalysts to be tested in rotating disk configuration. The synthesised freestanding electrodes were tested using a freestanding electrode tip, which screws the electrodes onto RDE.

Linear sweep voltammetry and chronoamperometry tests show that the pellet catalysts or supports show superior stability (no noticeable current loss after 40,000 s (11.11 h) test).

Furthermore, the degradation of the carbon electrode was studied and revealed that only the top layers of the carbon electrode were degraded with an increasing amount of oxygen content. A primary Zn air battery was assembled to demonstrate the ability of our freestanding electrodes-catalysts pellet to be used directly in electrochemical devices. The pellet's microstructure and chemical structure were optimised by varying the carbonisation temperature and pellet thickness. The higher the pellet's thickness, the higher the diffusion transfer. However, a better understanding of the type and distribution of active sites is still needed to impart an improved performance to the pellet.

3.2 SAMPLE PREPARATION

Reagents and solutions. All chemicals were used without further purifications. D –(+) Glucose (Sigma-Aldrich, BioReagent, ≥ 99.5 %), melamine (99%, Sigma Aldrich), potassium hydroxide hydrate (99.995%) Suprapur, deionised water (DI) (18.2 MΩ cm), absolute ethanol (≥ 99.9%, Fisher Scientific).

Synthesis of HTC carbon spheres. Glucose, a readily available monosaccharide, was used as an eco-friendly precursor and a source of carbon framework for doping nitrogen atoms. Hydrothermal carbonisation (HTC) of this six-carbon sugar yielded spherical particles with an average diameter of 340 nm. For each sample, 14 g of solid glucose dissolved in 140 ml DI water in a glass beaker, then stirred for 1 hour. The next stage of the synthesis was the HTC of the glucose solution. The prepared solutions were transferred to a 200 ml hydrothermal reactor (Kemi, Anhui, China), with the reactor then placed in a pressurised furnace (Memmert, Germany) at 200 °C for 12 hours. The obtained solid sample was further filter-washed with 500 mL water to remove any unreacted substances. After that, the obtained samples were

vacuum dried at 120 °C for 24 hours to remove any remaining moisture, producing dehydrated samples fit for milling. Milling was carried out using a pestle and mortar for around 20 mins to yield a fine powder of hydrothermal carbon spheres.

Synthesis of nitrogen-doped carbon spheres (NC700_0, NC800_0, NC900_0, NC1000_0). Melamine was chosen as the nitrogen precursor due to its rich N content and wide availability. Melamine was first mixed with HTC powder by a 1:1 mass ratio, and then milling was carried out for around 20 mins using a pestle and mortar to yield a well homogeneous fine powder. The carbonisation was then carried out in a tubular furnace by one-step carbonisation under N_2 atmosphere (gas flow rate: 0.5 L min^{-1}). The temperature was ramped up to T °C (T = 700, 800, 900, 1000) for 2 hours with a heating rate of 5 °C min^{-1}. The obtained samples were denoted as NC700_0, NC800_0, NC900_0, and NC1000_0, respectively.

Synthesis of nitrogen-doped carbon pellets (NC700_25, NC700_50, NC700_75, NC800_25, NC800_50, NC800_75, NC900_25, NC900_50, NC900_75, NC1000_25, NC1000_50, NC1000_75). Similar to the preparation of nitrogen-doped carbon spheres, melamine was first mixed with HTC powder by a 1:1 mass ratio, and then milling was carried out for around 20 mins using a pestle and mortar to yield a well homogeneous fine powder. To form a pellet shape sample, 25 mg of the obtained mixture was loaded into an 8 mm die, followed by a 780 MPa (4 tonnes) pressure applied on the mixture samples using a manual hydraulic press (Specac). The equation to calculate the pressure:

$$Pressure = \frac{Force}{Area} = \frac{mg}{\pi r^2} = \frac{4000 \times 9.8}{3.14 \times 0.004^2}\ Pa \approx 780\ MPa$$

The obtained brownish pellets were placed in the middle of a rectangular crucible, and the carbonisation was then carried out in a tubular furnace by one-step carbonisation under N_2 atmosphere (gas flow rate: 0.5 L min^{-1}). The temperature was ramped up to T °C (T = 700, 800,

900, 1000) for 2 hours with a heating rate of 5 °C min^{-1}. The obtained samples were denoted as NC700_25, NC800_25, NC900_25, and NC1000_25, respectively.

To investigate the thickness influence, pellets with different thicknesses were also prepared similarly. By loading different melamine/HTC mixture amounts, we can vary the thickness within a controllable range. Instead of 25 mg loading amount, pellet with 50 mg and 75 mg loading amount was also prepared, the obtained samples were denoted as NC700_50, NC700_75, NC800_50, NC800_75, NC900_50, NC900_75, NC1000_50, NC1000_75, respectively.

The equation to calculate the obtained density of pellet samples:

$$\rho = \frac{mass}{Volume} = \frac{m}{Thickness \times \pi \times \left(\frac{D}{2}\right)^2}$$

The Thickness value is the average of three measurements, D is the diameter of the pellet (the value is the average of the three measurements), and m is the mass of the pellet (the unit for density is g cm^{-3}).

3.3 RESULTS AND DISCUSSION

Nitrogen-doped pellets were denoted NCT_X, where T is the carbonisation temperature, and X is the pallet's thickness. The synthetic strategy is illustrated in **Figure 3.1**. Firstly, hydrothermal carbon spheres with abundant oxygen functionalities were prepared by hydrothermal carbonisation of the glucose. The obtained hydrothermal carbon spheres were mixed with nitrogen (melamine) with a 1:1 weight ratio, followed by a pelleting process where the mixture of the melamine and carbon was loaded into a die. The obtained brownish pellets were then carbonised under N_2 atmosphere. During the carbonization, melamine melted and decomposed into NH_3 to introduce the nitrogen into carbon substrate, and a hierarchical porous structure was generated; the obtained sample was noted as NC900_25. By varying the thickness

and carbonization temperatures, both physical and chemical structures were controlled. The final pellet samples were denoted as NCT_X, where T represents the carbonisation temperature, and X represents the input carbon mixture weight related to pellet's thickness. E.g. NC900_0, NC900_25, NC900_50, and NC900_75, represent samples carbonized at 900 °C with thickness of 0 (powder without pelleting), 25 (~ 0.35 mm), 50 (~ 0.75 mm), 75 (~ 1.05 mm).

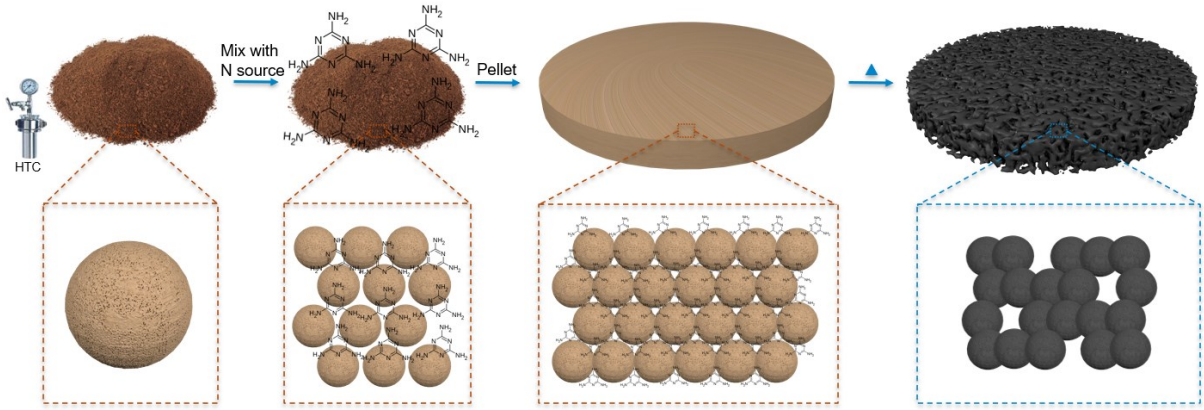

Figure 3.1 Scheme illustration for the synthesis of nitrogen-doped pellet.

After the carbonisation process, the NC800_25 pellet shrinks by ~ 20 % in diameter and ~ 1-3 % in thickness. The obtained NC900_25 is ~ 40 % weight compared to the prior pellet carbonisation. The small differences in the size of the pellet before and after carbonisation cumulated with a significantly reduced pellet weight suggests that abundant pores are formed during the carbonisation process, accompanied by the melting and decomposition of melamine.[172, 173] A pellet with many nanopores will facilitate electrolyte and ion transport contact when used as a fuel cell electrode.[174] Furthermore, pellets with different thicknesses and diameters can be easily fabricated by changing the die diameter.

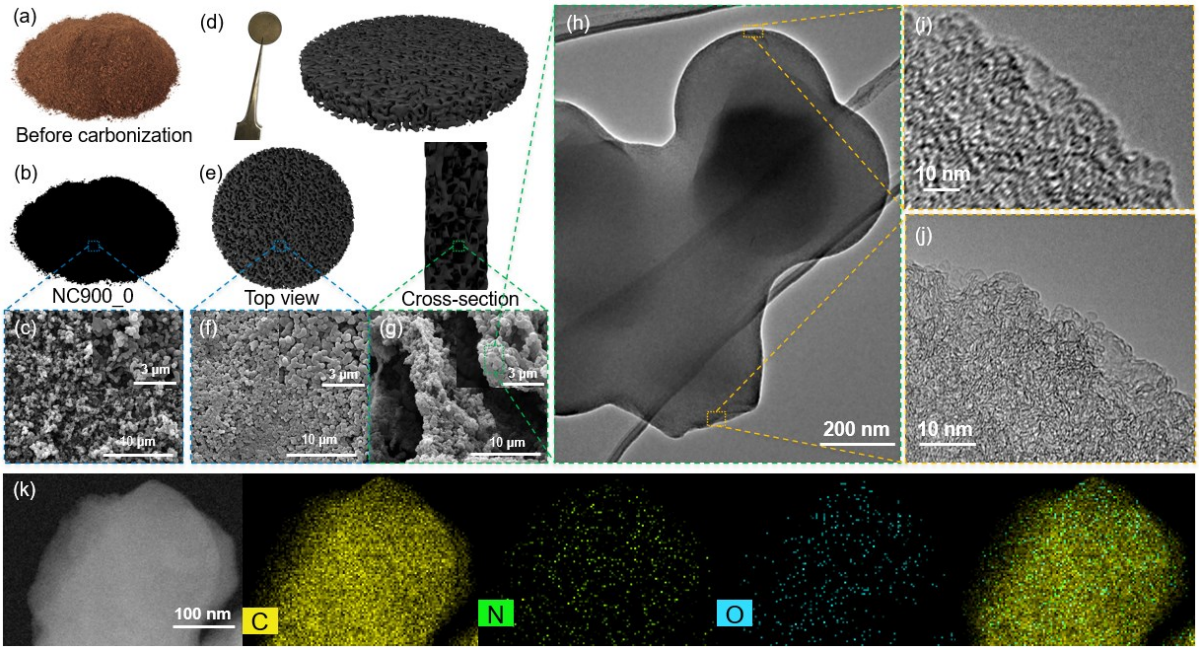

Figure 3.2 Image of a mixture of melamine and HTC spheres (a) before and (b) after carbonisation (NC900_0), (c) SEM image of NC900_0 (insert: zoom in SEM image of NC900_0). (d) Image of carbonised pellet sample, (e) top view and cross-section view of the pellet sample, (f) top-view SEM images of the carbonised sample (NC900_25), and (g) cross-section view SEM images of NC900_25 (insert: zoom in SEM images of NC900_25). (h) TEM images and (i-j) high-resolution TEM images of NC900_25. (k) HAADF-STEM image of NC900_25 and the EDS mapping results of NC900_25.

3.3.1 Morphology and structure characterisations

As shown in **Figure 3.2c-g,** NC900_25 consists of peanut shape spheres with a diameter of 492 nm, 50 nm smaller than NC900_0 (powder sample instead of pressed into pellet). The NC900_25 carbon spheres are compact and provide an inter-connected structure. The thickness of the electrode is ~ 0.34 mm as measured from both the cross-section scanning electron microscopy (SEM) image and calliper (measured three times and average the value). The microstructure of NC900_50 was investigated by transmission electron microscopy (TEM). The high-resolution TEM (HRTEM) confirms that the pellet consists of a highly amorphous microporous structure (**Figure 3.2i-j**). To further investigate the atom distributions in the pellet, the high-angle annular dark-field (HAADF) image and the elemental mappings of the carbon spheres are also obtained. The elemental mappings of carbon, nitrogen and oxygen in a single carbon sphere (**Figure 3.2 g-m)** reveal a uniform carbon, nitrogen, and oxygen distribution in

the NC900_25 pellet sample. The above results suggest that nitrogen is doped into the carbon substrate by the decomposition of melamine. The nitrogen doping in carbon nanomaterials would further modify the chemical and electronic properties of the carbon host and then enhance the oxygen adsorption compared with non-doped carbon materials.[74]

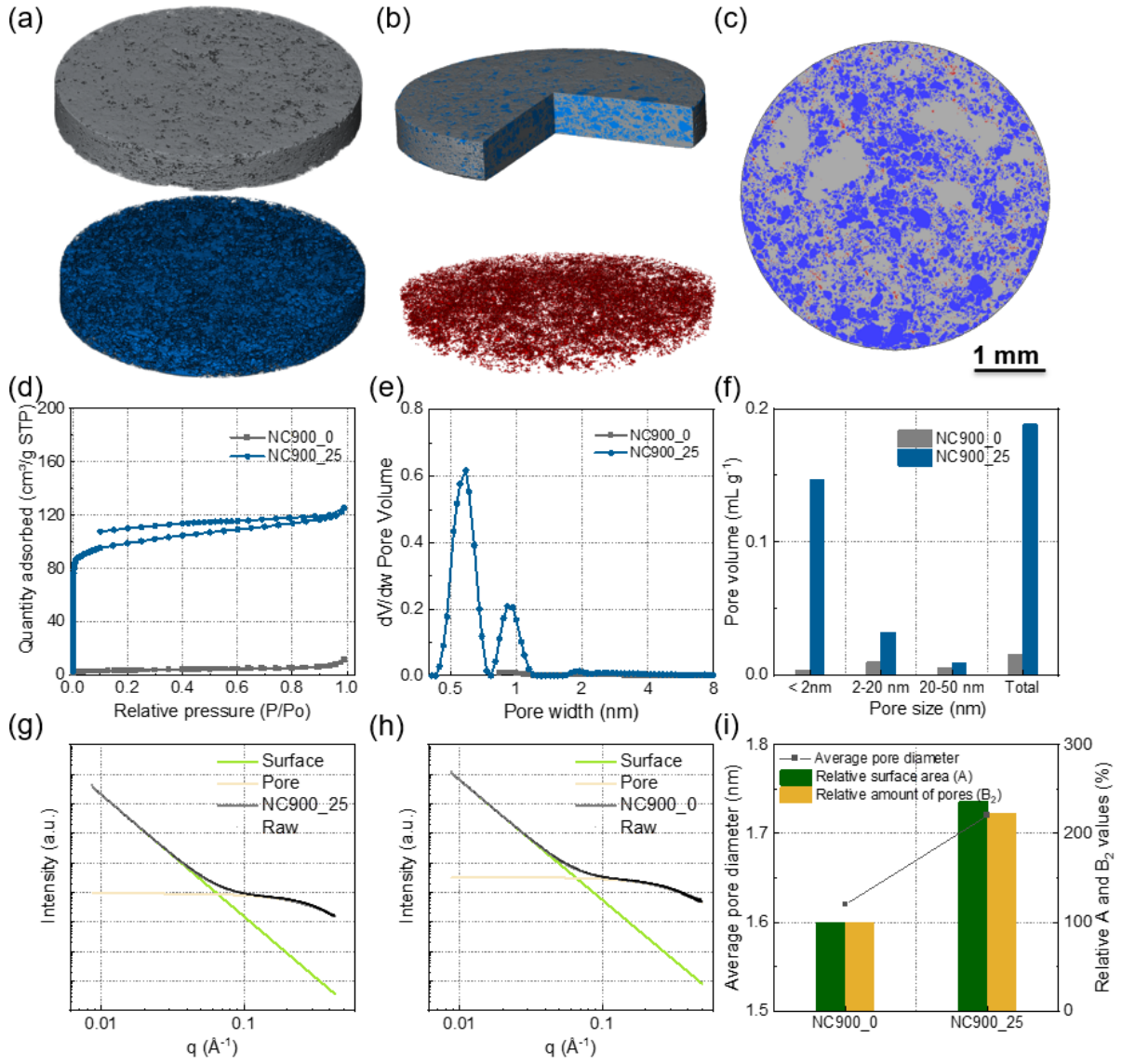

Figure 3.3 (a) Segmentations from reconstructed NC900_25 CT scan of carbon phase on the top and pore phase on the bottom, (b) 3D segment of NC900_25 on the top and isolated pores on the bottom, (c) 2D CT image of NC900_25 (grey represent carbon, blue represent pores connect to air and red represents isolated pores which are inaccessible to air). (d) N_2 adsorption isothermal curves of NC900_0 and NC900_25, (e) calculated pore size distribution from isothermal curves of NC900_0 and NC900_25, (f) comparison of the pore size distribution of NC900_0 and NC900_25. Fitted SAXS patterns of (g)

NC900_25 and (h) NC900_0, (i) comparison of average pore diameter, relative surface area (A value) and relative amount of pores (B_2 value) fitted from SAXS spectrums of NC900_0 and NC900_25.

Systematic characterisations were conducted to get insights into the porous structure from the nanoscale to the macroscale of the obtained pellet, which includes computed tomography (CT), physical adsorption, and small-angle X-ray scattering (SAXS). Nano X-ray computed tomography was carried out to visualise the carbonised pellet in 3D. The reconstruction of the image and segmentation process allowed us to calculate the porosity of pellet samples (**Figure 3.3a-c**). The irreversible isotherm might be the high amount of micropores that prevent the nitrogen molecules from getting out from the samples. Possible solutions such as increasing heating time and temperature can be applied in outgas step to get reversible isotherms. The lab CT systems produced a pixel resolution of 63.15 nm providing clear images and good contrast for the NC900_25 pellets. As shown in **Figure 3.3a**, NC900_25 presents a highly porous carbon network where 40 % of the volume could be assigned to the air, providing good accessibility of the electrolyte to the active sites if used as a freestanding electrode.

In contrast, the non-accessible isolated pore volume is only 2.8 % (**Figure 3.3c**). As shown in **Figure 3.3d**, N_2 physical adsorption was performed, and the BET method was used to determine the specific surface area and the pore size distribution of NC900_25. NC900_25 showed a specific surface area of 381 m^2 $g^{-1,}$ while the obtained NC900_0 has a low specific surface area with around only 13 m^2 g^{-1}. From the pore size distribution in **Figure 3e,f**, we could see that NC900_0 consists of a combination of micropore (< 2 nm) and mesopore (2-50 nm), where micropores contribute most of the pore volume.

SAXS pattern covers a wide length scale, and morphological information can be extracted from most possible microstructural features. The A slop value in q^{-4} at a low angle corresponding to the Porod's law of scattering by sharp interfaces could be ascribed to the macroscopic surface area.[175] The B_2 value in q^{-6} just after the Porod region corresponding to Guinier's law of

scattering by microporosity could be ascribed to the relative amount of pores.[175] Fitted SAXS results showed the average pore diameters for NC900_25 (1.72 nm) is bigger than NC900_0 (1.62 nm). Fitted A and B_2 values proportional to the total surface area and the total number of pores, respectively, were also fitted (**Figure 3.3h**).[176] Whereas NC900_25 showed 236 % total surface area and 223 % relative number of pores compared to NCS900_0.

The crystal structure and phase compositions of the NC900_25 were revealed by X-ray diffraction (XRD) (**Figure 3.4a**). The diffraction peak at 24.3 ° is indexed to the (002) graphite plane, a typical characteristic peak of graphitic carbon with a low degree of graphitisation. The Raman spectra of the NC900_25 display two peaks at 1349 cm^{-1} (D-band) and 1570 cm^{-1} (G-band) (**Figure 3.4b**). The I_D/I_G value of NC900_25 is calculated to be 1.17, slightly lower than NC900_0 (1.27), suggesting NC900_25 possesses a higher graphitization degree. These I_D/I_G values are signatures of low crystallinity carbon with disordered orientations.

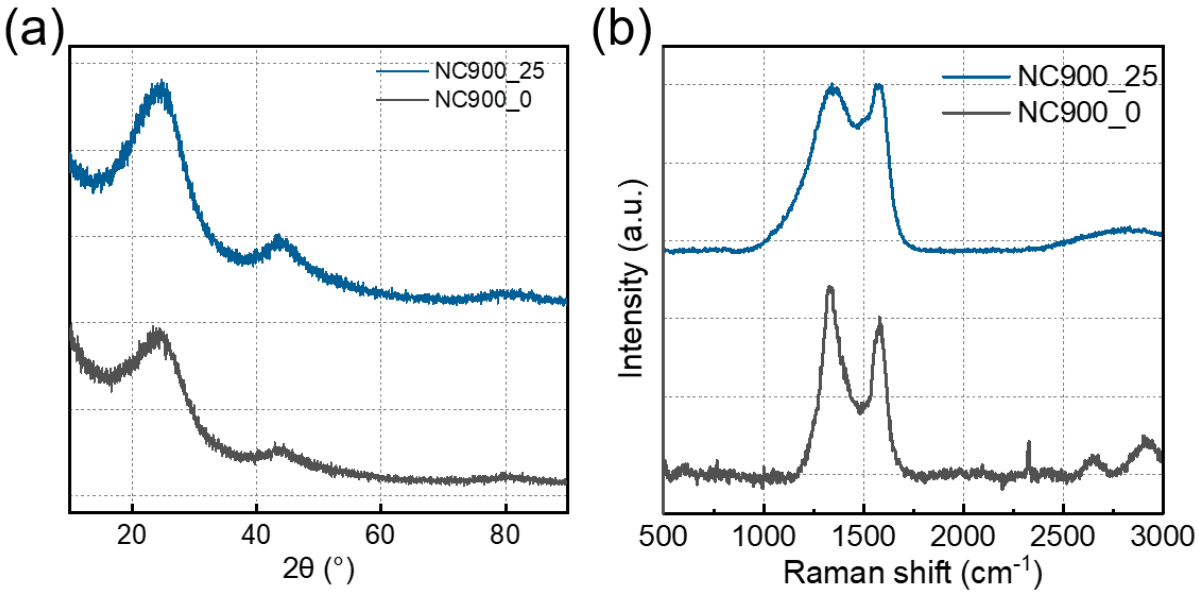

Figure 3.4 (a) XRD patterns of NC900_25 and NC900_0, (b) Raman spectra of NC900_25 and NC900_0.

3.3.2 Chemical characterisation

The surface chemical state of the NC900_25 and NC900_0 was characterised by X-ray photoelectron spectroscopy (XPS) in **Figure 3.5**. Both survey spectrums showed a pronounced

XPS C1s peak at 285 eV, a much weaker N1s peak at 400 eV and an O1s peak at 533 eV (**Figure 3.5a**). The atomic percentages were extracted from the survey spectrums, where NC900_25 shows 83.7 at%, 6.7 at%, and 9.6 at% for carbon, nitrogen, and oxygen, respectively, while NC900_0 shows 76.4 at%, 12.2 at%, and 11.4 at%. Elemental analysis was also performed to investigate the carbon and nitrogen content in NC900_25 and NC900_0, where NC900_25 and NC900_0 showed 5.8 wt% and 7.4 wt% nitrogen content, respectively. High-resolution XPS spectrums were conducted to get more insights into the chemical structures of the obtained nitrogen-doped carbon. As shown in **Figure 3.5 d-f**, the high-resolution XPS spectrums were deconvoluted (see above experimental method).[177] C1s spectrum of NC900_25 (**Figure 3.5d**) could be deconvoluted into six types where graphitic carbon and carbon in more than six-member ring (C-C_{high}) / carbon bonded to N (C_{sp2}-N) account for 56 % and 22 % of the total carbon content, respectively. N1s spectrum of NC900_25 can be deconvoluted into five types of nitrogen bonds, where pyridinic nitrogen and pyrrolic nitrogen accounts for 41.8 % and 31.0 % of the total nitrogen content. The contribution of nitrogen types to electrocatalytic activity is still under debate. However, a recent report showed that combining all three types of nitrogen could contribute to catalytic performance.[178]

Besides, inductively coupled plasma mass spectrometry (ICP-MS) was performed on both NC900_0 and NC900_25, and the Fe concentrations were lower than the detectable range (less than 2 ppb).

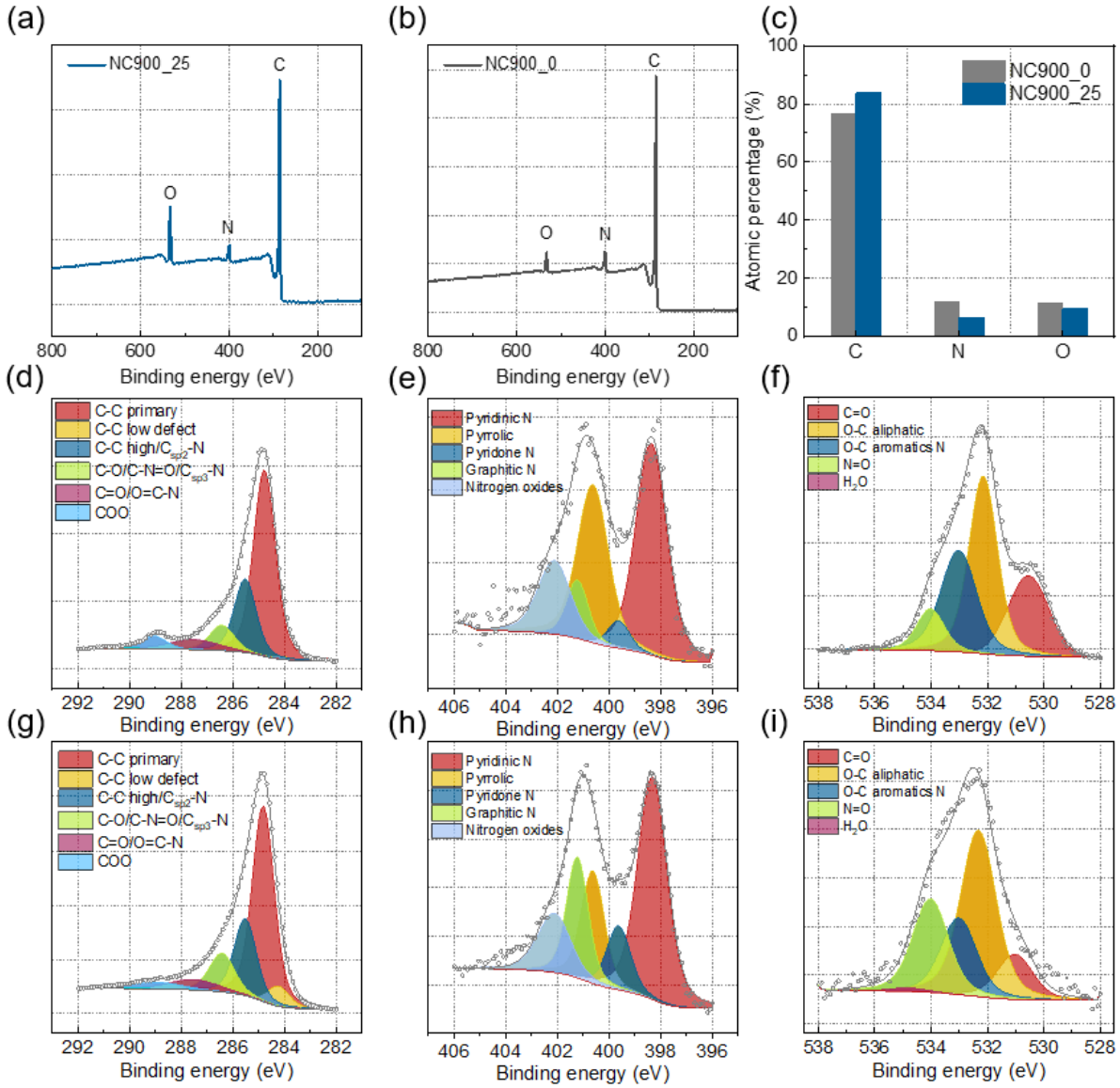

Figure 3.5 XPS survey spectrums of (a) NC900_25 and (b) NC900_0, (c) comparison of C, N, O atomic percentage of NC900_25 and NC900_0. Deconvoluted high-resolution spectrums of (d) C1s, (e) N1s, and (f) O1s for NC900_25. Deconvoluted high-resolution spectrums of (g) C1s, (h) N1s, and (i) O1s for NC900_0.

Moreover, it requires further investigation into how these increased oxygen functional groups could influence catalytic activity. Fourier transform infrared spectroscopy (FTIR) was performed to investigate the influence of the pelleting process on the chemical bonds of uncarbonized NC900_25 pellet and NC900_0 powder. It could be seen that both samples showed characteristic peaks belonging to melamine and HTC carbon (**Figure 3.6**). Compared to uncarbonized NC900_0, a stronger C=O bonding at 1702 cm^{-1} and a weaker O-H binding at 3117 cm^{-1} could be seen in uncarbonised NC900_25.

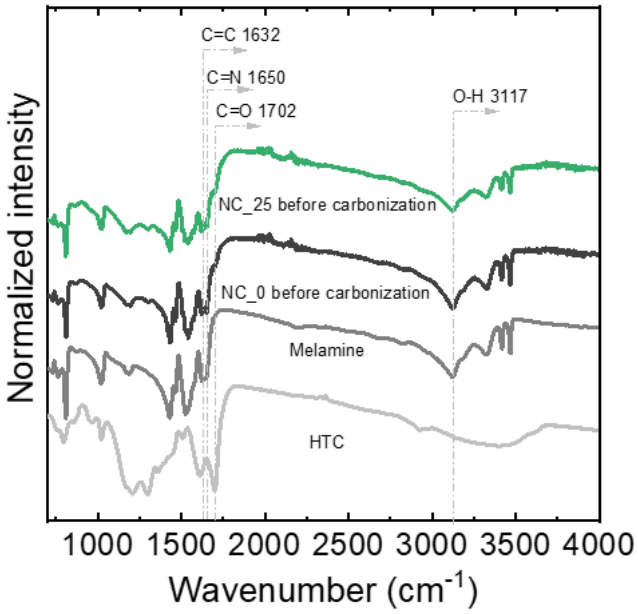

Figure 3.6 FTIR spectrum of HTC carbon, melamine, uncarbonized NC900_25, and uncarbonized NC900_0.

To conclude, NC900_25 has shown an interconnected porous carbon network with homogeneous nitrogen-doped in both macro and micro scales, facilitating the electrolyte mass transfer. Besides, NC900_25 showed a superior high surface area and abundant nitrogen. Which might be suitable for post-treatment to form isolated active sites.[127] Further, the electrochemical characterisations were performed to investigate the catalytic performance of these catalysts.

3.3.3 Electrochemical analysis in RDE

To investigate the kinetic performance of the obtained samples, a rotating disk electrode (RDE) was applied. In **Figure 3.7a**, the ORR catalytic performance of NC900_25, NC900_0, and commercial Pt/C (55-58 wt%) were evaluated by cyclic voltammetry (CV) under alkaline conditions (0.1 M KOH oxygen/nitrogen saturated). While in the absence of oxygen (Nitrogen saturated), a featureless CV was recorded, in the presence of oxygen, a clear peak appeared corresponding to the oxygen reduction reaction between 0.6 to 0.5V (vs RHE) for both samples (**Figure 3.7 b-c**). The peak was slightly more positive oxygen reduction peak and onset potential than those of NC900_0. LSV was carried out to evaluate the oxygen reduction kinetic activity (**Figure 3.7d-f**). The onset potential for both NC900_25 and NC900_0 is around 0.76 V. NC900_25, displaying a half-wave potential of 0.61 V (@ 1.5 mA cm^{-2}), which is 30 mV positive than NC900_0 ($E_{1/2}$ = 0.58 V). At the end of the sweeping potential, the limiting current density of NC900_25 achieved -2.92 mA $cm^{-2,}$ whereas NC900_0 is -2.68 mA cm^{-2}. With the same amount of catalysts loading, limiting current density suggests a similar amount of accessible active sites, which suggests NC900_25 possesses a similar amount of active sites to NC900_0. Nevertheless, the catalytic nitrogen-doped carbon is hard to compare with commercial Pt/C catalysts (E_{onset} = 1.04 V, $E_{1/2}$ = 0.89 V, and limiting current density @0.2V is -4.76 mA cm^{-2}). Further, chronoamperometry (CA) testing was performed to check the stability of NC900_25 in **Figure 3.7g**. After holding 10,000 s (2.77 h) at 0.63 V_{RHE}, 60 % of the current was retained for NC900_25, whereas Pt/C showed 76 % current retention. LSV before and after the CA was also recorded (**Figure 3.7h**). After 10,000 s (2.77 h) at 0.63 V_{RHE}, the potential negatively shifted 69 mV for NC900_25 samples. Overall, NC900_25 provides similar electrochemical performance to the powder samples. However, as testing in the three-

electrode set-up sacrifices the macro 3D structure merits, a freestanding electrode mimicking the RDE was introduced to test the pellet samples.

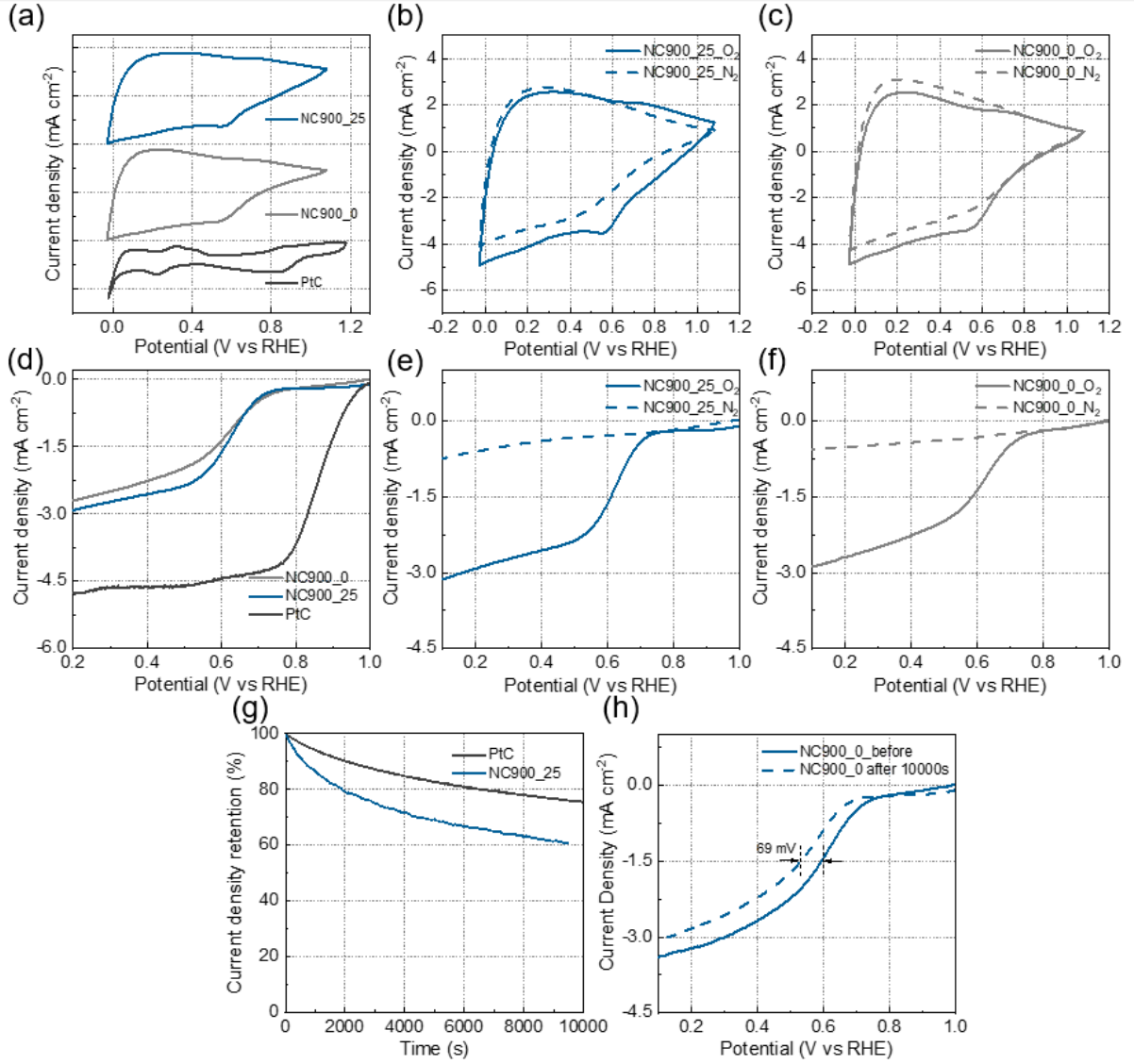

Figure 3.7 (a) CV curves at 0rpm, 100 mV s^{-1} scan rate for NC900_25, NC900_0, and Pt/C. CV curves for (b) NC900_25 and (c) NC900_0 recorded in oxygen/nitrogen saturated 0.1 M KOH conditions. (d) LSV curves at 1600 rpm, 10 mV s^{-1} scan rate for NC900_25, NC900_0, and Pt/C. LSV curves for (e) NC900_25 and (f) NC900_0 recorded in oxygen/nitrogen saturated 0.1 M KOH conditions. (g) Chronoamperometric responses of NC900_25 at 0.63 V_{RHE} and 1600 rpm. (h) LSV curves recorded before and after 10,000 s (2.77 h) CA test at 0.63 V_{RHE}. (Catalyst loading: 0.28 mg cm^{-2}, Pt loading 0.021 mg cm^{-2})

3.3.4 Testing freestanding electrode

To test the freestanding electrode without breaking it into powder, a special freestanding RDE tip was applied. The configuration of the freestanding RDE tip is shown in **Figure 3.8a**. Like

the conventional RDE electrode, it replaced the drop-casting catalyst layer to the pellet, NC900_25, in this case. Most freestanding/self-supported electrodes are limited by the high mass transfer barriers caused by their thickness. Freestanding tip offers rotation conditions for the pellet samples while testing to facilitate the mass transfer.

CV was performed to investigate the catalytic activity of NC900_25 under oxygen and nitrogen. Samples were rotating in the electrode and activated for 1500 seconds at 0.5 V (RHE) before starting the test. The commercial 40 wt % Pt/C carbon fibre paper was also tested for comparison. As depicted in **Figure 3.8b**, no ORR catalytic activity was observed under the bubbling of N_2. However, a significant reduction peak could be observed under the O_2 condition. Notably, the oxygen reduction peaks were only prominent under a slow scan rate for the pellet sample, suggesting high mass transfer barriers (**Figure 3.8c**). The onset potential of Pt/C paper for ORR in the 0.1 M KOH was around 1.05 V. It was more positive than that of NC900_25 (0.83 V). The ORR reduction peak current density for NC900_25 was 0.7 V. More importantly, previous studies had indicated that the area of the CV loop under N_2 rich electrolyte was regarded as a benchmark to appraise the electrochemically active surface area, which could significantly affect the ORR performance of catalysts. **Figure 3.8b** and **Figure 3.11a** shows that the voltammogram area follows the order of NC900_25 > Pt/C, implying that the NC900_25 electrodes had a great potential in catalysing ORR and further enhancing the performance of doping transitional metals such as Fe.

LSV was carried out to evaluate the oxygen reduction characteristics of NC900_25 and was shown in **Figure 3.8d-e**. The onset potentials determined from LSV curves of Pt/C and NC900_25 were 1.05 V and 0.89 V, respectively, which agreed with the CV results. As shown from Figure 3.8e, a significant fraction of current for NC900_25 was capacitive current (under N2) instead of the faradic current, while Pt/C carbon paper primarily shows faradic current. After extracting the current under N_2 conditions, the LSV curve of NC900_25 showed a similar

trend as NC900_25 tested in RDE but higher onset potential and higher limiting current density at 0.4 V, which was caused by different loading of the catalysts. With 3D structures, NC900_25 in pellet form provides more exposure of the sufficient electrochemically active are, and high conductivity substantially increase the chances of as-prepared electrode contact with the electrons and further accelerate the ORR process. Long-term stability was also an important indicator to evaluate the performance of the electrode. The NC900_25 was continuously run under 0.5 V for 40,000 s (11.11 h) under 0.1 M KOH with 1600 rpm rotation. As shown in **Figure 3.8g**, no noticeable current loss could be seen while the Pt/C paper suffers a 40 % current loss. This is different from the RDE test where NC900_25 powder loss nearly 40% current after 10,000 s (2.77 h), and which is probably due to the corrosion of the pellet continues to happen, but the inaccessible part of the pellet gain access to the electrolyte after the top layer is corroded and thus gives this long term stability. NC900_25 pellet was assembled into solid primary Zn-air batteries to demonstrate further its ability to be an actual device (**Figure 3.8i**). NC900_25 was used as an air cathode directly, the solid electrolyte was fabricated in the lab, and a polished Zn foil was used as the anode. The open-circuit voltage reached nearly 1.6 V, close to the theoretical value (1.65 V), and the current density reached 24 mA cm^{-2}. Thus, compared to the NC900_25 in powder form, the NC900_25 pellet showed higher onset

potential, higher limiting current, and much higher stability, all of which are likely to originate from the 3D carbon framework.

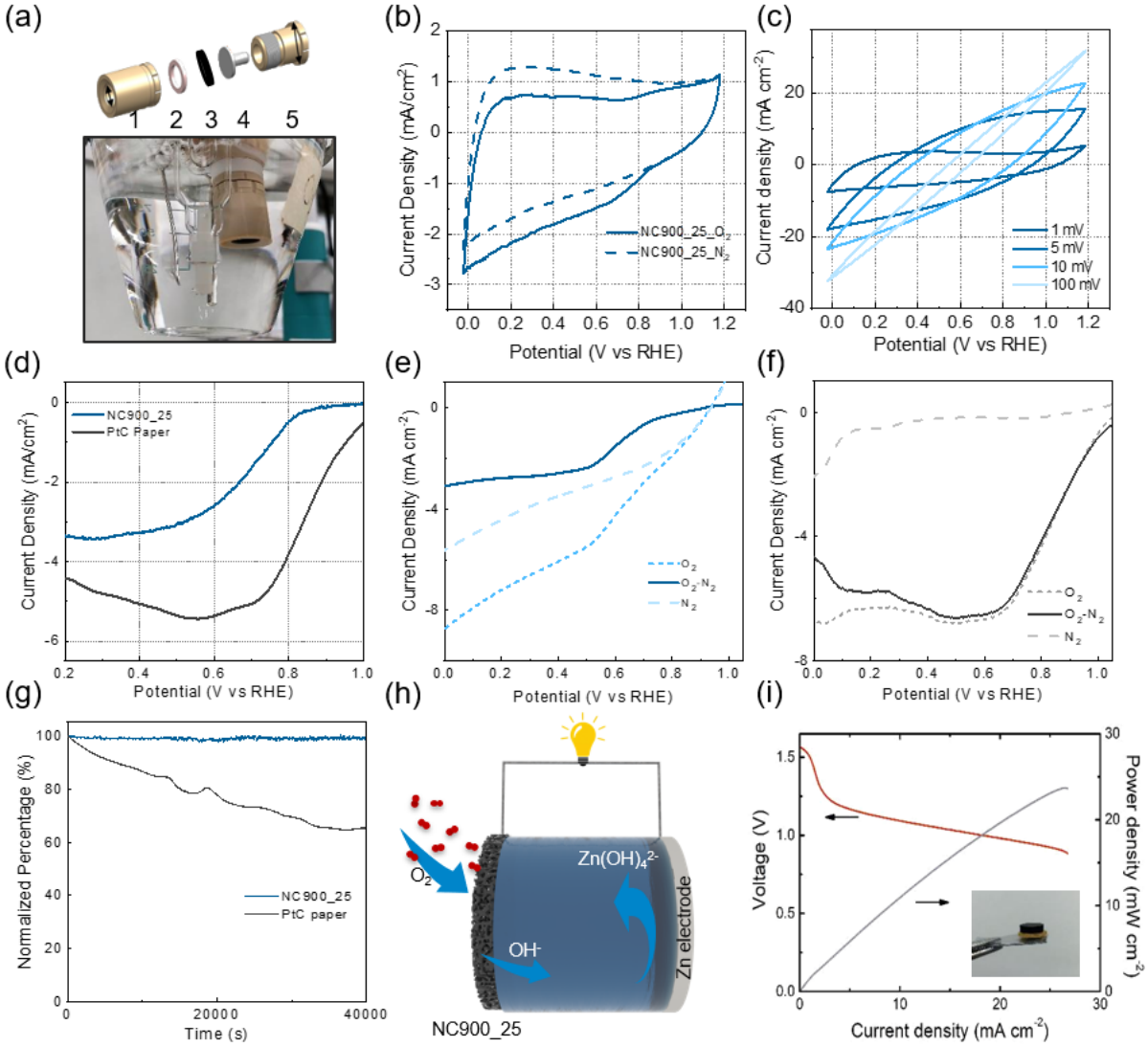

Figure 3.8 (a) Scheme of freestanding tip (1: PTFE, 2: silicon rubber, 3: pellet samples, 4: stainless steel, 5: PTFE holder), and a photo under testing conditions. (b) CV curves recorded under 1600 rpm in oxygen and nitrogen saturated 0.1 M KOH and a 0.1 mV s^{-1} scan rate for NC900_25. (c) CV curves at 1600 rpm in oxygen saturated 0.1 M KOH, 1-100 mV s^{-1} scan rates for NC900_25. (d) LSV curves recorded at 1600 rpm in oxygen saturated 0.1 M KOH, 1 mV s^{-1} scan rates for NC900_25 and Pt/C paper (background current extracted), LSV curves recorded at 1600 rpm in oxygen, nitrogen saturated, 0.1 M KOH, 1 mV s^{-1} scan rates for (e) NC900_25 and (f) Pt/C paper. (g) Chronoamperometric responses of NC900_25 and Pt/C paper at 0.477 V_{RHE} under 0.1 M oxygen saturated KOH with 1600 rpm rotation rate. (h) Schematic of working principle of Zn-air battery. (i) Discharge curve of the NC900_25 pellet.

The stability of the pellet was also investigated before and after the CA test. As shown in **Figure 3.9a**, no noticeable change could be seen in CV curves before/after the CA test. XPS was performed before and after cycling the pellet, a more prominent oxygen peak could be seen in XPS surveys, and the total amount of oxygen increased from 7.89 at% to 21.05 at%, suggesting the pellet surface might be oxidised during the oxygen reduction reaction. From the high-resolution XPS spectrums, no noticeable change or peak shift could be observed. The optical image of the NC900_25 pellet shows that more holes were generated on the pellet surface after the CA test.

Moreover, from the corresponding SEM images, it could be observed that the surface of the NC900_25 was corroded. However, it seems that the middle inside the NC900_@25 pellet was not affected, which suggest the surface of the pellet was reacting during the oxygen reduction reaction, and the inner pellet was not reacting much might due to the limited mass transfer of oxygen to the active sites. Additionally, more research efforts are needed to investigate the mass transfer limitations throughout the pellet and the degradation mechanism of the pellet during the oxygen reduction reaction.

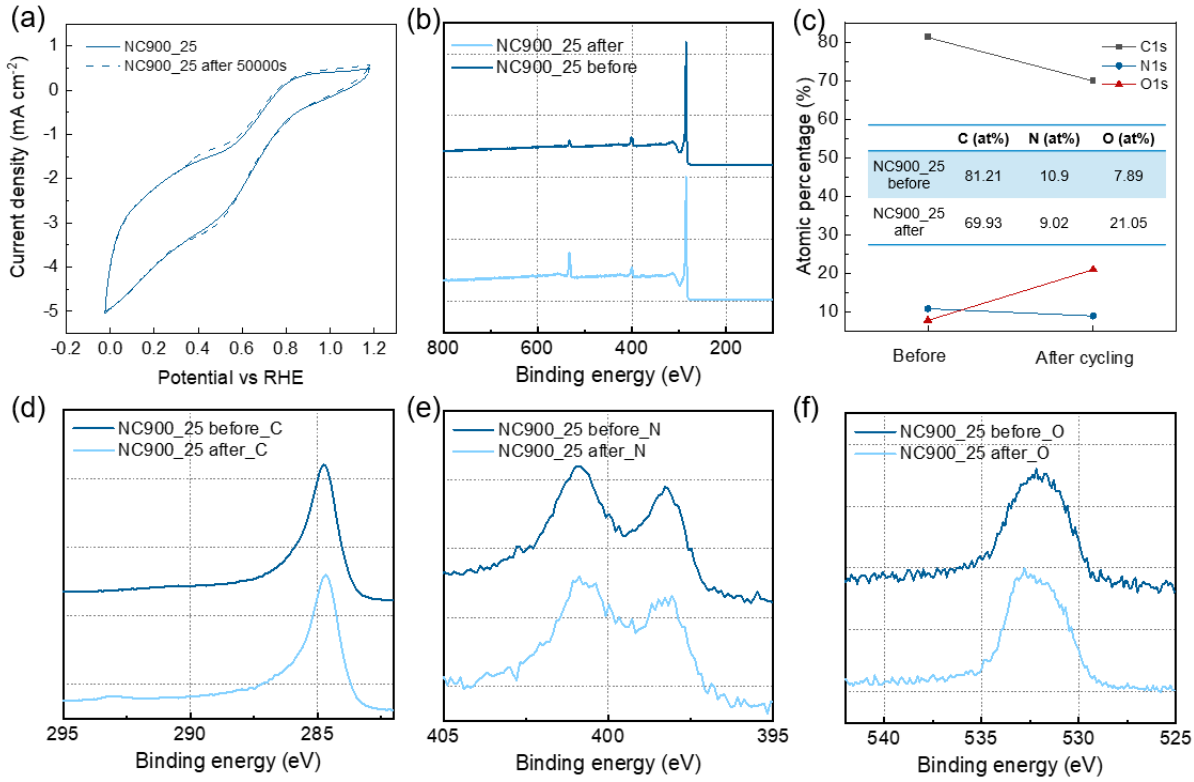

	C (at%)	N (at%)	O (at%)
NC900_25 before	81.21	10.9	7.89
NC900_25 after	69.93	9.02	21.05

Figure 3.9 (a) CV curves before and after the 50,000 s (13.89 h) CA test at 0.5 V under oxygen saturated 0.1 M KOH, 0.1 mV/s scan rate. (b) XPS survey spectrums of NC900_25 and after CA test, (c) comparison of surface elements changes before and after CA. High-resolution spectrums of (d) C1s, (e) N1s, and (f) O1s before and after the CA test (Intensity after normalised).

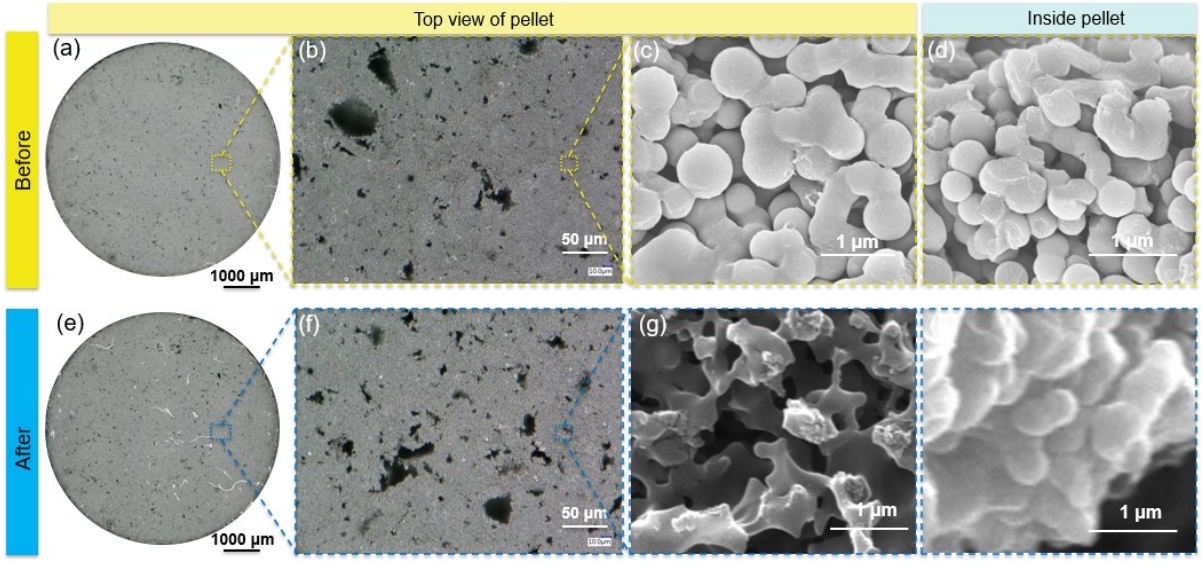

Figure 3.10 Optical microscopy images (a-b) before and (e-f) after CA test of NC900_25. SEM images of (c) top view and (d) inner pellet before CA test of NC900_25. SEM images of (g) top view and (h) inner pellet after CA test of NC900_25.

The freestanding tip method, CV, and LSV curves of Pt/C paper have been recorded (**Figure 3.11**). Similar to NC900_25 pellet sample, Pt/C paper also showed current density is proportional to the scan rate but more pronounced oxygen reducing peak at around 0.9 V_{RHE}. The thickness of the carbon fibre paper is 0.03 mm, which is almost ten times thinner than NC900_25 (0.2 - 0.3 mm), which indicate the thicker electrode gives more barrier for mass transfer. CV in **Figure 3.11b** showed oxygen reduction peaks starting at 1.05 V, more positive than Pt/C powder tested in RDE, which is caused by the higher amount of Pt. The rotation speed influence of the freestanding tip was also investigated (**Figure 3.11c**), where a clear difference could be seen after adding rotation to the freestanding electrode. This suggests that mass transfer plays an essential role in the freestanding electrode. Also, the mass transport issue might be tackled with proper testing configuration by adding pressurised oxygen.

To sum up, in the electrochemical characterisations, we have demonstrated the difference between testing powder and testing freestanding pellet. When testing in the three-electrode systems, similar electrochemical performance could be found in NC900_0 and NC900_25. However, when testing pelleting in freestanding electrode tip, a higher onset potential, higher current density, and higher stability with no obvious current loss after 40,000 s (11.11 h) were observed, which suggesting the contributions from the 3D structure of the pelleting, such as higher loading amount, interconnected hierarchical pore structures and abundant active sites.

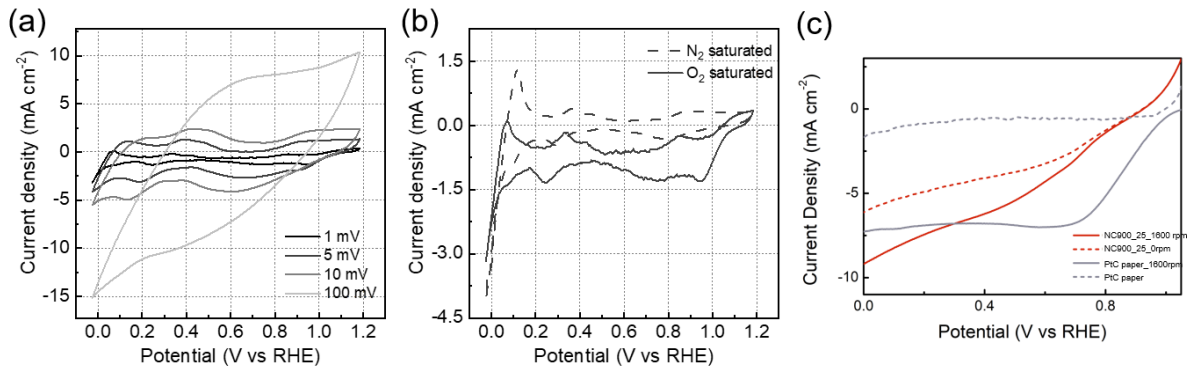

Figure 3.11 (a) CV curves recorded under 1600 rpm in oxygen and nitrogen saturated 0.1 M KOH, 100-1 mV s^{-1} scan rates for Pt/C paper. (b) CV curves at 1600 rpm in oxygen saturated 0.1 M KOH, 1

mV s^{-1} scan rate for Pt/C paper. (c) Comparing LSV curves of NC900_25 and Pt/C paper, with and without rotation, tested in O_2 saturated 0.1 M KOH with a 1 mV/s scan rate.

3.4 CONCLUSION

In conclusion, we have reported a facile, cost-effective, and scalable method for fabricating nitrogen-doped freestanding porous 3Dcarbon networks from biomass-derived sugar glucose. Multi-scale characterisation methods were performed to study both physical and chemical structures from nm to mm scale. A freestanding electrode test method was also proposed. The pellet showed superior stability and kinetic activity than powder samples because of its 3D tortuous structure with voids between particles. A primary solid Zn-air battery was assembled directly using the obtained pellet samples, which revealed its potential to serve as an air electrode. Besides, via post functionalisation and increasing the conductivity of pellet samples, pellet samples with more efficient electrochemical performance could be synthesised and thus pave a way to use them as air electrodes in energy conversion applications. Future work could focus on CT models to understand the tortuosity and design electrodes with better mass transfer. Some preliminary trails have been made to find optimized pellet thickness and carbonisation temperature conditions in the appendix. Moreover, computer modelling could speed up the process. Further applying the carbon electrode into a real gas diffusion layer will be desirable to understand its structure-performance relationship.

Chapter 4

ENGINEERING FeN_X ACTIVE SITES ON FREESTANDING 3D CARBON ELECTRODES FOR THE OXYGEN REDUCTION REACTION

4.1 INTRODUCTION

Transition metals (such as Fe, Co, Ni) with 3d unoccupied orbitals can accept additional electrons, consequently reducing the bonding strength between *OOH and *O/*OH intermediates, allowing them to catalyse the O_2 reduction process.[179] They have been considered low-cost alternatives to the commercial Pt/C catalysts. However, the ORR activity of conventional transition metal nanoparticles is lower than that of Pt/C counterparts by almost one order of magnitude, preventing their commercialisation and wide range implementation as eligible ORR catalysts.[180, 181] Strategies such as regulating the morphology and electronic structure have been applied to transition metal catalysts to improve their ORR activity. Nevertheless, reports achieving comparable activity and durability to Pt/C are scarce due to their low intrinsic activity.[44, 182, 183] Progress on non-noble catalysts has been made by designing atomically dispersed transition single atoms coordinated to nitrogen atoms doped within the carbon materials. These catalysts maximise their active sites utilisation and become the most promising earth-abundant catalysts that could replace the Pt/C catalysts in future fuel cells.[146]

In the last chapter, I have presented the synthesis of freestanding pellets with abundant nitrogen sites and high surface area. These abundant nitrogen dopants will serve as anchoring sites for single transition metal atoms on the respective freestanding carbon pellets. This chapter synthesised a freestanding pellet with atomically dispersed FeN_4 with improved catalytic activity than without Fe doping. STEM, SAXS/WAXS, XPS, EPR XAS, and RDE/RRDE were used to study the structure, catalytic performance, durability, and the type of active site of these catalysts.

The STEM and TEM measurements were performed by Rongsheng Cai (University of Manchester) and Hui Luo (Imperial College London). SAXS/WAXS were performed in Diamond Light Source in session SM27900, and the data were fitted by Zhenyu Guo (Imperial College London). EPR was performed and fitted by Angus Pedersen (Imperial College London). I planned the experiments, synthesised the materials, performed the remaining measurements and analysed the data.

4.2 SAMPLE PREPARATION

Reagents and solutions. All chemicals were used without further purifications. D –(+) Glucose (Sigma-Aldrich, BioReagent, ≥ 99.5 %), melamine (99 %, Sigma Aldrich), iron (III) chloride hexahydrate (Sigma Aldrich), potassium hydroxide hydrate (99.995 %) Suprapur, deionised water (DI) (18.2 MΩ cm^{-1}), absolute ethanol (≥ 99.9 %, Fisher Scientific).

Synthesis of HTC carbon spheres. Glucose, a readily available monosaccharide, was used as a sustainable bio-precursor and a carbon framework source for doping nitrogen atoms. The hydrothermal carbonisation (HTC) of this six-carbon sugar yielded spherical particles with an average diameter of 340 nm. For each sample, 14 g of solid glucose was dissolved in 140 ml DI water in glass beakers, then stirred for 1 hour. The next stage of the synthesis was HTC of the glucose solution. The prepared solutions were transferred to a 200 ml hydrothermal reactor (Kemi, Anhui, China), with the reactor then placed in a pressurised furnace (Memmert, Germany) at 200 °C for 12 hours. The obtained sample was further filter-washed with 500 mL water. After that, the obtained samples were vacuum dried at 120 °C for 24 hours to remove any remaining moisture, producing dehydrated samples fit for milling. Milling was carried out using a pestle and mortar for around 15 mins to yield a fine powder of hydrothermal carbon spheres.

Synthesis of nitrogen-doped carbon pellets (NC800_50). Melamine was first mixed with HTC powder by a 1:1 mass ratio, and then milling was carried out for around 20 mins using a pestle and mortar to yield a well homogeneous fine powder. Further, 50 mg of the obtained mixture was loaded into an 8 mm die, followed by a 780 MPa (4 tonnes) pressure applied on the mixture samples using a manual hydraulic press (Specac). The obtained brownish pellets were placed in the middle of a crucible, and the carbonisation was then carried out in a tubular furnace by one-step carbonisation under N_2 atmosphere (gas flow rate: 0.5 L min^{-1}). The temperature was ramped up to 800 °C for 2 hours with a heating rate of 5 °C min^{-1}. The obtained samples were denoted as NC800_50.

Synthesis of Fe, N codoped carbon pellet (Fe@900_50). $FeCl_3$ $6H_2O$ was used as the iron precursor, the amount of iron added was calculated as 3wt% of the NC800_50 pellet. The $FeCl_3 \cdot 6H_2O$ was then fully dissolved into the 5 ml absolute ethanol under 10 mins ice bath sonication to form $FeCl_3$ solution. NC800_50 was immersed into the $FeCl_3$ solution and sonicated for 10 mins in an ice bath, after which it was kept under nitrogen bubbling for 6 hours. The ethanol was evaporated overnight to let NC800_50 adsorb Fe^{3+} ions into the carbon framework. The obtained iron-loaded NC800_50 was then dried in a vacuum oven for 6 hours to 80 °C. The obtained pellet was then placed in the middle of a rectangular crucible, and the carbonisation was carried out in a tubular furnace under an N_2 atmosphere (gas flow rate: 0.5 L min^{-1}). The temperature was ramped up to 900 °C for 1 hour with a heating rate of 5 °C min^{-1}. After carbonisation, to remove the unstable iron species, the carbonised pellet was further treated with 1 M HCl for 6 hours on an agitation platform. Then, the pellet was vacuum dried at 80 °C for 6 hours. The obtained samples were denoted as Fe@NC900_50. To compare, the non-Fe doped NC800_50 was also carbonised again to 900 °C under the same conditions and equivalent post-treatment.

4.3 RESULTS AND DISCUSSION

The primary synthetic strategy is illustrated in **Figure 4.1**. Firstly, the nitrogen-doped porous carbon pellet was used as a framework to incorporate Fe into the substrate. Based on the optimizations presented in Appendix, a nitrogen-doped carbon pellet synthesised at 800 °C with a thickness of (~ 0.65 mm) was used (NC800_50, 50 represent the initial precursor loading). The NC800_50 was firstly impregnated with Fe precursors ($FeCl_3$), and the solvent was evaporated to allow the adsorption of Fe ions into the NC800_50. Then carbonisation (800 °C) was performed under inert N_2 gas (see sample preparation), during which the Fe ions were hybridised into the carbon support. The pellet sample was then treated with 1M HCl to remove any free metallic Fe species formed on the surface, allowing only Fe-N_x complexes to remain. The obtained sample was then denoted as Fe@NC900_50. The density of the Fe@NC900_50 is ~ 0.62 g cm^{-3}. For comparison, NC800_50 without Fe doping was carbonized directly at 900°C, denoted as NC900_50 in this chapter.

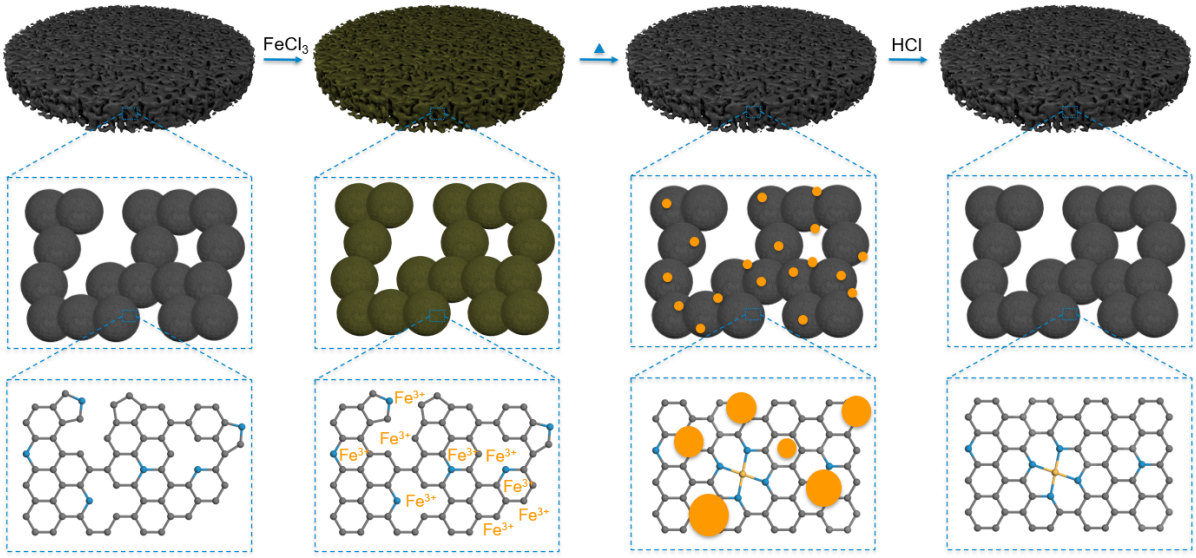

Figure 4.1 Schematic illustration for the synthesis of Fe@NC900_50 and the microstructure evolution in different scales (large yellow circles represent Fe particles; blue, grey and yellow atoms represent nitrogen, carbon, and Fe, respectively).

4.3.1 Morphology and structure characterisations

Scanning electron microscopy (SEM) images in **Figure 4.2** show that Fe@NC900_50 possesses a hierarchical macroporous structure with pores ranging from 10 to 100 micrometres. Such large pores/channels will facilitate the electrolyte transfer, while the interconnected

structure ensures the excellent mechanical property and stability of the pellet during electrochemical processes. The average particle size for Fe@NC900_50 is 333 nm which is similar to NC900_50 (324 nm). The thickness of the Fe@NC900_50 is 0.52 mm measured from SEM, while NC900 is 0.54 mm. Besides, no obvious Fe particles could be observed both on the surface of the pellet and inside the Fe@NC900_50 pellet. From the transmission electron microscopy (TEM) in **Figure 4.2c** and **Figure 4.2f**, no metal clusters or metallic oxides particles are observed, indicating that the aggregation of Fe atoms was prevented during the carbonizations attributed to the high nitrogen ligands and the high surface area of the carbon support. Also, more graphitized features could be observed in Fe@NC900_50, while NC900_50 showed mostly amorphous carbon features.

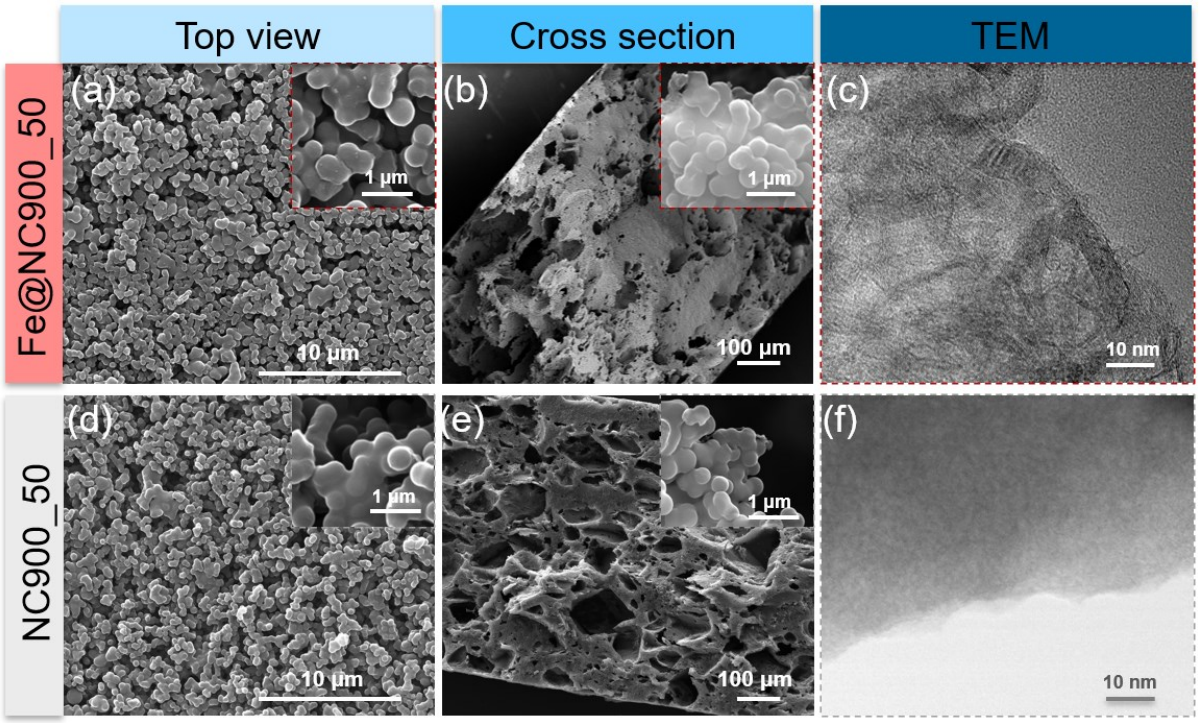

Figure 4.2 SEM images of Fe@NC900_50 from (a) top view and (b) cross-section. (c) TEM image of the Fe@NC900_50. (d) SEM images of NC900_50 from (d) top view and (e) cross-section. (f) TEM image of the NC900_50.

To further analyse the materials, high-resolution, high angle annular dark-field scanning transmission electron microscopy (HAADF-STEM) was employed. To gain better resolution, Fe@NC900_50 was milled in liquid nitrogen before preparing the TEM samples. **Figure 4.3a-**

b presents an overview of the morphology of Fe@NCS900_50. No noticeable Fe particles could be HAADF-STEM images of the Fe@NC900_50, which lies with the precious observation. Two distinguished structures were observed, which include carbon spheres and flakes. Energy-dispersive X-ray spectroscopy (EDS) was performed to map the presence of Fe species in the Fe@NC900_50. As can be seen in **Figure 4.3c-d**, the Fe signal is well distributed, suggesting that Fe may exist in the form of isolated sites. In the high-resolution HAADF-STEM images in **Figure 4.3d-e**, the isolated Fe single atoms are homogeneously dispersed on the N-C supports, as exhibited by the bright spots highlighted by yellow circles.

Further, to determine the Fe content in Fe@NC900_50, thermogravimetric analysis (TGA), Inductively coupled plasma mass spectrometry (ICP-MS), TEM-EDS and XPS were performed. The Fe content determined from ICP-MS, TGA, TEM-EDS, and XPS is 1.10 wt%, 1.13 wt%, 0.90 wt%, and 1.46 wt%, respectively. The original Fe input was 3 wt% of the whole pellet mass during the Fe doping process, which suggests nearly >50 wt% Fe was lost during the acid leaching.

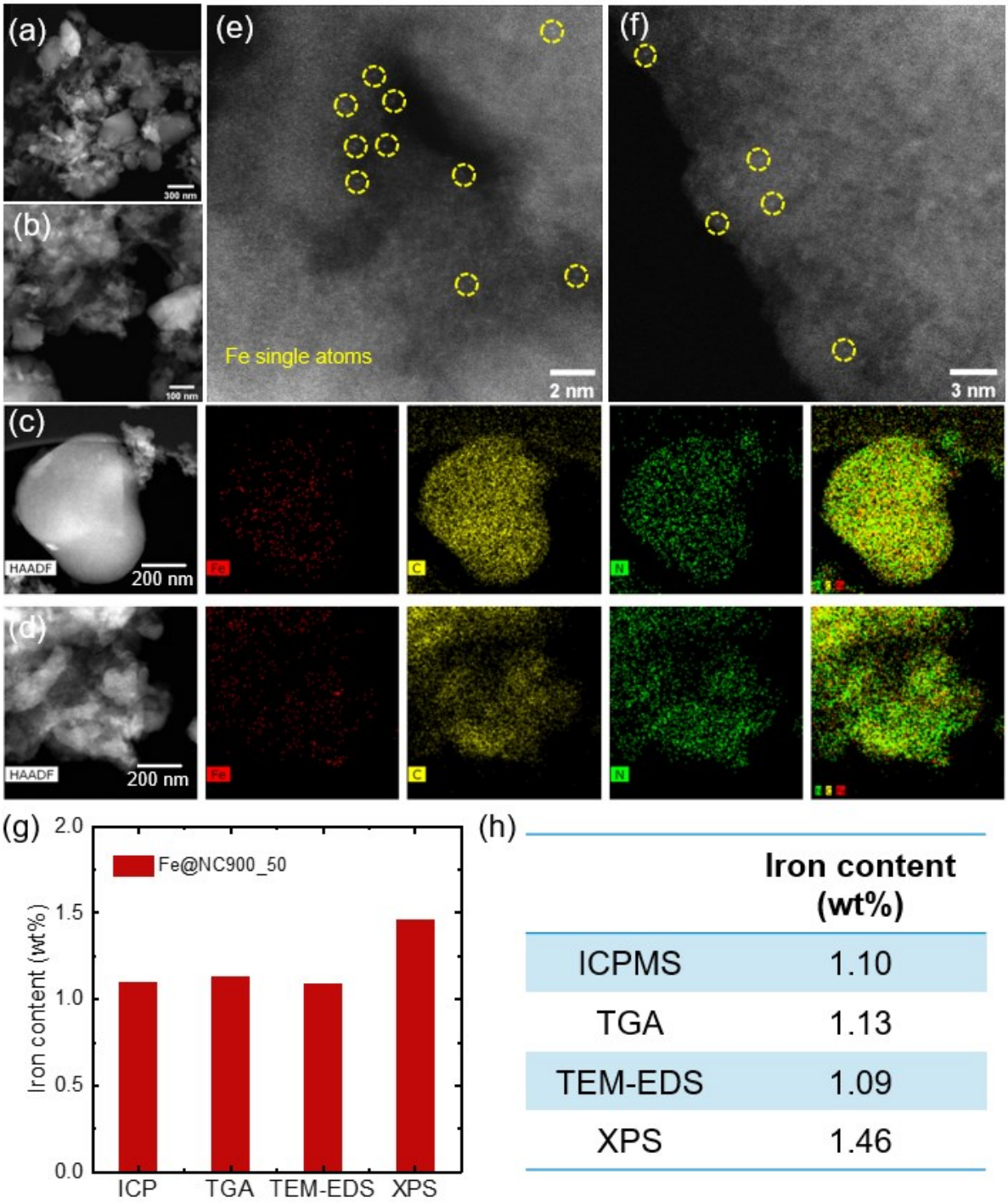

	Iron content (wt%)
ICPMS	1.10
TGA	1.13
TEM-EDS	1.09
XPS	1.46

Figure 4.3 (a)-(b) HAADF images of Fe@NC900_50, (c)-(d) EDS mapping results of Fe@NC900_50,

(e)-(f) High-resolution HAADF STEM images of the single Fe sites. (g)-(h) comparison of Fe contents in Fe@NC900_50 between different characterization techniques.

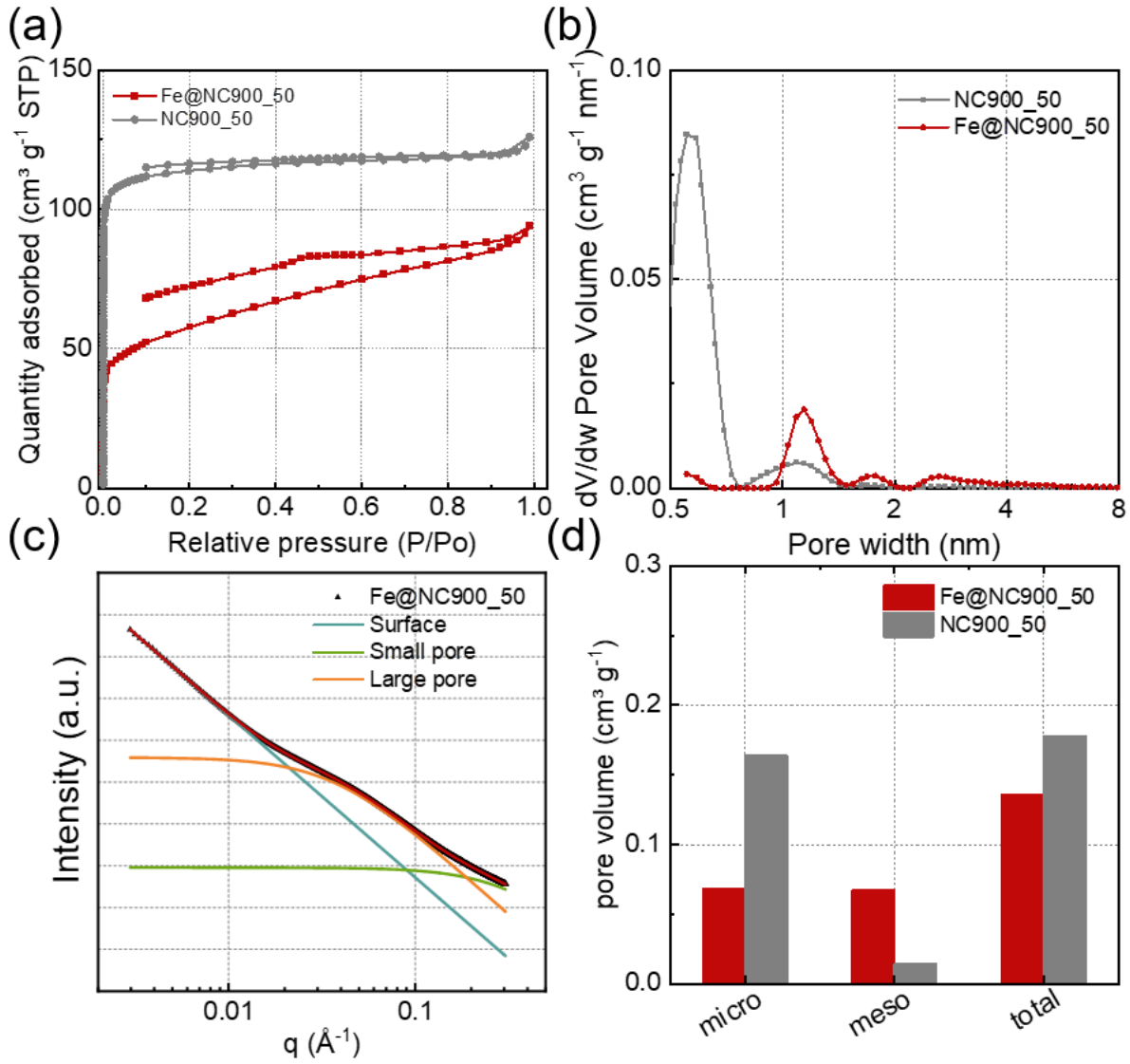

Figure 4.4 (a) N_2 isothermal adsorption curves of Fe@NC900_50 and NC900_50. (b) pore size distributions of Fe@NC900_50 and NC900_50, which was calculated from the NLDFT SD3 model. (c) Fitted SAXS pattern of Fe@NC900_50. (d) Comparison of the pore volume of Fe@NC900_50 and NC900_50.

Microstructures were studied by performing N_2 physical adsorption and small-angle X-ray scattering (SAXS). As shown in **Figure 4.4a**, the Brunauer-Emmett-Teller (BET) method was used to determine the specific surface area and the pore size distribution of Fe@NC900_50 and NC900_50. Fe@NC900_50 showed a specific surface area of 207 m^2 g^{-1}, while the NC900_50 showed a specific surface area of 451 m^2 g^{-1}. From the pore size distribution in **Figure 4.4b**,

Fe@NC900_50 showed a pore size at ~1.1 nm, while NC900_50 showed a pore size at 0.6 nm. Pore volume was compared in **Figure 4.4d**, where NC900_50 showed 90% micropores, and Fe@NC900_50 showed 50% micropores and 50% mesopores. SAXS pattern of Fe@NC900_50 was shown in **Figure 4.4c**. The average pore diameter calculated from SAXS is 2.7 nm. Fe@NC900_50 showed increased average pore size and increased mesopore volume compared to NC900_50, suggesting incorporating Fe-tuned the pore structure to have more mesopores.

To get more insights on the graphitization degree of the Fe@NC900_50, X-ray diffraction (XRD), Raman spectroscopy, wide-angle X-ray scattering (WAXS) were performed. From XRD patterns (**Figure 4.5a**), two broad peaks corresponding to carbon (001) and (200) could be seen in both Fe@NC900_50 and NC900_50. Positively shifted in the peaks of Fe@NC900_50 could be seen, which suggest a shorter carbon interlayer distance. From the WAXS spectrum of Fe@NC900_50 in **Figure 4.5c**, two sharp peaks corresponding to carbon (001) and (200) could also be observed. No metallic Fe peak could be seen in both XRD and WAXS patterns, suggesting a well-dispersed Fe species without agglomeration. The Raman spectra of the Fe@NC900_50 and NC@900_50 display two peaks at 1325 cm^{-1} (D-band) and 1580 cm^{-1} (G-band) (**Figure 4.5b**). The I_D/I_G value for Fe@NC900_50 is calculated to be 0.96, which is smaller than NC900_50 (I_D/I_G = 1.36). A noticeable 2D band (2750 cm^{-1}) could be observed in Fe@NC900_50, suggesting the number of graphene domains in the sample in Fe@NC900_50 increased.[184] The crystallite sizes (L_a) calculated for Fe@NC900_50 and NC900_50 were 4.54 nm and 3.21 nm, respectively. Therefore, we could conclude that Fe catalysed the formation of graphene domains and resulted in a higher graphitization degree in Fe@NC900_50, consistent with TEM results.

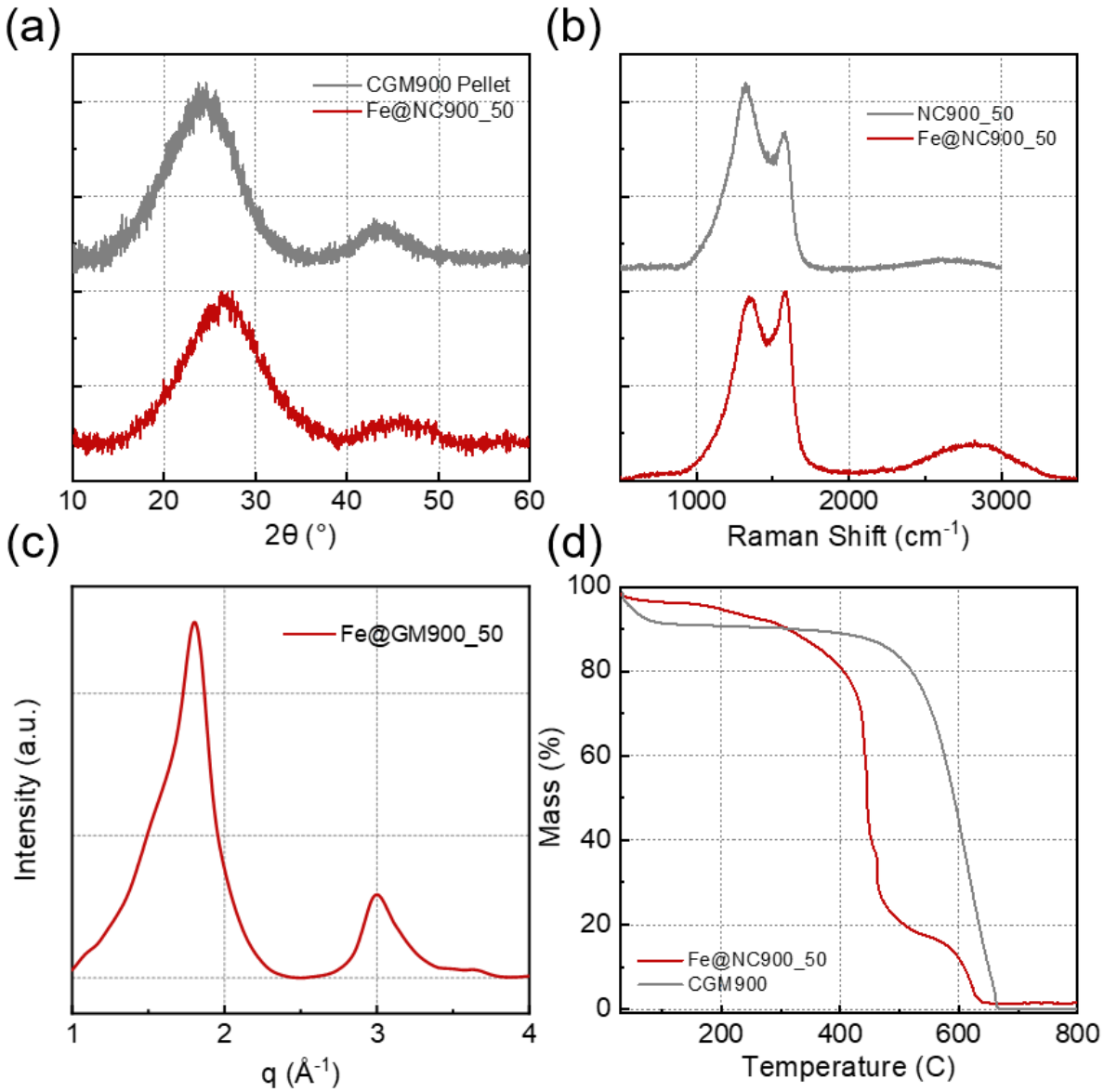

Figure 4.5 (a) XRD patterns of Fe@NC800_50 and NC800_50. (b) Ramen spectrums of Fe@NC800_50 and NC900_50. (c) WAXS spectrum of Fe@NC900_50. (d) TGA of Fe@NC900_50 and NC900.

4.3.2 Chemical structure characterization

To reveal the elemental composition of the catalysts, X-ray photoelectron spectroscopy (XPS) was performed. In **Figure 4.6a**, the XPS survey spectrum of Fe@NC900_50 shows the chemical composition of C (84.46 wt%), N (7.63 wt%), O (13.33 wt%), and Fe (1.46 wt%), while NC900_50 shows the chemical composition of C (70.67 wt%), N (12.61 wt%), and O (16.7 wt%). The deconvoluted N1s spectra revealed the presence of pyridinic nitrogen (398.2 eV), pyrrolic nitrogen (400.8 eV), graphitic nitrogen (401.6 eV), FeN_x (399.6 eV), and oxidized

nitrogen (403.2 eV) for Fe@NC900_50 in **Figure 4.6b**. Compared with N1s in NC900_50, Fe@NC900_50 showed less pyridinic nitrogen, suggesting pyridinic N reacts with Fe atoms to form FeN_x species. Besides, deconvoluted Fe2p spectra in **Figure 4.7a** showed that Fe exists as a mixture of 2^+ and 3^+ oxidation in Fe@NC900_50.

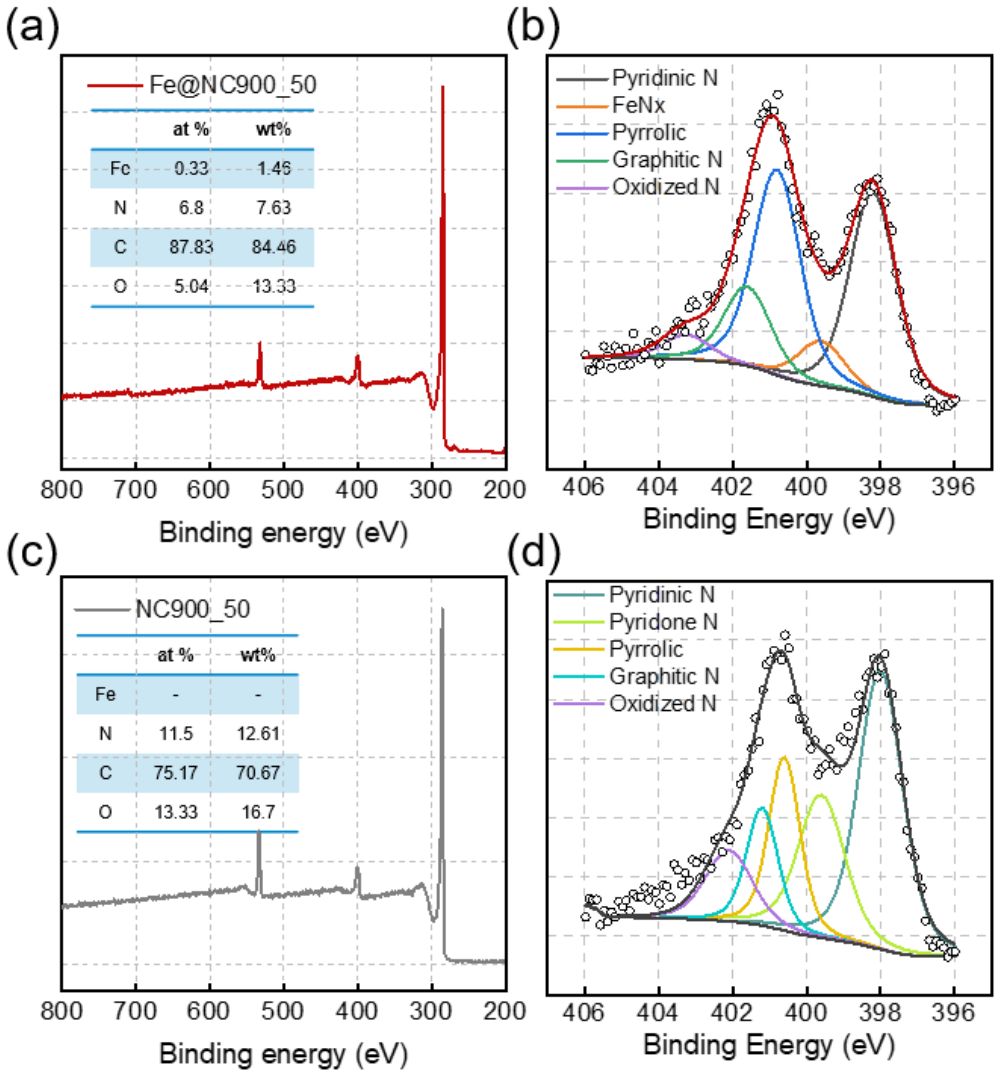

Figure 4.6 XPS survey spectrum for (a) Fe@NC900_50 and (c) NC900_50. Deconvoluted XPS N1s spectrums for (b) Fe@NC900_50, (d) NC900_50.

To further reveal the Fe species nature in Fe@NC900_50, X-ray absorption near-edge spectroscopy (XANES) and electron paramagnetic resonance (EPR) measurements were performed. From the Fe K-edge XANES in **Figure 4.7b**, it can be seen that the white lines of Fe@NC900_50 are in between reference Fe_2O_3 and FeO spectrums, indicating the Fe oxidation

state is in between 2^+ and 3^+, as consistent with XPS. Besides, Fe@NC900_50 showed a similar pre-edge feature compared with Fe phthalocyanine (FePc), which has well defined Fe-N_4 coordinated sites. Electron paramagnetic resonance (EPR) was performed to investigate the coordination of Fe^{3+} in Fe@NC900_50. EPR results shown in **Figure 4.7c** revealed that the rhombic symmetry systems with Fe^{3+} high spin (S = 5/2) could be determined, with $g \approx 6$ and $g \approx 2$ assigned to Fe^{3+} with square pyramidal coordination. Meanwhile, $g \approx 4.3$ originates from the Fe^{3+} with a rhombic ligand field.[185] So far, together with the morphology and chemical characterizations, we can conclude that the Fe exist as single FeN_x sites in the Fe@NC900_50. No obvious unstable species/clusters (iron oxides, iron carbides, and Fe) could be observed. To further understand the local structure of Fe sites, X-ray absorption fine structure (EXAFS) fitting will be presented in the next section.

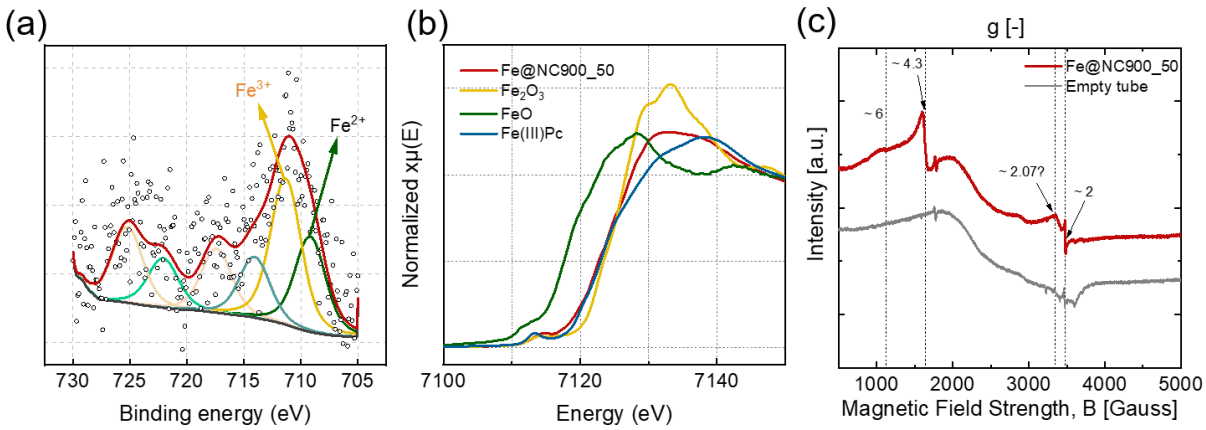

Figure 4.7 (a) High-resolution Fe2p spectrum of Fe@NC900_50. (b) Fe K edge XANES spectrums of Fe@NC900_50, reference Fe(III)Pc reference Fe_2O_3 and FeO. (c) X-band EPR of Fe@NC900_50 and empty EPR tube.

4.3.3 Atomic structure characterizations

Wavelet transform (WT) can provide both radial distance resolution and k space resolution, a powerful method for distinguishing the backscattering atom.[89, 186] As shown in **Figure 4.8a-c**, WT analysis of Fe@NC900_50 show only one intensity maximum at about ~ 4.2 $Å^{-1}$, which is approximately equal to that in the reference FePc (~ 4.2 $Å^{-1}$), but distinct from the feature of Fe_2O_3 (~ 7 $Å^{-1}$). The magnitude of the extended X-ray absorption fine structure (EXAFS)

Fourier Transforms (FTs) of Fe@NC900_50 and Fe reference samples are displayed in **Figure 4.8d**. The magnitude of the FT has a strong single peak centred around 1.6 $Å^{-1}$ (phase uncorrected) for Fe@NC900_50, distinct from those of the Fe_2O_3 and metallic Fe references but similar to the reference FePc, which confirmed the absence of Fe-oxides and metallic Fe. Together with STEM results, we can conclude that most of the Fe species in Fe@NC900_50 are Fe-N single sites.

As several different Fe-N_x structures have been reported, and each can result in different catalytic performances, it is essential to determine the local structure of the Fe-N_x structures.[99] Building optimized structure and simulating the XANES signal *via* density functional theory (DFT) calculations have become a powerful way to reveal the local structure of the single Fe sites.[89, 98, 187] Herein, reported theoretical XANES spectrums were used to compare with Fe@NC900_50 experimental data (**Figure 4.8e-f**).[187] Two possible matched structures FeN_4 and FeN_4-O_2, represent FeN_4 without oxygen ligand and one oxygen ligand attached to the centre Fe. By comparing these two different structures, the FeN_4 structure simulation (without O_2 ligand attached on the Fe) most closely matches the experimental result of Fe@NC900_50.

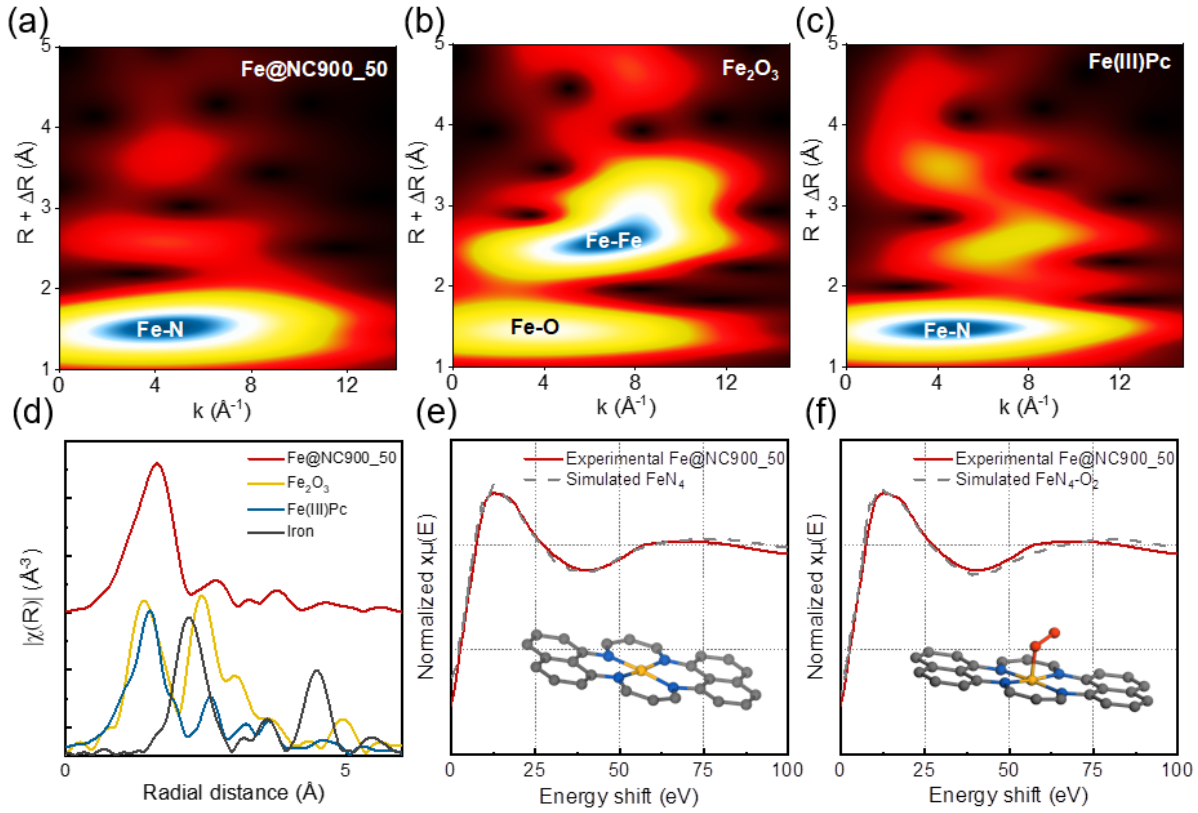

Figure 4.8 Wavelet transform of the k^2 weighted EXAFS data of (a) Fe@NC900_50, (b) Fe_2O_3, and (c) FePc. (d) Fourier transform of Fe K-edge EXAFS spectra for Fe@NC900_50 and references sample (Fe_2O_3, FePc, and Fe). Fe@NC900_50 experimental data compared with simulated (e) planar FeN_4 structure, (f) planer FeN_4 with on oxygen ligand bonding (FeN_4-O_2).

To shed light on chemical configuration of Fe-N single sites, FT EXAFS fittings were performed for Fe@NC900_50 using iFEFFIT programme.[188] All fittings are in good consistency with experimental data. The best fit values for EXAFS modelling of Fe@NC900_50 give a coordination number of 4.5 ± 0.2 for Fe-N at 2.06 ± 0.01 Å and 1.8 ± 0.4 for Fe-C/O at 1.88 ± 0.01 Å. In addition, coordination number 0.9 ± 0.2 for Fe-Fe at 2.56 ± 0.01 Å was required for fitting Fe@NC900_50. The presence of Fe-C and Fe-Fe signals suggests the existence of Fe carbides in the Fe@NC900_50, which are embedded in the carbon and survived from acid washing. Therefore, we propose that the Fe existed stoichiometrically as $FeN_{4.5}$ on the carbon substrate for Fe@NC900_50.

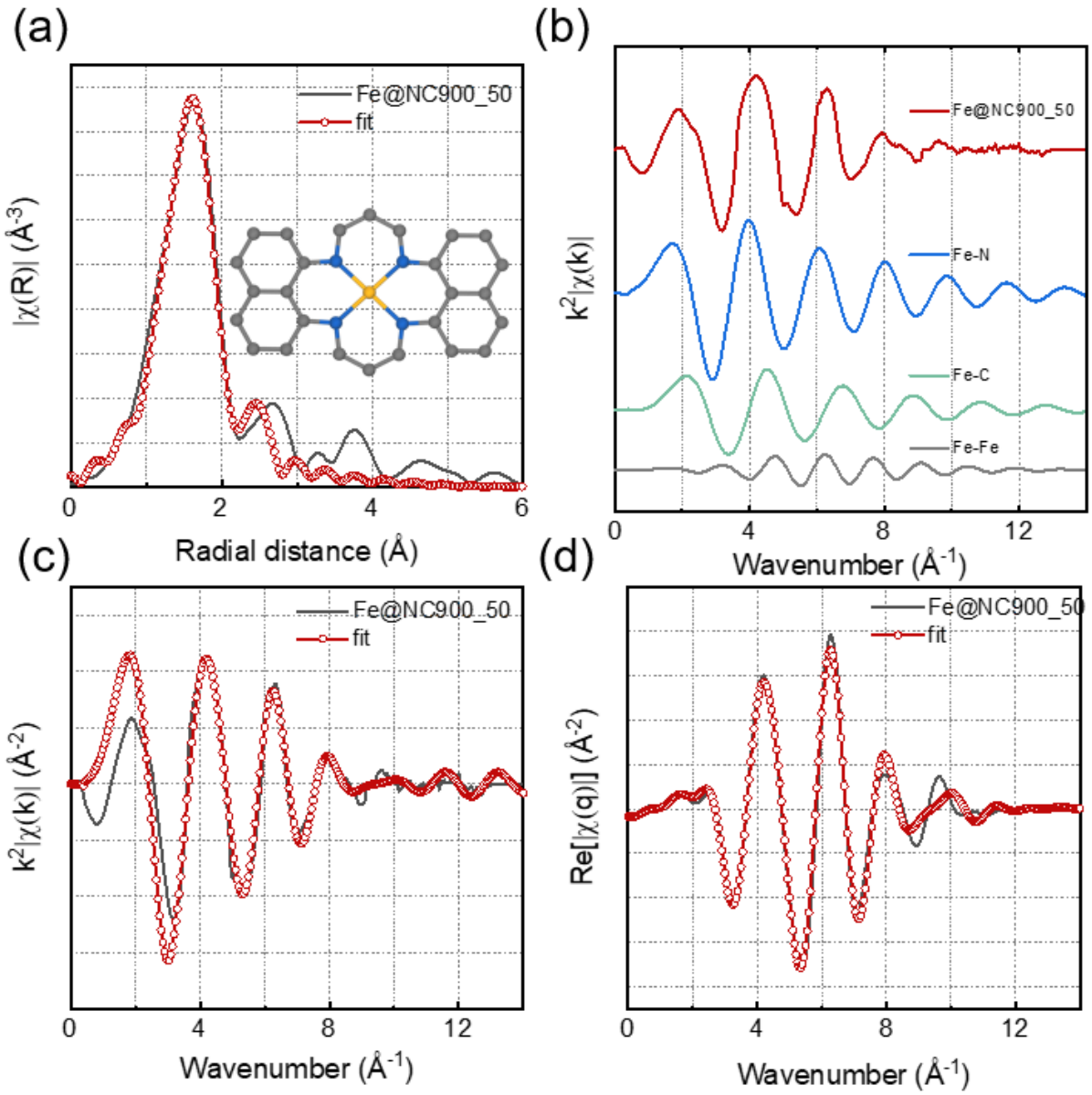

Figure 4.9 (a) The magnitude of EXAFS FT k^2-weight Fe K-edge spectra and fitting curve of Fe@NC900_50 in R space. (b) The magnitude FT k^2-weighted Fe K-edge EXAFS spectra of Fe@NC900_50, and Fe-N, Fe-C, and Fe-Fe paths. The magnitude of EXAFS FT k^2-weight Fe K-edge spectra and fitting curve of Fe@NC900_50 in (c) k space and (d) q space.

Table 4.1 EXAFS fitting parameters for Fe@NC900_50

Sample	Scattering pair	CN	R (Å)	ΔE_0 (eV)	σ^2 (10^{-3}Å^2)	R factor
Fe@NC900_50	Fe-N	4.5	2.06	0.73 ±1.86	0.005	0.0149
		±0.2	± 0.01		Fixed	
	Fe-C/O	1.8	1.88		0.005	

		±0.4	± 0.01		same as σ^2 (Fe-N)	
	Fe-Fe	0.9	2.56		0.01	
		±0.2	± 0.01		$2*\sigma^2$ (Fe-N)	

S_0^2 is the amplitude reduction factor ($S_0^2 = 1$), CN is the coordination number; R is the interatomic distance (the bond length between central atoms and surrounding coordination atoms); σ^2 is Debye-Waller factor (a measure of thermal and static disorder in absorber-scatterer distances); ΔE_0 is an edge-energy shift (the difference between the zero kinetic energy value of the sample and that of the theoretical model). R factor is used to value the goodness of the fitting.

To conclude, the above characterizations have shown we have successfully synthesised mostly single Fe sites on the nitrogen-doped carbon via post functionalization of the nitrogen-doped pellet. The abundant surface area heritage from NC800 provides anchor points for the Fe and the nitrogen sites, which assist the formation of single sites Fe-Nx-C. Besides, the incorporation of Fe catalysed the graphitization of carbon and tuned the pore structure towards meso pores. All these advantages suggest a higher electrocatalytic performance of the Fe@NC900_50.

4.3.4 Electrochemical characterizations in RDE

To investigate the kinetic performance of the obtained samples, a standard one-compartment three-electrode setup was used with rotating disk electrode, Ag/AgCl and Pt rod as working, reference, and counter electrodes, respectively. In **Figure 4.10**, the ORR catalytic performance of Fe@NC900_50, NC900_50, and commercial Pt/C (HISPEC 9100, Johnson Matthey, 55-58 wt% Pt) were evaluated by cyclic voltammetry (CV) under alkaline conditions and linear sweep voltammetry (LSV) under alkaline conditions (0.1 M KOH oxygen saturated) using a rotating disk electrode. From the CV curves in **Figure 4.10a**, one could observe that with FeN_4 sites, the oxygen reduction peak shift positively compared to NC900_50. From the LSV curves in **Figure 4.10b**, Fe@NC900_50 shows onset potential (0.89 V_{RHE}) and half-wave potential (0.76 V_{RHE}) potential, which is more positive than NC900_50 (E_{onset} = 0.752 V_{RHE} and $E_{1/2}$ = 0.578 V_{RHE}). The electron transfer number was studied using a rotating ring disk electrode (RRDE)

during the oxygen reduction process. As shown in **Figure 4.10d**, Fe@NC900_50 showed over average 3.5 electron process while NC900_50 showed an average 2.7 electron process, suggesting the incorporation of Fe in the Fe@NC900_50 dramatically increase the kinetics from two-electron to four-electron process. Further, chronoamperometry testing was performed to check the stability of Fe@NC900_50 (**Figure 4.10e**). After 10,000 s (2.77 h) at 0.6V_{RHE}, nearly 94% current was retained for Fe@NC900_50. We have shown that the incorporation of Fe improved electron kinetic activity and stability. Together with the characterizations, we could attribute the improved catalytic performance to the formation of Fe-N_4 sites, higher graphitization degree, and better pore structure in Fe@NC900_50.

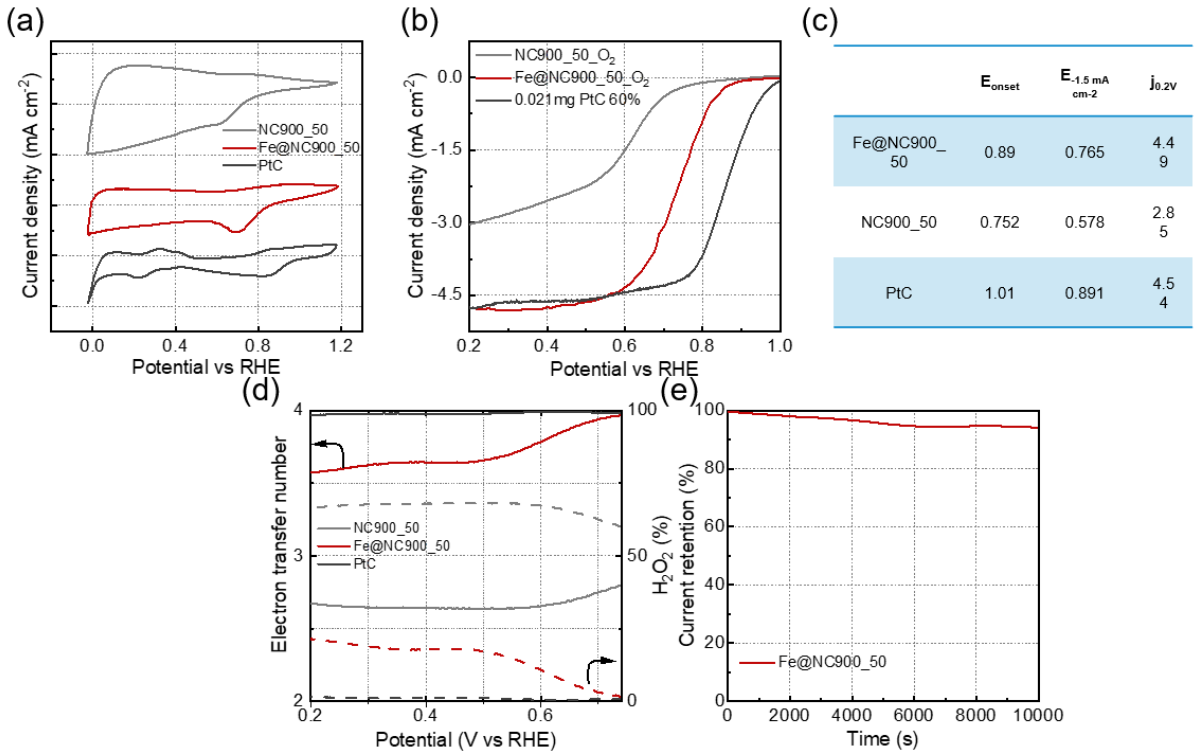

	E_{onset}	$E_{-1.5\ mA\ cm-2}$	$j_{0.2V}$
Fe@NC900_50	0.89	0.765	4.49
NC900_50	0.752	0.578	2.85
PtC	1.01	0.891	4.54

Figure 4.10 (a) CV curves of Fe@NC900_50, NC900_50, and Pt/C, tested in oxygen saturated 0.1 M KOH, with 0 rpm rotation and 100 mV s^{-1} scan rate. (b) LSV curves of Fe@NC900_50, NC900_50, and Pt/C, tested in oxygen saturated 0.1 M KOH, with 1600 rpm rotation and 10 mV s^{-1} scan rate. (c) Comparison of onset potential, halfwave potential (at 1.5 mA cm^{-2}), and limiting current (at 0.2 V_{RHE}). (d) Electron transfer number and H_2O_2 production rate of Fe@NC900_50, NC900_50, Pt/C. (e) Chronoamperometric responses of Fe@NC900_50 at 0.7 V_{RHE} with 1600 rpm.

So far, an iron, nitrogen co-doped freestanding electrode has been constructed with an improved catalytic performance by introducing Fe-N_x active sites. Ideally, the freestanding electrode is tested for electrochemical activity without breaking its structure (required during standard RDE testing to form a homogeneous ink slurry for drop-casting). Therefore, we carried out freestanding electrode electrochemical characterisation using the same methods as mentioned in the previous section, instead with the freestanding tip attached directly by screwing it onto the freestanding electrode to study the catalytic ability of Fe@NC900_50. Further advanced characterisation on the freestanding electrode was also carried out.

4.3.5 Electrochemical characterizations in freestanding electrode

As shown in **Figure 4.11**, the Fe@NC900_50 was tested as a freestanding electrode in the rotating electrode. The same configuration in **Figure 3.8a** was applied. CV and LSV were performed to investigate the catalytic activity of Fe@NC900_50. Under oxygen and nitrogen, samples were rotated and pre-conditioned for 1500 s at 0.5 V_{RHE} before starting the test. As depicted in **Figure 4.11a**, a reduction peak could be observed under the O_2 condition. LSV was carried out to evaluate the oxygen reduction characteristics of Fe@NC900_50 (**Figure 4.11b**), the N_2 current was extracted to exclude the capacitive current. The onset potentials determined from LSV curves were 0.89 V_{RHE}, more positive than NC900_50 (0.83 V_{RHE}), which agreed with the CV results. Besides, Fe@NC900_50 also showed a 116 mV positive half-wave potential than NC900_50 (0.74 V_{RHE} vs 0.624 V_{RHE}). A nearly 2.5 times higher current density could be observed at 0.2 V_{RHE} for Fe@NC900_50 than NC900_50. As shown in **Figure 4.11c**, long-term stability was also performed via the chronoamperometry test. The Fe@NC900_50 was continuously run under 0.5 V_{RHE} for 100,000 s (27.78 h) in 0.1 M KOH with 1600 rpm rotation. No significant current loss could be observed for both the Fe@NC900_50 and NC900_50. Compared with the NC900_50, Fe@NC900_50 showed a higher current density, almost double that of the NC900_50 (3 mA cm^{-2} vs 1.7 mA cm^{-2}). Therefore, Fe@NC900_50

presented both improved catalytic performances compared to NC900_50 as well as high stability. Specifically, the tuned pore structure, Fe-N_4 sites, and graphitization induced by the Fe contribute to the high catalytic performance. Meanwhile, the 3D structure contributes to the higher stability where no noticeable current loss could be observed after the 100,000 s (27.78 h) chronoamperometry test.

To further study the stability of the active site, ex-situ XAS and EPR were performed on Fe@NC900_50 before (BOL), and after (EOL) cycling in the 0.1 M KOH. 900 CV cycles was carried out in 0.1 M KOH, cycled Fe@NC900_50 was sealed directly after taking out from the electrolyte to minimize the influence during sample transport. As shown in Figure 4.11d, similar XANES spectra could be observed for both BOL and EOL, indicating no noticeable change of the FeN_4 sites. EXAFS fitting (**Figure 4.11e**) was carried out to obtain insights on the stability of the Fe@NC900_50. Interestingly, no change in the apparent Fe-N coordination number could be found before and after the test (CN_{BOL} = 4.5 vs CN_{EOL} = 4.5), confirming the stability of Fe-N sites. As shown in **Figure 4.11f**, no additional impurities could be seen in EOL Fe@NC900_50 spectra, suggesting the Fe species in EOL Fe@NC900_50 still exist as the Fe-N_4 structure. In addition, EOL Fe@NC900_50 sample exhibited a much sharper signal at $g \approx 4.3$, while the peak signal at $g \approx 6$ in EOL almost disappeared, suggesting ligands covered the Fe^{3+}-N_4 sites in EOL. Hence, the ex-situ post-mortem XAS and EPR have suggested the Fe-N_4 sites are stable on Fe@NC900_50, and no impurities could be found after 900 cycles.

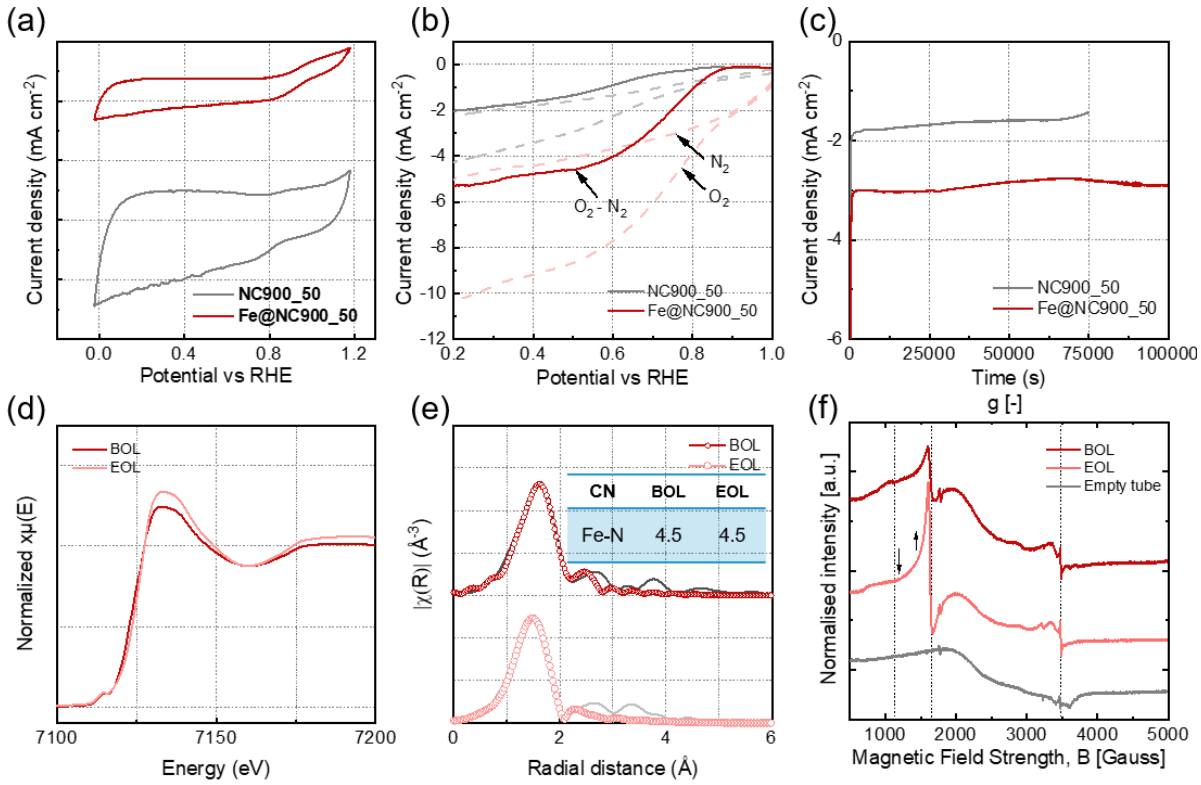

Figure 4.11 (a) CV curves for Fe@NC900_50 and NC900_50, recorded under 1600 rpm in oxygen saturated 0.1 M KOH with a 0.1 mV s^{-1} scan rate. (b) LSV curves for Fe@NC900_50 and NC900_50, recorded under 1600 rpm in oxygen and nitrogen saturated 0.1 M KOH with a 0.1 mV s^{-1} scan rate. (c) Chronoamperometric response of Fe@NC900_50 and NC900_50 at 0.5 V_{RHE} under 0.1 M oxygen saturated KOH with 1600 rpm. (d) XANES spectra of Fe@NC900_50 before (BOL) and after (EOL) cycled in 0.1 M KOH electrolyte, 900 CV cycles were performed with a 5 mV s^{-1} scan rate. (e) Fe-K edge R-space k^2 weight curves of Fe@NC900_50 before and after cycled (Inserted, comparison of coordination number of Fe-N before and after cycles). (f) X-band EPR spectra of Fe@NC900_50 before and after cycling.

4.3.6 Ex-situ XAS study to determine the active site and its behaviour during the oxygen reduction reaction

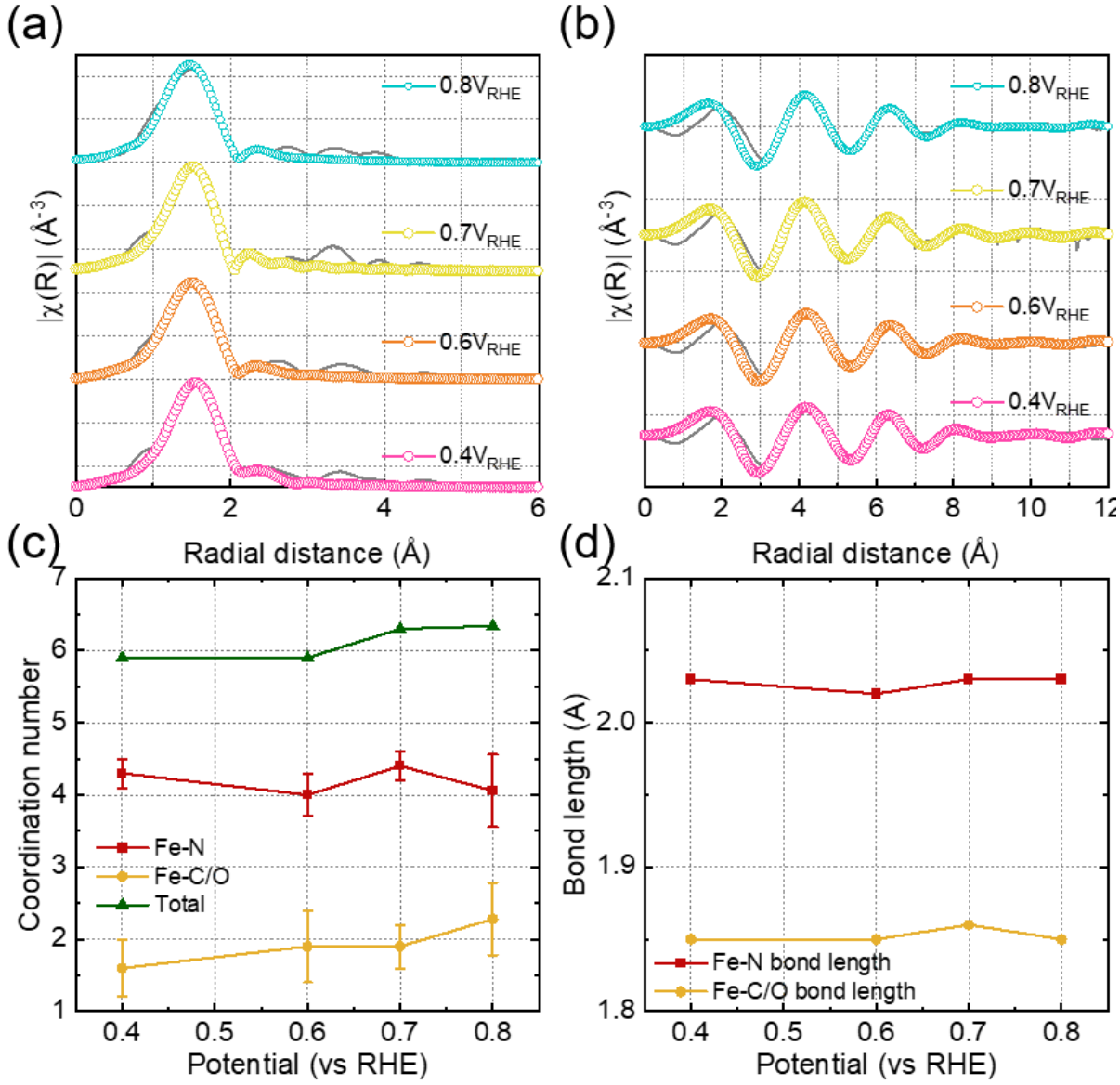

Figure 4.12 Ex-situ XAS study of the Fe@NC900_50. (a) Fe-K edge R-space k^2 weight curves of Fe@NC900_50 at different voltages. (b) Fe-K edge k-space k^2 weight curves of Fe@NC900_50 at different voltages. (c) Comparison of coordination number of Fe-N and Fe-C/O in the function of voltages. (d) Comparison of bond length of Fe-N and Fe-C/O in the function of voltages.

Ex-situ XAS as a function of potential was performed to help understand the ORR mechanism of Fe@NC900_50. Ex-situ samples were prepared by holding the Fe@NC900_50 samples at a different potential. To minimise the possible contamination, samples were sealed after taking them out from the electrolyte. EXAFS fittings were performed, and all fittings are in good consistency with experimental data (**Figure 4.12a-b**). As shown in **Figure 4.12c**, the

coordination number of Fe-N and Fe-O is shown as the function of potential. No obvious trend could be found in Fe-N, suggesting no noticeable loss of the Fe-N_4 sites. Interestingly, the coordination number for Fe-C/O is decreasing from 2.28 (0.8 V_{RHE}) to 1.6 (0.4 V_{RHE}), suggesting that the oxygen was first bonded on the Fe site and then detached. In addition, the total coordination number for both Fe-C/O and Fe-N also showed a decrease from 6.34 (0.8 V_{RHE}) to 5.9 (0.4 V_{RHE}), where the main drop is at 0.8 V to 0.6 V, suggesting one oxygen detached at this potential. As the binding and oxygen reduction on the Fe-N_4 sites could induce a change in the bond length, the bond length change of Fe-N and Fe-C/O were compared in the function of potential (**Figure 4.12d**). However, no noticeable bond length change could observe, which could cause by the low resolution/high noise from the ex-situ test.

Hence, the ex-situ XAS suggests the Fe in Fe-N_4 sites are responsible for reducing the oxygen. The oxygen is first bonded on the Fe and then be further reduced in lower potential. However, in-situ experiments are required to get precise bond changes to build an oxygen reduction mechanism model.

4.4 CONCLUSION

In this chapter, a freestanding electrode with FeN_4 sites has been successfully synthesised via post-treatment of an N-doped freestanding electrode. The abundant micropore and nitrogen sites on the N doped pellet have provided sites for Fe ions, leading to the formation of atomically dispersed Fe-N_4 sites. The incorporation of Fe also increased the graphitisation degree and tuned the pore structure, resulting in improved catalytic performance in Fe@NC900_50 compared with no Fe doping (NC900_50). Fe-N_4 sites in Fe@NC900_50 improved catalytic activity and stability, resulting in a high current density in Fe@NC900_50 in the freestanding chronoamperometry test (current density nearly two times higher than NC900_50). Through ex-situ XAS and EPR study, the Fe-N_4 were maintained stably without new phase forming after 900 cycles. Besides, ex-situ XAS also suggests that Fe-N_4 is the active

centre responsible for oxygen binding and reduction. In addition, we have shown that the nitrogen-doped freestanding pellet could be further tuned by combining the high stability from the 3D structure and improved catalytic activity from Fe doping forming single-atom sites. With a suitable post-treatment method, the electrocatalytic performance of the freestanding pellet could be tuned and extended to different electrocatalytic applications with fewer fabrication steps, which move closer to the industrial application. Compared with reduced graphene oxide films, modified carbon fibre paper, and metal mesh templated carbon films, pellet samples reported in this work are still inferior in the catalytic activities due to the mass transfer barriers in the thick pellet. Structural engineering could be the next step to improve the mass transfer inside pellet samples to address these issues.

Chapter 5

IRON, NITROGEN CO-DOPED CARBON SPHERES AS LOW COST, SCALABLE ELECTROCATALYSTS FOR THE OXYGEN REDUCTION REACTION

5.1 INTRODUCTION

Hydrogen and fuel cells play a key role towards reaching 2050 net-zero carbon emissions targets for generating CO_2 free electricity and transportation.[189] A key challenge in their development is that the oxygen reduction reaction (ORR) kinetics occurring at the fuel cell cathode is slow, restricting energy conversion efficiencies.[190] Pt-based catalysts perform best and are the materials that have been widely applied commercially. However, they suffer from scarcity and high cost, while further stability improvements are also required.[37] To achieve widespread and sustainable commercialization of fuel cells, the key goals are increasing their durability and decreasing their cost (US DOE 2025 targets: 5000 hours lifetime and \$ 40 / kW_{net} at 500,000 systems/year).[41, 42]

Great progress has been made to date in designing non-precious metal-based catalysts for fuel cells, including developing Fe, Co, Mn-based catalysts to have activities comparable to the noble-metal catalysts.[190-196] The M-N-C catalysts (where M is a transition metal) are among the most promising electrocatalysts.[197, 198] The key characteristic of these catalysts is the presence of M-N_x, which have shown high stability and high catalytic activity.[89] Of these materials, Fe-N-C catalysts have shown superior performance, which has attracted considerable recent attention from the research community.[100, 199-203] Various aspects, including the local structure of the Fe-N sites, synergetic performance of different iron species, stability of the Fe-N coordination structures, active sites evolution from raw precursors into the final carbon materials carbonization, and the oxygen reduction reaction pathways have been investigated.[99]

Although great progress has been made, there are still challenges in establishing the exact structure-to-property correlation in such catalysts, which is essential for the rational design and synthesis of new catalysts with tailored activities for wide ranges of electrocatalytic processes.[89]

Also, looking for a cost-effective and scalable way to synthesize effective catalysts and supports is necessary to support commercial uptake of the technology.[204] Hydrothermal carbonization converts biomass or biomass-derived precursors into oxygenated hydrothermal carbons, yield advantageous stable and conductive porous structures and superior catalytic activity by additional carbonization or hybridization with active carbonisation transitional metal and nitrogen sources.[205, 206]

Herein, a facile route is presented to construct scalable, low-cost iron nitrogen-doped carbon spheres (Fe@NCS) as high-performance ORR catalysts. The primary synthetic strategy is illustrated in **Figure 5.1**. Firstly, hydrothermal carbon spheres with abundant oxygen functionalities were prepared by hydrothermal carbonization (HTC) of xylose.[207] The obtained hydrothermal carbon spheres were then impregnated with iron precursors ($FeCl_2$ or $FeCl_3$) and nitrogen precursor (melamine), followed by two-step carbonization under inert N_2 gas (see experimental methods).[100] During the carbonization process, iron and nitrogen were hybridized into the carbon support, thus forming Fe@NCS. Fe@NCS powder was treated with 0.1 M HCl to remove any free metallic iron species formed on the surface, allowing only Fe-N_x complexes to remain (Fe@NCS-A, where A represents acid). Samples impregnated with $FeCl_2$ or $FeCl_3$ are denoted as Fe^{2+}@NCS-A and Fe^{3+}@NCS-A, respectively, where A refers to acid wash. 1.8 g of Fe@NCS catalyst (~ 51% yield) can be easily obtained in a one-batch, demonstrating the scalability of this reaction (**Figure S1**). For comparison, carbon spheres (CS) and nitrogen-doped carbon spheres (NCS) were also prepared.

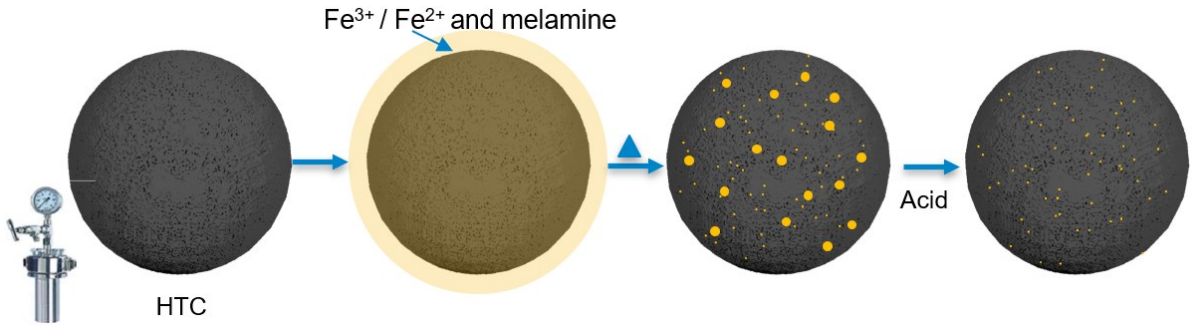

Figure 5.1 Schematic illustration for the synthesis of Fe@NCS-A.

In this chapter, iron, nitrogen co-doped carbon spheres (Fe@NCS) have been prepared by hydrothermal carbonisation and high-temperature post carbonisation. We have determined that FeN_4 is the main form of iron existing in the obtained Fe@NCS. Two different precursors containing Fe^{2+} and Fe^{3+} were compared. Fe^{2+}@NCS-A (Fe^{2+} precursor) shows better catalytic activity for the oxygen reduction reaction. This catalyst was studied in an anion exchange membrane fuel cell (AEMFC). A high open-circuit voltage was demonstrating the potential approach for developing high-performance, low-cost fuel cell catalysts.

The STEM and TEM measurements were performed by Rongsheng Cai (University of Manchester) and Hui Luo (Imperial College London). SAXS/WAXS were performed in Diamond Light Source in session SM27900, and the data were fitted by Zhenyu Guo (Imperial College London). AEMFC was assembled and tested by Emanuele Magliocca (University College London). EPR was performed and fitted by Angus Pederson (Imperial College London). I planned the experiments, synthesised the materials, performed the rest measurements and analysed the data.

5.2 SAMPLE PREPARATION

Reagents and solutions. All chemicals were used without further purifications. D-(+)-Xylose (≥ 99%, 150.13 g mol^{-1}, Sigma Aldrich), iron (II) chloride tetrahydrate (99.99 %, 198.81 g mol^{-1}, Sigma Aldrich), iron (III) chloride hexahydrate (≥ 99 %, 270.30 g mol^{-1}, Sigma Aldrich), melamine (99%, Sigma Aldrich), absolute ethanol (≥ 99.9%, Fisher Scientific), deionized

water (18.2 MΩ cm), nitric acid (70 %, Sigma Aldrich), and hydrochloride acid (37 % ACS reagent, Sigma Aldrich).

Synthesis of HTC Carbon Spheres (CS). Xylose, a readily available monosaccharide, was used as an eco-friendly precursor and the source of carbon framework for doping metal atoms. The hydrothermal carbonization (HTC) of this five-carbon sugar yielded monodispersed spherical particles with an average diameter of 320 nm (**Figure 5.2**). For each of the samples, 7 g of solid xylose was dissolved in 70 ml DI water in glass beakers which were then placed in a sonication bath for 5 minutes and stirred for 2 hours. The next stage of the synthesis was HTC of the xylose solution, whereby xylose solutions were transferred to a 100 ml hydrothermal reactor (*Kemi, Anhui, China*), with the reactor then placed in a pressurized furnace (*Memmert, Ger*many) at 200 °C for 12 hours. The obtained sample was further filter-washed with 500 mL water, and the inhomogeneous impurities were removed. After that, the obtained brownish powder (hydro-char) was washed with centrifugation (*Thermo Scientific, Heraeus Multifuge X1R, USA*) for 10 minutes at 12,000 rpm. The recovered hydro-char was vacuum dried at 105 °C for 24 hours to remove any remaining moisture, producing dehydrated samples fit for milling. Milling was carried out using a pestle and mortar to yield a fine powder of hydrothermal carbon spheres.

Synthesis of Nitrogen-doped Carbon Nanospheres (NCS). Melamine was chosen as the nitrogen precursor due to its rich N content and wide availability. 500 mg melamine was first dissolved in 50 mL of absolute EtOH via bath sonication for 10 minutes. Then, 500 mg of obtained brownish CS powder was added into the melamine solution and stirred for 2 hours at 300 rpm. The final solution was then rotatory dried (*Scilogex RE100-S, USA*) at 55 °C, and then moved to an 80 °C vacuum oven for an additional 12 hours. The obtained sample was milled using a pestle and mortar for 15 minutes to achieve a fine powder. The carbonization was then carried out in a tubular furnace (*Carbolite S.T.F., UK*) by a two-step process under

N_2 atmosphere (gas flow rate: 0.5 L min^{-1}); first, the furnace was heated at 600 °C for 2 hours with a heating rate of 5 °C $min^{-1,}$ and then the temperature was ramped up again to 900 °C for another 2 hours with a heating rate of 5 °C min^{-1}.

Synthesis of Iron, Nitrogen co-doped Nanospheres (Fe^{2+}@NCS, and Fe^{3+}@NCS). To obtain Fe^{2+}@NCS, and Fe^{3+}@NCS, 39.73 mg iron (II) chloride tetrahydrate (0.2 mol Fe) or 56.44 mg iron (III) chloride hexahydrate (0.208 mol Fe) was first dissolved into 50 mL of absolute EtOH via bath sonication for 10 minutes. The same synthesis process for the NCS was then carried out as presented above. The obtained samples were denoted as Fe^{2+}@NCS, and Fe^{3+}@NCS, where Fe^{2+}/Fe^{3+} represents the precursor's oxidation state.

Synthesis of Fe^{2+}@NCS-A, Fe^{3+}@NCS-A. The obtained Fe@NCS catalysts were further treated with 1M HCl for 12 hours at room temperature at 250 rpm on an agitation platform to remove free metal ions and unwanted impurities. Then, the resulting solutions containing Fe@NCS were centrifuged for 10 minutes at 12000 rpm to separate the catalyst from the acid. The wet catalyst was then vacuum dried at 105 °C for 12 hours. The obtained samples were denoted as Fe^{2+}@NCS-A, and Fe^{3+}@NCS-A, where A represents the HCl acid treatment. The chemical reactions involved in this process are shown in the following equations:

$$Fe + 2HCl \rightarrow FeCl_2 + H_2$$

$$FeO + 2HCl \rightarrow FeCl_2 + H_2O$$

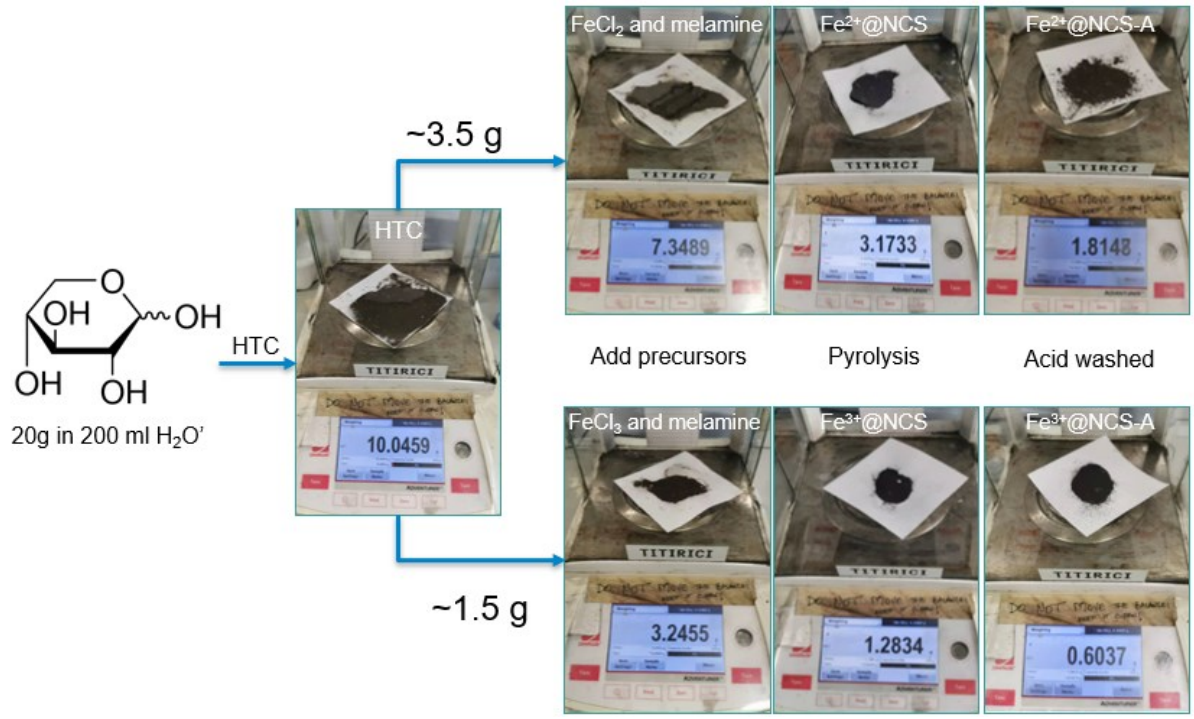

Figure 5.2 Schematic route shows mass changes of biomass derived catalysts at a different step in lab-scale with 'gram-production' ability.

5.3 RESULTS AND DISCUSSION

5.3.1 Morphology characterization

Scanning electron microscopy (SEM) images in **Figure 5.3** show that all samples present a well-defined spherical morphology, with diameters around 300-500 nm. Compared to the smooth surface of CS and NCS, Fe^{2+}@NCS-A displays a much rougher surface, likely due to the Fe assisting the graphitization of amorphous carbon.[208-210] A few smaller high-intensity nanoparticles (NPs) can also be seen in the SEM images of the Fe@NCS samples (**Figure 5.3c-d**), which are mostly removed by the HCl wash (**Figure 5.3e-f**). To further analyze the materials, high-resolution high-angle annular dark-field scanning transmission electron microscopy (HAADF-STEM) was employed.

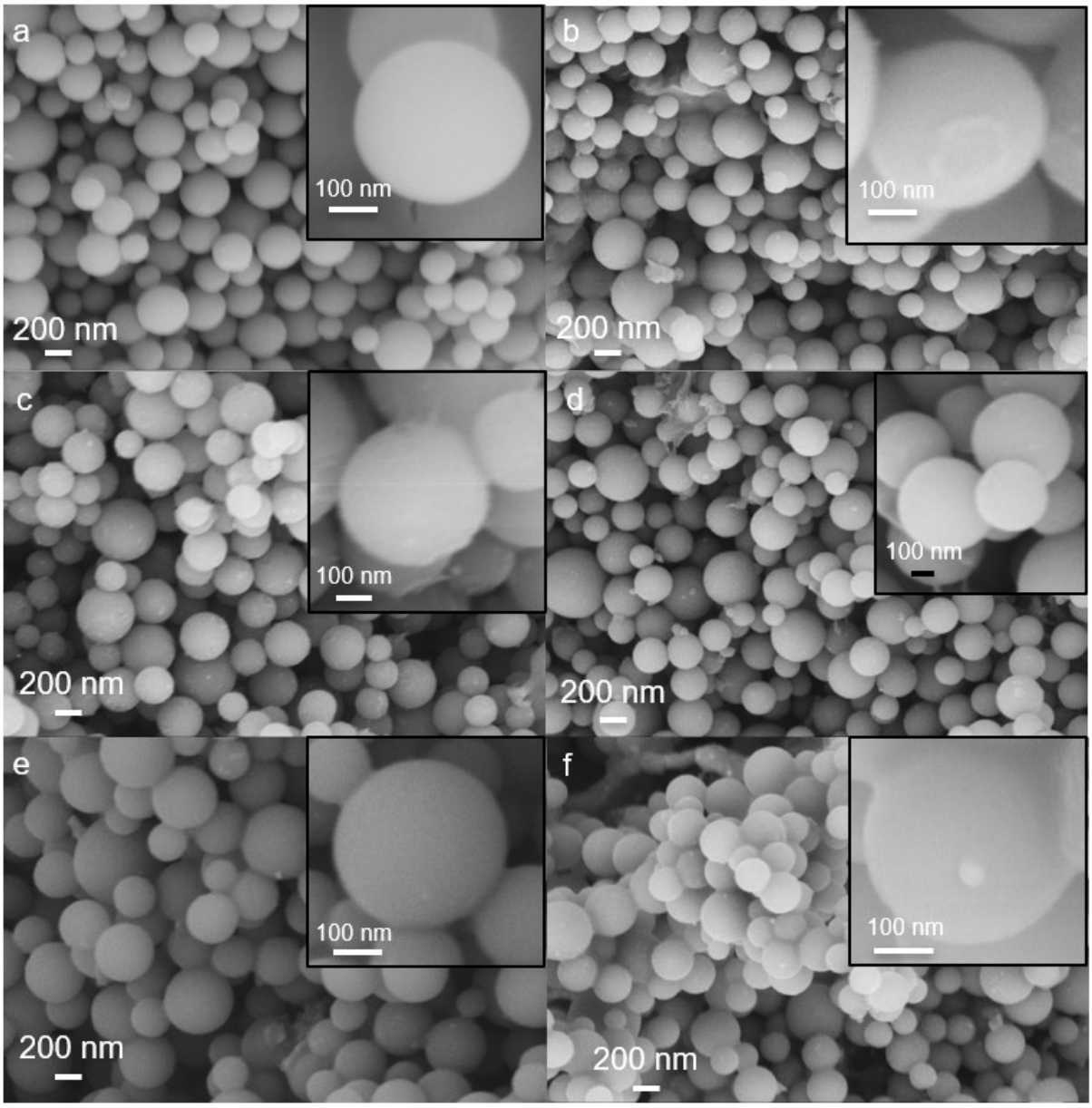

Figure 5.3 SEM images of (a) CS, (b) NCS, (c) Fe^{2+}@NCS, (d) Fe^{3+}@NCS, (e) Fe^{2+}@NCS-A, and (f) Fe^{3+}@NCS-A.

The overview of the morphology of the Fe^{2+}@NCS-A and Fe^{3+}@NCS-A was showed in HAADF-STEM images (**Figure 5.4a-b**). The carbon spheres in both Fe^{2+}@NCS-A and Fe^{3+}@NCS-A are in the range of 200 nm – 500 nm. After acid wash, the surface of most carbon spheres has uniform intensity with only a small portion of the carbon spheres showing the presence of the NPs (**Figure 5.5** and **Figure 5.6**). Energy-dispersive X-ray spectroscopy (EDS) was performed to map the presence of Fe species in the Fe^{2+}@NCS-A and Fe^{3+}@NCS-A samples. As can be seen in **Figure 5.4a-b**, for the carbon spheres where no NPs are visible, the

Fe signal is well-distributed, suggesting that Fe may exist in the form of isolated sites. The formation of the well-distributed sites has been reported elsewhere which could be attributed to several facts, such as 1) oxygen group-rich precursors, 2) low iron content, 3) high nitrogen content, 4) high surface area carbon support, etc.[127] The aim is to protect and prevent the Fe sites from agglomerating into particles. So far, no noticeable differences in morphology could be seen in both Fe^{2+}@NCS-A and Fe^{3+}@NCS-A.

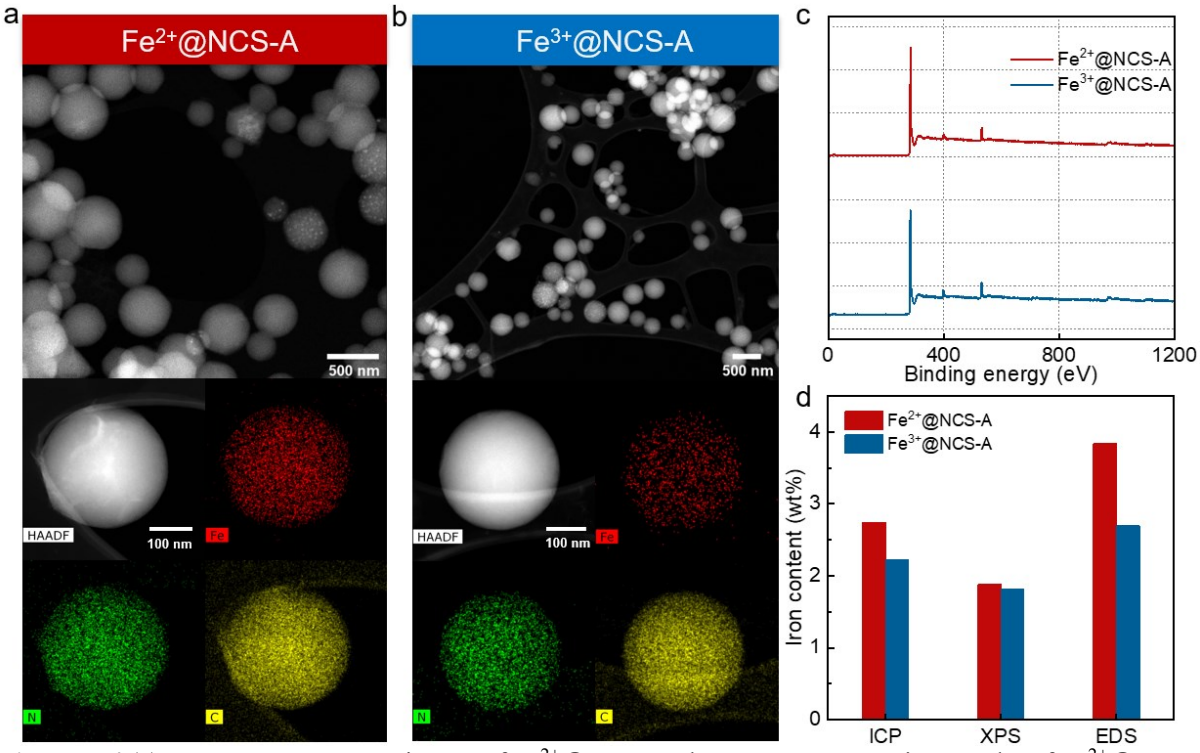

Figure 5.4 (a) top HAADF-STEM image of Fe^{2+}@NCS-A, bottom EDS mapping results of Fe^{2+}@NCS-A, (b) top HAADF-STEM image of Fe^{3+}@NCS-A, bottom EDS mapping results of Fe^{3+}@NCS-A, (c) XPS survey of Fe^{2+}@NCS-A and Fe^{3+}@NCS-A, and (d) the iron content of Fe^{2+}@NCS-A and Fe^{3+}@NCS-A from ICP-MS, XPS, and TEM-EDS.

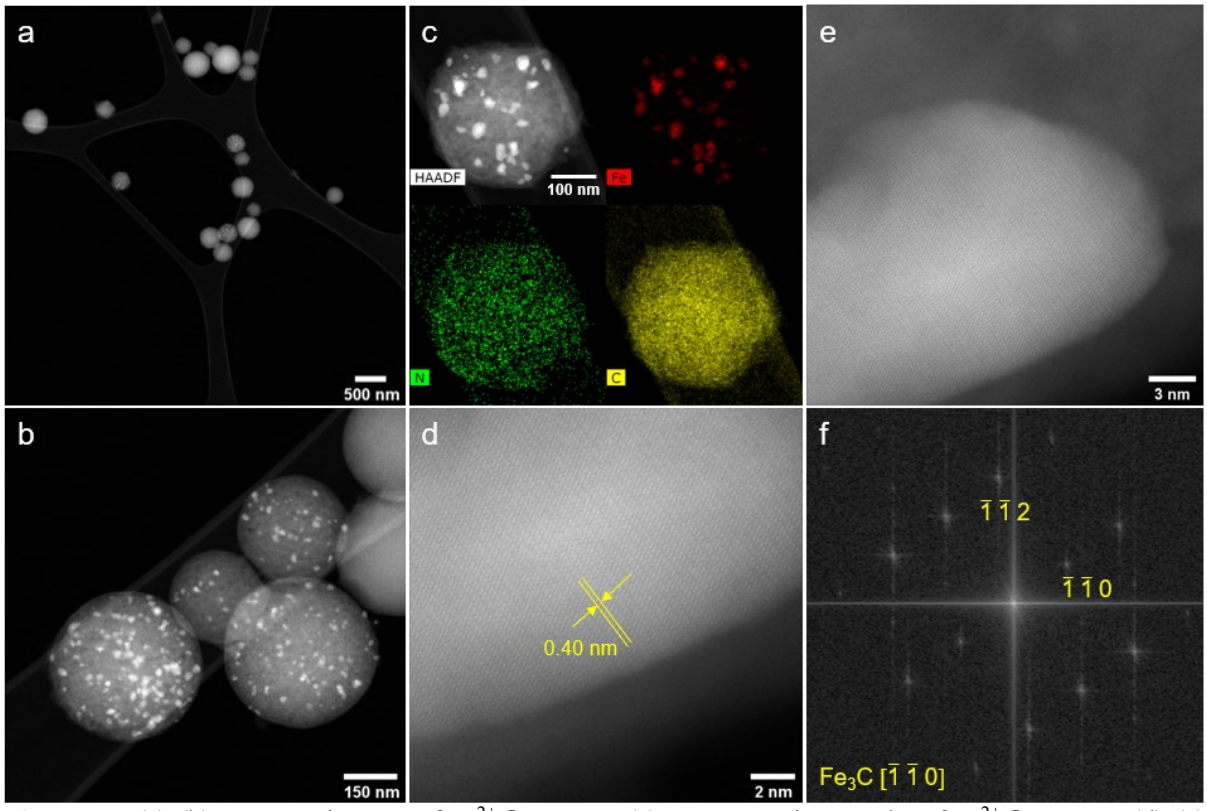

Figure 5.5 (a)-(b) HAADF images of Fe^{2+}@NCS-A, (c) EDS mapping results of Fe^{2+}@NCS-A, (d)-(e) High-resolution HAADF STEM images of the Fe nanoparticles and (f) their corresponding FFT images**.** The size of the carbon spheres is in the range of 200 nm - 500 nm, and the size of associated particles is in the range of 10 nm - 30 nm. Interplanar spacings measured from the FFT image are around 0.20, 0.23 and 0.40 nm, which correspond to the (002), ($\bar{1}\bar{1}2$) and ($\bar{1}\bar{1}0$) of reflections for Fe_3C (PDF card No.: 00-003-0989). EDS results show that the particles mainly consisted of Fe.

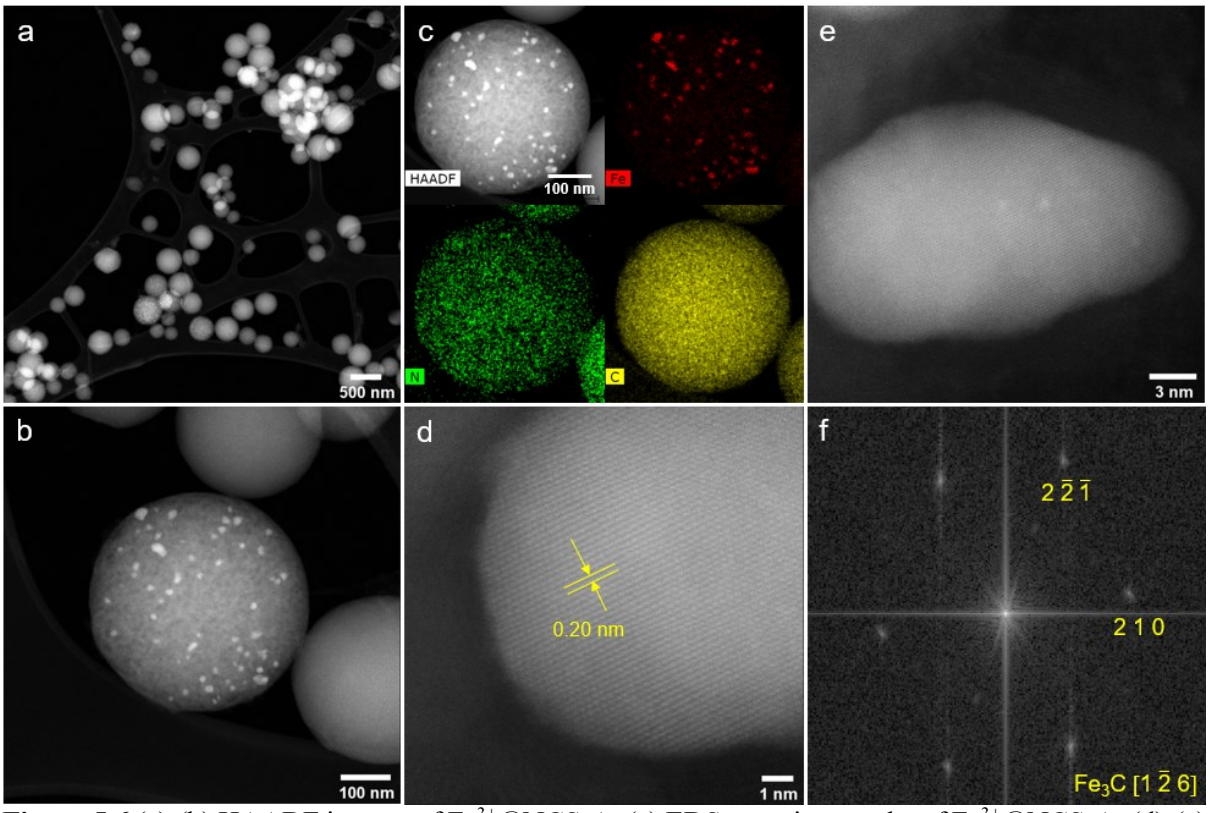

Figure 5.6 (a)-(b) HAADF images of Fe^{3+}@NCS-A, (c) EDS mapping results of Fe^{3+}@NCS-A, (d)-(e) High-resolution HAADF STEM images of the Fe nanoparticles and (f) their corresponding FFT images**.** Similar to Fe^{2+}@NCS, the size of the carbon spheres is in the range of 200 nm - 500 nm, and the size of associated bright particles is in the range of 10 nm - 30 nm. Interplanar spacings measured from the FT image in (f) are 0.19, 0.18 and 0.24nm, which correspond to $(0\bar{3}\bar{1})$, $(2\bar{2}\bar{1})$ and (210) of reflections for Fe_3C (PDF card No.:00-003-0989). EDS results show that the particles mainly consisted of Fe.

To get a complete picture of the obtained catalysts, the carbon spheres showing the presence of the NPs were also investigated. EDS was conducted (**Figure 5.5c** and **Figure 5.6c**), one could see the associated particles mainly consisted of Fe. From the high-resolution HAADF STEM images and their fast Fourier transform (FFT) images (**Figure 5.5d-f** and **Figure 5.6d-f**), it could be observed that the size of the associated particles in both samples are in the range of 10 - 30 nm. For Fe^{2+}@NCS-A, interplanar spacings measured from the FFT image are around 0.20, 0.23 and 0.40 nm, which correspond to the (002), $(\bar{1}\bar{1}2)$ and $(\bar{1}\bar{1}0)$ of reflections for Fe_3C (PDF#00-003-0989). As for Fe^{3+}@NCS-A, interplanar spacings measured from the FFT image are 0.19, 0.18 and 0.24nm, which correspond to $(0\,\bar{3}\bar{1})$, $(2\bar{2}\bar{1})$ and (210) of reflections for Fe_3C

(PDF#00-003-0989). These findings agree with the crystal structure suggested by XRD (**Figure 5.7**). The Fe_3C in some of the Fe^{2+}@NCS-A and Fe^{3+}@NCS-A samples might be due to the particles being embedded deep inside the carbon spheres (**Figure S5.8**), and therefore inaccessible to the HCl wash.

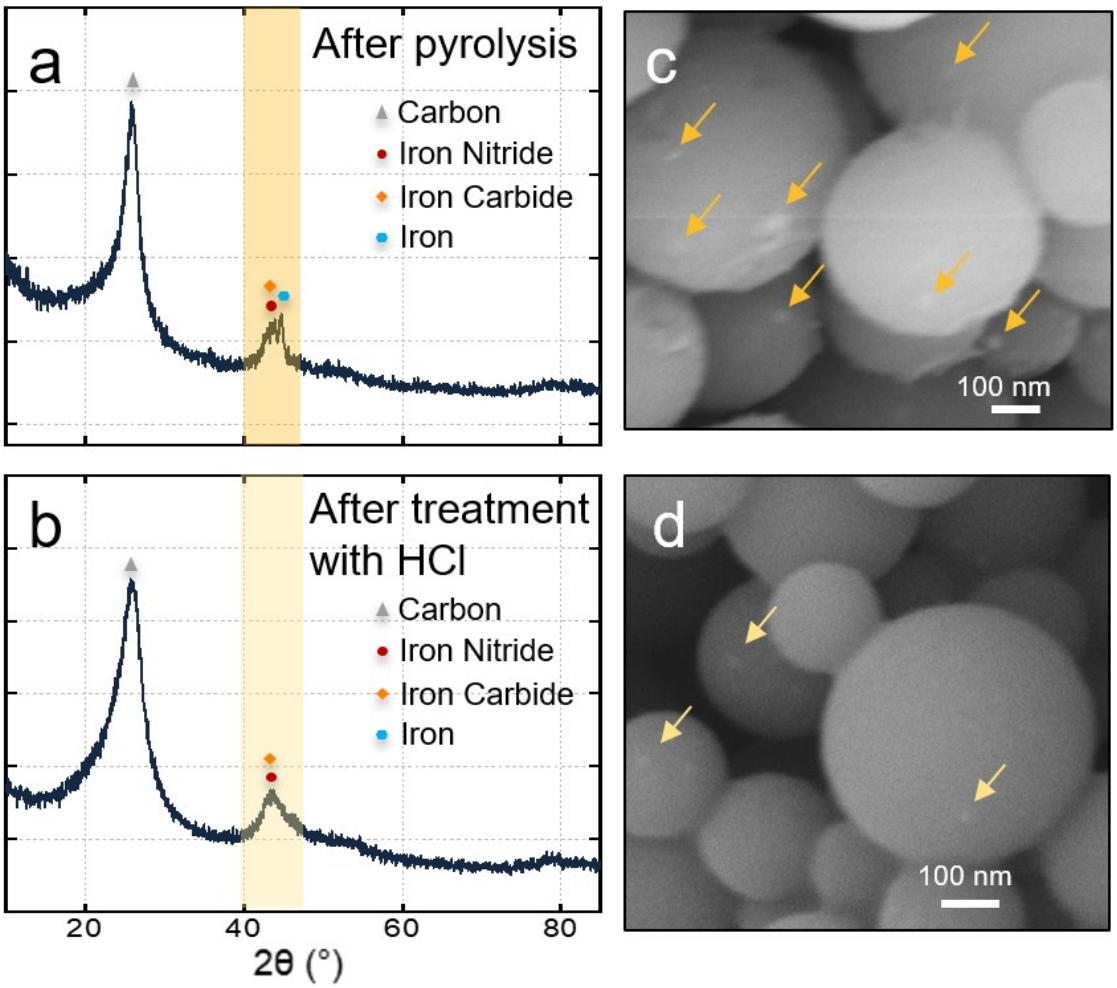

Figure 5.7 (a) XRD pattern and (c) SEM image of Fe^{2+}@NCS, (b) XRD pattern of Fe^{2+}@NCS-A (d) SEM image of Fe^{2+}@NCS-A. The powder X-ray diffraction (XRD) patterns of Fe^{2+}@NCS-A present two broad diffraction peaks centred at around 25. 7◦ and 43.3◦ of 2θ, corresponding to the (002) and (101) reflections of graphitised carbon. Correlating with the TEM images and powder diffraction file database, the peak at 43.3◦ also suggests the existence of iron nitride (PDF#00-003-1174), and FeC_3 (PDF#00-003-0989).

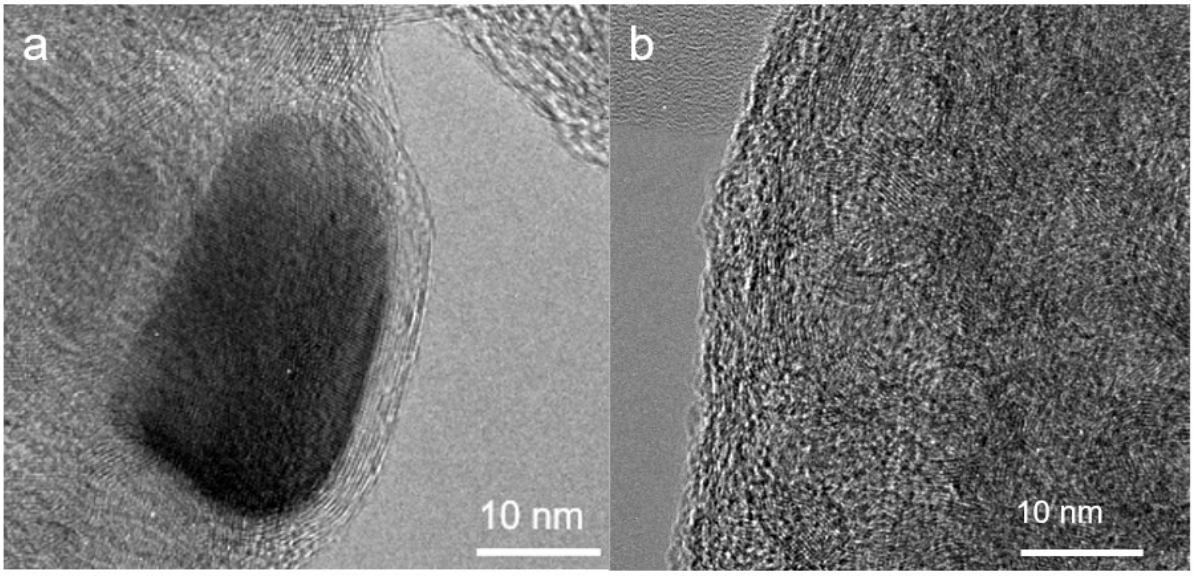

Figure 5.8 (a)TEM images of Fe_3C nanoparticles in Fe^{2+}@NCS-A, (b) TEM images of Fe^{2+}@NCS-A

5.3.2 Chemical structure characterizations

Carbon spheres with well-dispersed Fe sites are compared with carbon spheres fully loaded with Fe particles in **Figure 5.9**. From EDS mapping, both carbon spheres have nearly the same carbon signal intensity. The carbon spheres with only isolated Fe sites show a stronger N signal (~ 6 wt%), around three times more N signal intensity than the carbon spheres loaded with Fe NPs (~ 2wt%). This confirms that the N content plays a significant role in preventing Fe agglomeration. This inhomogeneous dispersion of N is most likely originated during catalysts preparation steps. However, further experiments are required to reveal the mechanism.

To reveal the elemental composition of the catalysts, X-ray photoelectron spectroscopy (XPS) was performed. In **Figure 5.4c**, the XPS survey spectrum of Fe^{2+}@NCS-A shows the chemical composition of C (84.2 wt%), N (5.77 wt%), O (8.15 wt%), and Fe (1.88 wt%) while Fe^{3+}@NCS-A shows the chemical composition of C (82.12 wt%), N (8.82 wt%) O (8.82 wt%) and Fe (1.82 wt%). Inductively coupled plasma mass spectrometry (ICP-MS) were also used to analyze the iron content of Fe^{2+}@NCS-A and Fe^{3+}@NCS-A. With XPS surveys and TEM-EDS (**Figure 5.4d**), iron content in Fe^{2+}@NCS-A is higher than that in Fe^{3+}@NCS-A.

Fe^{2+}@NCS showed 2.74 wt%, 1.88 wt%, and 3.84 wt% of iron content from ICP-MS, XPS, and TEM-EDS, respectively, while Fe^{3+}@NCS-A showed 2.22 wt%, 1.82 wt%, and 2.7 wt%, respectively. As ICP-MS is a bulk elemental analysis and XPS is more focused on the surface of catalysts, this suggests both Fe^{2+}@NCS-A and Fe^{3+}@NCS-A have similar Fe sites on the surface while Fe^{2+}@NCS-A has more Fe in bulk.

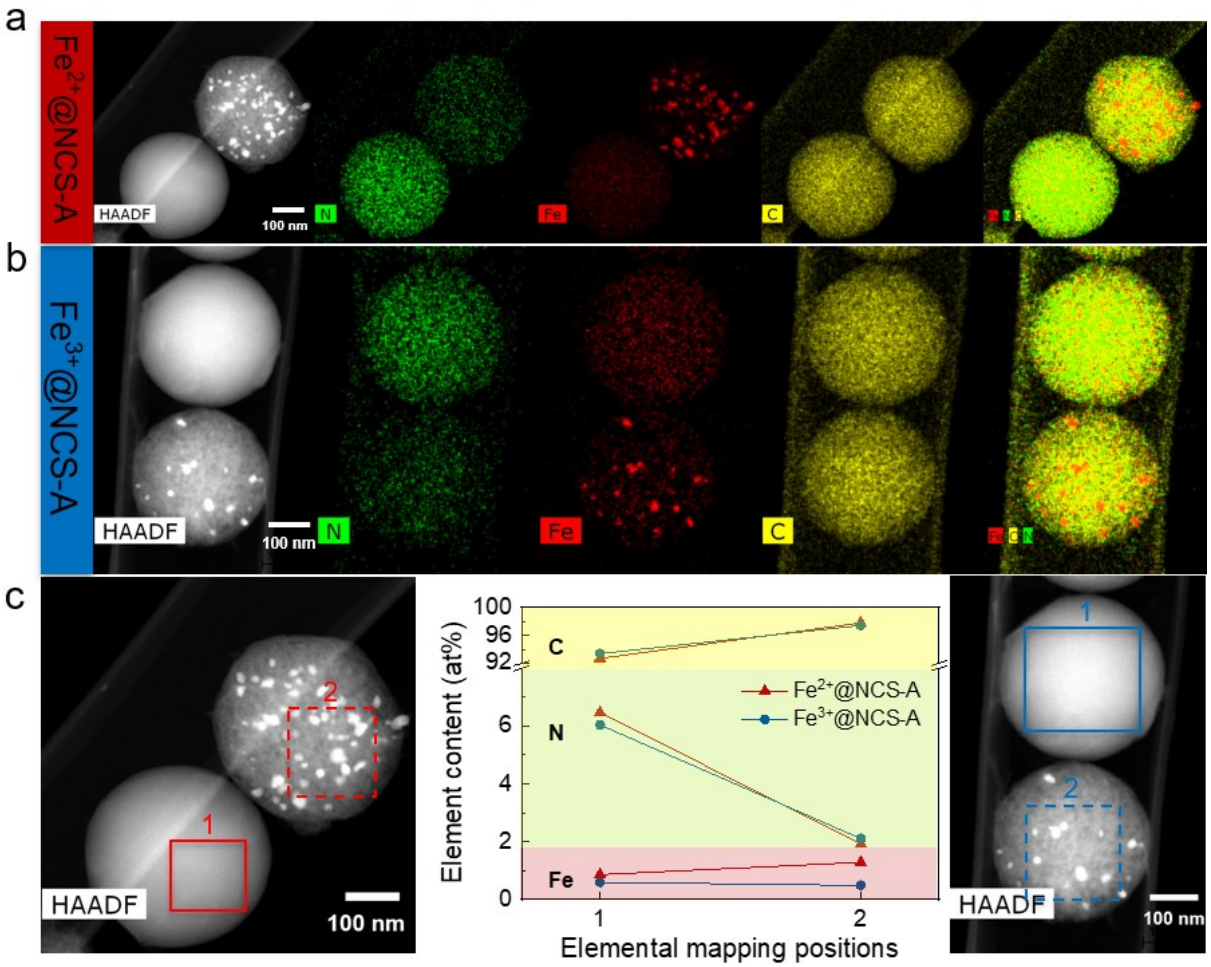

Figure 5.9 STEM EDS mapping results of (a) Fe^{2+}@NCS-A, (b) Fe^{3+}@NCS-A. (c) elemental content obtained from integrated EDS results (inserted frames 1 and 2 represent where the element signals were integrated). Fe signals are localised on the brighter nanoparticles, indicating the nanoparticles mainly consist of Fe. We cannot confirm whether C or N exist in the nanoparticles, since both C and N signals disperse homogeneously in the entire carbon spheres. However, one noticeable difference is that the N signal from iron nanoparticle spheres is much weaker than homogeneously dispersed carbon spheres. This indicates that higher nitrogen content might help the dispersion of Fe, while in the low nitrogen content, iron tends to form iron particles.

5.3.3 Atomic structure characterizations

To gain insights about the local structure of the Fe sites in Fe^{2+}@NCS-A, Fe^{3+}@NCS-A, and to confirm that Fe exists in atomic form, element-selective X-ray absorption fine structure spectroscopy experiments were conducted at the Fe K-edge. The magnitude of the extended X-ray absorption fine structure (EXAFS) Fourier Transforms (FTs) of Fe^{2+}@NCS-A and Fe^{3+}@NCS-A are displayed in **Figure 5.10a**. The magnitude of the FT has a strong single peak centred around 1.6 Å (phase uncorrected) for both Fe^{2+}@NCS-A and Fe^{3+}@NCS-A, distinct from those of the Fe_2O_3, and metallic Fe references, but similar to the reference iron phthalocyanine (FePc), which has well-defined Fe-N_4 coordinated sites. This result confirmed the absence of Fe-oxides and metallic Fe. Further, Fe EXAFS suggests the formation of Fe-N sites.

Wavelet transform (WT) can provide both radial distance resolution and k space resolution, which is a powerful method for distinguishing the backscattering atom.[211] As shown in **Figure 5.10b**, WT analysis of Fe^{2+}@NCS-A and Fe^{3+}@NCS-A both show only one intensity maximum at about ~ 4.2 $Å^{-1}$, which is very close to that in the reference FePc (~ 4.2 $Å^{-1}$), but distinct from the feature of Fe_2O_3 (~7 $Å^{-1}$). Therefore, the EXAFS and STEM data converge to the conclusion that the majority of the Fe species in Fe^{2+}@NCS-A, Fe^{3+}@NCS-A are Fe-N single sites, with a tiny amount of Fe_3C embedded in the carbon spheres where they are inaccessible to the HCl wash.

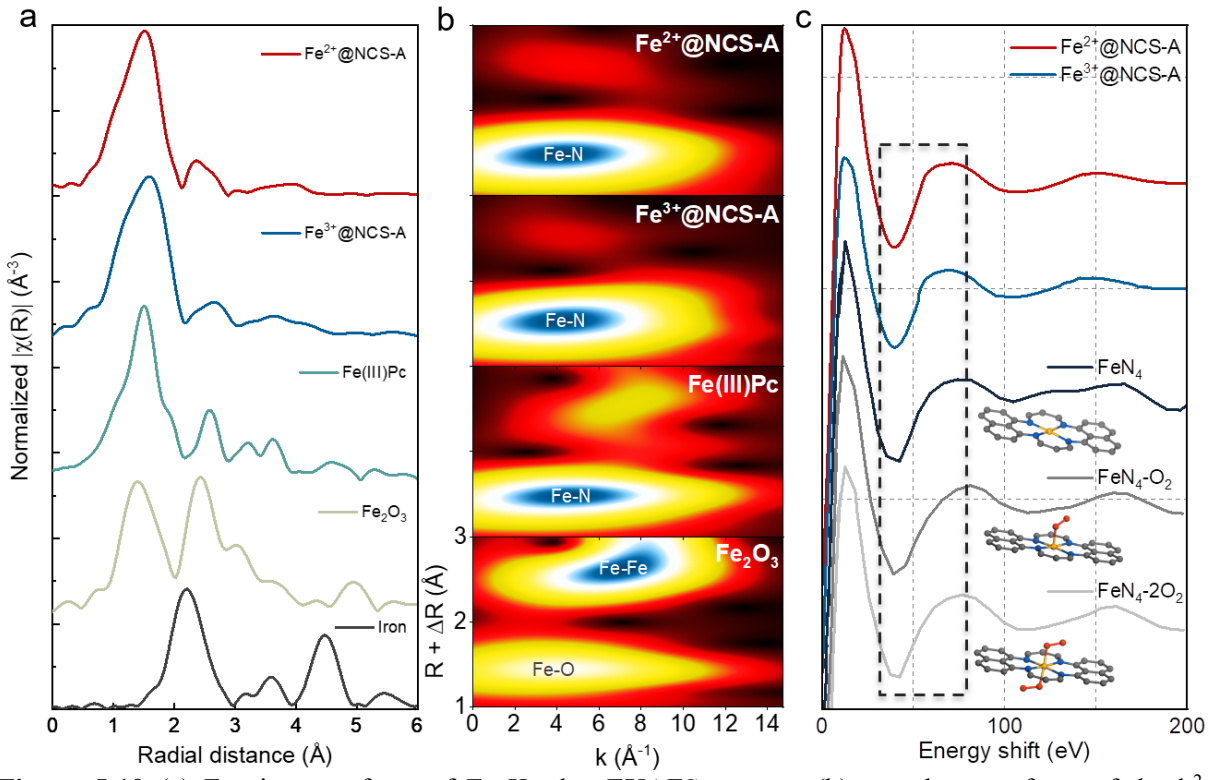

Figure 5.10 (a) Fourier transform of Fe K-edge EXAFS spectra, (b) wavelet transform of the k^2 weighted EXAFS data of Fe^{2+}@NCS-A, Fe^{3+}@NCS-A, Fe(III)Pc, and Fe_2O_3, (c) comparison between the K-edge XANES experimental spectrum of Fe^{2+}@NCS-A, and Fe^{3+}@NCS-A to the theoretical spectrums FeN_4, FeN_4-O_2, FeN_4-$2O_2$. The theoretical XANES spectrums were taken and reproduced with permission from ref [187]. Copyright 2015, Springer. (insert: theoretical Fe-N structures where red spheres are oxygen, yellow spheres are iron, grey spheres are carbon, and blue spheres are nitrogen)

As up to several different Fe-N_x structures have been reported, and each can result in different catalytic performances, it is essential to determine the local structure of the Fe-N_x structures.[99] Building optimized structure and simulating the X-ray absorption near edge structure (XANES) signal *via* density functional theory (DFT) calculations have become a powerful way to reveal the local structure of the single Fe sites.[89, 98, 187] Herein, reported theoretical XANES spectrums were used to compare with Fe^{2+}@NCS-A and Fe^{3+}@NCS-A experimental data (**Figure 5.10c**).[187] Only three possible matched structures FeN_4, FeN_4-O_2, FeN_4-$2O_2$ represent FeN_4 without oxygen ligand, one oxygen ligand, or two oxygen ligands attached to the centre Fe, respectively. By comparing

these three structures, FeN4 without ligand attached to Fe is the best-matched structure for Fe^{2+}@NCS-A and Fe^{3+}@NCS-A.

To shed light on chemical configuration of Fe-N single sites, FT EXAFS fittings were performed for Fe^{2+}@NCS-A, Fe^{3+}@NCS-A using iFEFFIT (**Figure 5.11a-b**, **d-e**, **Figure 5.12-13**).[188] All fittings are in good consistency with experimental data. The best fit values (Table S1) for EXAFS modelling of Fe^{2+}@NCS-A give an average coordination number of 4.0 ± 0.4 for Fe-N at 2.10 ± 0.01 Å and 2.4 ± 0.4 Fe-C at 1.92 ± 0.01 Å. Meanwhile, the average coordination numbers for Fe^{3+}@NCS-A are 3.4 ± 0.1 Fe-N at 2.08 ± 0.01 Å and 1.2 ± 0.3 Fe-C at 1.90 ± 0.01 Å. In addition, 0.5 ± 0.1 Fe-Fe was required for fitting Fe^{3+}@NCS-A (**Table 5.2**).[194, 212] The Fe-C signal is expected due to the presence of Fe_3C in these samples, as confirmed by STEM and EDS analyses. The absence of Fe-Fe signal in Fe^{2+}@NCS could be either due to minimal Fe_3C content or a much smaller average particle size of Fe_3C. Therefore, we propose that the iron existed primarily as Fe-N_x on the carbon substrate for both Fe^{2+}@NCS-A and Fe^{3+}@NCS-A, with Fe^{2+}@NCS-A being a fully stoichiometric Fe-N_4 species.

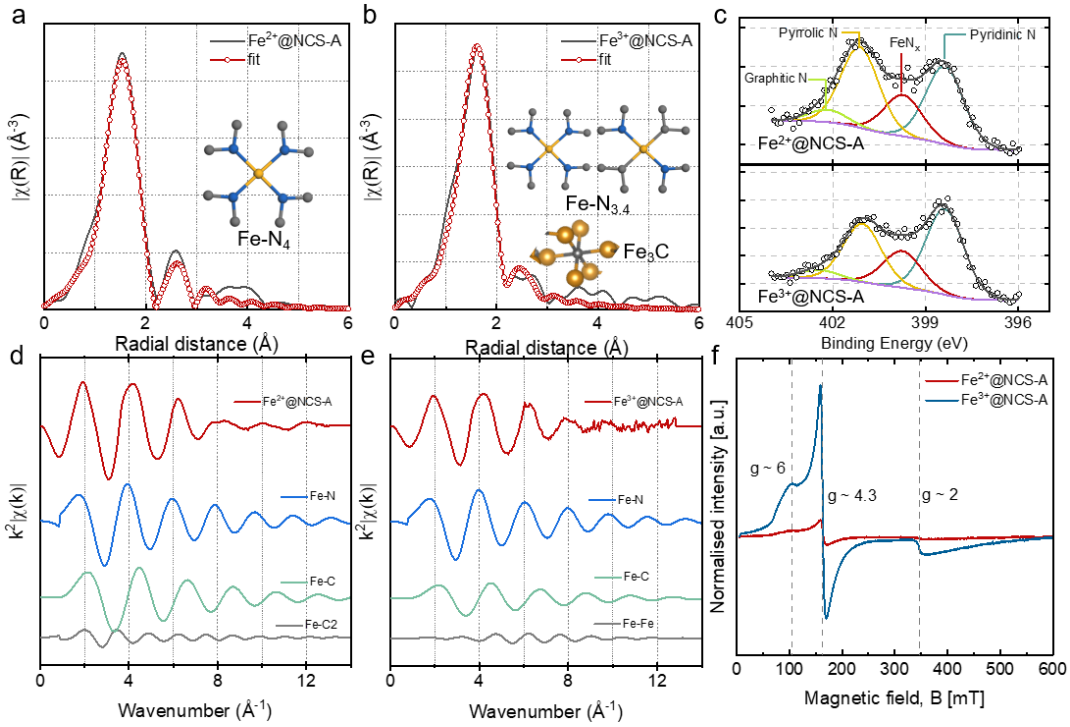

Figure 5.11 The magnitude of EXAFS FT k^2-weight Fe K-edge spectra and fitting curve of (a) Fe^{2+}@NCS-A, (b) Fe^{3+}@NCS-A, (c) high resolution of N 1s XPS spectrum of Fe^{2+}@NCS-A and Fe^{3+}@NCS-A, (d) the magnitude FT k^2-weighted Fe K-edge EXAFS spectra of Fe^{2+}@NCS-A and Fe-N, Fe-C, and Fe-C_{2nd} paths, (e) the magnitude FT k^2-weighted Fe K-edge EXAFS spectra of Fe^{3+}@NCS-A and Fe-N path, Fe-C path, and Fe-Fe path iron carbide, (f) X-band EPR of Fe^{3+}@NCS-A and Fe^{2+}@NCS-A.

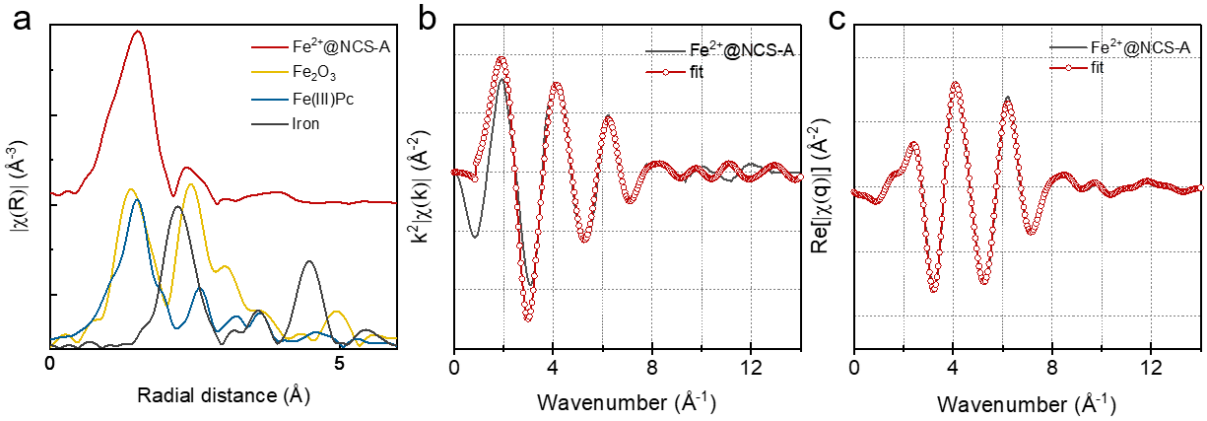

Figure 5.12 X-ray absorption analysis of Fe K-edge (a) R-space k^2 weight curves of Fe^{2+}@NCS-A and references samples Fe_2O_3, Fe(III)Pc, and iron foil, (b) Magnitude of Fourier Transform k^2-weighted Fe K-edge EXAFS spectra and fitting curve of Fe^{2+}@NCS-A, (c) q space fitting curve of Fe^{2+}@NCS-A.

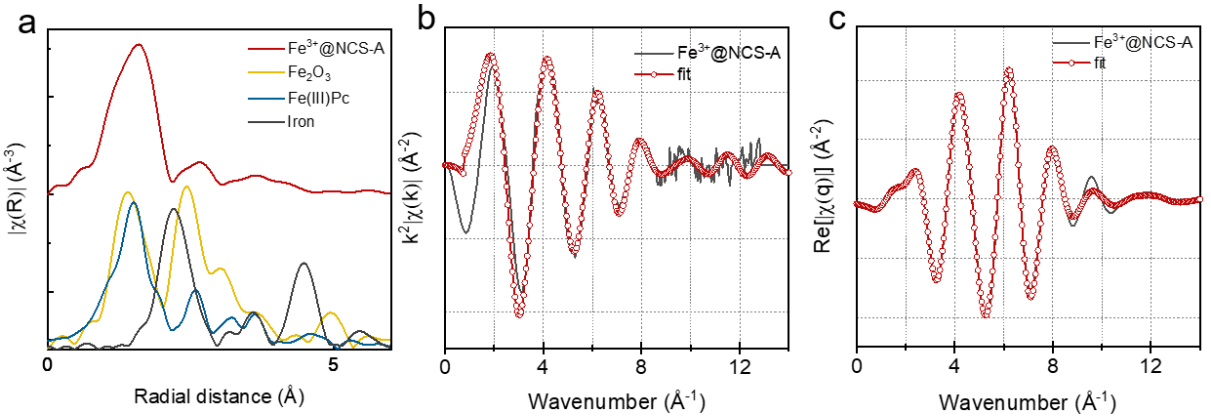

Figure 5.13 X-ray absorption analysis of Fe K-edge (a) R-space k^2 weight curves of Fe^{3+}@NCS-A and references samples Fe_2O_3, Fe(III)Pc, and iron foil, (b) Magnitude of Fourier Transform k^2-weighted Fe K-edge EXAFS spectra and fitting curve of Fe^{3+}@NCS-A, (d) q space fitting curve of Fe^{3+}@NCS-A.

5.3.4 Oxidation state characterizations

XPS supports the speciation of Fe obtained by EXAFS. The deconvoluted N1s spectra in **Figure 5.11c** show four types of nitrogen species for both samples, in which the peak at 399.9 eV can be assigned to FeN_x complexes (**Table 5.1**).[213-216] Besides, deconvoluted Fe2p spectra (**Figure 5.14a**) showed that Fe exist as a mixture of 2^+ and

3^+ oxidation in both Fe^{2+}@NCS-A and Fe^{3+}@NCS-A with more Fe^{2+} state in Fe^{2+}@NCS-A. Also, no noticeable presence of metallic Fe can be found in Fe2p spectra. Further, the oxidation states of the Fe in Fe^{2+}@NCS-A and Fe^{3+}@NCS-A were investigated using XANES and electron paramagnetic resonance (EPR). From the Fe K-edge XANES (**Figure 5.14b**) spectra, it can be seen that the white lines of Fe^{2+}@NCS-A and Fe^{3+}@NCS-A catalysts are in between the FeO and Fe_2O_3 references, indicating they have oxidation states in between 2^+ and 3^+ which more closed to 3^+. However, the XANES region could be influenced by the local coordination structure. It might be inaccurate to compare the oxidation state directly from XANES. Therefore, EPR was performed to investigate the electronic structure of Fe^{3+}@NCS-A and Fe^{2+}@NCS-A. EPR results shown in **Figure 5.11f** reveal that Fe^{3+}@NCS-A has a stronger response than Fe^{2+}@NCS-A, suggesting greater Fe^{3+} content in Fe^{3+}@NCS-A. From the EPR signals, rhombic symmetry systems with Fe^{3+} high spin (S = 5/2) can be determined, with $g \approx 6$ and $g \approx 2$ assigned to Fe^{3+} with square pyramidal coordination. Meanwhile, $g \approx 4.3$ originates from Fe^{3+} with a rhombic ligand field.[185] As stated in **Figure 5.4d**, iron content in Fe^{2+}@NCS-A is higher than that in Fe^{3+}@NCS-A. Thus the missing Fe signal in EPR suggests a higher Fe^{2+} content in the Fe^{2+}@NCS-A than Fe^{3+}@NCS-A. This difference in iron oxidation states might stem from the iron precursors that could be further responsible for a different catalytic activity.

Table 5.1 Elemental content determined from XPS

wt%	C	N	O	Fe	Pyridinic N	FeNx	Pyrrolic N	Graphitic N
Fe^{2+}@NCS-A	84.2	5.9	8.1	1.8	2.1	1.3	2.2	0.3
Fe^{3+}@NCS-A	82.1	7.6	8.8	1.8	3.4	1.7	2.3	0.2

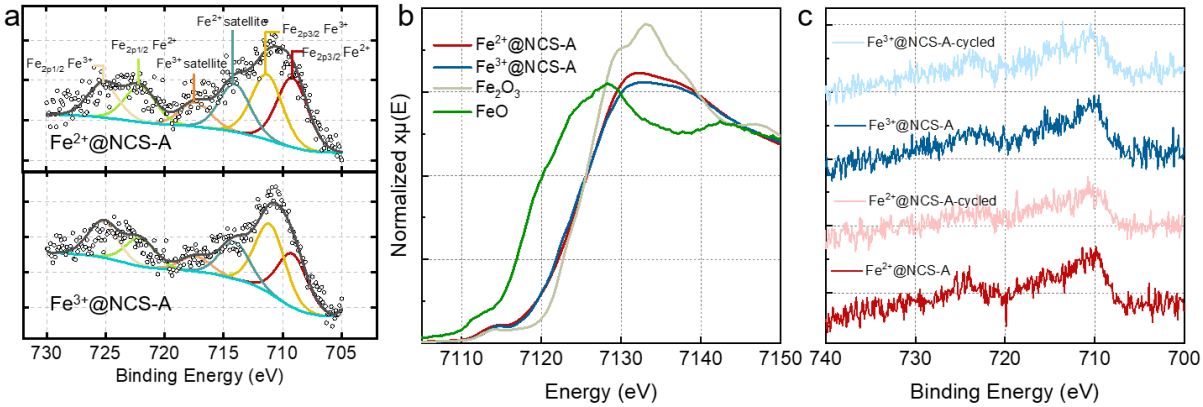

Figure 5.14 XPS high-resolution Fe2p spectrum of (a) Fe^{2+}@NCS-A and Fe^{3+}@NCS-A, (b) XANES spectra of Fe^{3+}@NCS-A, Fe^{2+}@NCS-A, Fe(II)Pc, Fe(III)Pc, and Iron, (c) comparison of Fe peak changes before/after CV 300 cycles in oxygen saturated 0.1M KOH, catalysts were loaded on carbon felt to perform the CV cycling. XPS reveals the elemental composition and chemical states of Fe in the catalysts. No obvious presence of metallic Fe can be found. No obvious shift could be found in the Fe peak by examining the Fe spectrums before and after CV cycling. The relatively low signal-to-noise ratios are caused by the low absolute Fe contents of the catalysts.

5.3.5 Physical structure characterizations

Besides Fe active sites, it has also been reported that the structure of the carbon support, such as surface area, pore size and graphitization contents, also plays a critical role. Therefore, to get more insights into the structural information from the obtained catalysts, wide angle X-ray scattering (WAXS), small angle X-ray scattering (SAXS), and nitrogen physical adsorption analyses were performed. Compared with NCS and CS, Fe^{2+}@NCS-A and Fe^{3+}@NCS-A show more pronounced graphitic features because the incorporation of iron can catalyze the graphitization of carbon substrate during carbonization (**Figure 5.8b**), which favours electron transfer based on the increased conductivity. Higher graphitization could also be seen in XRD and WAXS spectrums in **Figure 5.15**, where sharper and right-shifted (002) peaks are presented in Fe^{2+}@NCS-A and Fe^{3+}@NCS-A. No metallic iron peak and Fe_3C could be seen in the WAXS spectrum, suggesting the well-dispersed Fe without agglomeration. Besides, no noticeable difference could be seen from the XRD spectra of Fe^{2+}@NCS-A and Fe^{3+}@NCS-A.

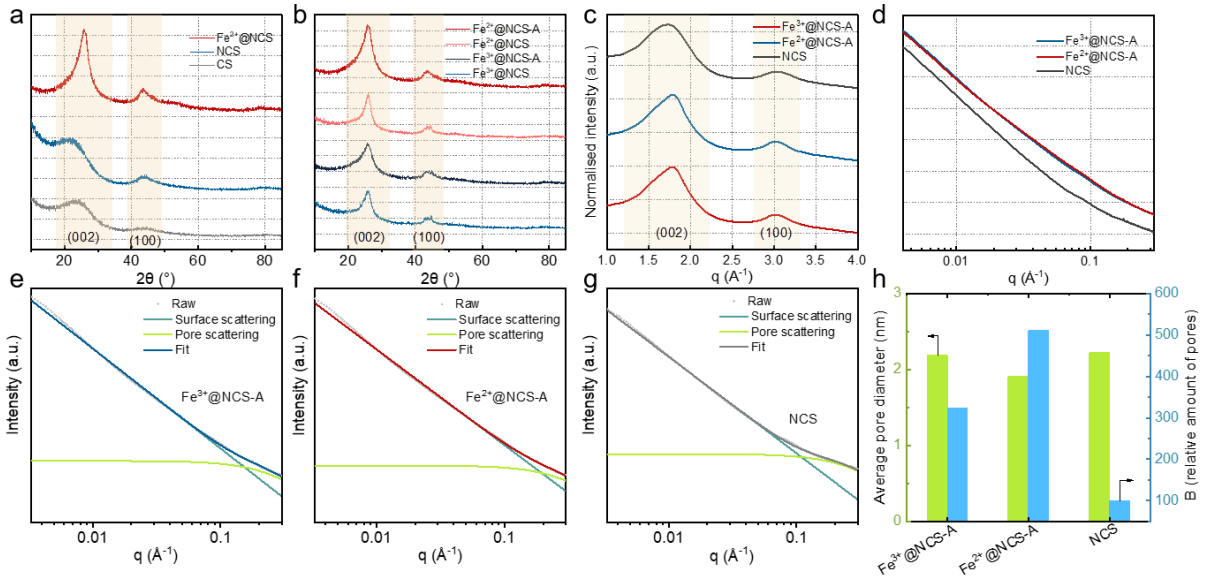

Figure 5.15 XRD patterns of (a)Fe^{2+}@NCS-A, NCS, and CS, (b) Fe^{2+}@NCS-A, Fe^{2+}@NCS, Fe^{3+}@NCS-A, and Fe^{3+}@NCS, (c) WAXS pattern of Fe^{2+}@NCS-A, Fe^{3+}@NCS-A, and NCS, (d) SAXS pattern of Fe^{2+}@NCS-A, Fe^{3+}@NCS-A, and NCS. Fitted SAXS pattern of (e) Fe^{3+}@NCS-A, (f) Fe^{2+}@NCS-A, and (g) NCS, (h) comparision of average pre diameter, and B values fitted from SAXS, the detailed fitting methods could be found in experimental part.

Furthermore, specific surfaces area of these samples were determined by using Brunauer-Emmett-Teller (BET) *via* N_2 physical adsorption (**Figure 5.16**). The Fe^{2+}@NCS-A, Fe^{3+}@NCS-A, and NCS showed a specific surface area of 70 m^2 g^{-1}, 42 m^2 g^{-1}, and 138 m^2 g^{-1}, respectively (**Figure 5.16c**). Fe doping reduced the surface area suggests that Fe species were adsorbed on the surface and encapsulated in cavities during the synthesis of Fe@NCS. Pore size distribution (**Figure 5.16g-i**) shows that NCS has pores at around 1 nm, where Fe^{2+}@NCS-A has pores at 1.2 nm, and Fe^{3+}@NCS-A has pores at both 1 nm and 1.2 nm, which showed that more micropores (pore width smaller than 2 nm) were blocked in Fe^{2+}@NCS-A. Besides, fitted SAXS results showed the average pore diameters for Fe^{2+}@NCS-A (1.91 nm) was smaller than Fe^{3+}@NCS-A (2.18 nm), and NCS (2.22 nm). B values represent the relative number of pores were also fitted, and the Fe^{2+}@NCS-A showed 510 % relative number of pores compare to NCS (100%), while Fe^{3+}@NCS-A showed 322 %. This increased the

relative number of pores due to the formation of closed pores invisible in BET. Together with BET, we could speculate that more Fe^{2+} adsorbed into bulk and that is why smaller closed pores were generated.

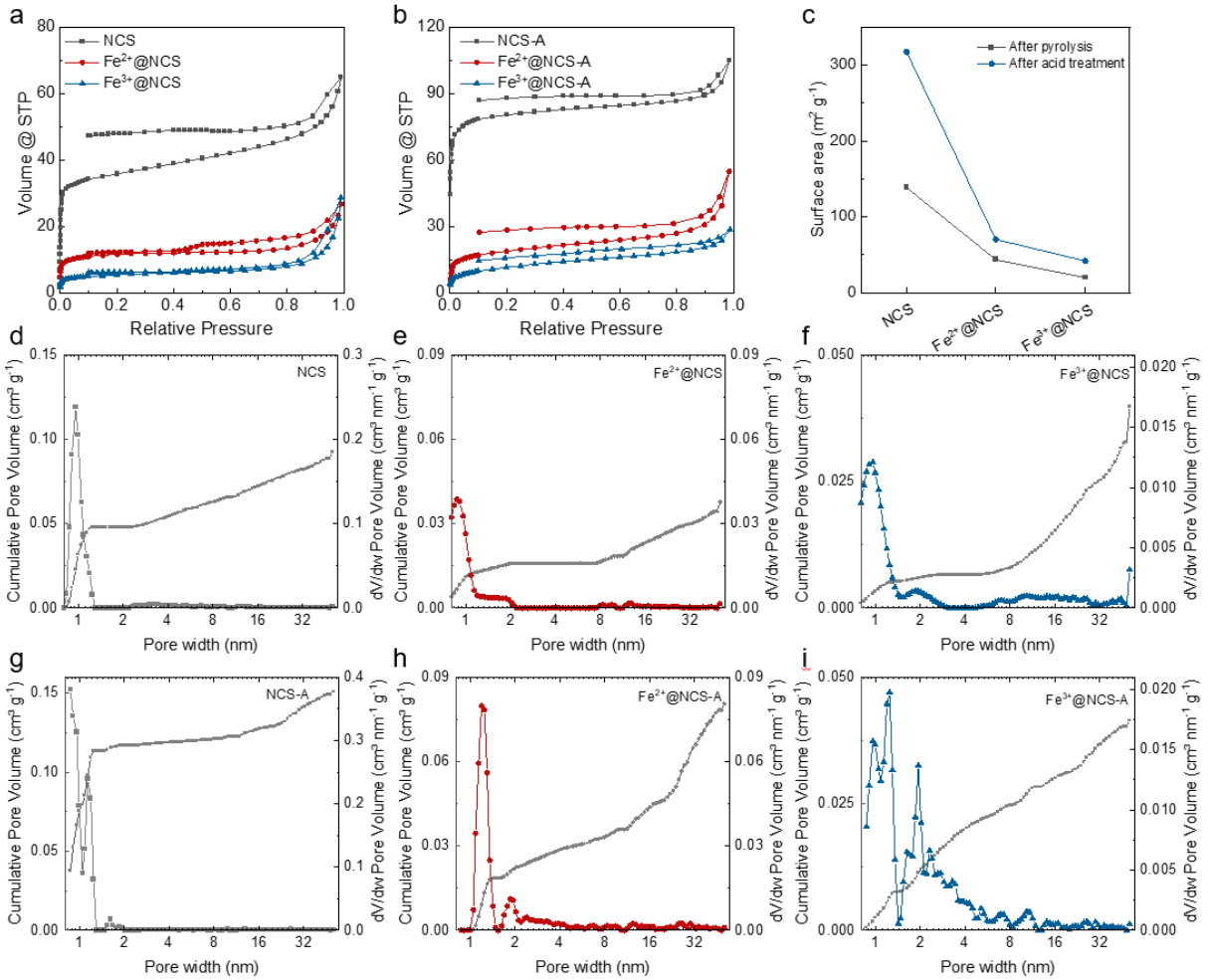

Figure 5.16 (a) N_2 adsorption isotherms of NCS, Fe^{2+}@NCS, and Fe^{3+}@NCS, (b) N_2 adsorption isotherms of NCS-A, Fe^{2+}@NCS-A, and Fe^{3+}@NCS-A, (c) Specific surface area obtained from nitrogen physical adsorption of NCS, Fe^{2+}@NCS, and Fe^{3+}@NCS after pyrolysis and after acid treatment., pore size distribution of (d) NCS, (e) Fe^{2+}@NCS, (f) Fe^{3+}@NCS-, (g) NCS-A, (h) Fe^{2+}@NCS-A, and (i) Fe^{3+}@NCS-A calculated based on HS-2D-NLDFT_Carbon_N2_77 model.

To conclude, Fe^{2+}@NCS-A has shown higher Fe^{2+} content, fully stoichiometric Fe-N_4 sites, and relatively low surface area but higher than Fe^{3+}@NCS-A. These factors have shown the chemical and structural differences caused by these two precursors with different oxidation states. Further, the electrochemical characterizations were performed to investigate the catalytic performance of these catalysts.

5.3.6 Electrochemical characterizations

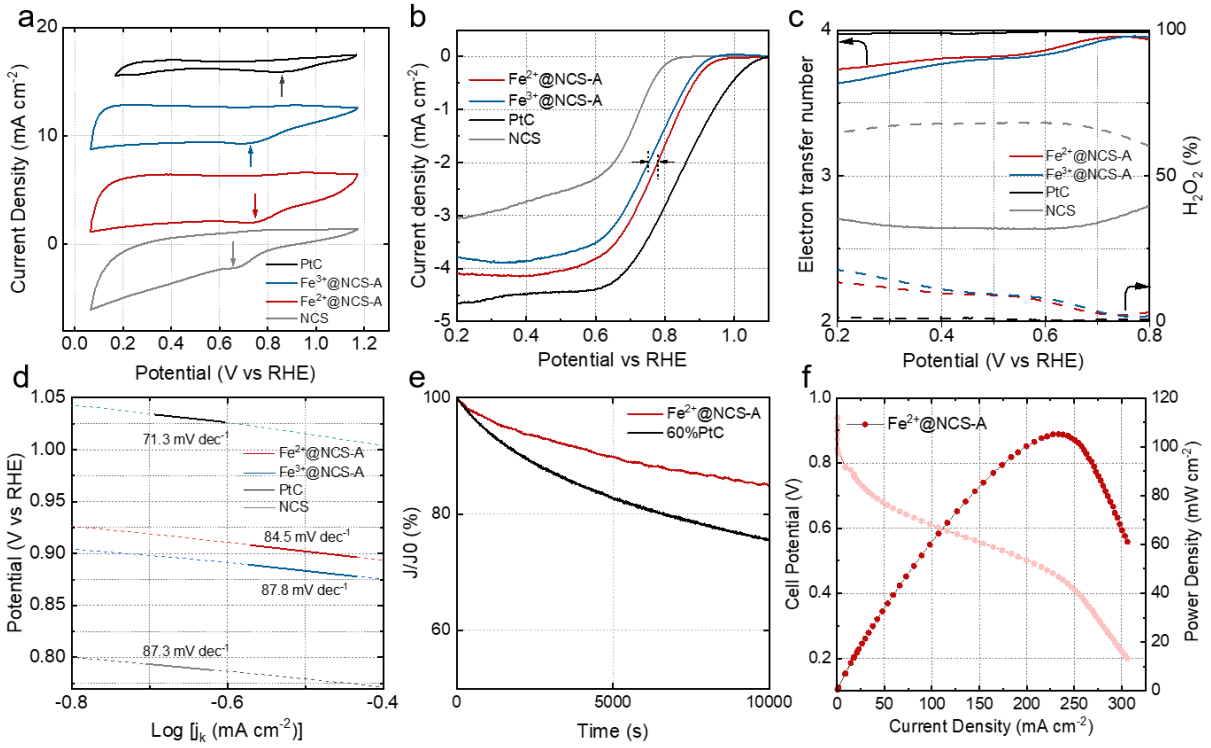

Figure 5.17 (a) CV curves at 0 rpm, 100 mV s^{-1} scan rate, (b) LSV curves at 1600 rpm, 10 mV s^{-1} scan rate, (c) electron transfer number and H_2O_2 production rate of Fe^{2+}@NCS-A, Fe^{3+}@NCS-A, Pt/C and NCS, (d) Tafel plots of Fe^{2+}@NCS-A, Fe^{3+}@NCS-A, NCS, and Pt/C, (e) chronoamperometric responses of Fe^{2+}@NCS-A and Pt/C at 0.7 V and 1600 rpm. All RDE/RRDE tests were performed in O_2-saturated 0.1 M KOH, background N_2 current was extracted. Reference electrode: Hg/HgO, counter electrode: graphite rod. Catalyst loading: 0.28 mg cm^{-2}, Pt loading 0.021 mg cm^{-2}. (f) AEMFC performance of Fe^{2+}@NCS-A cathode. Polarization curve and power density plotted as a function of current density. H_2-O_2 gases were fed at 0.3 L min^{-1} with no back-pressurization; cathode: 2.0 mg cm^{-2} of Fe^{2+}@NCS-A; anode: 0.70 mg cm^{-2} of PtRu; T_{cell} = 60 °C (RH 100 %). The membrane used in this work was low-density polyethylene-based (LDPE) anion exchange membrane and the ionomer was ETFE-benzyltrimethylammonium (BTMA) powder.

The ORR catalytic performance of NCS, Fe^{2+}@NCS-A, Fe^{3+}@NCS-A, and commercial Pt/C (55-58 wt%) were evaluated by cyclic voltammetry (CV) and linear sweep voltammetry (LSV) under alkaline conditions (0.1 M KOH oxygen saturated) using a rotating disk electrode (RDE). Among all the as-prepared catalysts, the Fe^{2+}@NCS-A shows the most promising ORR activity due to its higher amount of electroactive iron species. The CV (**Figure 5.17a**) curves of all samples show oxygen reduction peaks.

LSV (**Figure 5.17b**) curves of Fe^{2+}@NCS-A show an obvious positive oxygen reduction peak and onset potential (the potential where reaches - 0.1 mA cm^{-2}) at 0.94 V, more positive than those of NCS (0.81 V), and Fe^{3+}@NCS-A (0.91 V), 100 mV negative of Pt/C (1.04 V). Fe^{2+}@NCS-A also displays a half-wave potential of 0.79 V, which is 30 mV more positive than Fe^{3+}@NCS-A (0.76 V), suggesting a better catalytic activity in Fe^{2+}@NCS-A. (**Figure 5.17b**). The limiting current density of Fe^{2+}@NCS-A is higher than Fe^{3+}@NCS-A, suggesting more 4 electron pathway occurs in Fe^{2+}@NCS-A. As illustrated in **Figure 5.17d**, Fe^{2+}@NCS-A presents a Tafel slope value of 84.5 mV dec^{-1}, slightly smaller than Fe^{3+}@NCS-A (87.8 mV dec^{-1}), and NCS (87.3 mV dec^{-1}). Rotating ring disk electrode (RRDE) tests show an electron transfer number from 3.7 to 3.95 for both Fe^{2+}@NCS-A and Fe^{3+}@NCS-A. The decreasing trend of electron transfer number suggests 2-electron process increase at lower potential. H_2O_2 production showed an increasing trend from high potential to low potential (from 2 % - 18 %).

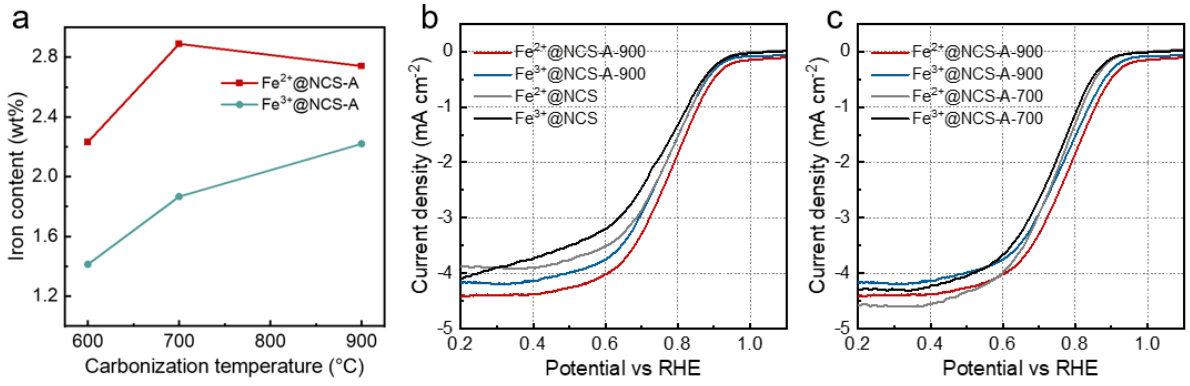

Figure 5.18 (a) The iron content of catalysts determined by ICP as a function of carbonisation temperature. Interestingly, at the same carbonisation temperatures, the iron content in Fe^{2+}@NCS-A is higher than Fe^{3+}@NCS-A. Moreover, the samples carbonised at higher temperature showed higher Fe contents than those carbonised at lower temperature, even after HCl washing, suggesting more Fe-N site formation at higher temperature. (b) LSV curves of Fe^{2+}@NCS and Fe^{2+}@NCS-A, Fe^{3+}@NCS and Fe^{3+}@NCS-A, (c) LSV curves of Fe^{2+}@NCS-A-900 and Fe^{3+}@NCS-A-900, Fe^{2+}@NCS-A-700 and Fe^{3+}@NCS-A-700.

Thus, the higher onset potential, higher half-wave potential, smaller Tafel slope value, and higher electron transfer number of Fe^{2+}@NCS-A are likely to originate from the different local coordination environments and the oxidation states of the Fe site as Fe^{2+}@NCS-A has a higher amount of Fe-N_4 sites and higher overall iron content in Fe^{2+}. However, more experiments are needed to reveal the detailed mechanism of whether and how Fe oxidation state influence the electrocatalysis steps. It should be mentioned here that the Fe_3C content in the two samples are minimal and embedded inside the carbon sphere structure, as demonstrated by our STEM, EXAFS, XPS, and WAXS data. Thus, the contribution from Fe_3C towards the ORR performance should be negligible.[217]

Furthermore, chronoamperometry testing was performed to check the stability of Fe^{2+}@NCS-A. After 10,000 s (2.77 h) at 0.7 V, due to the Fe-N singles sites, nearly 85 % of the current was retained for Fe^{2+}@NCS-A, whilst Pt/C only showed 76 % current retention (**Figure 5.17e**). Ex-situ XPS was performed before and after the CV cycling (**Figure 5.14c**) to investigate the active site change. No noticeable changes in the peak shape and the decreased peak intensity might be caused by the sample peeling off during the CV cycling, resulting in a lower intensity than before. To further explore the performance of Fe^{2+}@NCS-A in real operating devices, the electrochemical performance in anion exchange membrane fuel cells (AEMFCs) was also tested.[218] The operating AEMFCs were fed with H_2 and O_2 gases. The Fe^{2+}@NCS-catalyst achieved high open-circuit potentials at 0.96 V in the operating AEMFC compared to other comparable M-N-C catalysts (**Table 5.3**). Although it is still lower than Pt-based catalysts tested under similar conditions, it shows great potential after further electrode optimization.[219] The current density and power density demonstrating the promising approach for developing low-cost AEMFCs.

Table 5.2 EXAFS fitting parameters.

Sample	Scattering pair	CN	R (Å)	ΔE_0 (eV)	σ^2 (10^{-3} Å^2)	R factor
Fe^{2+}@NCS-A	Fe-N	4.0	2.10	3.01 +/- 1.65	0.005	0.0044
		+/- 0.4	± 0.01		Fixed	
	Fe-C	2.4	1.92		0.005	
		+/- 0.4	± 0.01	+/- 1.65	same as σ^2 (Fe-N)	
	Fe-C2	2.1	3.03		0.005	
		+/-0.6	± 0.01		2 x σ^2 (Fe-N)	
Fe^{3+}@NCS-A	Fe-N	3.4	2.08	2.21	0.005	0.00362
		+/-0.1	± 0.01		Fixed	
	Fe-C	1.2	1.90		same as σ^2 (Fe-N)	
		+/-0.3	± 0.01	+/- 1.25	Fixed	
	Fe-Fe	0.5	2.59		0.010	
		+/-0.1	± 0.01		2 x σ^2 (Fe-N)	

S_0^2 is the amplitude reduction factor ($S_0^2 = 0.85$)

Table 5.3 Summary of ORR activity of Fe@NCS with previously reported Fe-Based catalysts (* represents the values taken approximately from graph)

Catalysts	$E_{1/2}$ (V) vs. RHE (0.1 M KOH)	Tafel plot value (mV dec^{-1})	Onset potential (-0.1 mA cm^{-2})	Ref
Fe/N/CNT/PCF	0.78*	65.8	0.95	[220]
Fe/N-CNFs	0.78	-	0.94	[221]
Fe/N-NGA	0.79	52	0.97	[222]
Fe@C-FeNC-2	0.89	68	0.98	[223]
Fe N/C	0.88	68	0.98	[224]
Fe SAs N/C-20	0.91	-	0.98	[225]
C-Fe-Z8-Ar	0.82	70	0.94	[226]
Fe-CZIF-800-10	0.83	-	0.96	[227]
Ag/Graphene	0.72*	-	0.83	[228]
Fe-NC SAC	0.90*	48	0.97	[127]
3DOM Fe-N-C-900	0.87*	49	0.96	[229]

Co/N/C	0.79*	-	0.84	[230]
FeN/CNT	0.87*	-	0.95	[231]
FeN/CNT	0.87*	61.9	0.98	[232]
Fe-S-Phen/CNT	0.90*	52	0.99	[233]
Fe, Cu/N/C	0.92*	59.3	1.04	[234]
Fe/S, N/C	0.77*	-	0.93	[235]
Fe@NCS	0.79	84.5	0.94	This work

Table 5.4 Summary of Fuel cell performance of Fe@NCS with previously reported M-N-C catalysts (* represents the values taken approximately from graph)

Catalysts	**Open circuit potential (V)**	**Current density @ 0.6 V (mA cm^{-2})**	**Pmax (mW cm^{-2})**	**Ref**
Fe-N-CC	0.96	135	123	[219]
N-CNT	0.87	52*	62	[236]
FePc/MWCNT	0.96*	70*	135	[237]
NpGr	0.82	30	26	[238]
Co-Fe_3O_4/C	0.85	135*	175	[239]
NPOMC-L2	0.89*	125*	70	[240]
FePc/C-900	0.94*	200*	122	[241]
Fe-M-La/C-700	0.94	180*	135	[242]
Fe-S-Phen/CNT	0.98*	446*	630*	[233]
FeN/CNT	0.97*	556*	379*	[231]
Fe/N/CDC	1.01*	138	178*	[243]
Fe-N-comp	0.98*	205*	120*	[196]
Fe-N-Gra	1.05*	332*	243*	[195]
SiCDC/CNT(1:3)/FePc	0.98*	170*	182	[193]
Fe-N-CDC/CNT	0.97*	1108*	872*	[192]
Fe-N-C	1.02*	366*	219*	[244]
Fe/IL-PAN-A1000	1.02*	427*	290*	[245]
SHUb-Fe/N-A	0.96*	288*	234*	[246]
FeCoNC-at	1.02*	646*	415*	[247]
Fe@NCS	0.96V	125	108	This work

5.4 CONCLUSION

In summary, Fe, N co-doped carbon sphere electrocatalysts (Fe@NCS-A) were synthesized *via* a facile, green, and scalable method. The majority of Fe species were found to exist in Fe-N_4 sites, with a minimal amount aggregated into Fe_3C nanoparticles and embedded inside the carbon sphere structure. The optimized Fe-N_4 sites have been successfully obtained by starting with different Fe precursors, with Fe^{2+}@NCS-A showing a better ORR and AEMFC activity and durability. For the formation mechanism of Fe-N_4 sites, we propose that the N content is key for preventing Fe aggregation. At the same time, the starting precursor and carbonization conditions are essential for determining the final configuration of the Fe-N_4 sites. We have proved that iron precursors with different oxidation states can lead to variants in iron species, iron sites' coordination numbers, and oxidation states in the final product, consequently influencing the final catalytic performance. However, future efforts are needed to unveil the interactions of dopants and carbon support during the carbonization process and correlate these structural features with their electrocatalytic activity. Considering these catalysts' relatively low surface area, the next step could improve the surface area to unlock the full catalytic potential. This work addresses the factors that consider the oxidation states influence of precursors in the electrocatalyst design. It provides a new perspective on understanding the catalytic active sites.

Chapter 6

MATERIALS CHARACTERISATION

This chapter will introduce the working principles of characterizations techniques applied in this thesis.

6.1 SCANNING ELECTRON MICROSCOPE (SEM)

Scanning electron microscopy (SEM) relies on measuring the secondary or backscattered electrons emitted from samples (**Figure 6.1a**). During the operation, an electron beam (beam accelerated at 1 - 30 kV) is emitted and accelerated to pass through the condenser lens, aperture, deflector coils, and objective lens and finally hit the samples' surface.[248] Then, secondary and backscattered electrons emitted from samples will be captured by the detector, followed by a reconstruction of signals to obtain the topographic and composition of the samples. The magnifications that SEM could offer could reach 1 - 2 million times. SEM characterization was conducted on Zeiss Leo Gemini 1525. Pellet samples were cut into pieces to measure the cross-section and top morphology and attached on the conductive tape. For all samples, 10 nm gold coating was also applied to obtain a better resolution.

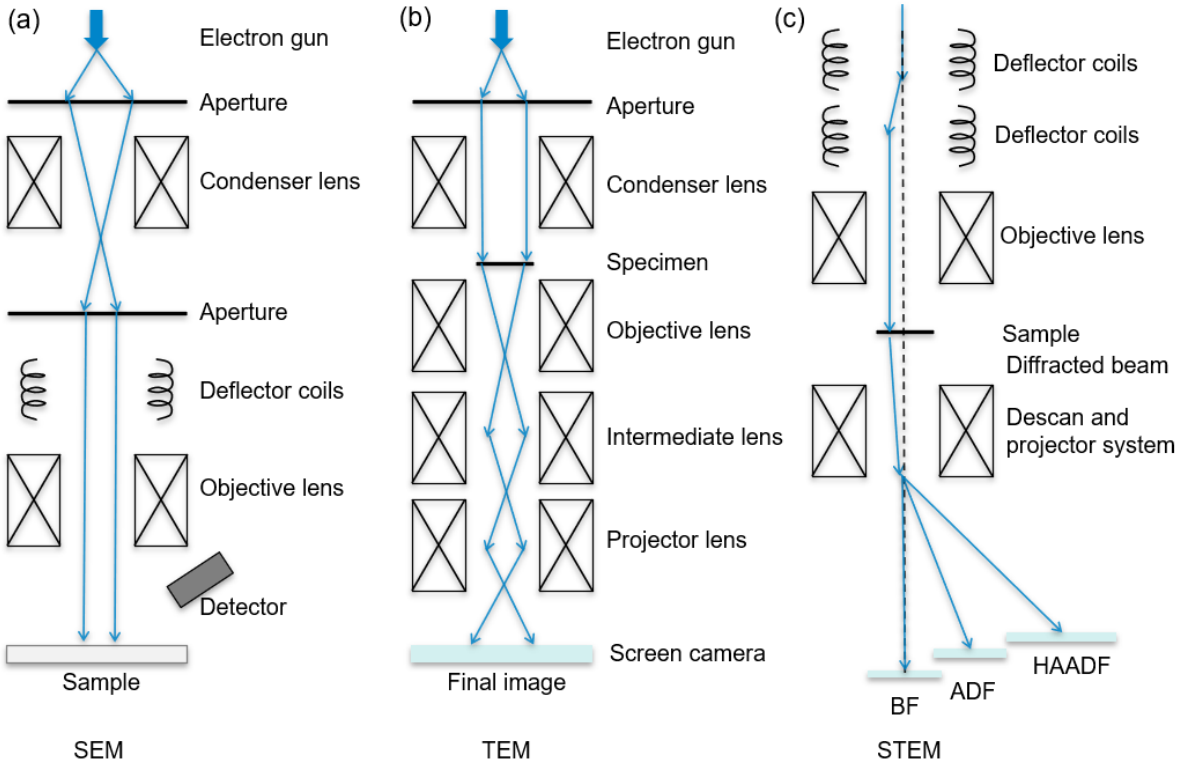

Figure 6.1 Schematic working principles of (a) SEM (b)TEM, and (c) STEM.

6.2 TRANSMISSION ELECTRON MICROSCOPE (TEM)

A transmission electron microscope (TEM) collects high energy electrons to gain a 2D image of the samples (**Figure 6.1b**). The beam from TEM could be accelerated at 60 – 300 kV,[249], giving users more than 50 million times magnification. To reveal the atomic structure, high-resolution transmission electron microscopy (HRTEM) could be applied. The high resolution of HRTEM is based on the phase shift of the atoms. Scanning transmission electron microscopy (STEM) encodes the spatial information which could get atomic-scale properties. The detection (**Figure 6.1c**) could be divided into bright field (BF), annular dark field (ADF), and high-angle annular dark-field (HAADF), where HAADF is the most common technique. The image contrast in HAADF is mainly from incoherent elastically scattered electrons.[248, 250]

HRTEM was conducted on all the electrode samples at an operating voltage of 300 kV. The samples were dispersed in ethanol and sonicated for 10 minutes, then cast onto lacey carbon mesh copper grids (Agar Scientific, Lacey carbon film 400 Cu). The grids were then placed in

a vacuum desiccator to assist the solvent's evaporation overnight before loading onto the TEM sample holder. The HAADF STEM imaging and EDS elemental mapping were performed using a Thermo Fisher Titan STEM (G2 80-200) equipped with a Cs probe corrector (CEOS), a ChemiSTEM Super-X E.D.X. detector and a HAADF detector operating with an inner angle of 55 mrad at 200 kV. The incident electron beam convergence angle was 21 mrad.

6.3 X-RAY ABSORPTION SPECTROSCOPY (XAS)

Studying nanostructure or even atomic structure is the key to understanding the catalytic process. X-ray absorption spectroscopy (XAS) has been a powerful tool to characterize catalysts to give nanoscale. An accelerated high energy X-rays shoot directly to the samples, and some X-rays are absorbed by the atoms in the sample, causing the excitation or ejection of a core electron. The energy edge we usually described formed at specific energy to excite an electron in the atoms. For example, ~ 7112 eV to excite an electron in the 1 s orbital of iron caused an edge form due to the sudden energy change. XAS contains two main segments – X-ray absorption near edge structure (XANES) gives geometry and oxidation state information of the catalysts (**Figure 6.2b**) and extended. X-ray absorption fine structure (EXAFS) gives neighbouring atoms information (**Figure 6.2c**).

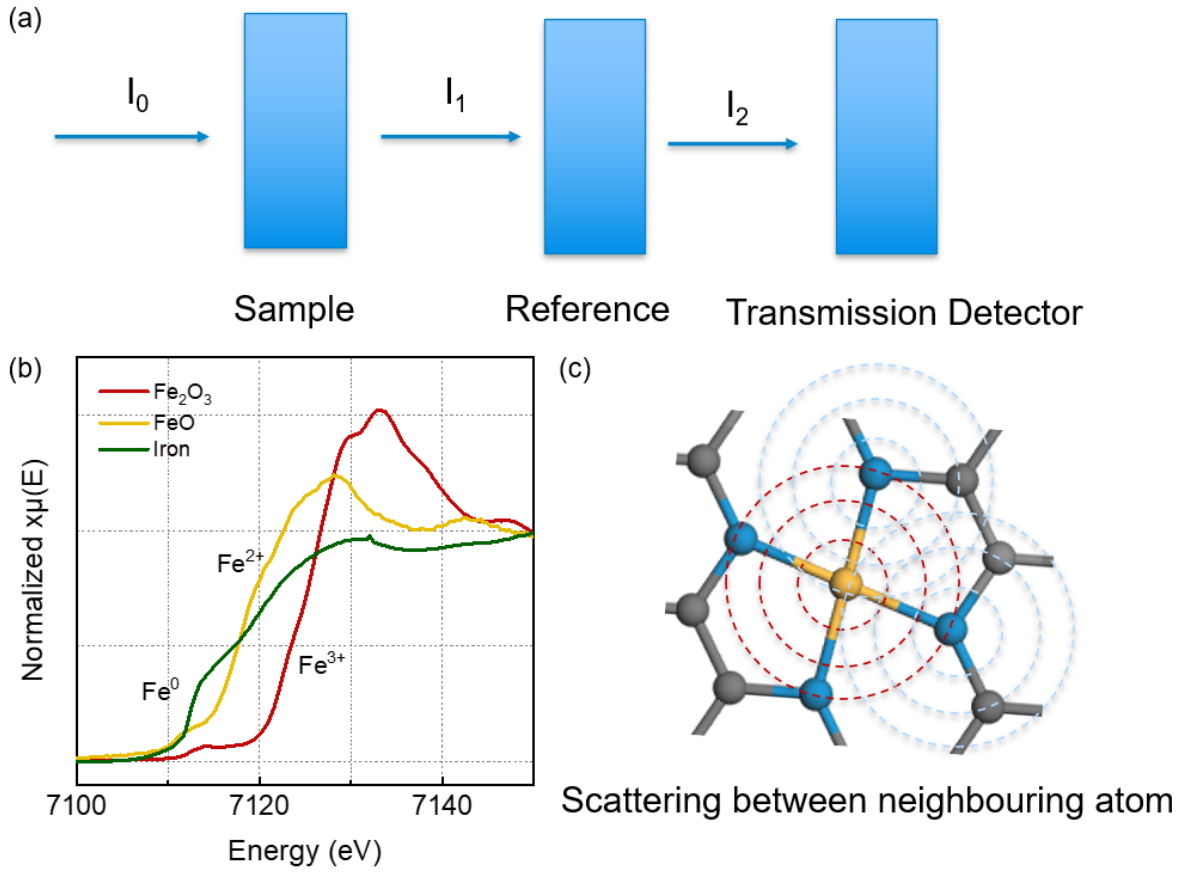

Figure 6.2 (a) schematic of beam going through samples with input intensity I_0, and output intensity I_1. (b) XANES region of the XAS, information such as different species and oxidation states could be obtained. (c) Schematic of the scattering between the centre atom and neighbour atoms.

EXAFS could provide the local coordination environments originating from the scattering between the central atom and the neighbour atoms. The absorption coefficient *μ(E)*, can be obtained the intensity of the beam before (I_0) and after (I_1) transmitting the samples:

$$\mu(\mathrm{E}) = \ln (I_0/I_1)$$

Caused by the scattering between atoms, oscillations of the energy to the energy of the absorption edge could be obtained.

$$\chi(\mathrm{E}) = (\mu(\mathrm{E}) - \mu_0(\mathrm{E}))/\mu_0(\mathrm{E})$$

Herein, a wavenumber k is defined as:

$$k = \frac{1}{\hbar}\sqrt{2m_e(E - E_0)}$$

Where m_e is the mass of an electron, $\hbar$ is plank constant, E is the energy of the incident photon, E_0 is the energy of the absorption edge. k ($k = \frac{2\pi}{\lambda}$) could be derived from by substituting the wavelength ($\lambda = \frac{\hbar}{p}$, where p is the momentum of the electron; $T = \frac{p2}{2m_e}$, where T is the kinetic energy of the photoelectron; besides $T = E - E_0$) into the wavenumber. Furthermore, the probability of absorption $\chi \propto \cos\left(2\pi\frac{2D}{\lambda}\right)$ where D is the distance from the absorbing atom to the scattering atom, taking k and scattering properties of the neighbouring atoms, we could obtain[251]:

$$\chi(k) = f(k)\cos\left(2\pi\frac{2D}{\lambda}\right)$$

However, several factors need to be added to make $\chi(k)$ represent the scattering probability better, such as multiple neighbouring atoms, phase shift, spherical waves, inelastic scattering, in which the absorbing atom is not the same as the initial state. Therefore, the following equation was obtained to describe $\chi(k)$:[251]

$$\chi(k) = S_0^2 \sum_i Ni\frac{f_i(k)}{kD_i 2} e^{-\frac{2Di}{\lambda k}} e^{-2k2\sigma^2} sin(2kD_i + \delta i(k))$$

Where S_0^2 D is the amplitude reduction factor, D is the absorber-scatter distance (half path length), N is degeneracy (coordination number), and σ^2 is the mean square relative displacement (Debye-Waller factor).[251]

XAS *sample preparation:* To obtain a good XAS signal, 15 - 20mg samples (85 - 90 wt%) were well mixed with 1.5 - 3 mg (10-15 wt%) cellulose and pressed into 5 mm pellet with a thickness of 0.5 – 1 mm, 5 microliters of DI water was added into the mixture before pelleting to help maintain the pellet structure. *XAS analysis:* XAS measurements were performed at beamline B18 of Diamond Light Source in transmission and fluorescence mode using Stern-

Heald geometry using ion chambers. Transmission mode data were used due to their superior quality. The data were normalised to the incoming incident energy and processed with the Athena software. An E_0 value of 7112.0 eV was used to calibrate all data to the first inflexion point of the absorption K-edge of an Fe foil. EXAFS curve fitting was performed with Artemis. Fe-N_4-C structure was built, and geometry optimised using Dmol3. The optimised structures were calculated through FEFF 8 to obtain the paths.

The EXAFS spectra were obtained by subtracting pre-edge and post-edge background from the overall absorption and then normalising to the edge step. Subsequently, the $\chi(k)$ data of 3.0 to 10 A^{-1} was used for Fourier transformed to real R space using a Hanning window (dk = 1.0 $Å^{-1}$) to separate the EXAFS contributions from different coordination shells. To obtain the quantitative structural parameters around central atoms, least-squares curve parameter fitting was performed using the ARTEMIS module of IFEFFIT software packages. The addition of a shell in EXAFS modelling was justified by significantly lowering the reduced chi-square value. $S0^2 = 0.85 \pm 0.03$ was obtained by fixing the coordination number of powdered Fe standards to their known crystallographic structure.

6.4 X-RAY PHOTOELECTRON SPECTROSCOPY (XPS)

X-ray photoelectron spectroscopy (XPS) is the most popular characterization to study the surface chemistry of materials. Monoenergetic X-rays are used to irradiate the materials. The incoming photon reacts with the materials, followed by the emitting of photoelectrons from the materials. A detector is applied to measure the kinetic energies of the emitted photoelectrons. Based on the kinetic energies of the emitted photoelectrons, both the type and the amount of the surface element could be determined. The energy loss is enormous during photoelectron transfer to the material's surface, and only near-surface photoelectrons can be detected. Therefore, the XPS has high surface sensitivity, where the characterized depth could be 5-10 nm).[252, 253]

XPS analysis was performed using a Thermo Scientific Nexsa XPS system with a monochromatic Al K*a* X-ray source. Samples were placed on the copper tape and vacuumed overnight before performing in the machine. The data was analysed using Thermo Avantage software, and deconvolution of the spectrums were conducted. Specifically, C1s spectrums could be deconvoluted into graphitic carbon (C-$C_{primary}$), defective carbons in five-member rings (C-C_{low}), carbon in more than six-member ring (C-C_{high})/carbon bonded to N in pyridinic, pyrrolic in both defect and defect-free regions (C_{sp2}-N), ether ground found in esters and lactone (C-O)/graphitic nitrogen in aromatics (C_{sp3}-N) / nitrogen oxides (C-N=O), pyridine, amide/carbonyl groups (C=O/N-(C_{sp2}=O)/N-C(O)-C). N1s spectrums could be deconvoluted into the pyridinic group in aromatics (C=N-C), pyrrolic group in aromatics (C-(NH)-C), graphitic nitrogen in aromatics (C-(NC)-C), nitrogen oxides (O=N-C), and pyridone (O=CNC)/amine group (H-N-H). O1s spectrums could be deconvoluted into C=O, O-C aliphatic, O-C aromatics N, oxygen bonded to nitrogen, and water due to the moisture content.

6.5 GAS SORPTION MEASUREMENT

Nitrogen physical adsorption is applied to determine the specific surface area and pore size distribution of the materials. The test performs at 77 K for the physical nitrogen adsorption, and the whole testing tube is under pressure. At the lowest pressure, nitrogen is first adsorbed into the microstructures in the materials and forms a single layer of nitrogen molecules on the surface of the nanostructures. As the pressure increases, multiple layers form, and bigger pores of the materials will also be filled. Based on the Brunauer-Emmett and Teller theory (BET), the specific surface area could be calculated.[254] The pore size distribution could also be obtained via non-local density functional theory (NLDFT), which assumes that all pores and surfaces are homogeneous.[255]

Nitrogen physical adsorptions were conducted at −196 °C in the Micromeritics 3Flex system. Powder samples were wrapped into aluminium foil. Pellet samples were analysed without

aluminium foil. All samples were degassed under 200 °C for 17 hours to remove all residue moisture, and samples mass were weighed by microbalance. The BET surface area was deduced from an isotherm analysis in the relative pressure range of 0.0002−0.02. The total pore volume was calculated from the amount of nitrogen adsorbed at a relative pressure of 0.98. The pore size distribution was calculated by the HS-2D-NLDFT_Carbon_N2_77 method using adsorption and desorption parts of the isothermal data.

6.6 X-RAY DIFFRACTOMETER (XRD)

X-ray diffraction (XRD) was used to study the crystalline structure of materials. Based on the constructive interference of monochromatic X-rays and the crystallinity structure of the samples, crystallinity information of the samples could be obtained.[256]

XRD patterns of obtained samples were measured with a powder X-ray diffractometer (XRD PANanalytical's X'PERTPRO) with Ni-filters Cu Ka radiation (λ_1 = 1.5406 Å and λ_2 = 1.5444 Å) and an X'Celerator multistrip detector). The scanned two theta ranges from 10° to 85° at 3° min^{-1}. Powder/pellet samples were placed on a sample holder while analysing. To reduce the noise in the final signal, the sample holder was rotating at 90° per second.

6.7 SMALL ANGLE X-RAY SCATTERING (SAXS)

Samples in Chapter 3 was performed on a SAXSpoint 2.0 instrument, using Cu-Kα radiation with a wavelength of 1.541 Å. Samples were loaded to powder sample holders with a Kapton window for beam transmission. Scattered X-rays were detected by a 2D areal detector (Eiger R 1M, Dectris, Baden, Switzerland) with a nominal sample-to-detector distance of 561 mm. Data was collected as a stack of 3 * 5min frames and averaged. The 2D patterns were reduced using SAXSanalysis software. The 1D SAXS profiles, as obtained upon azimuthal averaging of the 2D SAXS patterns, were used for analysis.

Samples in Chapter 4 and 5 were performed in I22, Diamond. Samples were loaded on to samples holder, and the samples test was performed in beamline I22, Diamond Light Source, UK. Beam energy was 12.4 keV with a wavelength of 1 A. The SAXS sample-detector distance was 5719.2 mm, and the WAXS sample-detector distance: 166.32 mm. Data was collected as a stack of 100 * 0.1 s frames and averaged.

A Porod method proposed by Stevens and Dahn[257] were employed to small-angle X-ray scattering (SAXS) data to probe the pore size of the carbon samples. The equation proposed by Stevens and Dahn is as follows:

$$I(q) = \frac{A}{q^a} + \frac{B_1 a_1^4}{(1 + a_1^2 q^2)^2} + D$$

Where I(q) is the scattered intensity as a function of q, A is a scale factor for the surface scattering at low q, proportional to the total surface area. B_1 is a scale factor for the pore scattering, proportional to the micropore surface area. D is a constant background, and a_1 is the characteristic length and associated with the radius of a spherical pore, by $R = a_1 \times \sqrt{10}$. Further, this equation can be modified so that B_2 becomes proportional to the number of pores by adding an a_1^2 term:

$$I(q) = \frac{A}{q^a} + \frac{B_2 a_1^6}{(1 + a_1^2 q^2)^2} + D$$

The A value and B_2 values fitted from the SAXS data represent the relative total surface area and relative amount of pores, respectively.

Furthermore, an additional term can be added with a different characteristic length a_2 if pores of an intermediate size are present, so the SAXS intensity can therefore be expressed by

$$I(q) = \frac{A'}{q^{a'}} + \frac{B_3 a_3^6}{(1 + a_3^2 q^2)^2} + \frac{C}{(1 + a_4^2 q^2)^2} + D$$

Where B_3 is now proportional to the total number of nanopores, and a_3 represent the size of nanopores. The C is proportional to the total surface area of the intermediate size pores, and a4 represent the characteristic length of the intermediate size pore.

6.8 RAMAN SPECTROSCOPY

Raman spectroscopy was performed on a 514 mm wavelength using a Senterra II spectrometer. When analysing, samples were placed on a glass slide, and the Raman spectra were collected between 500 cm^{-1} and 3000m^{-1}. The peak positions and the intensities were determined by the combination of Gaussian−Lorentzian line shapes in OriginPro 2020. The crystallite sizes (L_a) were calculated from the I_D/I_G via the following equation:

$$L_a = C_\lambda \cdot \frac{I_G}{I_D}$$

The C_λ value was calculated from Matthews et al.[258, 259], where $C_\lambda = 4.36$ for $\lambda = 514$ nm.

6.9 FOURIER TRANSFORM INFRARED (FTIR) SPECTROSCOPY

Fourier transform infrared (FTIR) spectroscopy was conducted on a Cary 630 FTIR spectrometer. The background signal was extracted before each sample scan, and the obtained spectrum was averaged over 16 scans between 700 cm^{-1} and 4000 cm^{-1}.

6.10 THERMOGRAVIMETRIC ANALYSIS (TGA)

Thermogravimetric analysis (TGA) was performed on TGA from TA instrument. 5-10 mg of samples were loaded for each run. Samples were heated to 1000 °C with 10 °C min^{-1} under air condition.

6.11 INDUCTIVELY COUPLED PLASMA MASS SPECTROMETRY (ICP-MS)

Inductively coupled plasma mass spectrometry (ICP-MS) is a powerful technique with high sensitivity to detect as low as parts-per-trillion level elements. Sample solutions were ionised into atomic and polyatomic ions by inductively coupled plasma, which was further sorted by

the mass-to-charge ratio (m/z) by mass spectrophotometer and detected by the ion detector. Standards with different ion concentrations of the targeted metals were used to calibrate the

ICP-MS characterizations were conducted by A Nu Instruments Nu Plasma multiple collectors inductively coupled plasma mass spectrometer. Before analysing, the carbon samples were carefully weighed and digested by aqua regia using a MARS 6 microwave at 1500 W for 20 min. The solutions were further filtered and diluted with 2 % HNO_3 and 1 % HCl to achieve a Fe < 500 ppb concentration. Standards iron solutions (10 ppb to 500 ppb) were tested to calibrate the ion concentration. For each sample, two duplicates were prepared for accuracy.

6.12 COMPUTED TOMOGRAPHY (CT)

Computed tomography (CT) was performed for one pellet sample in Electrochemical Innovation Lab, University College London. 3D images acquired were used to examine pore size distribution and the accessible pre to air. All X-ray imaging was conducted ex-situ on pellet samples directly using a ZEISS Xradia 520 Versa (Carl Zeiss Microscopy Inc., Pleasanton, USA) micro-CT system. X-ray CT scans were carried out with an X-ray source tube voltage of 60 kV− with an exposure time of 50 s per projection image, and a total of 1028 projection images were collected per scan using 40× magnification. Reconstruction of the radiographic data was achieved using a cone-beam filtered back-projection algorithm implemented in Zeiss Scout and Scan software resulting in a reconstructed voxel size (μm) of 0.203 × 0.203 × 0.203.

6.13 ELECTRON PARAMAGNETIC RESONANCE (EPR)

Electron paramagnetic resonance (EPR) measurements were performed at Imperial College London. Ca. 3-10 mg of sample was filled into a capillary with an inner diameter of 3 mm Wilmad® quartz (CFQ) EPR tubes (Sigma-Aldrich) that were weighed before and after filling to determine the precise mass of each sample. Continuous-wave (CW) EPR spectra were

recorded on an X-band CW ELEXSYS E500 EPR spectrometer (Bruker, Germany) equipped with a cryogen-free variable temperature cryostat (Oxford Instruments, Oxfordshire, UK). EPR spectra were recorded at ≈ 9.7 GHz under non-saturating Fe(III) conditions, corresponding to an incident microwave power of 2 mW (at 5 K). A magnetic field frequency of 100 kHz, modulation amplitude of 1 G, power attenuation of 20 dB and receiver gain 75 dB were used with the external magnetic field sweeping in 1190 steps from 5 to 600 mT. For non-Lorentzian lines observed in the EPR spectra, one should use the turning point to evaluate the effective g values.

6.14 ELECTROCHEMICAL CHARACTERIZATIONS

Rotating disk electrode (RDE) test. Inks containing the different catalysts were prepared for RDE testing to evaluate their performance for oxygen reduction reaction (ORR) catalysis. 8 mg of catalyst powder (pellet samples were ground into the powder by pestle and motor) was weighed and mixed with 1400 µl of deionised (DI) water, 528 µl of EtOH and 72 µl of 5 wt% Nafion©D-521 dispersion in water and 1-propanol (Alfa Aesar). The Nafion© dispersion was used as a binder for the components of the ink. The inks were then placed in a bath sonicator for 10 minutes before undergoing ultrasonic liquid processing in a probe sonicator (Fisherbrand model 705, U.S.A.) for 10 minutes per sample, under a 5 seconds on and 5 seconds off regime. The working electrodes were then prepared by pipetting 5 µl of the inks onto a polished glassy carbon electrode of diameter 3 mm, resulting in a catalyst loading of 0.28 mg cm^{-2}. The catalyst modified electrodes were left rotating at 700 rpm for 1 hour to dry at room temperature before electrochemical testing. A commercial 60 wt% Pt/C (JM HiSPEC 9100) working electrode was prepared in the same way, using 1 mg of Pt/C instead of 8 mg, which resulted in a Pt loading of 0.021 mg cm^{-2}. Electrochemical tests were conducted in alkaline (50 ml 0.1 M KOH, 99.995% suprapur) conditions for comparison purposes in a three-electrode system, with the continuous bubbling of oxygen (N5.8) through the electrolytes. The electrochemical data was gathered at

room temperature and ambient pressure on an RDE system using an AUTOLAB PGSTAT 101 and a MULTI AUTOLAB M101. The configuration included a three-electrode system formed of a glassy carbon 3 mm diameter RDE working electrode, a platinum rod as the counter electrode, and the 3 M Saturated KCl Ag/AgCl electrode (Ag/AgCl) as the reference electrode. Cyclic voltammetry (CV) curves were acquired by cycling the potential after purging O_2 for 30 minutes. Linear sweep voltammograms (LSV) were acquired at an electrode rotation speed of 1600 rpm with a scan rate of 10 mV s^{-1} in an O_2-saturated solution unless stated otherwise. The potentials recorded against Ag/AgCl in these experiments were converted to the potential vs reference hydrogen electrode (RHE) by using the following derivative of the Nernst equation:

$$E_{RHE} = E_{Ag/AgCl} + 0.059pH + E^{\circ}_{Ag/AgCl}$$

$E_{Ag/AgCl}$ was the potential measured with respect to Ag/AgCl and $E^{\circ}_{Ag/AgCl}$ is 0.21 V at 20 °C.

For chapter 5: The configuration included a three-electrode system formed of a glassy carbon 5 mm diameter RDE working electrode, a graphite rod as the counter electrode, and the Hg/HgO as the reference electrode. Cyclic voltammetry (CV) curves were acquired by cycling the potential after purging O_2 for 30 minutes. Linear sweep voltammograms (LSV) were acquired at an electrode rotation speed of 1600 rpm with a scan rate of 10 mV s^{-1} in an O_2-saturated solution unless stated otherwise. The potentials have been converted to a reversible hydrogen electrode (RHE) by following a calibration method reported.[260]

For the ring rotating disk electrode (RRDE) tests, the same method and ink preparation as RDE was applied. The working electrode was 5 mm GC disk with a Pt ring electrode at 375 μm gap. 14 μL of the slurry was deposited onto the GC disk of RRDE to make the same mass loading per unit area as RDE. The electron transfer number n and H_2O_2 yield were calculated via the following equation：

$$n = \frac{4I_D}{I_D + (I_R / N)}$$

$$H_2O_2\% = 100 \times \frac{2I_R / N}{I_D + (I_R / N)}$$

Where I_D represents the current collected from the disk, I_R represents the current collected from the Pt ring, N represents the collect efficiency determined by the structure of RRDE (N = 0.249, was provided by the manufacturer).

Freestanding electrode characterisations. To test the freestanding electrode without breaking it into the powder and keep the macro hierarchical porous structure, the pellet samples were tested in a freestanding electrode that mimics the rotating disk electrode. It was loaded onto the freestanding tip directly by screwing it onto the electrode, as shown in the scheme below. The freestanding tip consists of PEEK outer shell, stainless steel (ORR non-active, LSV curves could be found in Figure) was applied as a current collector.

Solid-state Zn-air batteries were assembly and characterised. A polished zinc foil (0.10 mm thickness) was used as the anode. The gel polymer electrolyte was prepared as follows: 1.0 g polyvinyl alcohol (PVA) powder (MW 19500, Aladdin) was dissolved in 10.0 mL deionised water at 95 ºC under magnetic stirring for 2.0 h. Then, the 1.0 mL of 18.0 M KOH filled with 0.10 M ZnCl2 (dissolved in KOH to form zincate, $Zn(OH)_4^{2-}$) was added electrolyte solution was kept stirring at 95 ºC for 40 min. Then the solution was a freeze at -5 ºC over 12 h and then thawed at room temperature. The procedure was repeated twice to gelate the PVA robustly. The primary solid-state Zn-air battery was then assembled with an air electrode and zinc foil placed on the two sides of PVA gel.

6.15 GDE FABRICATION AND ANION EXCHANGE MEMBRANE FUEL CELLS (AEMFC)

For the anode gas diffusion electrode (GDE), a PtRu/C (Alfa Aesar, Johnson Matthey HiSpec 12100, 50 wt% Pt and 25 wt% Ru) catalyst and the ETFE-g-poly (VBTMAC) ionomer powder (IEC = 1.24 ± 0.06 mmol/g), 20 wt% of the total solid mass, were mixed using H_2O: IPA (1:1) as solvent. This catalyst ink was homogenised with ultrasound for 30 min, then sprayed onto a Freudenberg H23C8 carbon paper gas diffusion substrate with a microporous layer using an ultrasonic automatised coated system (ExactaCoat, Sono-Tek). For the cathode G.D.E., Fe^{2+}@NCS-A was used as a catalyst instead. The geometric surface areas of all GDEs were 5.0 cm^2, the loading for the anode was 0.70 mg_{PtRu} cm^{-2} and 2.0 mg_{cat} cm^{-2} for the cathode. The Anion Exchange Membrane (AEM) used in this work was a radiation-grafted low-density polyethylene (LDPE) film (25 μm, IEC = 2.87 ± 0.05 mmol g^{-1}) with covalently-bound cationic headgroups.[218, 261]

Both the anode, cathode GDEs and membrane were hydrated in DI water for 20 min and then soaked two times in aqueous 1.0 M KOH to remove impurities and ion exchange the quaternary ammonium hydroxide groups before cell assembly. AEMFCs with 5 cm^2 active area were assembled in single-cell hardware with a single channel serpentine flow field, using 4.5 N m torque (5 cm^2 fuel cell fixture supplied by Scribner, U.S.A.). The pitch was kept around 25 % of the total GDE thickness using Teflon gaskets. No prior hot-pressing of the membrane electrode assembly (MEA) was used.

An 850e fuel cell test station (Scribner Associates, U.S.A.) was used for testing. The fuel cell temperature was controlled at 60 °C. H_2 and O_2 gas feeds were supplied to the anode and cathode, respectively, with flow rates of 0.3 L min^{-1} (SLPM) with no back-pressurisation (RH = 100 %). The MEA was activated by discharging the cell at a constant voltage of 0.5 V during cell heating, retaining this cell voltage until a steady current density was observed. Beginning-

of-life AEMFC performance data were collected under controlled galvanostatic discharge steps where data (at each current density) was only recorded once the potentials had stabilised. The internal ohmic resistance was estimated using the 850e instrument's internal current interrupt method.

Chapter 7

CONCLUSION AND OUTLOOK

7.1 CONCLUSION REMARKS

The oxygen reduction reaction is the limiting step to convert hydrogen into electricity in the fuel cell, hindering its further application into the market. The design and synthesis of new electrocatalysts for the oxygen reduction reaction could accelerate the application of fuel cells. This research aims to synthesize freestanding electrodes that could be applied in fuel cells in a sustainable and low-cost way. A freestanding carbon electrode was proposed, and its active sites modulation was successfully carried out to improve its electrocatalytic performance. Besides, the influence of different iron precursors on the final catalysts was studied.

The main conclusions in this thesis include:

1. A facile, cost-effective, and scalable method was proposed to fabricate nitrogen-doped freestanding porous 3D carbon electrodes from glucose. The as-obtained carbon electrode showed superior stability and similar kinetic activity compared with powder samples. A primary solid Zn-air battery was assembled using the obtained pellet samples, which revealed its potential to serve as an air electrode.

2. The influence of carbonisation temperatures and pellet thickness were further studied Appendix 9.1). We concluded that the electrochemical performance of the carbon electrode was dominated by competition between the active sites and the total length of the electron transfer path. We have identified the case of NC800_50 as showing the lowest onset potential and highest limiting current. This is due to its high N content, high surface area, high graphitisation level and relatively thin thickness (less resistance).

These studies could help us control the pellet structures to meet the requirements of target applications, which could be suitable for broader applications.

3. The freestanding electrode with FeN_4 sites has been successfully synthesised via post-treatment of an N-doped freestanding electrode. The abundant micropore and nitrogen sites on the N doped pellet have provided sites for iron ions, leading to the formation of atomically dispersed Fe-N_4 sites. The incorporation of iron also increased the graphitisation degree and tuned the pore structure, resulting in improved catalytic performance in Fe@NC900_50 compared with no iron doping (NC900_50). Moreover, incorporating Fe sites in Fe@NC900_50 also improved the catalytic activity and stability, resulting in a high current density in Fe@NC900_50 in the freestanding CA test (current density nearly two times higher than NC900_50). Through ex-situ XAS in chapter 4, a decrease of the Fe-C/O coordination number could be seen with the potential decrease, which suggests that Fe is the active centre and is responsible for oxygen binding and reduction. Our results confirm that Fe-N sites are important for ORR activity.

4. Fe, N co-doped carbon sphere powder electrocatalysts (Fe@NCS-A) were synthesized via a facile, green, and scalable method. The majority of Fe species were found to exist in Fe-N_4 sites, with a minimal amount aggregated into Fe_3C nanoparticles and embedded inside the carbon sphere structure. The optimized Fe-N_4 sites have been successfully obtained by starting with different Fe precursors, with Fe^{2+}@NCS-A showing a better ORR and AEMFC activity and durability. For the formation mechanism of Fe-N_4 sites, we propose that the N content is key for preventing Fe aggregation. At the same time, the starting precursor and carbonization conditions are essential for determining the final configuration of the Fe-N_4 sites. We have shown that iron precursors with different oxidation states can lead to variants in iron species, iron

sites' coordination numbers, and oxidation states in the final product, consequently influencing the final catalytic performance. However, future efforts are needed to unveil the interactions of dopants and carbon support during the carbonization process and correlate these structural features with their electrocatalytic activity.

The main novelties in this thesis include:

1. To address the low conductivity and stability issues, a scalable freestanding carbon electrode was proposed. The pressing of nitrogen precursors and hydrothermal carbon provides abundant active sites, porosity, and conductivity.

2. The nitrogen-doped carbon pellet could serve as a versatile air electrode modified to fit targeted applications. This provides new perspectives for designing electrocatalysts based on carbon electrodes.

3. The special configuration of the carbon electrode makes it suitable for in-situ measurements, which provides new ways to study the reaction mechanism.

4. Comparing the oxidation states of iron precursors help us understand the formation mechanism of the Fe-N-C catalysts, which provides a new perspective on designing the active catalytic sites

7.2 OUTLOOK

For oxygen reduction reactions, the primary goals are to increase stability, improve performance, and reduce cost. The future works could carry on from the following sections:

1. Optimizing the structure of the freestanding electrode to increase the mass transfer.

2. Maximum the iron loading for the pellet via either increasing the nitrogen amount or modifying the heat treatment procedure seems to be efficient ways to increasing the catalytic activity.

3. Validate the carbon electrode in a mini fuel cell could be its first step towards application. However, it is challenging to design the mini cell configuration to fit the electrode.

4. To further check the difference of the active sites from different iron precursors, Mossbauer or in-situ XAS during samples pyrolysis could be applied to understand the evolution of the iron sites.

Chapter 8

BIBLIOGRAPHY

1. Agency, I. E. *World Energy Outlook 2020*; IEA: Paris, 2020.

2. Oreskes, N., The Scientific Consensus on Climate Change. *Science* **2004,** *306* (5702), 1686-1686.

3. Bednaršek, N.; Tarling, G. A.; Bakker, D. C. E.; Fielding, S.; Jones, E. M.; Venables, H. J.; Ward, P.; Kuzirian, A.; Lézé, B.; Feely, R. A.; Murphy, E. J., Extensive dissolution of live pteropods in the Southern Ocean. *Nature Geoscience* **2012,** *5* (12), 881-885.

4. Change, I. P. o. C. *Global Warming of 1.5°C.An IPCC Special Report on the impacts of global warming of 1.5°C above pre-industrial levels and related global greenhouse gas emission pathways, in the context of strengthening the global response to the threat of climate change, sustainable development, and efforts to eradicate poverty*; 2018.

5. Orr, J. C.; Fabry, V. J.; Aumont, O.; Bopp, L.; Doney, S. C.; Feely, R. A.; Gnanadesikan, A.; Gruber, N.; Ishida, A.; Joos, F.; Key, R. M.; Lindsay, K.; Maier-Reimer, E.; Matear, R.; Monfray, P.; Mouchet, A.; Najjar, R. G.; Plattner, G. K.; Rodgers, K. B.; Sabine, C. L.; Sarmiento, J. L.; Schlitzer, R.; Slater, R. D.; Totterdell, I. J.; Weirig, M. F.; Yamanaka, Y.; Yool, A., Anthropogenic ocean acidification over the twenty-first century and its impact on calcifying organisms. *Nature* **2005,** *437* (7059), 681-6.

6. Bonan, G. B., Forests and Climate Change: Forcings, Feedbacks, and the Climate Benefits of Forests. *Science* **2008,** *320* (5882), 1444-1449.

7. Dessler, A. E.; Zhang, Z.; Yang, P., Water-vapor climate feedback inferred from climate fluctuations, 2003–2008. *Geophys Res Lett* **2008,** *35* (20).

8. Bellerby, R. G. J., Ocean acidification without borders. *Nature Climate Change* **2017,** *7* (4), 241-242.

9. Dore, J. E.; Lukas, R.; Sadler, D. W.; Church, M. J.; Karl, D. M., Physical and biogeochemical modulation of ocean acidification in the central North Pacific. *Proceedings of the National Academy of Sciences* **2009,** *106* (30), 12235-12240.

10. Agency, I. E. *Net Zero by 2050 - A Roadmap for the Global Energy Sector*; 2021.

11. Nations, U. *Paris Agreement*; 2015.

12. Trends in atmospheric carbon dioxide. https://gml.noaa.gov/ccgg/trends/mlo.html.

13. Commission, E. *Final report of the High-Level Panel of the European Decarbonisation Pathways Initiative*; Publications Office of the EU: Luxembourg, 2018.

14. Smil, V., *Energy: A Beginner's Guide*. Oneworld Publications: 2006.

15. Archer, C. L.; Jacobson, M. Z., Evaluation of global wind power. *Journal of Geophysical Research: Atmospheres* **2005,** *110* (D12).

16. Agency, I. E. *Technology Roadmap Hydrogen and Fuel Cells*; 2015.

17. Díaz-González, F.; Sumper, A.; Gomis-Bellmunt, O.; Villafáfila-Robles, R., A review of energy storage technologies for wind power applications. *Renewable and Sustainable Energy Reviews* **2012,** *16* (4), 2154-2171.

18. Chen, H.; Cong, T. N.; Yang, W.; Tan, C.; Li, Y.; Ding, Y., Progress in electrical energy storage system: A critical review. *Prog Nat Sci* **2009,** *19* (3), 291-312.

19. Cano, Z. P.; Banham, D.; Ye, S.; Hintennach, A.; Lu, J.; Fowler, M.; Chen, Z., Batteries and fuel cells for emerging electric vehicle markets. *Nat Energy* **2018,** *3* (4), 279-289.

20. Tseng, P.; Lee, J.; Friley, P., A hydrogen economy: opportunities and challenges. *Energy* **2005,** *30* (14), 2703-2720.

21. Winter, M.; Brodd, R. J., What Are Batteries, Fuel Cells, and Supercapacitors? *Chem Rev* **2004,** *104* (10), 4245-4270.

22. Grove, W. R., XXIV. On voltaic series and the combination of gases by platinum. *The London, Edinburgh, and Dublin Philosophical Magazine and Journal of Science* **1839,** *14* (86-87), 127-130.

23. Grove, W. R., LXXII. On a gaseous voltaic battery. *The London, Edinburgh, and Dublin Philosophical Magazine and Journal of Science* **1842,** *21* (140), 417-420.

24. Thomas, S. J. M., W. R. GROVE, THE FUEL CELL AND THE HYDROGEN ECONOMY. 110-126.

25. Cifrain, M.; Kordesch, K., Hydrogen/oxygen (air) fuel cells with alkaline electrolytes. In *Handbook of Fuel Cells*, 2010.

26. Merle, G.; Wessling, M.; Nijmeijer, K., Anion exchange membranes for alkaline fuel cells: A review. *J Membrane Sci* **2011,** *377* (1), 1-35.

27. Kordesch, K.; Cifrain, M., A comparison between the alkaline fuel cell (AFC) and the polymer electrolyte membrane (PEM) fuel cell. In *Handbook of Fuel Cells*, 2010.

28. Firouzjaie, H. A.; Mustain, W. E., Catalytic Advantages, Challenges, and Priorities in Alkaline Membrane Fuel Cells. *ACS Catal* **2020,** *10* (1), 225-234.

29. Barbir, F., Chapter Ten - Fuel Cell Applications. In *PEM Fuel Cells (Second Edition)*, Barbir, F., Ed. Academic Press: Boston, 2013; pp 373-434.

30. Vogler, F.; Sattler, G., 3 - Hydrogen-fueled marine transportation. In *Compendium of Hydrogen Energy*, Ball, M.; Basile, A.; Veziroğlu, T. N., Eds. Woodhead Publishing: Oxford, 2016; pp 35-65.

31. Jörissen, L., APPLICATIONS – STATIONARY | Residential Energy Supply: Fuel Cells. In *Encyclopedia of Electrochemical Power Sources*, Garche, J., Ed. Elsevier: Amsterdam, 2009; pp 108-123.

32. Ferreira-Aparicio, P.; Conde, J. J.; Chaparro, A. M., 2 - Fundamentals and components of portable hydrogen fuel-cell systems. In *Portable Hydrogen Energy Systems*, Ferreira-Aparicio, P.; Chaparro, A. M., Eds. Academic Press: 2018; pp 15-39.

33. Bolognesi, S.; Cecconet, D.; Capodaglio, A. G., 5 - Agro-industrial wastewater treatment in microbial fuel cells. In *Integrated Microbial Fuel Cells for Wastewater Treatment*, Abbassi, R.; Yadav, A. K.; Khan, F.; Garaniya, V., Eds. Butterworth-Heinemann: 2020; pp 93-133.

34. Gillis, E.; O'Sullivan, J., Fuel Cells, Applications in Stationary Power Systems. In *Encyclopedia of Physical Science and Technology (Third Edition)*, Meyers, R. A., Ed. Academic Press: New York, 2003; pp 235-251.

35. Gangloff, J. J., Jr.; Kast, J.; Morrison, G.; Marcinkoski, J., Design Space Assessment of Hydrogen Storage Onboard Medium and Heavy Duty Fuel Cell Electric Trucks. *J. Electrochem. En. Conver. Stor.* **2017,** *14* (2).

36. Greeley, J.; Markovic, N. M., The road from animal electricity to green energy: combining experiment and theory in electrocatalysis. *Energy Environ Sci* **2012,** *5* (11), 9246-9256.

37. Cui, C.; Gan, L.; Heggen, M.; Rudi, S.; Strasser, P., Compositional segregation in shaped Pt alloy nanoparticles and their structural behaviour during electrocatalysis. *Nat Mater* **2013,** *12* (8), 765-771.

38. Survey, U. S. G., Mineral commodity summaries 2020. **2020**.

39. Whiston, M. M.; Azevedo, I. L.; Litster, S.; Whitefoot, K. S.; Samaras, C.; Whitacre, J. F., Expert assessments of the cost and expected future performance of proton exchange membrane fuel cells for vehicles. *Proceedings of the National Academy of Sciences* **2019,** *116* (11), 4899-4904.

40. Ma, Z.; Cano, Z. P.; Yu, A.; Chen, Z.; Jiang, G.; Fu, X.; Yang, L.; Wu, T.; Bai, Z.; Lu, J., Enhancing Oxygen Reduction Activity of Pt-based Electrocatalysts: From Theoretical Mechanisms to Practical Methods. *Angew Chem* **2020,** *59* (42), 18334-18348.

41. Thompson, S. T.; James, B. D.; Huya-Kouadio, J. M.; Houchins, C.; DeSantis, D. A.; Ahluwalia, R.; Wilson, A. R.; Kleen, G.; Papageorgopoulos, D., Direct hydrogen fuel cell electric vehicle cost analysis: System and high-volume manufacturing description, validation, and outlook. *J Power Sources* **2018,** *399*, 304-313.

42. Thompson, S. T.; Papageorgopoulos, D., Platinum group metal-free catalysts boost cost competitiveness of fuel cell vehicles. *Nat Catal* **2019,** *2* (7), 558-561.

43. Wroblowa, H. S.; Yen Chi, P.; Razumney, G., Electroreduction of oxygen: A new mechanistic criterion. *J Electroanal Chem Interf Electrochem* **1976,** *69* (2), 195-201.

44. Wang, X.; Li, Z.; Qu, Y.; Yuan, T.; Wang, W.; Wu, Y.; Li, Y., Review of Metal Catalysts for Oxygen Reduction Reaction: From Nanoscale Engineering to Atomic Design. *Chem* **2019,** *5* (6), 1486-1511.

45. Ramaswamy, N.; Mukerjee, S., Alkaline Anion-Exchange Membrane Fuel Cells: Challenges in Electrocatalysis and Interfacial Charge Transfer. *Chem Rev* **2019,** *119* (23), 11945-11979.

46. Nørskov, J. K.; Rossmeisl, J.; Logadottir, A.; Lindqvist, L.; Kitchin, J. R.; Bligaard, T.; Jónsson, H., Origin of the Overpotential for Oxygen Reduction at a Fuel-Cell Cathode. *The Journal of Physical Chemistry B* **2004,** *108* (46), 17886-17892.

47. Shen, J.; Meng, L.; Liu, Y.; Chen, C.; Zhu, Y.; Li, C., Preparation of Co–N carbon nanosheet oxygen electrode catalyst by controlled crystallization of cobalt salt precursors for all-solid-state Al–air battery. *RSC Adv* **2018,** *8* (39), 22193-22198.

48. Jiao, Y.; Zheng, Y.; Jaroniec, M.; Qiao, S. Z., Origin of the Electrocatalytic Oxygen Reduction Activity of Graphene-Based Catalysts: A Roadmap to Achieve the Best Performance. *J Am Chem Soc* **2014,** *136* (11), 4394-4403.

49. Yang, X.; Xia, D.; Kang, Y.; Du, H.; Kang, F.; Gan, L.; Li, J., Unveiling the Axial Hydroxyl Ligand on Fe N4 C Electrocatalysts and Its Impact on the pH-Dependent Oxygen Reduction Activities and Poisoning Kinetics. *Adv Sci* **2020,** *7* (12), 2000176.

50. Stamenkovic, V. R.; Mun, B. S.; Arenz, M.; Mayrhofer, K. J. J.; Lucas, C. A.; Wang, G.; Ross, P. N.; Markovic, N. M., Trends in electrocatalysis on extended and nanoscale Pt-bimetallic alloy surfaces. *Nat Mater* **2007,** *6* (3), 241-247.

51. Karlberg, G.; Rossmeisl, J.; Nørskov, J. K., Estimations of electric field effects on the oxygen reduction reaction based on the density functional theory. *Phys Chem Chem Phys* **2007,** *9* (37), 5158-5161.

52. Man, I. C.; Su, H.-Y.; Calle-Vallejo, F.; Hansen, H. A.; Martínez, J. I.; Inoglu, N. G.; Kitchin, J.; Jaramillo, T. F.; Nørskov, J. K.; Rossmeisl, J., Universality in Oxygen Evolution Electrocatalysis on Oxide Surfaces. *ChemCatChem* **2011,** *3* (7), 1159-1165.

53. Stephens, I. E. L.; Bondarenko, A. S.; Grønbjerg, U.; Rossmeisl, J.; Chorkendorff, I., Understanding the electrocatalysis of oxygen reduction on platinum and its alloys. *Energy Environ Sci* **2012,** *5* (5), 6744-6762.

54. Tang, C.; Wang, H.-F.; Zhang, Q., Multiscale Principles To Boost Reactivity in Gas-Involving Energy Electrocatalysis. *Accounts of Chemical Research* **2018,** *51* (4), 881-889.

55. Li, M.; Zhao, Z.; Cheng, T.; Fortunelli, A.; Chen, C.-Y.; Yu, R.; Zhang, Q.; Gu, L.; Merinov, B. V.; Lin, Z.; Zhu, E.; Yu, T.; Jia, Q.; Guo, J.; Zhang, L.; Goddard, W. A.; Huang, Y.; Duan, X., Ultrafine jagged platinum nanowires enable ultrahigh mass activity for the oxygen reduction reaction. *Science* **2016,** *354* (6318), 1414-1419.

56. Chen, C.; Kang, Y.; Huo, Z.; Zhu, Z.; Huang, W.; Xin, H. L.; Snyder, J. D.; Li, D.; Herron, J. A.; Mavrikakis, M.; Chi, M.; More, K. L.; Li, Y.; Markovic, N. M.; Somorjai, G. A.; Yang, P.; Stamenkovic, V. R., Highly crystalline multimetallic nanoframes with three-dimensional electrocatalytic surfaces. *Science* **2014,** *343* (6177), 1339-1343.

57. Liu, J.; Jiao, M.; Lu, L.; Barkholtz, H. M.; Li, Y.; Wang, Y.; Jiang, L.; Wu, Z.; Liu, D.-j.; Zhuang, L.; Ma, C.; Zeng, J.; Zhang, B.; Su, D.; Song, P.; Xing, W.; Xu, W.; Wang, Y.; Jiang, Z.; Sun, G., High performance platinum single atom electrocatalyst for oxygen reduction reaction. *Nat Commun* **2017,** *8* (1), 15938.

58. Chong, L.; Wen, J.; Kubal, J.; Sen, F. G.; Zou, J.; Greeley, J.; Chan, M.; Barkholtz, H.; Ding, W.; Liu, D.-J., Ultralow-loading platinum-cobalt fuel cell catalysts derived from imidazolate frameworks. *Science* **2018,** *362* (6420), 1276-1281.

59. Shen, A.; Zou, Y.; Wang, Q.; Dryfe, R. A. W.; Huang, X.; Dou, S.; Dai, L.; Wang, S., Oxygen Reduction Reaction in a Droplet on Graphite: Direct Evidence that the Edge Is More Active than the Basal Plane. *Angewandte Chemie* **2014,** *126* (40), 10980-10984.

60. Shen, A.; Zou, Y.; Wang, Q.; Dryfe, R. A. W.; Huang, X.; Dou, S.; Dai, L.; Wang, S., Oxygen Reduction Reaction in a Droplet on Graphite: Direct Evidence that the Edge Is More Active than the Basal Plane. *Angew Chem* **2014,** *53* (40), 10804-10808.

61. Jia, Y.; Chen, J.; Yao, X., Defect electrocatalytic mechanism: concept, topological structure and perspective. *Mater Chem Front* **2018,** *2* (7), 1250-1268.

62. Tao, L.; Wang, Q.; Dou, S.; Ma, Z.; Huo, J.; Wang, S.; Dai, L., Edge-rich and dopant-free graphene as a highly efficient metal-free electrocatalyst for the oxygen reduction reaction. *Chem Commun* **2016,** *52* (13), 2764-2767.

63. Yan, X.; Jia, Y.; Yao, X., Defects on carbons for electrocatalytic oxygen reduction. *Chem Soc Rev* **2018,** *47* (20), 7628-7658.

64. Li, L.; Yang, H.; Miao, J.; Zhang, L.; Wang, H.-Y.; Zeng, Z.; Huang, W.; Dong, X.; Liu, B., Unraveling Oxygen Evolution Reaction on Carbon-Based Electrocatalysts: Effect of Oxygen Doping on Adsorption of Oxygenated Intermediates. *ACS Energy Lett* **2017,** *2* (2), 294-300.

65. Tang, C.; Zhang, Q., Nanocarbon for Oxygen Reduction Electrocatalysis: Dopants, Edges, and Defects. *Adv Mater* **2017,** *29* (13), 1604103.

66. Yan, D.; Li, Y.; Huo, J.; Chen, R.; Dai, L.; Wang, S., Defect Chemistry of Nonprecious-Metal Electrocatalysts for Oxygen Reactions. *Adv Mater* **2017,** *29* (48), 1606459.

67. Jia, Y.; Zhang, L.; Du, A.; Gao, G.; Chen, J.; Yan, X.; Brown, C. L.; Yao, X., Defect Graphene as a Trifunctional Catalyst for Electrochemical Reactions. *Adv Mater* **2016,** *28* (43), 9532-9538.

68. Tao, L.; Qiao, M.; Jin, R.; Li, Y.; Xiao, Z.; Wang, Y.; Zhang, N.; Xie, C.; He, Q.; Jiang, D.; Yu, G.; Li, Y.; Wang, S., Bridging the Surface Charge and Catalytic Activity of a Defective Carbon Electrocatalyst. *Angew Chem* **2019,** *58* (4), 1019-1024.

69. Jiang, Y. F.; Yang, L. J.; Sun, T.; Zhao, J.; Lyu, Z. Y.; Zhuo, O.; Wang, X. Z.; Wu, Q.; Ma, J.; Hu, Z., Significant Contribution of Intrinsic Carbon Defects to Oxygen Reduction Activity. *ACS Catal* **2015,** *5* (11), 6707-6712.

70. Gong, K.; Du, F.; Xia, Z.; Durstock, M.; Dai, L., Nitrogen-Doped Carbon Nanotube Arrays with High Electrocatalytic Activity for Oxygen Reduction. *Science* **2009,** *323* (5915), 760-764.

71. Qu, L.; Liu, Y.; Baek, J.-B.; Dai, L., Nitrogen-Doped Graphene as Efficient Metal-Free Electrocatalyst for Oxygen Reduction in Fuel Cells. *ACS Nano* **2010,** *4* (3), 1321-1326.

72. Faisal, S. N.; Haque, E.; Noorbehesht, N.; Zhang, W.; Harris, A. T.; Church, Tamara L.; Minett, A. I., Pyridinic and graphitic nitrogen-rich graphene for high-performance supercapacitors and metal-free bifunctional electrocatalysts for ORR and OER. *RSC Adv* **2017,** *7* (29), 17950-17958.

73. Lai, L.; Potts, J. R.; Zhan, D.; Wang, L.; Poh, C. K.; Tang, C.; Gong, H.; Shen, Z.; Lin, J.; Ruoff, R. S., Exploration of the active center structure of nitrogen-doped graphene-based catalysts for oxygen reduction reaction. *Energy Environ Sci* **2012,** *5* (7), 7936-7942.

74. Guo, D.; Shibuya, R.; Akiba, C.; Saji, S.; Kondo, T.; Nakamura, J., Active sites of nitrogen-doped carbon materials for oxygen reduction reaction clarified using model catalysts. *Science* **2016,** *351* (6271), 361-365.

75. Yang, L.; Jiang, S.; Zhao, Y.; Zhu, L.; Chen, S.; Wang, X.; Wu, Q.; Ma, J.; Ma, Y.; Hu, Z., Boron-Doped Carbon Nanotubes as Metal-Free Electrocatalysts for the Oxygen Reduction Reaction. *Angew Chem* **2011,** *50* (31), 7132-7135.

76. Jeon, I.-Y.; Zhang, S.; Zhang, L.; Choi, H.-J.; Seo, J.-M.; Xia, Z.; Dai, L.; Baek, J.-B., Edge-Selectively Sulfurized Graphene Nanoplatelets as Efficient Metal-Free Electrocatalysts for Oxygen Reduction Reaction: The Electron Spin Effect. *Adv Mater* **2013,** *25* (42), 6138-6145.

77. Liu, Z.-W.; Peng, F.; Wang, H.-J.; Yu, H.; Zheng, W.-X.; Yang, J., Phosphorus-Doped Graphite Layers with High Electrocatalytic Activity for the O2 Reduction in an Alkaline Medium. *Angew Chem* **2011,** *50* (14), 3257-3261.

78. Yao, Z.; Nie, H.; Yang, Z.; Zhou, X.; Liu, Z.; Huang, S., Catalyst-free synthesis of iodine-doped graphenevia a facile thermal annealing process and its use for electrocatalytic oxygen reduction in an alkaline medium. *Chem Commun* **2012,** *48* (7), 1027-1029.

79. Jeon, I.-Y.; Choi, H.-J.; Choi, M.; Seo, J.-M.; Jung, S.-M.; Kim, M.-J.; Zhang, S.; Zhang, L.; Xia, Z.; Dai, L.; Park, N.; Baek, J.-B., Facile, scalable synthesis of edge-halogenated graphene nanoplatelets as efficient metal-free eletrocatalysts for oxygen reduction reaction. *Sci Rep* **2013,** *3*, 1810.

80. Wang , S.; Iyyamperumal , E.; Roy, A.; Xue, Y.; Yu, D.; Dai, L., Vertically Aligned BCN Nanotubes as Efficient Metal-Free Electrocatalysts for the Oxygen Reduction Reaction: A Synergetic Effect by Co-Doping with Boron and Nitrogen. *Angew Chem* **2011,** *50* (49), 11756-11760.

81. Zhang, J.; Zhao, Z.; Xia, Z.; Dai, L., A metal-free bifunctional electrocatalyst for oxygen reduction and oxygen evolution reactions. *Nat Nanotechnol* **2015,** *10* (5), 444.

82. Zhao, Y.; Yang, L.; Chen, S.; Wang, X.; Ma, Y.; Wu, Q.; Jiang, Y.; Qian, W.; Hu, Z., Can Boron and Nitrogen Co-doping Improve Oxygen Reduction Reaction Activity of Carbon Nanotubes? *J Am Chem Soc* **2013,** *135* (4), 1201-1204.

83. Tang, Z.; Pei, Z.; Wang, Z.; Li, H.; Zeng, J.; Ruan, Z.; Huang, Y.; Zhu, M.; Xue, Q.; Yu, J.; Zhi, C., Highly anisotropic, multichannel wood carbon with optimized heteroatom doping for supercapacitor and oxygen reduction reaction. *Carbon* **2018,** *130*, 532-543.

84. Peng, X.; Zhang, L.; Chen, Z.; Zhong, L.; Zhao, D.; Chi, X.; Zhao, X.; Li, L.; Lu, X.; Leng, K.; Liu, C.; Liu, W.; Tang, W.; Loh, K. P., Hierachically Porous Carbon Plates Derived from Wood as Bifunctional ORR/OER Electrodes. *Adv Mater* **2019,** *0* (0), 1900341.

85. Huang, X.; Shen, T.; Zhang, T.; Qiu, H.; Gu, X.; Ali, Z.; Hou, Y., Efficient Oxygen Reduction Catalysts of Porous Carbon Nanostructures Decorated with Transition Metal Species. *Adv Energy Mater* **2020,** *10* (11), 1900375.

86. Ou, H.; Wang, D.; Li, Y., How to select effective electrocatalysts: Nano or single atom? *Nano Select* **2020,** *n/a* (n/a), 492-511.

87. Du, L.; Zhang, G.; Liu, X.; Hassanpour, A.; Dubois, M.; Tavares, A. C.; Sun, S., Biomass-derived nonprecious metal catalysts for oxygen reduction reaction: The demand-oriented engineering of active sites and structures. *Carbon Energy* **2020,** *2* (4), 561-581.

88. Tang, C.; Chen, L.; Li, H.; Li, L.; Jiao, Y.; Zheng, Y.; Xu, H.; Davey, K.; Qiao, S.-Z., Tailoring Acidic Oxygen Reduction Selectivity on Single-Atom Catalysts via Modification of First and Second Coordination Spheres. *J Am Chem Soc* **2021,** *143* (20), 7819-7827.

89. Fei, H.; Dong, J.; Feng, Y.; Allen, C. S.; Wan, C.; Volosskiy, B.; Li, M.; Zhao, Z.; Wang, Y.; Sun, H.; An, P.; Chen, W.; Guo, Z.; Lee, C.; Chen, D.; Shakir, I.; Liu, M.; Hu, T.; Li, Y.; Kirkland, A. I.; Duan, X.; Huang, Y., General synthesis and definitive structural identification of MN4C4 single-atom catalysts with tunable electrocatalytic activities. *Nat Catal* **2018,** *1* (1), 63-72.

90. Setyowati, V. A.; Huang, H.-C.; Liu, C.-C.; Wang, C.-H., Effect of Iron Precursors on the Structure and Oxygen Reduction Activity of Iron–Nitrogen–Carbon Catalysts. *Electrochim Acta* **2016,** *211*, 933-940.

91. Oh, H.-S.; Kim, H., The role of transition metals in non-precious nitrogen-modified carbon-based electrocatalysts for oxygen reduction reaction. *J Power Sources* **2012,** *212*, 220-225.

92. Jasinski, R., A New Fuel Cell Cathode Catalyst. *Nature* **1964,** *201* (4925), 1212-1213.

93. Chen, Z. W.; Higgins, D.; Yu, A. P.; Zhang, L.; Zhang, J. J., A review on non-precious metal electrocatalysts for PEM fuel cells. *Energy Environ Sci* **2011,** *4* (9), 3167-3192.

94. Bing, Y.; Liu, H.; Zhang, L.; Ghosh, D.; Zhang, J., Nanostructured Pt-alloy electrocatalysts for PEM fuel cell oxygen reduction reaction. *Chem Soc Rev* **2010,** *39* (6), 2184-2202.

95. Zhang, C.; Zhang, W.; Zheng, W., Transition Metal-Nitrogen-Carbon Active Site for Oxygen Reduction Electrocatalysis: Beyond the Fascinations of TM-N4. *ChemCatChem* **2019,** *11* (2), 655-668.

96. Chen, Y.; Matanovic, I.; Weiler, E.; Atanassov, P.; Artyushkova, K., Mechanism of Oxygen Reduction Reaction on Transition Metal–Nitrogen–Carbon Catalysts: Establishing the Role of Nitrogen-containing Active Sites. *ACS Appl Energy Mater* **2018,** *1* (11), 5948-5953.

97. Ramaswamy, N.; Tylus, U.; Jia, Q.; Mukerjee, S., Activity Descriptor Identification for Oxygen Reduction on Nonprecious Electrocatalysts: Linking Surface Science to Coordination Chemistry. *J Am Chem Soc* **2013,** *135* (41), 15443-15449.

98. Li, J.; Sougrati, M. T.; Zitolo, A.; Ablett, J. M.; Oğuz, I. C.; Mineva, T.; Matanovic, I.; Atanassov, P.; Huang, Y.; Zenyuk, I.; Di Cicco, A.; Kumar, K.; Dubau, L.; Maillard, F.; Dražić, G.; Jaouen, F., Identification of durable and non-durable FeNx sites in Fe–N–C materials for proton exchange membrane fuel cells. *Nat Catal* **2020,** *4* (1), 10-19.

99. Mao, K.; Yang, L.; Wang, X.; Wu, Q.; Hu, Z., Identifying Iron–Nitrogen/Carbon Active Structures for Oxygen Reduction Reaction under the Effect of Electrode Potential. *J Phys Chem Lett* **2020,** *11* (8), 2896-2901.

100. Li, J.; Jiao, L.; Wegener, E.; Richard, L. L.; Liu, E.; Zitolo, A.; Sougrati, M. T.; Mukerjee, S.; Zhao, Z.; Huang, Y.; Yang, F.; Zhong, S.; Xu, H.; Kropf, A. J.; Jaouen, F.; Myers, D. J.; Jia, Q., Evolution Pathway from Iron Compounds to Fe1(II)–N4 Sites through Gas-Phase Iron during Pyrolysis. *J Am Chem Soc* **2020,** *142* (3), 1417-1423.

101. Zhou, M.; Yang, C.; Chan, K.-Y., Structuring Porous Iron-Nitrogen-Doped Carbon in a Core/Shell Geometry for the Oxygen Reduction Reaction. *Adv Energy Mater* **2014,** *4* (18), 1400840.

102. Qiu, X.; Yan, X.; Pang, H.; Wang, J.; Sun, D.; Wei, S.; Xu, L.; Tang, Y., Isolated Fe Single Atomic Sites Anchored on Highly Steady Hollow Graphene Nanospheres as an Efficient Electrocatalyst for the Oxygen Reduction Reaction. *Adv Sci (Weinh)* **2019,** *6* (2), 1801103.

103. Qiao, M.; Ferrero, G. A.; Fernández Velasco, L.; Vern Hor, W.; Yang, Y.; Luo, H.; Lodewyckx, P.; Fuertes, A. B.; Sevilla, M.; Titirici, M.-M., Boosting the Oxygen Reduction Electrocatalytic Performance of Nonprecious Metal Nanocarbons via Triple Boundary Engineering Using Protic Ionic Liquids. *ACS Appl Mater Interfaces* **2019,** *11* (12), 11298-11305.

104. Cao, S.; Qu, T.; Li, Y.; Zhang, A.; Xue, L.; Zhao, Y.; Zheng, L.; Chen, A.; Shui, J., Electrocatalytically Active Hollow Carbon Nanospheres Derived from PS-b-P4VP Micelles. *Part Part Syst Char* **2018,** *35* (4), 1700404.

105. Zou, J.; Wang, B.; Zhu, B.; Yang, Y.; Han, W.; Dong, A., Fe, N, S-codoped carbon frameworks derived from nanocrystal superlattices towards enhanced oxygen reduction activity. *Nano Convergence* **2019,** *6* (1), 4.

106. Zhang, M.; Wang, C.; Luo, R.; Zhang, W.; Chen, S.; Yan, X.; Qi, J.; Sun, X.; Wang, L.; Li, J., A phenolic resin-assisted strategy for MOF-derived hierarchical Co/N-doped carbon rhombic dodecahedra for electrocatalysis. *J Mater Chem A* **2019,** *7* (10), 5173-5178.

107. Lai, Q.; Zhao, Y.; Zhu, J.; Liang, Y.; He, J.; Chen, J., Directly Anchoring Highly Dispersed Copper Sites on Nitrogen-Doped Carbon for Enhanced Oxygen Reduction Electrocatalysis. *ChemElectroChem* **2018,** *5* (14), 1822-1826.

108. Han, Y.; Wang, Y.-G.; Chen, W.; Xu, R.; Zheng, L.; Zhang, J.; Luo, J.; Shen, R.-A.; Zhu, Y.; Cheong, W.-C.; Chen, C.; Peng, Q.; Wang, D.; Li, Y., Hollow N-Doped Carbon Spheres with Isolated Cobalt Single Atomic Sites: Superior Electrocatalysts for Oxygen Reduction. *J Am Chem Soc* **2017,** *139* (48), 17269-17272.

109. Guo, F.; Yang, H.; Liu, L.; Han, Y.; Al-Enizi, A. M.; Nafady, A.; Kruger, P. E.; Telfer, S. G.; Ma, S., Hollow capsules of doped carbon incorporating metal@metal sulfide and metal@metal oxide core–shell nanoparticles derived from metal–organic framework composites for efficient oxygen electrocatalysis. *J Mater Chem A* **2019,** *7* (8), 3624-3631.

110. Wang, H.-F.; Tang, C.; Zhang, Q., A review of graphene-based 3D van der Waals hybrids and their energy applications. *Nano Today* **2019,** *25*, 27-37.

111. Soni, R.; Bhange, S. N.; Kurungot, S., 3-D Nanoribbon-Like Pt-Free Oxygen Reduction Reaction Electrocatalyst Derived from Waste Leather for Anion Exchange Membrane Fuel Cell and Zinc-Air Battery. *Nanoscale* **2019,** *11* (16), 7893-7902.

112. Yu, S.-H.; Lee, D. J.; Park, M.; Kwon, S. G.; Lee, H. S.; Jin, A.; Lee, K.-S.; Lee, J. E.; Oh, M. H.; Kang, K.; Sung, Y.-E.; Hyeon, T., Hybrid Cellular Nanosheets for High-Performance Lithium-Ion Battery Anodes. *J Am Chem Soc* **2015,** *137* (37), 11954-11961.

113. Wang, B.; Wang, X.; Zou, J.; Yan, Y.; Xie, S.; Hu, G.; Li, Y.; Dong, A., Simple-Cubic Carbon Frameworks with Atomically Dispersed Iron Dopants toward High-Efficiency Oxygen Reduction. *Nano Lett* **2017,** *17* (3), 2003-2009.

114. Li, L.; He, J.; Wang, Y.; Lv, X.; Gu, X.; Dai, P.; Liu, D.; Zhao, X., Metal–organic frameworks: a promising platform for constructing non-noble electrocatalysts for the oxygen-reduction reaction. *J Mater Chem A* **2019,** *7* (5), 1964-1988.

115. Wan, X.; Liu, X.; Li, Y.; Yu, R.; Zheng, L.; Yan, W.; Wang, H.; Xu, M.; Shui, J., Fe–N–C electrocatalyst with dense active sites and efficient mass transport for high-performance proton exchange membrane fuel cells. *Nature Catalysis* **2019**.

116. Li, X.; Ni, L.; Zhou, J.; Xu, L.; Lu, C.; Yang, G.; Ding, W.; Hou, W., Encapsulation of Fe nanoparticles into an N-doped carbon nanotube/nanosheet integrated hierarchical architecture as an efficient and ultrastable electrocatalyst for the oxygen reduction reaction. *Nanoscale* **2020,** *12* (26), 13987-13995.

117. Xu, H.; Wang, D.; Yang, P.; Liu, A.; Li, R.; Li, Y.; Xiao, L.; Ren, X.; Zhang, J.; An, M., Atomically dispersed M–N–C catalysts for the oxygen reduction reaction. *J Mater Chem A* **2020,** *8* (44), 23187-23201.

118. Zhang, Z.; Gao, X.; Dou, M.; Ji, J.; Wang, F., Biomass Derived N-Doped Porous Carbon Supported Single Fe Atoms as Superior Electrocatalysts for Oxygen Reduction. *Small* **2017,** *13* (22), 1604290.

119. Yang, G.; Zhang, Z.; Kang, X.; Li, L.; Li, Y.; Sun, Y., Fe–N–C Composite Catalyst Derived from Solid Digestate for the Oxygen Reduction Reaction in Microbial Fuel Cells. *ACS Appl Energy Mater* **2020,** *3* (12), 11929-11938.

120. Borghei, M.; Lehtonen, J.; Liu, L.; Rojas, O. J., Advanced Biomass-Derived Electrocatalysts for the Oxygen Reduction Reaction. *Adv Mater* **2018,** *30* (24), 1703691.

121. Liu, W.-J.; Jiang, H.; Yu, H.-Q., Emerging applications of biochar-based materials for energy storage and conversion. *Energy Environ Sci* **2019,** *12* (6), 1751-1779.

122. Guo, C.; Tong, X.; Guo, X.-Y., Nitrogen-doped mesoporous network-like carbon as an efficient metal-free electrocatalyst for oxygen reduction reaction. *Int J Hydrogen Energy* **2016,** *41* (48), 22941-22951.

123. Liu, X.; Amiinu, I. S.; Liu, S.; Cheng, K.; Mu, S., Transition metal/nitrogen dual-doped mesoporous graphene-like carbon nanosheets for the oxygen reduction and evolution reactions. *Nanoscale* **2016,** *8* (27), 13311-13320.

124. Zhang, X.; Yu, D.; Zhang, Y.; Guo, W.; Ma, X.; He, X., Nitrogen- and sulfur-doped carbon nanoplatelets via thermal annealing of alkaline lignin with urea as efficient electrocatalysts for oxygen reduction reaction. *RSC Adv* **2016,** *6* (106), 104183-104192.

125. Zhang, M.; Jin, X.; Wang, L.; Sun, M.; Tang, Y.; Chen, Y.; Sun, Y.; Yang, X.; Wan, P., Improving biomass-derived carbon by activation with nitrogen and cobalt for supercapacitors and oxygen reduction reaction. *Appl Surf Sci* **2017,** *411*, 251-260.

126. Chaudhari, K. N.; Song, M. Y.; Yu, J.-S., Transforming Hair into Heteroatom-Doped Carbon with High Surface Area. *Small* **2014,** *10* (13), 2625-2636.

127. Zhao, L.; Zhang, Y.; Huang, L.-B.; Liu, X.-Z.; Zhang, Q.-H.; He, C.; Wu, Z.-Y.; Zhang, L.-J.; Wu, J.; Yang, W.; Gu, L.; Hu, J.-S.; Wan, L.-J., Cascade anchoring strategy for general mass production of high-loading single-atomic metal-nitrogen catalysts. *Nat Commun* **2019,** *10* (1), 1278.

128. Biller, P.; Ross, A. B., 17 - Production of biofuels via hydrothermal conversion. In *Handbook of Biofuels Production (Second Edition)*, Luque, R.; Lin, C. S. K.; Wilson, K.; Clark, J., Eds. Woodhead Publishing: 2016; pp 509-547.

129. Bergius, F. *Nobel Lecture - Chemical reactions under high pressure*; 1932.

130. Titirici, M.-M.; White, R. J.; Falco, C.; Sevilla, M., Black perspectives for a green future: hydrothermal carbons for environment protection and energy storage. *Energy Environ Sci* **2012,** *5* (5), 6796-6822.

131. Titirici, M.-M.; White, R. J.; Brun, N.; Budarin, V. L.; Su, D. S.; del Monte, F.; Clark, J. H.; MacLachlan, M. J., Sustainable carbon materials. *Chem Soc Rev* **2015,** *44* (1), 250-290.

132. Sevilla, M.; Fuertes, A. B., The production of carbon materials by hydrothermal carbonization of cellulose. *Carbon* **2009,** *47* (9), 2281-2289.

133. Baccile, N.; Laurent, G.; Babonneau, F.; Fayon, F.; Titirici, M.-M.; Antonietti, M., Structural Characterization of Hydrothermal Carbon Spheres by Advanced Solid-State MAS 13C NMR Investigations. *J Phys Chem C* **2009,** *113* (22), 9644-9654.

134. Lu, X.; Pellechia, P. J.; Flora, J. R. V.; Berge, N. D., Influence of reaction time and temperature on product formation and characteristics associated with the hydrothermal carbonization of cellulose. *Bioresource Technol* **2013,** *138*, 180-190.

135. Shen, Y., A review on hydrothermal carbonization of biomass and plastic wastes to energy products. *Biomass Bioenergy* **2020,** *134*, 105479.

136. Higgins, L. J. R.; Brown, A. P.; Harrington, J. P.; Ross, A. B.; Kaulich, B.; Mishra, B., Evidence for a core-shell structure of hydrothermal carbon. *Carbon* **2020,** *161*, 423-431.

137. Higgins, L. J. R.; Sahle, C. J.; Balasubramanian, M.; Mishra, B., X-ray Raman scattering for bulk chemical and structural insight into green carbon. *Phys Chem Chem Phys* **2020,** *22* (33), 18435-18446.

138. Ding, Y.; Greiner, M.; Schlögl, R.; Heumann, S., A Metal-Free Electrode: From Biomass-Derived Carbon to Hydrogen. *ChemSusChem* **2020,** *13* (16), 4064-4068.

139. Qian, H.-S.; Yu, S.-H.; Luo, L.-B.; Gong, J.-Y.; Fei, L.-F.; Liu, X.-M., Synthesis of Uniform Te@Carbon-Rich Composite Nanocables with Photoluminescence Properties and Carbonaceous Nanofibers by the Hydrothermal Carbonization of Glucose. *Chem Mater* **2006,** *18* (8), 2102-2108.

140. White, R. J.; Tauer, K.; Antonietti, M.; Titirici, M.-M., Functional Hollow Carbon Nanospheres by Latex Templating. *J Am Chem Soc* **2010,** *132* (49), 17360-17363.

141. Fang, Z.; Tang, K.; Lei, S.; Li, T., CTAB-assisted hydrothermal synthesis of Ag/C nanostructures. *Nanotechnology* **2006,** *17* (12), 3008-3011.

142. Livage, J., Hydrothermal Synthesis of Nanostructured Vanadium Oxides. *Mater.* **2010,** *3* (8), 4175-4195.

143. Zhang, Z.; Yang, S.; Li, H.; Zan, Y.; Li, X.; Zhu, Y.; Dou, M.; Wang, F., Sustainable Carbonaceous Materials Derived from Biomass as Metal-Free Electrocatalysts. *Adv Mater* **2019,** *31* (13), 1805718.

144. Ma, Z.-Y.; Yu, Z.-L.; Xu, Z.-L.; Bu, L.-F.; Liu, H.-R.; Zhu, Y.-B.; Qin, B.; Ma, T.; Zhan, H.-J.; Xu, L.; Wu, H.-A.; Ding, H.; Yu, S.-H., Origin of Batch Hydrothermal Fluid Behavior and Its Influence on Nanomaterial Synthesis. *Matter* **2020,** *2* (5), 1270-1282.

145. Gasteiger, H. A.; Kocha, S. S.; Sompalli, B.; Wagner, F. T., Activity benchmarks and requirements for Pt, Pt-alloy, and non-Pt oxygen reduction catalysts for PEMFCs. *Appl Catal B Environ* **2005,** *56* (1), 9-35.

146. Chen, Y.; Ji, S.; Chen, C.; Peng, Q.; Wang, D.; Li, Y., Single-Atom Catalysts: Synthetic Strategies and Electrochemical Applications. *Joule* **2018,** *2* (7), 1242-1264.

147. Tian, L. L.; Yang, J.; Weng, M. Y.; Tan, R.; Zheng, J. X.; Chen, H. B.; Zhuang, Q. C.; Dai, L. M.; Pan, F., Fast Diffusion of O2 on Nitrogen-Doped Graphene to Enhance Oxygen Reduction and Its Application for High-Rate Zn-Air Batteries. *ACS Appl Mater Interfaces* **2017,** *9* (8), 7125-7130.

148. Fan, J.; Chen, M.; Zhao, Z.; Zhang, Z.; Ye, S.; Xu, S.; Wang, H.; Li, H., Bridging the gap between highly active oxygen reduction reaction catalysts and effective catalyst layers for proton exchange membrane fuel cells. *Nat Energy* **2021,** *6* (5), 475-486.

149. Schuler, T.; Chowdhury, A.; Freiberg, A. T.; Sneed, B.; Spingler, F. B.; Tucker, M. C.; More, K. L.; Radke, C. J.; Weber, A. Z., Fuel-Cell Catalyst-Layer Resistance via Hydrogen Limiting-Current Measurements. *J Electrochem Soc* **2019,** *166* (7), F3020-F3031.

150. Kongkanand, A.; Mathias, M. F., The Priority and Challenge of High-Power Performance of Low-Platinum Proton-Exchange Membrane Fuel Cells. *J Phys Chem Lett* **2016,** *7* (7), 1127-1137.

151. Ohma, A.; Mashio, T.; Sato, K.; Iden, H.; Ono, Y.; Sakai, K.; Akizuki, K.; Takaichi, S.; Shinohara, K., Analysis of proton exchange membrane fuel cell catalyst layers for reduction of platinum loading at Nissan. *Electrochim Acta* **2011,** *56* (28), 10832-10841.

152. Pan, L.; Ott, S.; Dionigi, F.; Strasser, P., Current challenges related to the deployment of shape-controlled Pt alloy oxygen reduction reaction nanocatalysts into low Pt-loaded cathode layers of proton exchange membrane fuel cells. *Current Opinion in Electrochemistry* **2019,** *18*, 61-71.

153. Shi, S.; Weber, A. Z.; Kusoglu, A., STRUCTURE-TRANSPORT RELATIONSHIP OF PERFLUOROSULFONIC-ACID MEMBRANES IN DIFFERENT CATIONIC FORMS. *Electrochim Acta* **2016,** *220*, 517-528.

154. Zalitis, C. M.; Kramer, D.; Kucernak, A. R., Electrocatalytic performance of fuel cell reactions at low catalyst loading and high mass transport. *Phys Chem Chem Phys* **2013,** *15* (12), 4329-4340.

155. Inaba, M.; Jensen, A. W.; Sievers, G. W.; Escudero-Escribano, M.; Zana, A.; Arenz, M., Benchmarking high surface area electrocatalysts in a gas diffusion electrode: measurement of oxygen reduction activities under realistic conditions. *Energy Environ Sci* **2018,** *11* (4), 988-994.

156. Yu, X.; Lai, S.; Xin, S.; Chen, S.; Zhang, X.; She, X.; Zhan, T.; Zhao, X.; Yang, D., Coupling of iron phthalocyanine at carbon defect site via π-π stacking for enhanced oxygen reduction reaction. *Appl Catal B Environ* **2021,** *280*, 119437.

157. Ramaswamy, N.; Kumaraguru, S., Materials and Design Selection to Improve High Current Density Performance in PEMFC. *ECS Transactions* **2018,** *85* (13), 835-842.

158. Breitwieser, M.; Klingele, M.; Vierrath, S.; Zengerle, R.; Thiele, S., Tailoring the Membrane-Electrode Interface in PEM Fuel Cells: A Review and Perspective on Novel Engineering Approaches. *Adv Energy Mater* **2018,** *8* (4), 1701257.

159. Dai, L.; Xue, Y.; Qu, L.; Choi, H. J.; Baek, J. B., Metal-free catalysts for oxygen reduction reaction. *Chem Rev* **2015,** *115* (11), 4823-92.

160. Ma, T. Y.; Dai, S.; Qiao, S. Z., Self-supported electrocatalysts for advanced energy conversion processes. *Mater Today* **2016,** *19* (5), 265-273.

161. Jiang, S.; Li, J.; Fang, J.; Wang, X., Fibrous-Structured Freestanding Electrodes for Oxygen Electrocatalysis. *Small* **2021,** *17* (9), 1903760.

162. Sievers, G. W.; Bowen, J. R.; Brüser, V.; Arenz, M., Support-free nanostructured PtCu electrocatalyst for the oxygen reduction reaction prepared by alternating magnetron sputtering. *J Power Sources* **2019,** *413*, 432-440.

163. Sievers, G. W.; Jensen, A. W.; Quinson, J.; Zana, A.; Bizzotto, F.; Oezaslan, M.; Dworzak, A.; Kirkensgaard, J. J. K.; Smitshuysen, T. E. L.; Kadkhodazadeh, S.; Juelsholt, M.; Jensen, K. M. Ø.; Anklam, K.; Wan, H.; Schäfer, J.; Čépe, K.; Escudero-Escribano, M.; Rossmeisl, J.; Quade, A.; Brüser, V.; Arenz, M., Self-supported Pt–CoO networks combining high specific activity with high surface area for oxygen reduction. *Nat Mater* **2021,** *20* (2), 208-213.

164. Ji, D.; Fan, L.; Li, L.; Peng, S.; Yu, D.; Song, J.; Ramakrishna, S.; Guo, S., Atomically Transition Metals on Self-Supported Porous Carbon Flake Arrays as Binder-Free Air Cathode for Wearable Zinc−Air Batteries. *Adv Mater* **2019,** *0* (0), 1808267.

165. Cai, X.; Xia, B. Y.; Franklin, J.; Li, B.; Wang, X.; Wang, Z.; Chen, L.; Lin, J.; Lai, L.; Shen, Z., Free-standing vertically-aligned nitrogen-doped carbon nanotube arrays/graphene as air-breathing electrodes for rechargeable zinc–air batteries. *J Mater Chem A* **2017,** *5* (6), 2488-2495.

166. Liu, D.; Zhang, X.; Sun, Z.; You, T., Free-standing nitrogen-doped carbon nanofiber films as highly efficient electrocatalysts for oxygen reduction. *Nanoscale* **2013,** *5* (20), 9528-31.

167. Li, Y. X.; Ge, X. B.; Wang, L. D. Y.; Liu, J.; Wang, Y.; Feng, L. X., A free standing porous Co/Mo architecture as a robust bifunctional catalyst toward water splitting. *RSC Adv* **2017,** *7* (19), 11568-11571.

168. Pasaogullari, U.; Wang, C. Y., Two-phase transport and the role of micro-porous layer in polymer electrolyte fuel cells. *Electrochim Acta* **2004,** *49* (25), 4359-4369.

169. Lu, Z. Y.; Xu, W. W.; Ma, J.; Li, Y. J.; Sun, X. M.; Jiang, L., Superaerophilic Carbon-Nanotube-Array Electrode for High-Performance Oxygen Reduction Reaction. *Adv Mater* **2016,** *28* (33), 7155-7161.

170. Li, Y.; Ge, X.; Wang, L.; Liu, J.; Wang, Y.; Feng, L., A free standing porous Co/Mo architecture as a robust bifunctional catalyst toward water splitting. *RSC Adv* **2017,** *7* (19), 11568-11571.

171. Wang, G.; Yu, M.; Feng, X., Carbon materials for ion-intercalation involved rechargeable battery technologies. *Chem Soc Rev* **2021,** *50* (4), 2388-2443.

172. Barrio, J.; Volokh, M.; Shalom, M., Polymeric carbon nitrides and related metal-free materials for energy and environmental applications. *J Mater Chem A* **2020,** *8* (22), 11075-11116.

173. Liu, F.; Song, S.; Xue, D.; Zhang, H., Folded Structured Graphene Paper for High Performance Electrode Materials. *Adv Mater* **2012,** *24* (8), 1089-1094.

174. Wang, S.; Xia, L.; Yu, L.; Zhang, L.; Wang, H.; Lou, X. W., Free-Standing Nitrogen-Doped Carbon Nanofiber Films: Integrated Electrodes for Sodium-Ion Batteries with Ultralong Cycle Life and Superior Rate Capability. *Adv Energy Mater* **2016,** *6* (7), 1502217.

175. Saurel, D.; Segalini, J.; Jauregui, M.; Pendashteh, A.; Daffos, B.; Simon, P.; Casas-Cabanas, M., A SAXS outlook on disordered carbonaceous materials for electrochemical energy storage. *Energy Storage Mater* **2019,** *21*, 162-173.

176. Xie, F.; Xu, Z.; Jensen, A. C. S.; Ding, F.; Au, H.; Feng, J.; Luo, H.; Qiao, M.; Guo, Z.; Lu, Y.; Drew, A. J.; Hu, Y.-S.; Titirici, M.-M., Unveiling the role of hydrothermal carbon dots as anodes in sodium-ion batteries with ultrahigh initial coulombic efficiency. *J Mater Chem A* **2019,** *7* (48), 27567-27575.

177. Ayiania, M.; Smith, M.; Hensley, A. J. R.; Scudiero, L.; McEwen, J.-S.; Garcia-Perez, M., Deconvoluting the XPS spectra for nitrogen-doped chars: An analysis from first principles. *Carbon* **2020,** *162*, 528-544.

178. Jorge, A. B.; Jervis, R.; Periasamy, A. P.; Qiao, M.; Feng, J.; Tran, L. N.; Titirici, M.-M., 3D Carbon Materials for Efficient Oxygen and Hydrogen Electrocatalysis. *Adv Energy Mater* **2020,** *10* (11), 1902494.

179. Yang, G.; Zhu, J.; Yuan, P.; Hu, Y.; Qu, G.; Lu, B. A.; Xue, X.; Yin, H.; Cheng, W.; Cheng, J.; Xu, W.; Li, J.; Hu, J.; Mu, S.; Zhang, J. N., Regulating Fe-spin state by atomically dispersed Mn-N in Fe-N-C catalysts with high oxygen reduction activity. *Nat Commun* **2021,** *12* (1), 1734.

180. Zhu, C.; Li, H.; Fu, S.; Du, D.; Lin, Y., Highly efficient nonprecious metal catalysts towards oxygen reduction reaction based on three-dimensional porous carbon nanostructures. *Chem Soc Rev* **2016,** *45* (3), 517-531.

181. Gewirth, A. A.; Varnell, J. A.; DiAscro, A. M., Nonprecious Metal Catalysts for Oxygen Reduction in Heterogeneous Aqueous Systems. *Chem Rev* **2018,** *118* (5), 2313-2339.

182. Nie, Y.; Li, L.; Wei, Z., Recent advancements in Pt and Pt-free catalysts for oxygen reduction reaction. *Chem Soc Rev* **2015,** *44* (8), 2168-2201.

183. Shao, M.; Chang, Q.; Dodelet, J.-P.; Chenitz, R., Recent Advances in Electrocatalysts for Oxygen Reduction Reaction. *Chem Rev* **2016,** *116* (6), 3594-3657.

184. Ferrari, A. C.; Basko, D. M., Raman spectroscopy as a versatile tool for studying the properties of graphene. *Nat Nanotechnol* **2013,** *8* (4), 235-246.

185. Wagner, S.; Auerbach, H.; Tait, C. E.; Martinaiou, I.; Kumar, S. C. N.; Kübel, C.; Sergeev, I.; Wille, H.-C.; Behrends, J.; Wolny, J. A.; Schünemann, V.; Kramm, U. I., Elucidating the Structural Composition of an Fe–N–C Catalyst by Nuclear- and Electron-Resonance Techniques. *Angew Chem* **2019,** *58* (31), 10486-10492.

186. Wan, X.; Liu, X.; Li, Y.; Yu, R.; Zheng, L.; Yan, W.; Wang, H.; Xu, M.; Shui, J., Fe–N–C electrocatalyst with dense active sites and efficient mass transport for high-performance proton exchange membrane fuel cells. *Nat Catal* **2019,** *2* (3), 259-268.

187. Zitolo, A.; Goellner, V.; Armel, V.; Sougrati, M.-T.; Mineva, T.; Stievano, L.; Fonda, E.; Jaouen, F., Identification of catalytic sites for oxygen reduction in iron- and nitrogen-doped graphene materials. *Nat Mater* **2015,** *14* (9), 937-942.

188. Ravel, B.; Newville, M., ATHENA and ARTEMIS Interactive Graphical Data Analysisusing IFEFFIT. *Phys Scripta* **2005**, 1007.

189. Change, C. o. C. *Reducing UK emissions - 2019 Progress Report to Parliament*; 2019.

190. Lefèvre, M.; Proietti, E.; Jaouen, F.; Dodelet, J.-P., Iron-Based Catalysts with Improved Oxygen Reduction Activity in Polymer Electrolyte Fuel Cells. *Science* **2009,** *324* (5923), 71-74.

191. Sarapuu, A.; Kibena-Põldsepp, E.; Borghei, M.; Tammeveski, K., Electrocatalysis of oxygen reduction on heteroatom-doped nanocarbons and transition metal–nitrogen–carbon catalysts for alkaline membrane fuel cells. *J Mater Chem A* **2018,** *6* (3), 776-804.

192. Lilloja, J.; Kibena-Põldsepp, E.; Sarapuu, A.; Douglin, J. C.; Käärik, M.; Kozlova, J.; Paiste, P.; Kikas, A.; Aruväli, J.; Leis, J.; Sammelselg, V.; Dekel, D. R.; Tammeveski, K., Transition-Metal- and Nitrogen-Doped Carbide-Derived Carbon/Carbon Nanotube Composites as Cathode Catalysts for Anion-Exchange Membrane Fuel Cells. *ACS Catal* **2021,** *11* (4), 1920-1931.

193. Praats, R.; Käärik, M.; Kikas, A.; Kisand, V.; Aruväli, J.; Paiste, P.; Merisalu, M.; Leis, J.; Sammelselg, V.; Zagal, J. H.; Holdcroft, S.; Nakashima, N.; Tammeveski, K., Electrocatalytic oxygen reduction reaction on iron phthalocyanine-modified carbide-derived carbon/carbon nanotube composite electrocatalysts. *Electrochim Acta* **2020,** *334*, 135575.

194. Ratso, S.; Ranjbar Sahraie, N.; Sougrati, M. T.; Käärik, M.; Kook, M.; Saar, R.; Paiste, P.; Jia, Q.; Leis, J.; Mukerjee, S.; Jaouen, F.; Tammeveski, K., Synthesis of highly-active Fe–N–C catalysts for PEMFC with carbide-derived carbons. *J Mater Chem A* **2018,** *6* (30), 14663-14674.

195. Sibul, R.; Kibena-Põldsepp, E.; Ratso, S.; Kook, M.; Sougrati, M. T.; Käärik, M.; Merisalu, M.; Aruväli, J.; Paiste, P.; Treshchalov, A.; Leis, J.; Kisand, V.; Sammelselg, V.; Holdcroft, S.; Jaouen, F.; Tammeveski, K., Iron- and Nitrogen-Doped Graphene-Based Catalysts for Fuel Cell Applications. *ChemElectroChem* **2020,** *7* (7), 1739-1747.

196. Ratso, S.; Käärik, M.; Kook, M.; Paiste, P.; Kisand, V.; Vlassov, S.; Leis, J.; Tammeveski, K., Iron and Nitrogen Co-doped Carbide-Derived Carbon and Carbon Nanotube Composite Catalysts for Oxygen Reduction Reaction. *ChemElectroChem* **2018,** *5* (14), 1827-1836.

197. Gupta, S.; Tryk, D.; Bae, I.; Aldred, W.; Yeager, E., Heat-treated polyacrylonitrile-based catalysts for oxygen electroreduction. *J Appl Electrochem* **1989,** *19* (1), 19-27.

198. Chen, S.; Bi, F.; Xiang, K.; Zhang, Y.; Hao, P.; Li, M.; Zhao, B.; Guo, X., Reactive Template-Derived CoFe/N-Doped Carbon Nanosheets as Highly Efficient Electrocatalysts toward Oxygen Reduction, Oxygen Evolution, and Hydrogen Evolution. *ACS Sustainable Chem Eng* **2019,** *7* (18), 15278-15288.

199. Pegis, M. L.; Martin, D. J.; Wise, C. F.; Brezny, A. C.; Johnson, S. I.; Johnson, L. E.; Kumar, N.; Raugei, S.; Mayer, J. M., Mechanism of Catalytic O2 Reduction by Iron Tetraphenylporphyrin. *J Am Chem Soc* **2019,** *141* (20), 8315-8326.

200. Wang, Y.; Tang, Y.-J.; Zhou, K., Self-Adjusting Activity Induced by Intrinsic Reaction Intermediate in Fe–N–C Single-Atom Catalysts. *J Am Chem Soc* **2019,** *141* (36), 14115-14119.

201. Zitolo, A.; Ranjbar-Sahraie, N.; Mineva, T.; Li, J.; Jia, Q.; Stamatin, S.; Harrington, G. F.; Lyth, S. M.; Krtil, P.; Mukerjee, S.; Fonda, E.; Jaouen, F., Identification of catalytic sites in cobalt-nitrogen-carbon materials for the oxygen reduction reaction. *Nat Commun* **2017,** *8* (1), 957.

202. Tian, J.; Morozan, A.; Sougrati, M. T.; Lefèvre, M.; Chenitz, R.; Dodelet, J.-P.; Jones, D.; Jaouen, F., Optimized Synthesis of Fe/N/C Cathode Catalysts for PEM Fuel Cells: A Matter of Iron–Ligand Coordination Strength. *Angew Chem* **2013,** *52* (27), 6867-6870.

203. Sahraie, N. R.; Kramm, U. I.; Steinberg, J.; Zhang, Y.; Thomas, A.; Reier, T.; Paraknowitsch, J.-P.; Strasser, P., Quantifying the density and utilization of active sites in non-precious metal oxygen electroreduction catalysts. *Nat Commun* **2015,** *6* (1), 8618.

204. Li, A.; Nicolae, S. A.; Qiao, M.; Preuss, K.; Szilágyi, P. A.; Moores, A.; Titirici, M.-M., Homogenous Meets Heterogenous and Electro-Catalysis: Iron-Nitrogen Molecular Complexes within Carbon Materials for Catalytic Applications. *ChemCatChem* **2019,** *11* (16), 3602-3625.

205. Wang, K.; Wang, H.; Ji, S.; Feng, H.; Linkov, V.; Wang, R., Biomass-derived activated carbon as high-performance non-precious electrocatalyst for oxygen reduction. *RSC Adv* **2013,** *3* (30), 12039-12042.

206. Titirici, M.-M.; Antonietti, M., Chemistry and materials options of sustainable carbon materials made by hydrothermal carbonization. *Chem Soc Rev* **2010,** *39* (1), 103-116.

207. Titirici, M.-M.; Antonietti, M.; Baccile, N., Hydrothermal carbon from biomass: a comparison of the local structure from poly- to monosaccharides and pentoses/hexoses. *Green Chem* **2008,** *10* (11), 1204-1212.

208. Zhong, H.; Shi, C.; Li, J.; Yu, R.; Yu, Q.; Liu, H.; Yao, Y.; Wu, J.; Zhou, L.; Mai, L., Cobalt decorated nitrogen-doped carbon bowls as efficient electrocatalysts for the oxygen reduction reaction. *Chem Commun* **2020,** *56* (32), 4488-4491.

209. Feng, T.; Zhang, M., A mixed-ion strategy to construct CNT-decorated Co/N-doped hollow carbon for enhanced oxygen reduction. *Chem Commun* **2018,** *54* (82), 11570-11573.

210. Thompson, E.; Danks, A. E.; Bourgeois, L.; Schnepp, Z., Iron-catalyzed graphitization of biomass. *Green Chem* **2015,** *17* (1), 551-556.

211. Funke, H.; Scheinost, A.; Chukalina, M., Wavelet analysis of extended x-ray absorption fine structure data. *Phys Rev B* **2005,** *71* (9), 094110.

212. Ratso, S.; Zitolo, A.; Käärik, M.; Merisalu, M.; Kikas, A.; Kisand, V.; Rähn, M.; Paiste, P.; Leis, J.; Sammelselg, V.; Holdcroft, S.; Jaouen, F.; Tammeveski, K., Non-precious metal cathodes for anion exchange membrane fuel cells from ball-milled iron and nitrogen doped carbide-derived carbons. *Renew Energ* **2021,** *167*, 800-810.

213. Leonard, N. D.; Wagner, S.; Luo, F.; Steinberg, J.; Ju, W.; Weidler, N.; Wang, H.; Kramm, U. I.; Strasser, P., Deconvolution of Utilization, Site Density, and Turnover Frequency of Fe–Nitrogen–Carbon Oxygen Reduction Reaction Catalysts Prepared with Secondary N-Precursors. *ACS Catal* **2018,** *8* (3), 1640-1647.

214. Artyushkova, K.; Kiefer, B.; Halevi, B.; Knop-Gericke, A.; Schlogl, R.; Atanassov, P., Density functional theory calculations of XPS binding energy shift for nitrogen-containing graphene-like structures. *Chem Commun* **2013,** *49* (25), 2539-2541.

215. Artyushkova, K.; Serov, A.; Rojas-Carbonell, S.; Atanassov, P., Chemistry of Multitudinous Active Sites for Oxygen Reduction Reaction in Transition Metal–Nitrogen–Carbon Electrocatalysts. *J Phys Chem C* **2015,** *119* (46), 25917-25928.

216. Kattel, S.; Atanassov, P.; Kiefer, B., A density functional theory study of oxygen reduction reaction on non-PGM Fe–Nx–C electrocatalysts. *Phys Chem Chem Phys* **2014,** *16* (27), 13800-13806.

217. Xue, H.; He, T.; Chabu, J. M.; Liu, J.; Wu, H.; Zheng, J.; Tan, M.; Ma, J.; Shen, R.; Deng, L.; Zhang, Y., Iron Single Clusters Anchored on N-Doped Porous Carbon as Superior Trace-Metal Catalysts toward Oxygen Reduction. *Adv Mater Interfaces* **2018,** *5* (7), 1701345.

218. Poynton, S. D.; Slade, R. C. T.; Omasta, T. J.; Mustain, W. E.; Escudero-Cid, R.; Ocón, P.; Varcoe, J. R., Preparation of radiation-grafted powders for use as anion exchange ionomers in alkaline polymer electrolyte fuel cells. *J Mater Chem A* **2014,** *2* (14), 5124-5130.

219. Ferrero, G. A.; Preuss, K.; Marinovic, A.; Jorge, A. B.; Mansor, N.; Brett, D. J. L.; Fuertes, A. B.; Sevilla, M.; Titirici, M.-M., Fe–N-Doped Carbon Capsules with Outstanding Electrochemical Performance and Stability for the Oxygen Reduction Reaction in Both Acid and Alkaline Conditions. *ACS Nano* **2016,** *10* (6), 5922-5932.

220. Li, M.; Xiong, Y.; Liu, X.; Han, C.; Zhang, Y.; Bo, X.; Guo, L., Iron and nitrogen co-doped carbon nanotube@hollow carbon fibers derived from plant biomass as efficient catalysts for the oxygen reduction reaction. *J Mater Chem A* **2015,** *3* (18), 9658-9667.

221. Song, L.-T.; Wu, Z.-Y.; Zhou, F.; Liang, H.-W.; Yu, Z.-Y.; Yu, S.-H., Sustainable Hydrothermal Carbonization Synthesis of Iron/Nitrogen-Doped Carbon Nanofiber Aerogels as Electrocatalysts for Oxygen Reduction. *Small* **2016,** *12* (46), 6398-6406.

222. Yin, H.; Zhang, C.; Liu, F.; Hou, Y., Hybrid of Iron Nitride and Nitrogen-Doped Graphene Aerogel as Synergistic Catalyst for Oxygen Reduction Reaction. *Adv Funct Mater* **2014,** *24* (20), 2930-2937.

223. Jiang, W.-J.; Gu, L.; Li, L.; Zhang, Y.; Zhang, X.; Zhang, L.-J.; Wang, J.-Q.; Hu, J.-S.; Wei, Z.; Wan, L.-J., Understanding the High Activity of Fe–N–C Electrocatalysts in Oxygen Reduction: Fe/Fe3C Nanoparticles Boost the Activity of Fe–Nx. *J Am Chem Soc* **2016,** *138* (10), 3570-3578.

224. Ye, G.; Zhao, K.; He, Z.; Huang, R.; Liu, Y.; Liu, S., Fe-Nx Sites Enriched Carbon Micropolyhedrons Derived from Fe-Doped Zeolitic Imidazolate Frameworks with Reinforced Fe-N Coordination for Efficient Oxygen Reduction Reaction. *ACS Sustainable Chem Eng* **2018,** *6* (11), 15624-15633.

225. Jiang, R.; Li, L.; Sheng, T.; Hu, G.; Chen, Y.; Wang, L., Edge-Site Engineering of Atomically Dispersed Fe–N4 by Selective C–N Bond Cleavage for Enhanced Oxygen Reduction Reaction Activities. *J Am Chem Soc* **2018,** *140* (37), 11594-11598.

226. Wang, X.; Zhang, H.; Lin, H.; Gupta, S.; Wang, C.; Tao, Z.; Fu, H.; Wang, T.; Zheng, J.; Wu, G.; Li, X., Directly converting Fe-doped metal–organic frameworks into highly active and stable Fe-N-C catalysts for oxygen reduction in acid. *Nano Energy* **2016,** *25*, 110-119.

227. Li, G.; Zhang, J.; Li, W.; Fan, K.; Xu, C., 3D interconnected hierarchical porous N-doped carbon constructed by flake-like nanostructure with Fe/Fe3C for efficient oxygen reduction reaction and supercapacitor. *Nanoscale* **2018,** *10* (19), 9252-9260.

228. Ren, Y.; Zhao, H.; Li, J.; Wang, R.; Wei, Z., Facile preparation of a Ag/graphene electrocatalyst with high activity for the oxygen reduction reaction. *RSC Adv* **2020,** *10* (26), 15650-15655.

229. Zhang, X.; Han, X.; Jiang, Z.; Xu, J.; Chen, L.; Xue, Y.; Nie, A.; Xie, Z.; Kuang, Q.; Zheng, L., Atomically dispersed hierarchically ordered porous Fe–N–C electrocatalyst for high performance electrocatalytic oxygen reduction in Zn-Air battery. *Nano Energy* **2020,** *71*, 104547.

230. Liang, H.-W.; Wei, W.; Wu, Z.-S.; Feng, X.; Müllen, K., Mesoporous Metal–Nitrogen-Doped Carbon Electrocatalysts for Highly Efficient Oxygen Reduction Reaction. *J Am Chem Soc* **2013,** *135* (43), 16002-16005.

231. Sa, Y. J.; Seo, D.-J.; Woo, J.; Lim, J. T.; Cheon, J. Y.; Yang, S. Y.; Lee, J. M.; Kang, D.; Shin, T. J.; Shin, H. S.; Jeong, H. Y.; Kim, C. S.; Kim, M. G.; Kim, T.-Y.; Joo, S. H., A General Approach to Preferential Formation of Active Fe–Nx Sites in Fe–N/C Electrocatalysts for Efficient Oxygen Reduction Reaction. *J Am Chem Soc* **2016,** *138* (45), 15046-15056.

232. Ahn, S. H.; Yu, X.; Manthiram, A., "Wiring" Fe-Nx-Embedded Porous Carbon Framework onto 1D Nanotubes for Efficient Oxygen Reduction Reaction in Alkaline and Acidic Media. *Adv Mater* **2017,** *29* (26), 1606534.

233. Woo, J.; Yang, S. Y.; Sa, Y. J.; Choi, W.-Y.; Lee, M.-H.; Lee, H.-W.; Shin, T. J.; Kim, T.-Y.; Joo, S. H., Promoting Oxygen Reduction Reaction Activity of Fe–N/C Electrocatalysts by Silica-Coating-Mediated Synthesis for Anion-Exchange Membrane Fuel Cells. *Chem Mater* **2018,** *30* (19), 6684-6701.

234. Sun, H.; Wang, M.; Zhang, S.; Liu, S.; Shen, X.; Qian, T.; Niu, X.; Xiong, J.; Yan, C., Boosting Oxygen Dissociation over Bimetal Sites to Facilitate Oxygen Reduction Activity of Zinc-Air Battery. *Adv Funct Mater* **2021,** *31* (4), 2006533.

235. Chen, S.; Yan, Y.; Hao, P.; Li, M.; Liang, J.; Guo, J.; Zhang, Y.; Chen, S.; Ding, W.; Guo, X., Iron Nanoparticles Encapsulated in S,N-Codoped Carbon: Sulfur Doping Enriches Surface Electron Density and Enhances Electrocatalytic Activity toward Oxygen Reduction. *ACS Appl Mater Interfaces* **2020,** *12* (11), 12686-12695.

236. Venkateswara Rao, C.; Ishikawa, Y., Activity, Selectivity, and Anion-Exchange Membrane Fuel Cell Performance of Virtually Metal-Free Nitrogen-Doped Carbon Nanotube Electrodes for Oxygen Reduction Reaction. *J Phys Chem C* **2012,** *116* (6), 4340-4346.

237. Kruusenberg, I.; Matisen, L.; Shah, Q.; Kannan, A. M.; Tammeveski, K., Non-platinum cathode catalysts for alkaline membrane fuel cells. *Int J Hydrogen Energy* **2012,** *37* (5), 4406-4412.

238. Palaniselvam, T.; Valappil, M. O.; Illathvalappil, R.; Kurungot, S., Nanoporous graphene by quantum dots removal from graphene and its conversion to a potential oxygen reduction electrocatalyst via nitrogen doping. *Energy Environ Sci* **2014,** *7* (3), 1059-1067.

239. Wang, C.-H.; Yang, C.-W.; Lin, Y.-C.; Chang, S.-T.; Chang, S. L. Y., Cobalt–iron(II,III) oxide hybrid catalysis with enhanced catalytic activities for oxygen reduction in anion exchange membrane fuel cell. *J Power Sources* **2015,** *277*, 147-154.

240. Lee, S.; Choun, M.; Ye, Y.; Lee, J.; Mun, Y.; Kang, E.; Hwang, J.; Lee, Y.-H.; Shin, C.-H.; Moon, S.-H.; Kim, S.-K.; Lee, E.; Lee, J., Designing a Highly Active Metal-Free Oxygen Reduction Catalyst in Membrane Electrode Assemblies for Alkaline Fuel Cells: Effects of Pore Size and Doping-Site Position. *Angew Chem* **2015,** *54* (32), 9230-9234.

241. Miller, H. A.; Bellini, M.; Oberhauser, W.; Deng, X.; Chen, H.; He, Q.; Passaponti, M.; Innocenti, M.; Yang, R.; Sun, F.; Jiang, Z.; Vizza, F., Heat treated carbon supported iron(ii)phthalocyanine oxygen reduction catalysts: elucidation of the structure–activity relationship using X-ray absorption spectroscopy. *Phys Chem Chem Phys* **2016,** *18* (48), 33142-33151.

242. Huang, H.-C.; Lin, Y.-C.; Chang, S.-T.; Liu, C.-C.; Wang, K.-C.; Jhong, H.-P.; Lee, J.-F.; Wang, C.-H., Effect of a sulfur and nitrogen dual-doped Fe–N–S electrocatalyst for the oxygen reduction reaction. *J Mater Chem A* **2017,** *5* (37), 19790-19799.

243. Ratso, S.; Kruusenberg, I.; Käärik, M.; Kook, M.; Puust, L.; Saar, R.; Leis, J.; Tammeveski, K., Highly efficient transition metal and nitrogen co-doped carbide-derived carbon electrocatalysts for anion exchange membrane fuel cells. *J Power Sources* **2018,** *375*, 233-243.

244. Lilloja, J.; Mooste, M.; Kibena-Põldsepp, E.; Sarapuu, A.; Zulevi, B.; Kikas, A.; Piirsoo, H.-M.; Tamm, A.; Kisand, V.; Holdcroft, S.; Serov, A.; Tammeveski, K., Mesoporous iron-nitrogen co-doped carbon material as cathode catalyst for the anion exchange membrane fuel cell. *Journal of Power Sources Advances* **2021,** *8*, 100052.

245. Mooste, M.; Kibena-Põldsepp, E.; Vassiljeva, V.; Kikas, A.; Käärik, M.; Kozlova, J.; Kisand, V.; Külaviir, M.; Cavaliere, S.; Leis, J.; Krumme, A.; Sammelselg, V.; Holdcroft, S.; Tammeveski, K., Electrospun Polyacrylonitrile-Derived Co or Fe Containing Nanofibre Catalysts for Oxygen Reduction Reaction at the Alkaline Membrane Fuel Cell Cathode. *ChemCatChem* **2020,** *12* (18), 4568-4581.

246. Mooste, M.; Tkesheliadze, T.; Kozlova, J.; Kikas, A.; Kisand, V.; Treshchalov, A.; Tamm, A.; Aruväli, J.; Zagal, J. H.; Kannan, A. M.; Tammeveski, K., Transition metal phthalocyanine-modified shungite-based cathode catalysts for alkaline membrane fuel cell. *Int J Hydrogen Energy* **2021,** *46* (5), 4365-4377.

247. Kisand, K.; Sarapuu, A.; Danilian, D.; Kikas, A.; Kisand, V.; Rähn, M.; Treshchalov, A.; Käärik, M.; Merisalu, M.; Paiste, P.; Aruväli, J.; Leis, J.; Sammelselg, V.; Holdcroft, S.; Tammeveski, K., Transition metal-containing nitrogen-doped nanocarbon catalysts derived from 5-methylresorcinol for anion exchange membrane fuel cell application. *J Colloid Interf Sci* **2021,** *584*, 263-274.

248. Schweizer, P. Gezielte Manipulation einzelner Defekte in Schichtkristallen und 2D-Materialien. 2019.

249. Meyer, J. C.; Eder, F.; Kurasch, S.; Skakalova, V.; Kotakoski, J.; Park, H. J.; Roth, S.; Chuvilin, A.; Eyhusen, S.; Benner, G.; Krasheninnikov, A. V.; Kaiser, U., Erratum: Accurate Measurement of Electron Beam Induced Displacement Cross Sections for Single-Layer Graphene [Phys. Rev. Lett. 108, 196102 (2012)]. *Phys Rev Lett* **2013,** *110* (23), 239902.

250. Reimer, L., Electron Optics of a Scanning Electron Microscope. In *Scanning Electron Microscopy: Physics of Image Formation and Microanalysis*, Reimer, L., Ed. Springer Berlin Heidelberg: Berlin, Heidelberg, 1998; pp 13-56.

251. Calvin, S., *XAFS for everyone*. CRC Press: 2013.

252. Briggs, D., Handbook of X-ray Photoelectron Spectroscopy C. D. Wanger, W. M. Riggs, L. E. Davis, J. F. Moulder and G. E.Muilenberg Perkin-Elmer Corp., Physical Electronics Division, Eden Prairie, Minnesota, USA, 1979. 190 pp. $195. *Surf Interface Anal* **1981,** *3* (4), v-v.

253. Lucas, C. A., Surface Structure Determination by Interference Techniques. In *Surface Analysis – The Principal Techniques*, 2009; pp 391-478.

254. Skalny, J.; Hearn, N., 13 - Surface Area Measurements. In *Handbook of Analytical Techniques in Concrete Science and Technology*, Ramachandran, V. S.; Beaudoin, J. J., Eds. William Andrew Publishing: Norwich, NY, 2001; pp 505-527.

255. Sing, K., The use of nitrogen adsorption for the characterisation of porous materials. *Colloids Surf. A Physicochem. Eng. Asp.* **2001,** *187-188*, 3-9.

256. Borie, B., X-Ray Diffraction in Crystals, Imperfect Crystals, and Amorphous Bodies. *J Am Chem Soc* **1965,** *87* (1), 140-141.

257. Stevens, D. A.; Dahn, J. R., An In Situ Small-Angle X-Ray Scattering Study of Sodium Insertion into a Nanoporous Carbon Anode Material within an Operating Electrochemical Cell. *J Electrochem Soc* **2000,** *147* (12), 4428.

258. Herdman, J. D.; Connelly, B. C.; Smooke, M. D.; Long, M. B.; Miller, J. H., A comparison of Raman signatures and laser-induced incandescence with direct numerical simulation of soot growth in non-premixed ethylene/air flames. *Carbon* **2011,** *49* (15), 5298-5311.

259. Matthews, M. J.; Pimenta, M. A.; Dresselhaus, G.; Dresselhaus, M. S.; Endo, M., Origin of dispersive effects of the Raman D band in carbon materials. *Phys Rev B* **1999,** *59* (10), R6585-R6588.

260. Wei, C.; Rao, R. R.; Peng, J.; Huang, B.; Stephens, I. E. L.; Risch, M.; Xu, Z. J.; Shao-Horn, Y., Recommended Practices and Benchmark Activity for Hydrogen and Oxygen Electrocatalysis in Water Splitting and Fuel Cells. *Adv Mater* **2019,** *31* (31), 1806296.

261. Wang, L.; Brink, J. J.; Liu, Y.; Herring, A. M.; Ponce-González, J.; Whelligan, D. K.; Varcoe, J. R., Non-fluorinated pre-irradiation-grafted (peroxidated) LDPE-based anion-exchange membranes with high performance and stability. *Energy Environ Sci* **2017,** *10* (10), 2154-2167.

262. Wan, L.; Wang, J.; Xie, L.; Sun, Y.; Li, K., Nitrogen-Enriched Hierarchically Porous Carbons Prepared from Polybenzoxazine for High-Performance Supercapacitors. *ACS Appl Mater Interfaces* **2014,** *6* (17), 15583-15596.

263. Zhang, Z.; Zhang, Y.; Mu, X.; Du, J.; Wang, H.; Huang, B.; Zhou, J.; Pan, X.; Xie, E., The carbonization temperature effect on the electrochemical performance of nitrogen-doped carbon monoliths. *Electrochim Acta* **2017,** *242*, 100-106.

264. Collins, J.; Gourdin, G.; Foster, M.; Qu, D., Carbon surface functionalities and SEI formation during Li intercalation. *Carbon* **2015,** *92*, 193-244.

Chapter 9

APPENDIX

9.1 INVESTIGATION OF THE CARBONIZATION TEMPERATURE AND PELLET THICKNESS INFLUENCE (APPENDIX FOR CHAPTER 3)

Pellets with different thicknesses were controlled by adding a certain amount of HTC/melamine mixture. Thus, pellets before carbonisation have 25 mg, 50 mg, and 75 mg of weight, respectively, were synthesised. After carbonisation at different temperatures (700 – 1000 °C), the as-prepared pellet samples were denoted as NCT_X. The influences of carbonisation temperatures and the pellet thickness will be explored in the following sections to get more insights into the N-doped porous pellet formation mechanism.

9.1.1 Control the morphology

As shown in **Figure 9.1a** and **b**, the thickness could be controlled by the input weight of the glucose/melamine mixture, where 25mg, 50mg, and 75mg were used to synthesise pellets with different thicknesses. After carbonization, the obtained pellet weight was ~ 8-9 mg for NC_25 pellet, ~ 18-25 mg for NC_50 pelleting, and ~ 26-32 mg for NC_75 pelleting, respectively. Approximately 60% in weight loss could be seen in most pellets samples, which contains decomposition of melamine and escaping of the oxygen functional groups. Shrinkage in the pellet diameter could be seen with the increase of carbonisation temperature in **Figure 9.1c**. The density for the as-prepared pellets was calculated by using their weight to divide into the total volume. We could observe that the pelleting process altered the thermo stability of the pellet, suggesting that the pelleting process increases the adhesion between individual HTC particles.

As high pressure pelleting may change/create new between each HTC carbon particle, FTIR was conducted on uncarbonized pellets of different thickness to investigate the influence of the pelleting process on the interactions between each particle (**Figure 9.2**). Data was normalized

between each sample. With increased thickness, a slightly increased peaks at 3117 cm-1 (O-H), 1702 cm^{-1} (C=O) and 1650 cm^{-1} (C=N) could be seen, suggesting the formation of C=O, O-H and C=N bonds during the pelleting process.

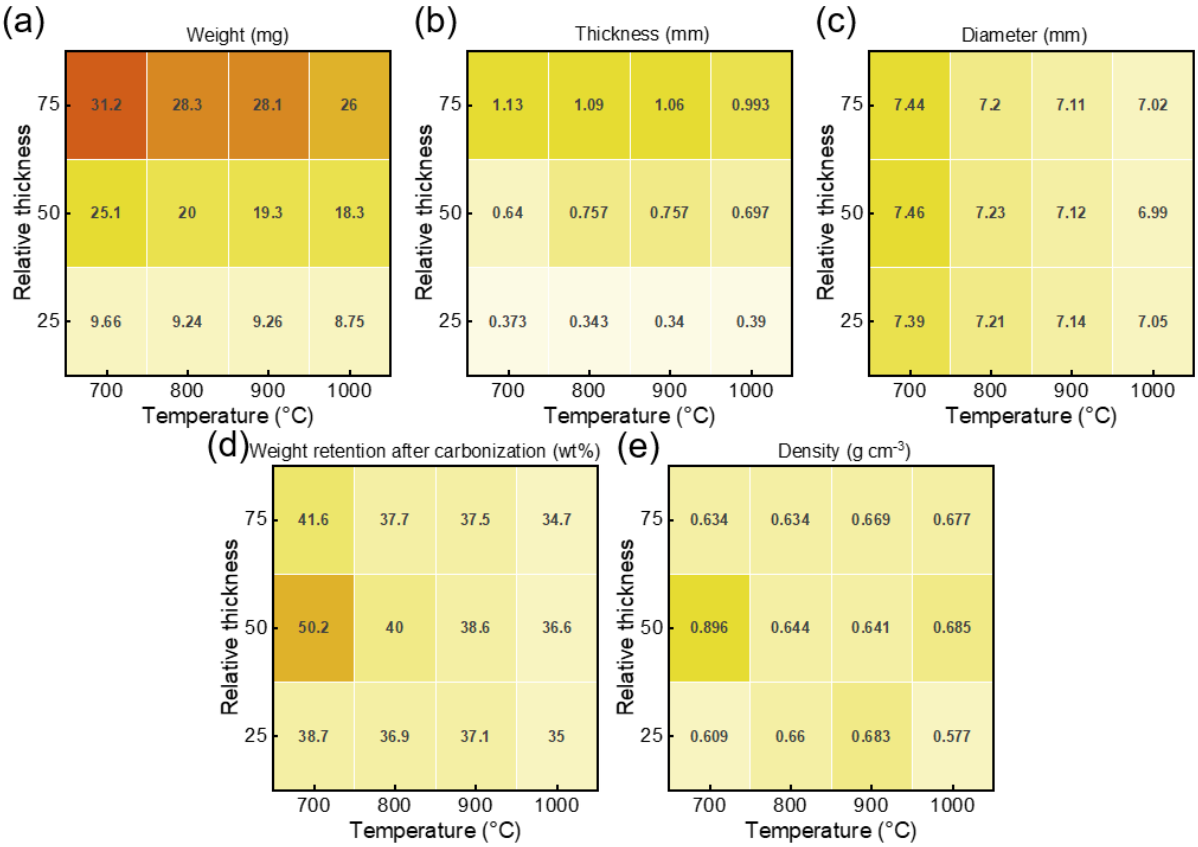

Figure 9.1 Carbonization temperatures and pellet thickness comparison of as-obtained pellet samples in (a) weight (b) thickness, (c) diameter, (d) weight retention after carbonization, (e) density. (Darker colour means higher value)

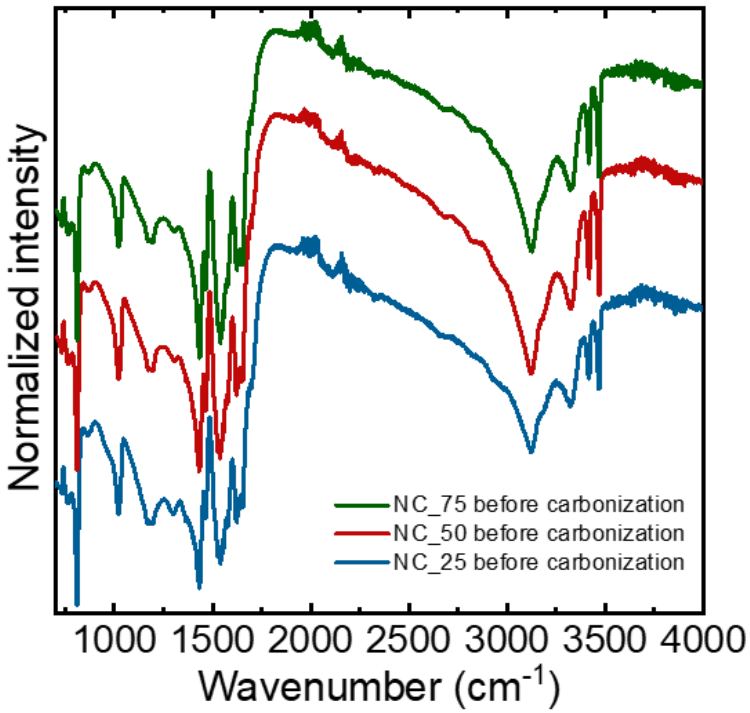

Figure 9.2 FTIR spectrums of uncarbonized NC25, NC_50, and NC_75.

Further, the SEM was performed to study the morphology of the samples. As shown in **Figure 9.3-9.6**, all pellet samples offered a porous interconnected structure both inside and on the carbon pellet's surface. The particles size for all samples was measured by ImageJ software. 30-50 particles were selected for each sample. The particle size for powder samples (NC700-1000_0) is ~ 500 - 600 nm. As for pellet samples, distorted particles could be found on the surface of the pellet, which gives a slightly higher average size (500 – 600 nm) than inner particles (450 - 550 nm in diameter). As shown in **Figure 9.4e-f**, all pellet samples showed an average particle size of around 450 - 550 nm. A broader particle size distribution could also be seen. As shown in **Figure 9.7**, no noticeable particle size trend changes on the temperature and pellet thickness. The small size variation might cause by the HTC process.

With the above physical measurements, we could speculate that after pelleting the HTC/melamine mixture, oxygen functional groups on the HTC surface were bonded together, which might influence the thermo stability of the pellet and thus lead to different yields at different thicknesses. With the increase of pellet thickness, the yield increased, which might be

caused by the trapping of melamine residue or caused by increased oxygen bonding stability. However, from the XPS analysis in Section 3.3.2, no high nitrogen content could be seen in NC900_25 while only an increased oxygen content could be seen, which requires more investigations. During the carbonisation, the HTC/melamine pellet will suffer the most weight loss before 600 C, where melamine decomposes happens, and most oxygen functional groups will be removed to expose the high surface area. The pellet will also shrink horizontally where particles become compact. The density of the pellet almost keeps the same at a different temperature, suggesting oxygen functional groups were further removed. However, no significant particle size decrease could be seen, which suggests the changes are too small.

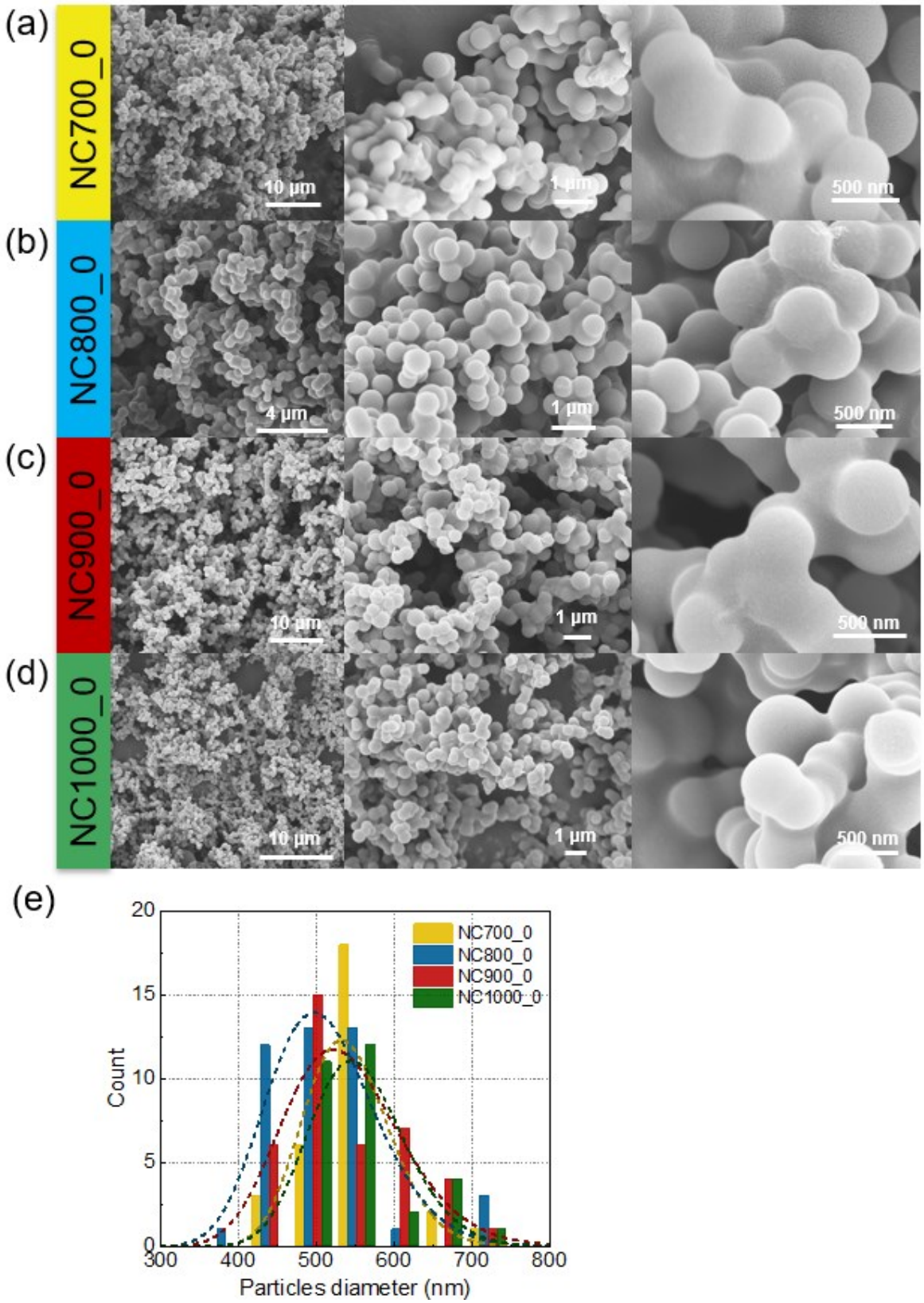

Figure 9.3 SEM images of (a) NC700_0, (b) NC800_0, (c) NC900_0, and (d) NC1000_0. (e) Particle size distribution of NC700_0, NC_800_0, NC900_0, and NC1000_0.

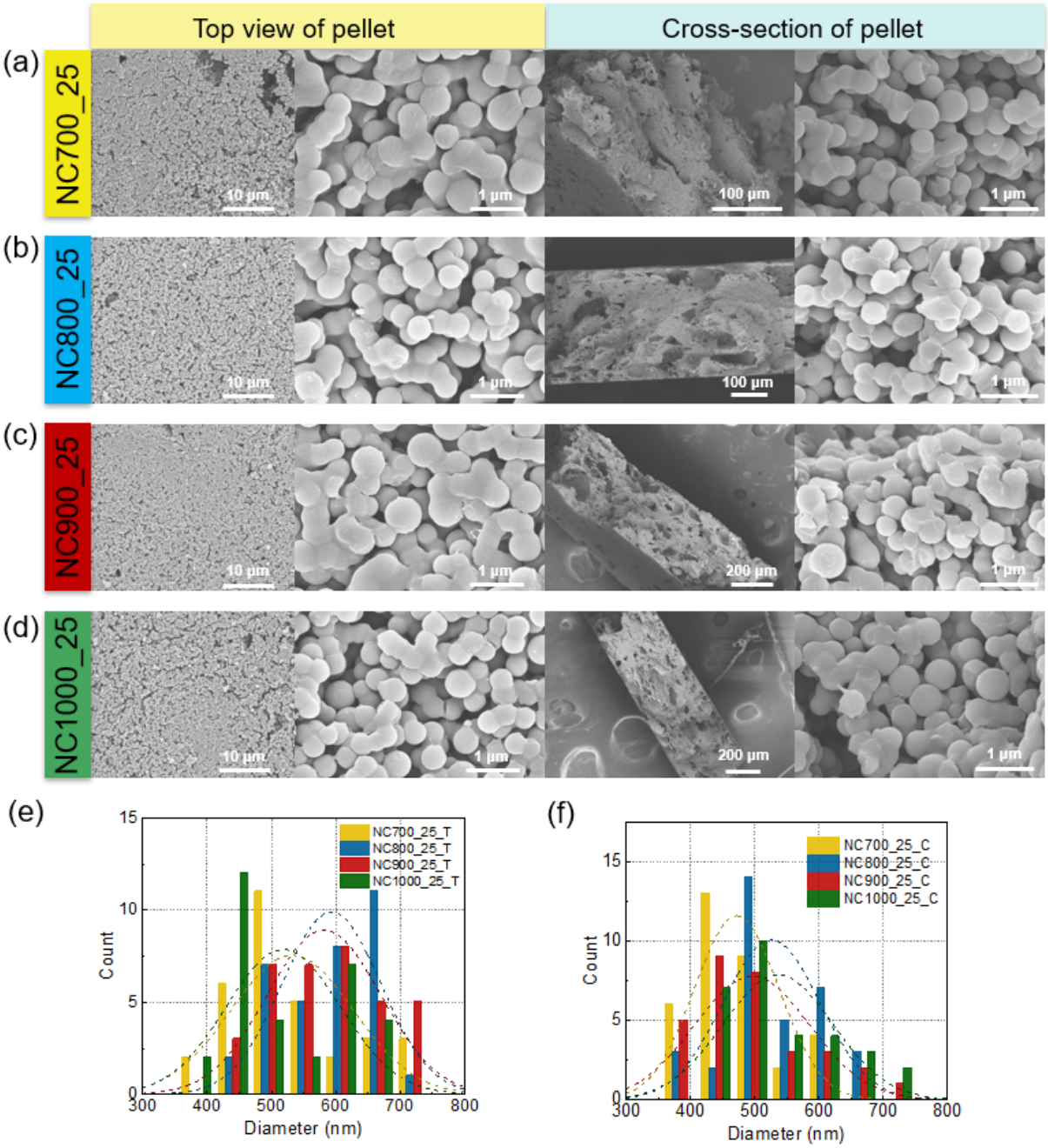

Figure 9.4 SEM images of (a) NC700_25, (b) NC800_25, (c) NC900_25, and (d) NC1000_25. (e) Pellet surface particle size distribution of NC700_0, NC_800_0, NC900_0, and NC1000_0, (f) Pellet inner particle size distribution of NC700_0, NC_800_0, NC900_0, and NC1000_0.

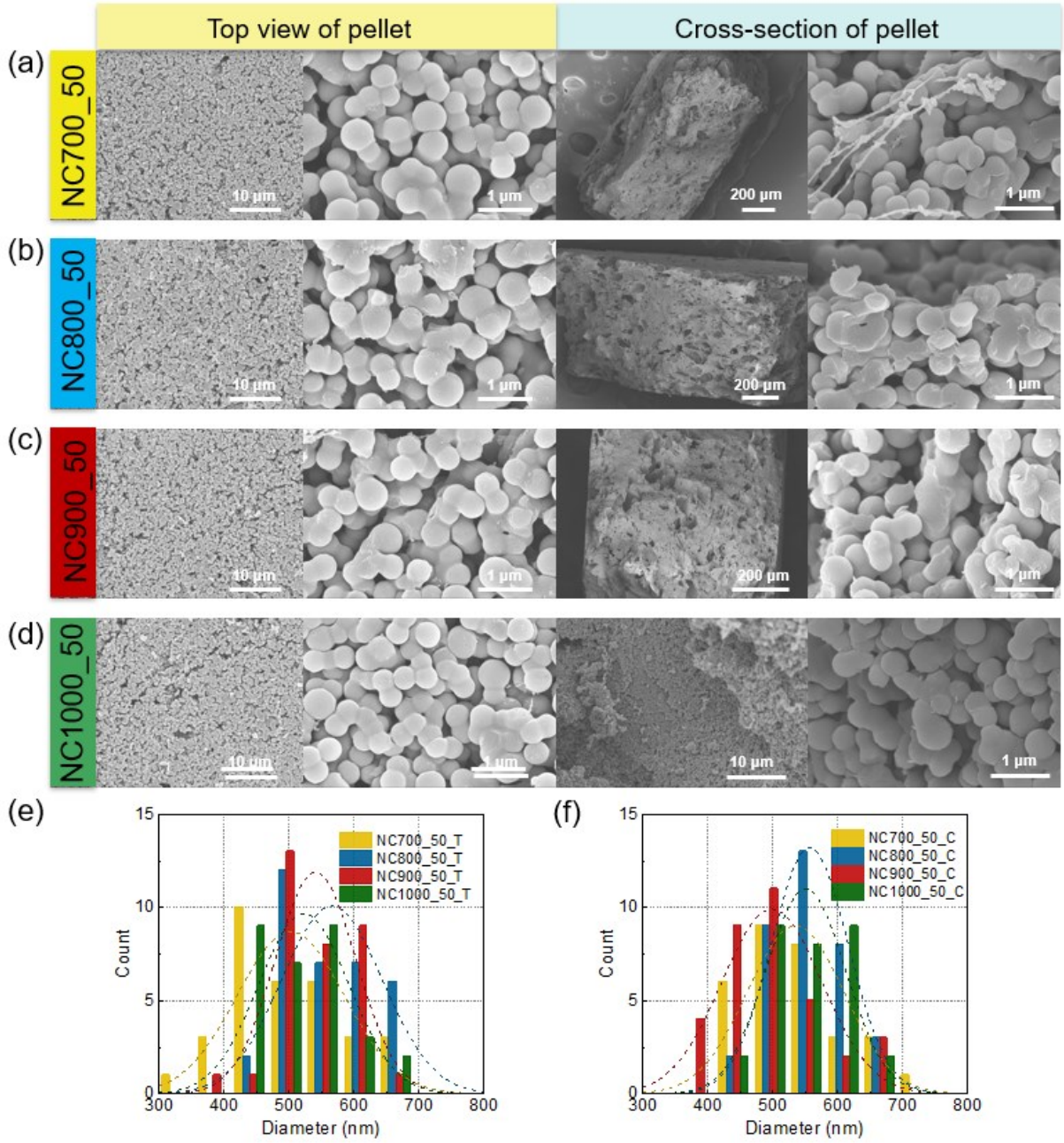

Figure 9.5 SEM images of (a) NC700_50, (b) NC800_50, (c) NC900_50, and (d) NC1000_50. (e) Pellet surface particle size distribution of NC700_0, NC_800_0, NC900_0, and NC1000_0, (f) pellet inner particle size distribution of NC700_0, NC_800_0, NC900_0, and NC1000_0.

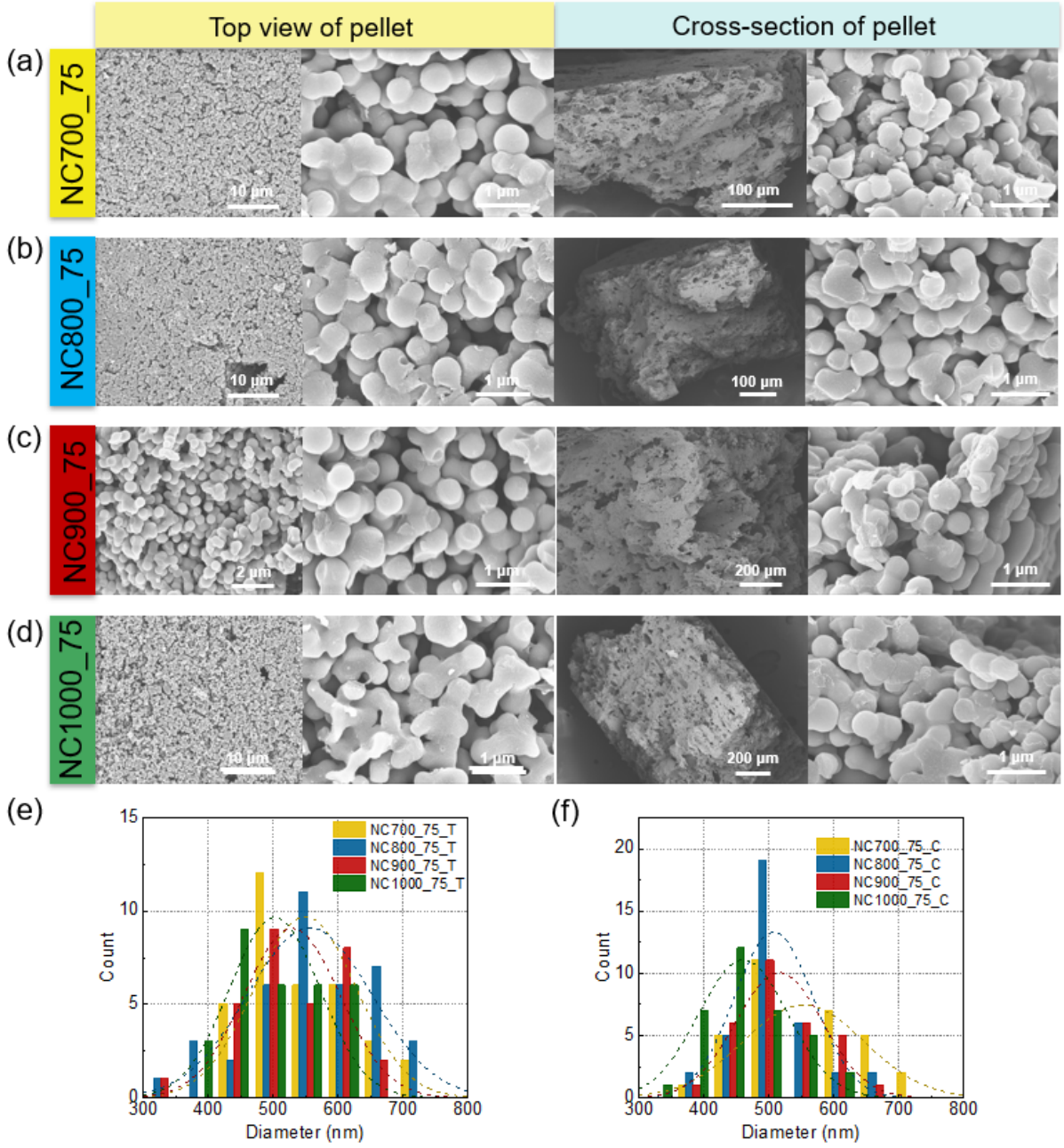

Figure 9.6 SEM images of (a) NC700_75, (b) NC800_75, (c) NC900_75, and (d) NC1000_75. (e) Pellet surface particle size distribution of NC700_0, NC_800_0, NC900_0, and NC1000_0, (f) pellet inner particle size distribution of NC700_0, NC_800_0, NC900_0, and NC1000_0.

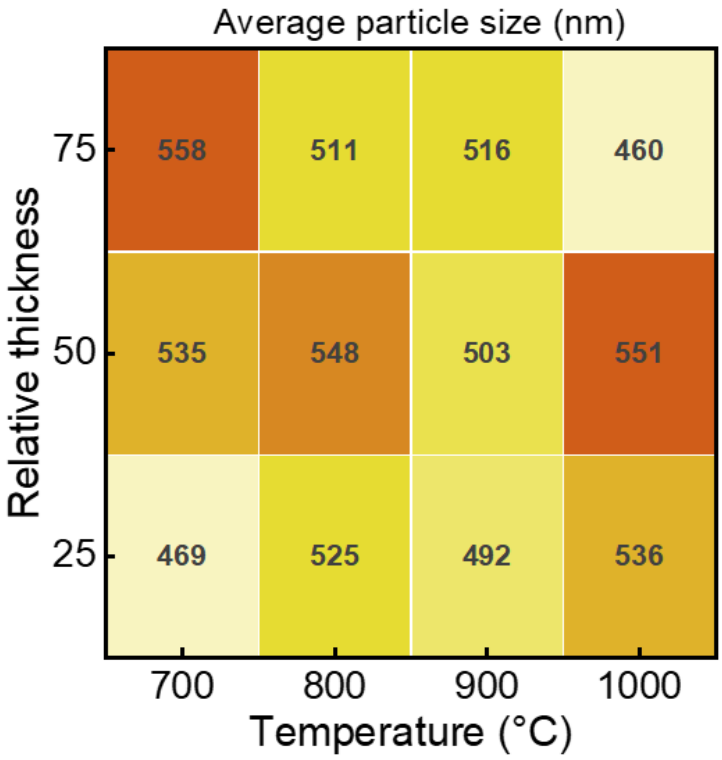

Figure 9.7 Average inner particle size of as-prepared pellet samples. (Darker colour means larger particle size)

9.1.2 Control the microstructure

Physical adsorption and SAXS characterisations were performed to obtain pore structural information to study the micro pore formation mechanism. From the N_2 adsorption isotherms (**Figure 9.8a-c**), one could see that both carbonisation temperatures and pellet thickness could significantly influence the specific surface area of the as-prepared samples. Specifically, with an increased carbonisation temperature, a reduced surface area could be seen (**Figure 9.8d**) and pore volume in **Figure 9.8e**. Both pellet specific surface area and pore volume increase with the pellet thickness. Pore size distributions were determined from the NLDFT model (**Figure 9.9**). Pellet samples have smaller pores (~ 0.6 nm) than powder samples (~ 0.8 nm), suggesting the pelleting process might distort the pore structures. It is important to mention that the pellets were directly tested without breaking as freestanding carbon electrodes. As melamine can decompose within the carbonisation pellet and generate gas, there might be structural pores between the particles caused by this process. Therefore, pellets were grounded

into powder using pestle and mortar and N_2 physical adsorption performed on the powdered samples for comparison. As shown in **Figure 9.10**, similar isothermal curves, specific surface area, and pore volume could be observed, suggesting the surface area was contributed from carbon particles.

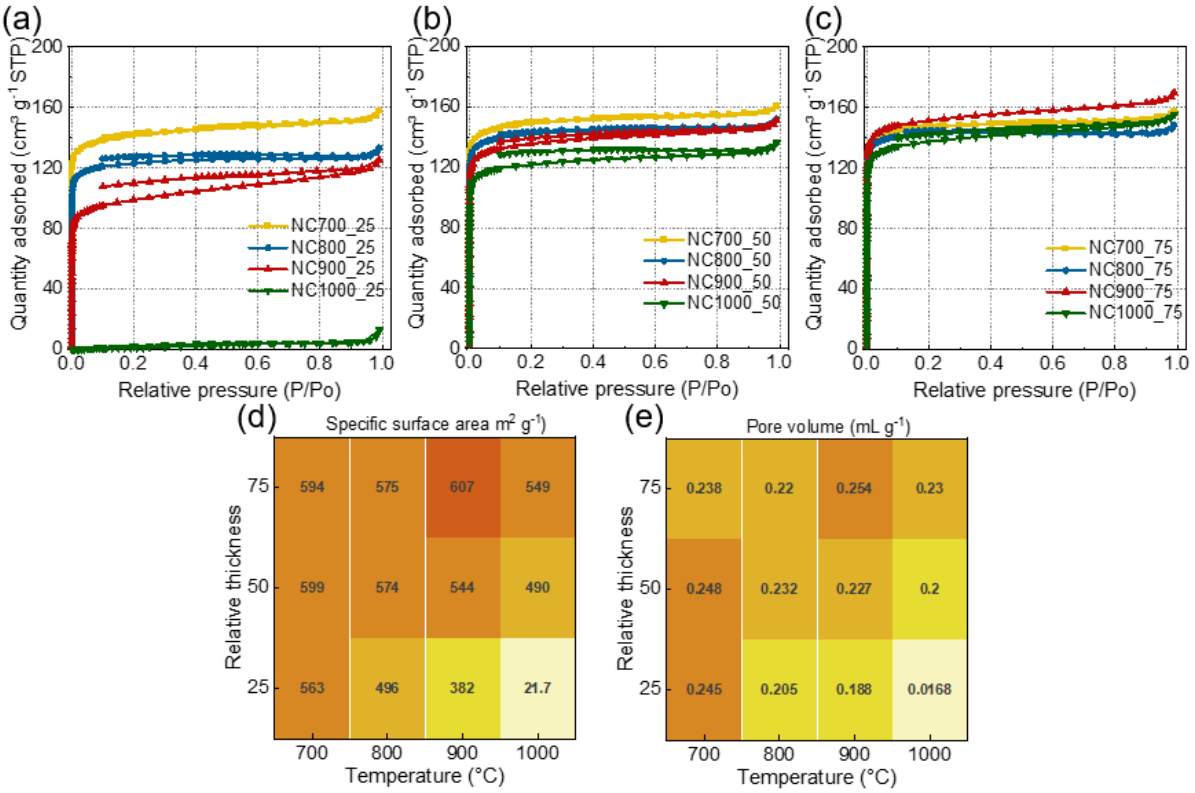

Figure 9.8 N2 adsorption isotherms for (a) NC700-1000_25, (b) NC700-1000_50, and (c) NC700-1000_75. Comparison of (d) specific surface area and (e) pore volume.

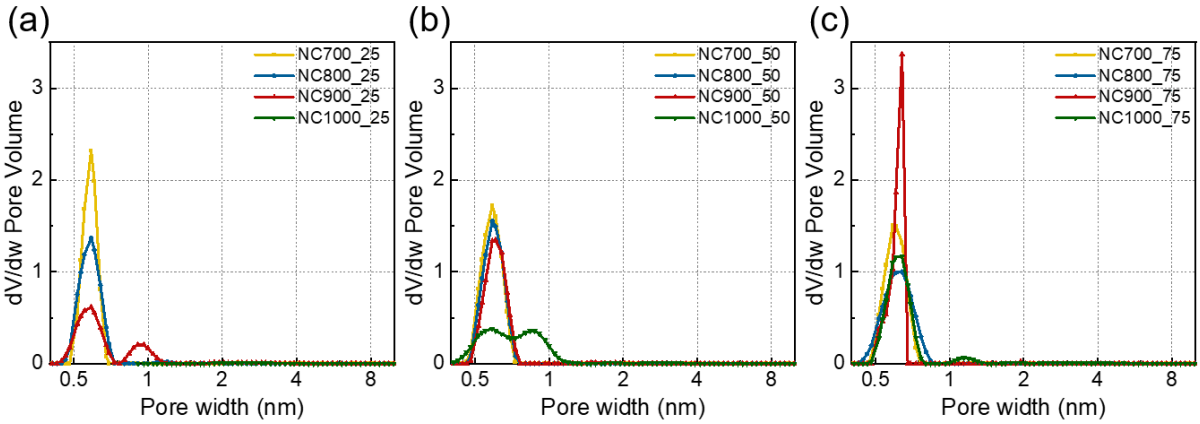

Figure 9.9 Pore size distribution for (a) NC700-1000_25, (b) NC700-1000_50, and (c) NC700-1000_75. (Darker colour means higher specific surface area and pore volume, respectively)

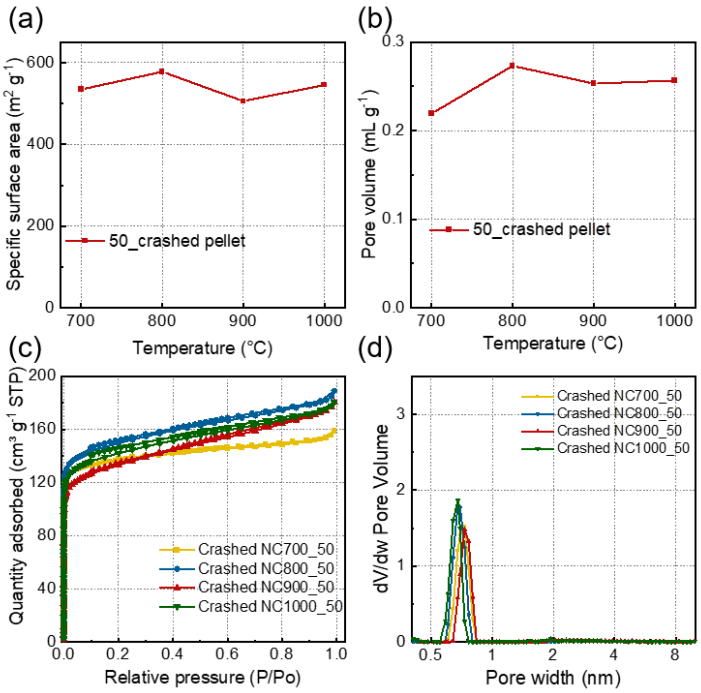

Figure 9.10 (a) Specific surface area of crashed NC700-1000_50. (b) The pore volume of crashed NC700-1000_50. (c) Isothermal curves of crashed NC700-1000_50. (d) Pore size distribution of crashed NC700-1000_50.

Fitted SAXS results showed that carbonisation temperatures and pellet thickness could influence the average pore diameter and relative amount of pores (B_2 value). As can be seen in **Figure 9.11d-e**, pore diameter increased with an increasing temperature from 700 °C to 900 °C and followed by a decreasing pore diameter from 900 °C to 1000 °C, reaching the highest value in NC900_75 (2.22 nm) and lowest value in NC700_25 (1.31 nm). On the contrary, NC900_75 (23.9 %) gives the lowest amount of the pore while NC700_25 (100%) gives the highest. This suggests that small pores tend to aggregate into bigger pores. Thus the amount of pore decreases. Besides, a bigger pore diameter could be observed in a thicker pellet. Raman spectroscopy was performed to get graphitisation information, and the fitted Id/Ig values were in **Figure 9.12b**. The decreasing of the Id/Ig values could be seen in decreasing the pellet thickness and increasing the carbonization temperature, suggesting a higher graphitized structure in higher temperatures.

The specific surface area, pore-volume, average pore diameter, total amount of pores, and graphitization degrees of the as-obtained samples were characterised. The results showed that both carbonization temperature and pellet thickness could influence all these microstructures, allowing us to tune these parameters to the desired applications. Specifically, the highest surface area is 600 m^2 g^{-1}, generated before 600 °C and is likely heritage from the HTC carbon spheres. The surface area and graphitization decreased with the temperature, while the thicker pellet preserves the higher surface area and increases the graphitization degree. This suggests the higher kinetics and better electrocatalytic performance in the pellet samples as the larger surface area could contribute to more active sites while a higher graphitization degree facilitates the electron transfer.

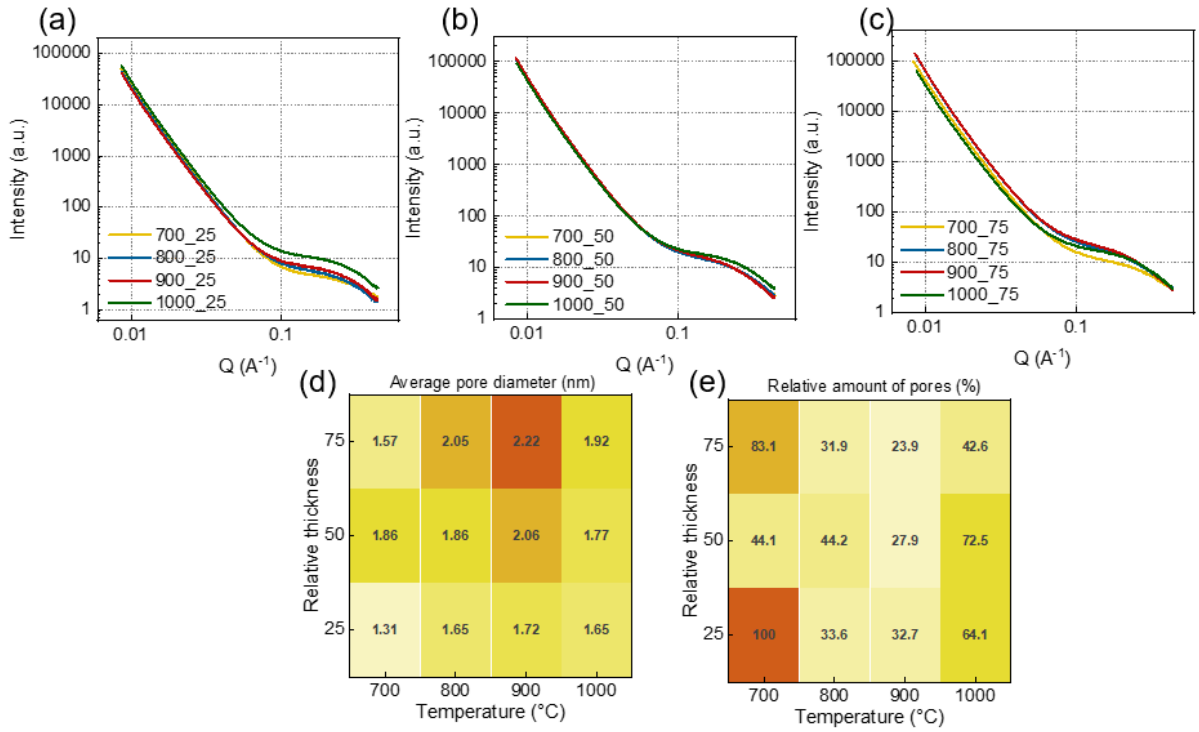

Figure 9.11 SAXS spectrums of (a) NC700-1000_25, (b) NC700-1000_50, (c) NC700-1000_75. Comparison of (d) average pore diameter and (e) relative amount of pores. (Darker colour means larger pore diameter and high relative amount of pores, respectively)

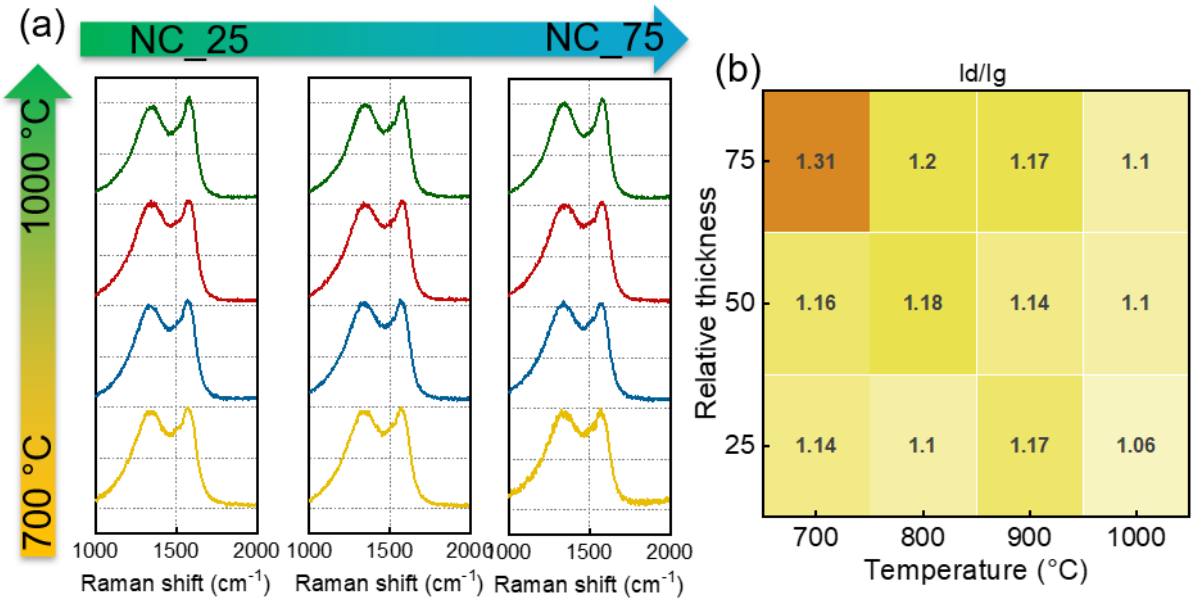

Figure 9.12 (a) Raman spectrums of as-prepared pellet samples. (b) Comparison of I_d/I_g value. (Darker colour means higher Id/Ig value)

9.1.3 Control the chemical structure

As shown in XPS survey spectrums in **Figure 9.13**, all samples showed a pronounced C (285 eV), much weaker N (400 eV) and O (533 eV) peaks. By comparing the atomic percentages of each sample via XPS (**Figure 9.14a**), we could see carbon content located mostly at 73.5 – 83.7 at%. Nitrogen content (**Figure 9.14b**) can vary from 5.26 – 15.8 at%, and a decrease of nitrogen content with the carbonisation temperatures could be observed, which could be ascribed to the unstable, weak bonding between nitrogen and carbon atoms at high temperature[262, 263]. When comparing nitrogen content in the same thickness, the nitrogen content in all samples suffers from a dramatic decrease at different temperatures from over 12.3 at% to 7.5 at% (NC_75), 10.9 at to 5.26 at%(NC_50), and 13.9 to 6.63 at% (NC_25), suggesting the thermal stability of bonds have been changed in different pellet thickness where NC_50 reached the higher thermal stability of nitrogen. Besides, at the same carbonization temperature, an increasing nitrogen content could be observed. Also, oxygen content could be seen in **Figure 9.14c**, and no significant trend could be found in the functional of the carbonization temperature and pellet thickness.[264]

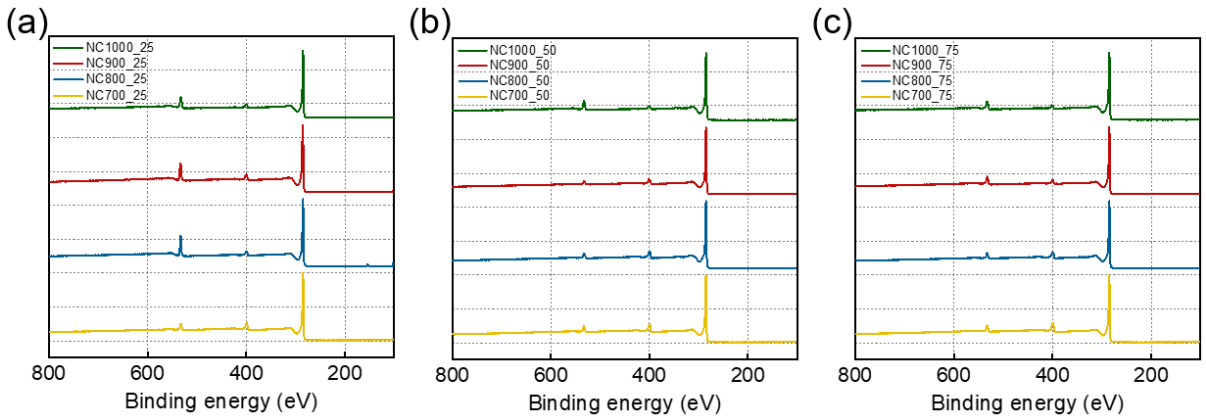

Figure 9.13 XPS surveys of (a) NC700-1000_25, (b) NC700-1000_50, and (c) NC700-1000_75.

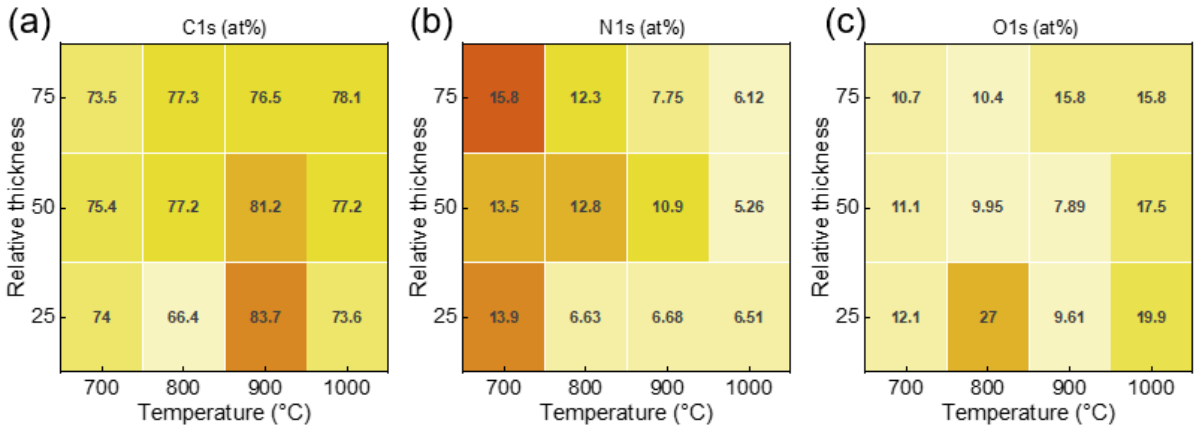

Figure 9.14 Elemental comparison of the as-prepared pellet samples. (a) Carbon content, (b) nitrogen content, and (c) oxygen content. (Darker colour means higher element content)

High-resolution spectrums of C1s, N1s, O1s were fitted to get more insights into the evolution of the pellet samples. No noticeable carbon composition differences could be found in carbon type shifts (**Figure 9.15**). N1s in **Figure 9.16** showed a trend changing with the increased carbonization temperature, where the intensity of pyridinic nitrogen peak decrease while the intensity of graphitic nitrogen increase. Nitrogen sites, especially pyridinic nitrogen and graphitic nitrogen, have been considered to contribute to the electrocatalytic activity.[74, 178] Thus, comparing pyridinic nitrogen and graphitic nitrogen has been made in **Figure 2.27b-c**. Overall, a decreasing trend of pyridinic nitrogen content could be observed with an increasing carbonization temperature. A similar sudden to overall nitrogen content could be seen in the pyridinic nitrogen, where 50 thickness gives higher pyridinic nitrogen preserves at high

temperature. No noticeable trend could be found in the pyridinic nitrogen content with pellet thickness. In terms of the graphitic nitrogen in **Figure 9.16c**, NC700_75 shows the highest amount of graphitic nitrogen, and NC800_50 showed the second high amount of graphitic. Besides, fitted O1s high-resolution spectrums could be seen in **Figure 9.17**, and one main peak centre locate at 532.5 eV suggests corresponding to aliphatic C-O bond.

To sum up, the chemical structures of the obtained samples have been revealed. By correlating carbon, nitrogen, and oxygen contents in the function of both carbonization temperature and pellet thickness, we have shown that carbonization temperatures and pellet thickness could influence the chemical structures of the obtained samples. In specific, pellet thickness at 50 could preserve more pyridinic and graphitic nitrogen at high temperatures.

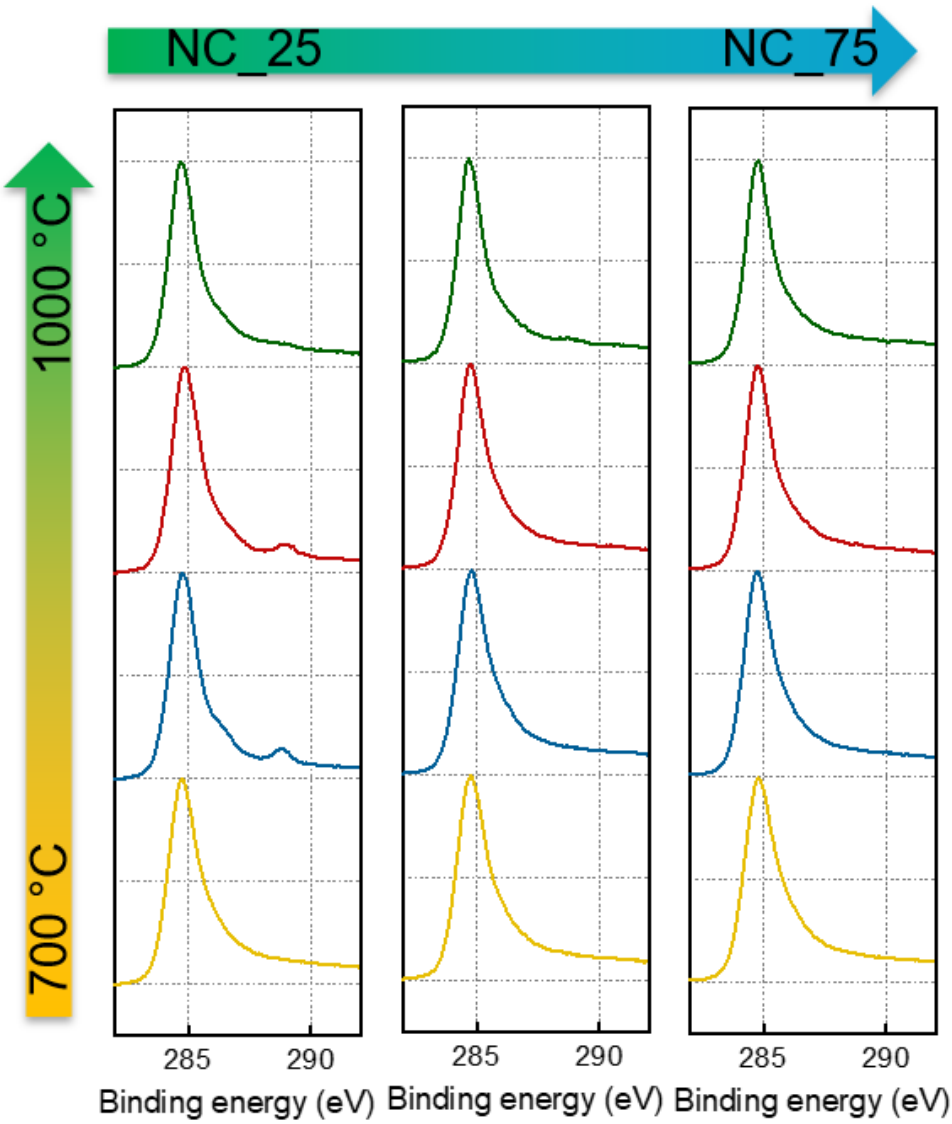

Figure 9.15 XPS high-resolution C1s spectrums evolution in the function of carbonization temperatures (from bottom to top: 700 °C to 1000 °C) and the thickness (from left to right: NC_25 to NC_75).

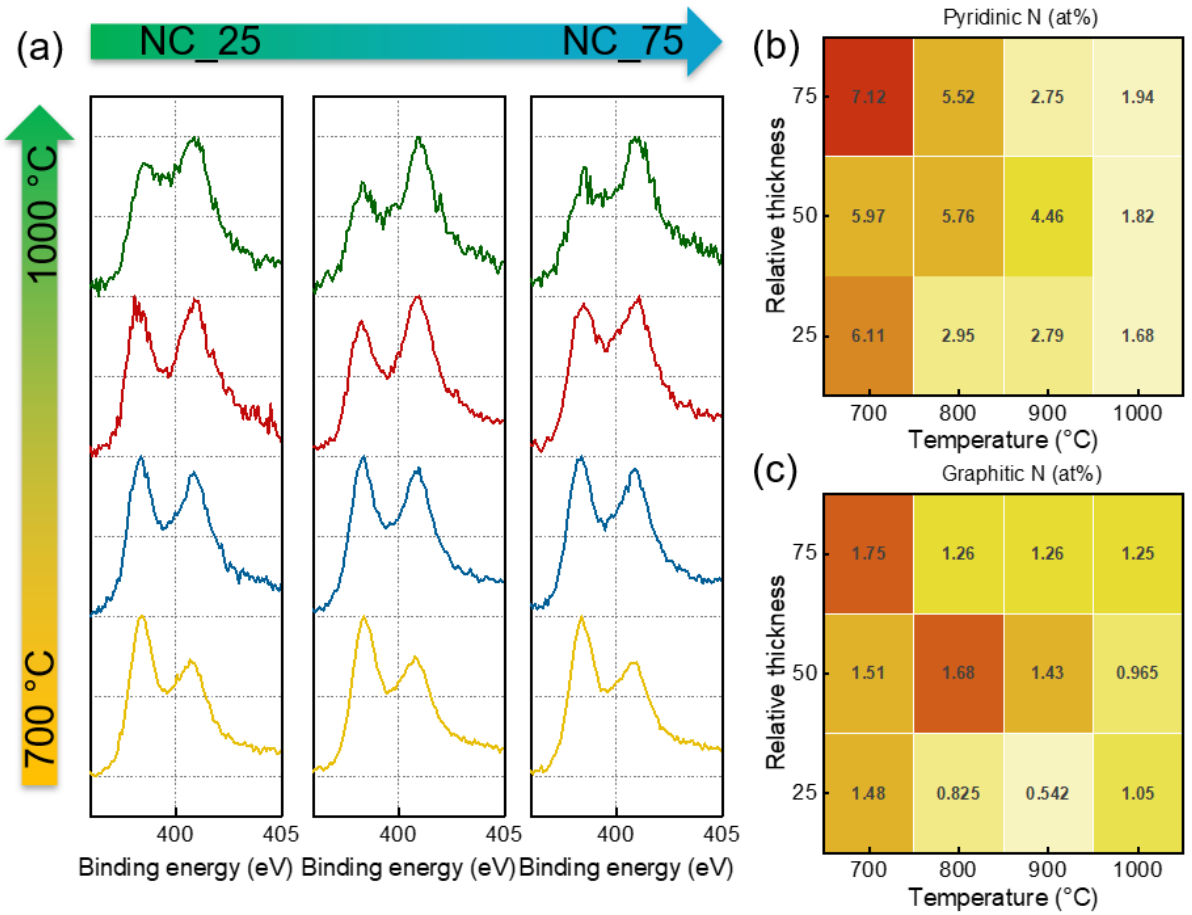

Figure 9.16 (a) XPS high-resolution N1s spectrums evolution in the function of carbonization temperatures (from bottom to top: 700 °C to 1000 °C) and the function of the thickness (from left to right: NC_25 to NC_75). (b) Pyridinic nitrogen content comparison of as-prepared pellet

samples. (c) Graphitic nitrogen content comparison for the as-prepared pellet samples. (Darker colour means higher nitrogen contents)

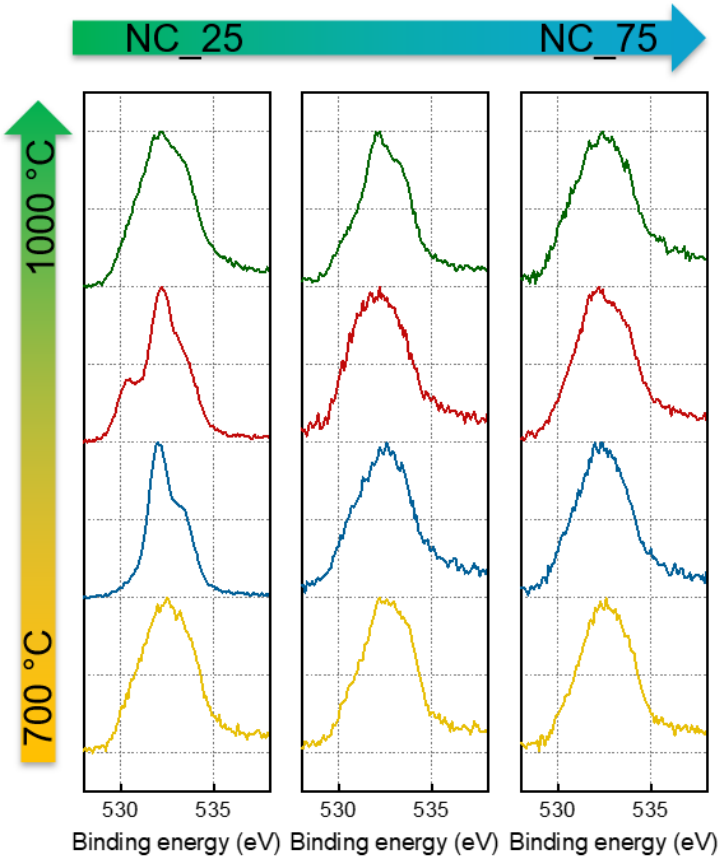

Figure 9.17 XPS high-resolution O1s spectrums evolution in the function of carbonization temperatures (from bottom to top: 700 °C to 1000 °C) and the thickness (from left to right: NC_25 to NC_75).

9.1.4 Electrochemical performance in RDE

To study how the structures could influence the final catalytic properties. RDE tests were carried on for the as-prepared samples. CV, LSV, and EIS were performed in both oxygen and nitrogen saturated 0.1 M KOH electrolyte. The onset potential, halfwave potential, and limiting current density were compared in **Figure 9.18**. As shown in **Figure 9.18**, carbonization temperature and pellet thickness could influence the onset potential, halfwave potential and limit current density. In terms of the influence of the carbonization temperature on the onset potential (**Figure 9.18a**), a decreasing onset potential with increasing carbonization temperature could be seen in thick pellets (NC_50 and NC_75 series), while no apparent trends could be found in NC_25 and NC_0 series. In terms of the pellet thickness influence to the

onset potential, an increasing onset potential with increasing pellet thickness could be seen in all samples. With the microstructure and chemical structure analysis, nitrogen contents, especially pyridinic nitrogen and graphitic nitrogen content, and specific surface area could be the main factors for the higher onset potential. Halfwave represents a mixture region of both mass transfer and kinetics, and it is also compared in **Figure 9.18b**. Both pellet thickness and carbonization have shown a correlation to the halfwave potential, where it decreases with the decrease of carbonization temperature and increase with the increase of pellet thickness. At the mass transfer control region (**Figure 9.18c**), the activity most relates to accessible active sites and the graphitization degree, increasing the total oxygen reduction current and decreasing the current loss during transport. The limiting current reached a high value in NC1000_50 and a second high value in NC700_75, attributed to the higher graphitization degree and higher nitrogen amount, respectively.

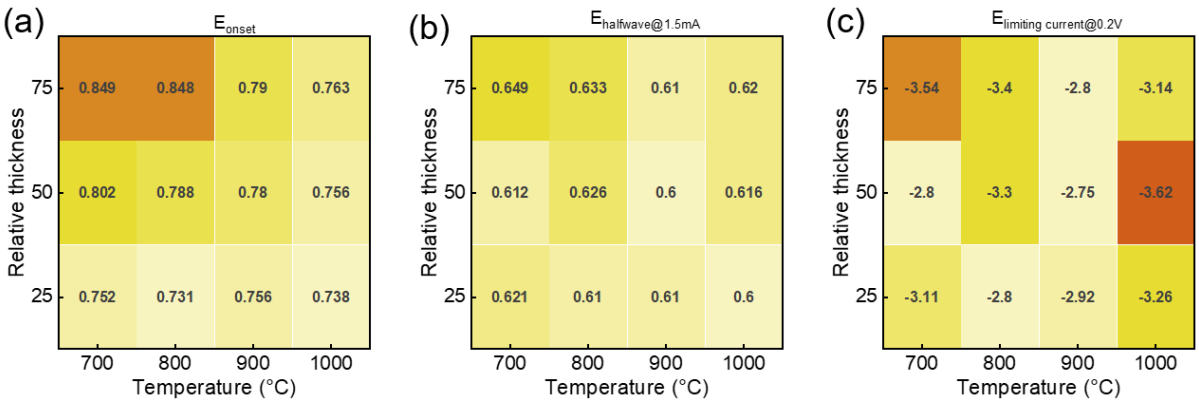

Figure 9.18 RDE three-electrode test, (a) Onset potential comparison. (b) Halfwave potential @ 1.5mA comparison. (c) Limiting current comparison at 0.2 V vs RHE. All pellet samples were crashed into power and tested in the RDE system. (Darker colour means higher E and limiting current values, respectively)

To sum up, together with the physical and chemical structures of the obtained pellet samples. A correlation has been set up on the microstructures and chemical structures, where the pyridinic, graphitic surface area could contribute to the onset potential. Besides, in the mass transfer region where all accessible active sites are utilized, higher graphitization degree and

surface area contribute to the limiting current. Therefore, by varying the carbonization temperature and pellet thickness, pellet samples with different structures could be obtained directly influencing their kinetic activities.

9.1.5 Electrochemical performance in freestanding electrode tip

To get more insights into the electrochemical performance without breaking pellet into powder, pellet samples were tested in the freestanding electrode. The onset potential and limiting current were compared in **Figure 9.19**. Both pellet thickness and carbonization temperature showed an influence on the catalytic activities. With an increasing carbonization temperature, a slightly increase onset potential could be found, but all in a similar range (0.84 to 0.86 V). On the contrary, relative high onset potentials could be observed in 50 thickness. In terms of the limiting current, the highest value could be found in NC800_50. A thicker pellet offers less current, which might cause by the higher resistance in the thicker pellet. These results suggest the thickness of the pellet plays an essential role in pellet form, which could relate to the length of the electron transfer route, whereas the thicker the pellet, the longer the transfer route and higher current loss. However, this requires more experiments and ideally modelling based on the CT scan to get more insights.

Similarly, increasing the carbonization temperature will result in a higher graphitization degree and decrease the current loss and results. Besides, a thicker pellet offers more active sites, as mentioned in the previous section. Therefore, the competition between active sites and conductivity dominates the final electrochemical performance in the pellet form, where NC800-900_50 provides an optimized electrochemical performance.

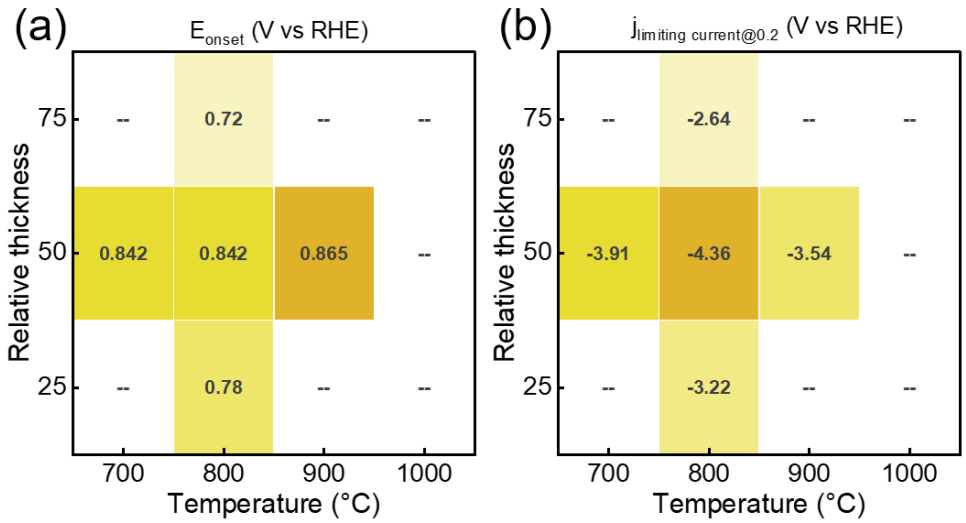

Figure 9.19 Freestanding electrode test. (a) Onset potential comparison for the as-prepared pellet samples. (b) Limiting current @ 0.2 V_{RHE} comparisons for the as-prepared pellet samples. (Darker colour means higher E values and limiting current, respectively)

To sum up, in this appendix section, we studied the influence of carbonisation temperatures and pellet thickness. We controlled the morphology, microstructure and chemical structure via different carbonisation temperatures and pellet thickness. We concluded that the pellet's electrochemical performance was dominated by competition between the active sites and the total length of the electron transfer path. We have identified the case of NC800_50 as showing the lowest onset potential and highest limiting current. This is due to the combination of high N content, nitrogen type, high surface area, high graphitisation level, and relatively thin thickness. These studies could help us identifying the optimised methods to control pellet structures to meet the requirements of target applications.

9.2 XAS FITTING PARAMETERS FOR CHAPTER 4

Table 9.1 XAS fitting parameters of Fe@NC900_50

Sample	Scattering pair	CN	R (Å)	ΔE_0 (eV)	σ^2 (10^{-3}Å^2)	R factor
Fe@NC900_50	Fe-N	4.5	2.06	0.73 +/- 1.86	0.005	0.01149
		+/- 0.2	± 0.01		Fixed	
	Fe-C	1.8	1.88		0.005	
		+/- 0.4	± 0.01		same as σ^2 (Fe-N)	
	Fe-Fe	0.9	2.56		0.01	
		+/-0.2	± 0.01		2*σ^2 (Fe-N)	

Table 9.2 XAS fitting parameters of Fe@NC900_50_900 cycles

Sample	Scattering pair	CN	R (Å)	ΔE_0 (eV)	σ^2 (10^{-3}Å^2)	R factor
Fe@NC900_50_900 cycles	Fe-N	4.5	2.01	-5.34 +/- 2.55	0.005	0.01129
		+/- 0.4	± 0.01		Fixed	
	Fe-C	2.1	1.84		0.005	
		+/- 0.6	± 0.01		same as σ^2 (Fe-N)	
	Fe-Fe	0.3	2.50		0.01	

		+/- 0.2	± 0.01		$2*\sigma^2$ (Fe-N)	

Table 9.3 XAS fitting parameters of Fe@NC900_50_0.8V_{RHE}

Sample	Scattering pair	CN	R (Å)	ΔE_0 (eV)	σ^2 (10^{-3}Å^2)	R factor
Fe@NC900_50_0.8V_{RHE}	Fe-N	4.06	2.03	-4.96 +/- 2.49	0.005	0.0096
		+/- 0.5	± 0.01		Fixed	
	Fe-C	2.28	1.85		0.005	
		+/- 0.5	± 0.01		same as σ^2 (Fe-N)	
	Fe-Fe	0.3	2.51		0.01	
		+/- 0.2	± 0.01		$2*\sigma^2$ (Fe-N)	

Table 9.4 XAS fitting parameters of Fe@NC900_50_0.7V_{RHE}

Sample	Scattering pair	CN	R (Å)	ΔE_0 (eV)	σ^2 (10^{-3}Å^2)	R factor
Fe@NC900_50_0.7V_{RHE}	Fe-N	4.4	2.03	-3.53	0.005	0.0038

		+/- 0.2	± 0.01	+/- 1.11	Fixed	
	Fe-C	1.9	1.86		0.005	
		+/- 0.3	± 0.01		same as σ^2 (Fe-N)	
	Fe-Fe	0.09	2.52		0.01	
		+/- 0.1	± 0.01		$2*\sigma^2$ (Fe-N)	

Table 9.5 XAS fitting parameters of Fe@NC900_50_0.6V_{RHE}

Sample	Scattering pair	CN	R (Å)	ΔE_0 (eV)	σ^2 ($10^{-3}Å^2$)	R factor
Fe@NC900_50_0.6V_{RHE}	Fe-N	4	2.02	-3.83 +/- 2.11	0.005	0.0090
		+/- 0.3	± 0.01		Fixed	
	Fe-C	1.9	1.85		0.005	
		+/- 0.5	± 0.01		same as σ^2 (Fe-N)	
	Fe-Fe	0.3	2.51		0.01	

		+/- 0.2	± 0.01		$2*\sigma^2$ (Fe-N)	

Table 9.6 XAS fitting parameters of Fe@NC900_50_0.5V_{RHE}

Sample	Scattering pair	CN	R (Å)	ΔE_0 (eV)	σ^2 ($10^{-3}Å^2$)	R factor
Fe@NC900_50_0.5V_{RHE}	Fe-N	3.4	2.05	-1.90 +/- 2.54	0.005	0.0073
		+/- 0.4	± 0.01		Fixed	
	Fe-C	1.9	1.87		0.005	
		+/- 0.5	± 0.01		same as σ^2 (Fe-N)	
	Fe-Fe	1.24	2.52		0.01	
		+/- 0.2	± 0.01		$2*\sigma^2$ (Fe-N)	

Table 9.7 XAS fitting parameters of Fe@NC900_50_0.4V_{RHE}

Sample	Scattering pair	CN	R (Å)	ΔE_0 (eV)	σ^2 ($10^{-3}Å^2$)	R factor
Fe@NC900_50_0.4V_{RHE}	Fe-N	4.3	2.03	-3.08	0.005	0.0062

		+/- 0.2	± 0.01	+/- 1.75	Fixed	
	Fe-C	1.6	1.85		0.005	
		+/- 0.4	± 0.01		same as σ^2 (Fe-N)	
	Fe-Fe	0.74	2.52		0.01	
		+/- 0.2	± 0.01		$2*\sigma^2$ (Fe-N)	

9.3 CIF FILE FOR OPTIMIZED ARTEMIS FITTING STRUCTURE

Optimized Fe-N_4 structure

FeN_4 structure

x	y	z
C	0.19755	0.32979	0.31221
C	0.26539	0.33134	0.34716
N	0.29741	0.23659	0.3472
N	0.17137	0.23374	0.28148
N	0.17873	0.02603	0.24033
C	0.11273	0.03148	0.20537
C	0.07597	0.12769	0.20831
C	0.10578	0.2257	0.24421
C	0.07844	-0.06167	0.16352
C	0.01098	-0.0589	0.12919
C	-0.02628	0.03255	0.13187
C	0.00663	0.12631	0.17079
C	0.21158	-0.06793	0.23406
C	0.18043	-0.16126	0.19301
C	0.1136	-0.15657	0.15832
N	0.30469	0.02885	0.30664
C	0.27933	-0.06642	0.26964
C	0.22011	-0.25377	0.19021
C	0.28614	-0.25218	0.22413
C	0.31827	-0.15803	0.26515
C	0.15977	0.42258	0.30796
C	0.09333	0.41504	0.27156
C	0.06489	0.31793	0.23942

C	-0.03294	0.2186	0.16963
C	-0.00232	0.31207	0.20388
C	0.29793	0.42595	0.37748
C	0.25921	0.51943	0.37305
C	0.19304	0.5178	0.34038
C	0.36382	0.23158	0.37908
C	0.39922	0.32574	0.41257
C	0.36505	0.42158	0.40982
C	0.40012	0.13491	0.37963
C	0.37056	0.03716	0.3418
C	0.41229	-0.05427	0.34034
C	0.38481	-0.1504	0.30085
C	0.46644	0.32277	0.44873
C	0.50277	0.23048	0.45287
C	0.46953	0.13638	0.41649
C	0.47915	-0.04874	0.37847
C	0.50912	0.04412	0.41756
C	-0.10135	0.21534	0.13324
C	-0.09473	0.03303	0.09589
C	-0.13196	0.12344	0.09686
C	0.57097	0.22977	0.49079
C	0.57725	0.04712	0.45604
C	0.6078	0.13898	0.49276
Fe	0.236	0.1293	0.3097
H	-0.01363	-0.13061	0.09942
H	0.08679	-0.22585	0.12664
H	0.19598	-0.32551	0.15926
H	0.31617	-0.32257	0.22093
H	0.06169	0.48367	0.26639
H	-0.03201	0.38288	0.20224
H	0.28444	0.59198	0.3965
H	0.16388	0.58904	0.3367
H	0.39284	0.49173	0.43408
H	0.41727	-0.21819	0.29955
H	0.49159	0.39494	0.47467
H	0.50915	-0.11926	0.3778
H	-0.12969	0.2874	0.13382
H	-0.11788	-0.03993	0.06688
H	-0.18477	0.12236	0.06837
H	0.59434	0.30293	0.5182
H	0.60553	-0.02499	0.45592
H	0.66042	0.13989	0.52263

FeN_4-O

	x	y	z
C	0.08335	0	0.22667
C	0.04167	0.125	0.22667
C	0.1667	0	0.22667
C	0.2081	0.12459	0.22648
C	0.33335	0	0.22667

C	0.2916	0.12336	0.22617
C	0.4167	0	0.22667
C	0.45844	0.12337	0.22617
C	0.58335	0	0.22667
C	0.54195	0.12459	0.22647
C	0.6667	0	0.22667
C	0.70837	0.125	0.22667
C	0.08335	0.25	0.22667
C	0.04167	0.375	0.22667
C	0.16802	0.25048	0.2268
C	0.2125	0.37392	0.22931
C	0.33289	0.24642	0.22712
N	0.29455	0.36835	0.23089
C	0.41715	0.24643	0.22708
N	0.45548	0.3684	0.23061
C	0.58203	0.25048	0.2268
C	0.53755	0.37392	0.22924
C	0.6667	0.25	0.22667
C	0.70837	0.375	0.22667
C	0.08335	0.5	0.22667
C	0.04167	0.625	0.22667
C	0.17044	0.5	0.22932
C	0.21249	0.62608	0.22934
N	0.29456	0.63163	0.23087
N	0.4555	0.63164	0.23073
C	0.57961	0.5	0.22925
C	0.53756	0.62609	0.22929
C	0.6667	0.5	0.22667
C	0.70837	0.625	0.22667
C	0.08335	0.75	0.22667
C	0.04167	0.875	0.22667
C	0.16802	0.74952	0.22683
C	0.2081	0.87541	0.22649
C	0.3329	0.75357	0.22709
C	0.29161	0.87663	0.22616
C	0.41716	0.75356	0.22706
C	0.45844	0.87664	0.22615
C	0.58204	0.74953	0.22682
C	0.54195	0.87542	0.22648
C	0.6667	0.75	0.22667
C	0.70837	0.875	0.22667
Fe	0.37504	0.49995	0.25815
H	-0.02523	0.125	0.22667
H	0.77528	0.125	0.22667
H	-0.02523	0.375	0.22667
H	0.77528	0.375	0.22667
H	-0.02523	0.625	0.22667
H	0.77528	0.625	0.22667
H	-0.02523	0.875	0.22667
H	0.77528	0.875	0.22667

O	0.3753	0.50003	0.36754

FeN_4-O_2

	x	y	z
C	0.08335	0	0.22667
C	0.04167	0.125	0.22667
C	0.1667	0	0.22667
C	0.20809	0.12457	0.22614
C	0.33335	0	0.22667
C	0.29157	0.12316	0.22582
C	0.4167	0	0.22667
C	0.45848	0.12316	0.22587
C	0.58335	0	0.22667
C	0.54195	0.12457	0.2262
C	0.6667	0	0.22667
C	0.70837	0.125	0.22667
C	0.08335	0.25	0.22667
C	0.04167	0.375	0.22667
C	0.16802	0.25036	0.22636
C	0.21258	0.37368	0.22851
C	0.33286	0.24604	0.22648
N	0.29443	0.36806	0.22923
C	0.4172	0.24605	0.22657
N	0.45562	0.36805	0.22945
C	0.58203	0.25036	0.22641
C	0.53746	0.37368	0.22863
C	0.6667	0.25	0.22667
C	0.70837	0.375	0.22667
C	0.08335	0.5	0.22667
C	0.04167	0.625	0.22667
C	0.17043	0.50012	0.22945
C	0.21248	0.62636	0.23051
N	0.2945	0.63166	0.23406
N	0.45557	0.63169	0.23413
C	0.57961	0.50012	0.22948
C	0.53757	0.62636	0.23049
C	0.6667	0.5	0.22667
C	0.70837	0.625	0.22667
C	0.08335	0.75	0.22667
C	0.04167	0.875	0.22667
C	0.16801	0.74964	0.22742
C	0.20808	0.87551	0.22709
C	0.33289	0.7539	0.22956
C	0.29161	0.87664	0.2272
C	0.41717	0.75389	0.22957
C	0.45844	0.87665	0.2272
C	0.58204	0.74964	0.2274
C	0.54197	0.87551	0.22708
C	0.6667	0.75	0.22667
C	0.70837	0.875	0.22667

Fe	0.37493	0.49836	0.25264
H	-0.02523	0.125	0.22667
H	0.77528	0.125	0.22667
H	-0.02523	0.375	0.22667
H	0.77528	0.375	0.22667
H	-0.02523	0.625	0.22667
H	0.77528	0.625	0.22667
H	-0.02523	0.875	0.22667
H	0.77528	0.875	0.22667
O	0.37485	0.48256	0.36891
O	0.37491	0.36447	0.40664

FeN_4-$2O_2$

	x	y	z
C	0.08335	0	0.22667
C	0.04167	0.125	0.22667
C	0.1667	0	0.22667
C	0.20809	0.12457	0.22614
C	0.33335	0	0.22667
C	0.29157	0.12316	0.22582
C	0.4167	0	0.22667
C	0.45848	0.12316	0.22587
C	0.58335	0	0.22667
C	0.54195	0.12457	0.2262
C	0.6667	0	0.22667
C	0.70837	0.125	0.22667
C	0.08335	0.25	0.22667
C	0.04167	0.375	0.22667
C	0.16802	0.25036	0.22636
C	0.21258	0.37368	0.22851
C	0.33286	0.24604	0.22648
N	0.29443	0.36806	0.22923
C	0.4172	0.24605	0.22657
N	0.45562	0.36805	0.22945
C	0.58203	0.25036	0.22641
C	0.53746	0.37368	0.22863
C	0.6667	0.25	0.22667
C	0.70837	0.375	0.22667
C	0.08335	0.5	0.22667
C	0.04167	0.625	0.22667
C	0.17043	0.50012	0.22945
C	0.21248	0.62636	0.23051
N	0.2945	0.63166	0.23406
N	0.45557	0.63169	0.23413
C	0.57961	0.50012	0.22948
C	0.53757	0.62636	0.23049
C	0.6667	0.5	0.22667
C	0.70837	0.625	0.22667
C	0.08335	0.75	0.22667
C	0.04167	0.875	0.22667

C	0.16801	0.74964	0.22742
C	0.20808	0.87551	0.22709
C	0.33289	0.7539	0.22956
C	0.29161	0.87664	0.2272
C	0.41717	0.75389	0.22957
C	0.45844	0.87665	0.2272
C	0.58204	0.74964	0.2274
C	0.54197	0.87551	0.22708
C	0.6667	0.75	0.22667
C	0.70837	0.875	0.22667
Fe	0.37505	0.49977	0.23169
H	-0.02523	0.125	0.22667
H	0.77528	0.125	0.22667
H	-0.02523	0.375	0.22667
H	0.77528	0.375	0.22667
H	-0.02523	0.625	0.22667
H	0.77528	0.625	0.22667
H	-0.02523	0.875	0.22667
H	0.77528	0.875	0.22667
O	0.375	0.49354	0.37802
O	0.37479	0.35048	0.40845
O	0.37499	0.50623	0.08537
O	0.31204	0.59876	0.05451